

DESIGN AND CONSTRUCTION OF THE SPIRIT TPC

By

Suwat Tangwancharoen

A DISSERTATION

Submitted to
Michigan State University
in partial fulfillment of the requirements
for the degree of

Physics-Doctor of Philosophy

2016

ABSTRACT

DESIGN AND CONSTRUCTION OF THE SPIRIT TPC

By

Suwat Tangwancharoen

The nuclear symmetry energy, the density dependent term of the nuclear equation of state (EOS), governs important properties of neutron stars and dense nuclear matter. At present, it is largely unconstrained in the supra-saturation density region. This dissertation concerns the design and construction of the S π RIT Time Projection Chamber (S π RIT TPC) at Michigan State University as part of an international collaborations to constrain the symmetry energy at supra-saturation density. The S π RIT TPC has been constructed during the dissertation and transported to Radioactive Isotope Beam Factory (RIBF) at RIKEN, Japan where it will be used in conjunction with the SAMURAI Spectrometer. The detector will measure yield ratios for pions and other light charged particles produced in central collisions of neutron-rich heavy ions such as $^{132}\text{Sn} + ^{124}\text{Sn}$. The dissertation describes the design and solutions to the problem presented by the measurement. This also compares some of the initial fast measurement of the TPC to calculation of the performance characteristics.

ACKNOWLEDGMENTS

The design and construction of the SAMURAI Pion-Reconstruction and Ion Tracker Time Projection Chamber ($S\pi$ RIT TPC) involved an international collaboration to study and constrain the symmetry energy term in the nuclear equation of state (EOS) at twice supra-saturation density. The TPC design and construction as well as many additional aspects of the project were supported financially by the U.S. and U.S. part of the collaboration who obtained a \$1.2M grant from DOE to construct the TPC and to ship it to RIKEN. The U.S. grants also provided partial travel support for the U.S. participants to go to RIKEN to install the TPC as well as to do commissioning and physics experiments.

The SAMURAI magnet, the laser calibration system, the gas-handling system, the mounting structure, the beam tracking, the TPC electronics, data acquisition, ancillary trigger detectors and other equipment required for these measurements were to be provided by our Japanese collaborators in the original proposal. The Japan group obtained a grant from the Ministry of Education, Culture, Sport, Science and Technology (MEXT) to purchase the GET electronics. The followings give a rough description of the shared tasks between the US and Japan group.

Packing/Dismantling and shipping (MSU): To arrange packing, dismantling and shipping of the $S\pi$ RIT equipment to/from RIKEN.

Housing (RIKEN): Provision of Room to install the equipment.

Preparation of the $S\pi$ RIT Device (MSU and RIKEN): Installation of GET electronics and tests.

Installation of the $S\pi$ RIT Device in the experimental area (MSU and RIKEN): Installation of the full $S\pi$ RIT Device, including the Time Projection Chamber into SAMU-

RAI and coupling to beam line.

Beam tracking (RIKEN: SAMURAI Collaboration): Resolution, timing, PPAC or MWPC,

Spectrometers (RIKEN: SAMURAI Collaboration): Installation, tests, calibration and maintenance of all detection systems of the apparatus.

Data Acquisition at RIKEN (RIKEN): Coupling with RIKEN DAQ Tests Calibrations.

With time, other international groups joined the project. For the ancillary trigger detectors: The Chinese group provided the Active collimator veto counter, the Polish collaborators provided the Katana forward veto forward wall while the side multiplicity arrays were constructed by the Kyoto group. Our Polish group also built a trigger box for the experiment. The R3B group from GSI in Germany provided the NeuLAND neutron detector array as well as two highly enriched ^{112}Sn and ^{124}Sn targets (600 mg/cm²). The students in the Korean group made very significant contributions to software development both for online and offline analysis.

To facilitate communications and to avoid misunderstanding, a weekly teleconference meeting on the project was convened between the US and Japan group. Other groups such as the Korean group and occasionally the Polish group also joined.

The TPC project was funded in October 1, 2010. The enclosure and the first version of the target mechanism was constructed at Texas A&M while the main part of the detector was designed and constructed at Michigan State University. After construction was finished in May, 2013 and initial testing at MSU, the device was shipped to RIKEN in February, 2014. The GET electronics was fully installed in August, 2015. The TPC underwent its first beam test in October, 2015. It was later commissioned inside the SAMURAI magnet in

April, 2016. The $S\pi$ RIT TPC was then successfully used in two experiments in conjunction with the SAMURAI dipole magnet at RIKEN, Japan in May 2016.

My major responsibility for the project is to design and to test the gating grid driver which is used to control the operation of the gating grid. After the first commission run minor changes were made to the driver circuit. The driver was then used successfully in the second commission runs and two experiments (a total two weeks of beam time). After some tuning, the new driver was able to control the operation of the gating grid as expected.

The design and construction of the TPC was mainly led by Jon Barney, Justin Estee, Rebecca Shane, Alan McIntosh and Bob Olsen under the supervision of Professors William Lynch and Betty Tsang. When I joined the MSU $S\pi$ RIT TPC group in the Fall of 2011, I became involved with all phases of the construction of the TPC as described in this thesis. I helped whenever I was needed. I took the lead responsibility in designing gating grid driver and the construction of the voltage step down (VSD). The VSD can step down the high voltage from the cathode (20000 V) to ground without sparking. This high voltage would be required for Hydrogen or Helium based counter gases. Until now, the TPC has only be used with P10 gas which requires a voltage of 7000 V or less. I tested and planned the procedures to build the voltage step down as described in Chapter 2.5. Additionally, to evaluate the performance of the TPC, My colleagues (Justin Estee and Yaofeng Zhang) and I ran a series of simulations using GARFIELD, a program for simulating drift chamber and function of the gating grid. These results help us understand how to tune the detector.

My work with the TPC project also involved solving problems encountered in other areas. Subsequently, I developed expertise in all gluing procedures, (including gluing of the circuit boards for the gating grid, ground and anode wires) and leak checking the I also learned how to run SpiRIT ROOT to obtain the first results when half of the GET electronics

(6000 channels) was installed. I did the data analysis and worked with Prof. Lynch to demonstrate that the initial design of the "ZAP" adapter board that was used to connect the GET electronics to the TPC would produce unacceptably larger noise due to its large capacitance. This analysis led us to abandon that design involving flexible circuit boards in favor of the present design, which does not add significantly to the intrinsic noise of the GET electronics.

My analysis was also instrumental in suggesting that there was non-uniformity in the gains of the original GET electronics as they were shipped to Japan. My results on selected channels were confirmed by Genie Jhang, a Korean graduate student who was responsible for the software, but the French engineers did not believe the results because no such linearity was reported by any other group. Jon Barney then demonstrated that this was not due to a defect in the connections between GET electronics and the TPC. To understand better this problem, we explored the non-uniformity in the positive input signal mode (used by $S\pi$ RIT) and the negative input signal mode (used by the ATTPC) and discovered that the non-uniformity was not present in the negative input mode. When Genie and the RIKEN group showed that all channels of the GET electronics exhibited the same non-uniform behavior on positive , we could convince the French engineers to seriously look for the problem and they found a flaw in the design, that required modifyig the module. Thus all the AGET and ADC (ASAD) boards were returned to France for repair and caused a delay of the project by 6 months and required us to abandon the first beam time slot that we had pushed to obtain.

The project would not be successful without the tremendous effort of the team. I would like to thank all my colleagues for the support during my stay at MSU working on my Ph.D. thesis and valuable advices from my advisor, Bill Lynch and from Betty Tsang. The names

of those who have made contributions to the S π RIT project are listed below. The Postdocs who were supported by the DOE grants, graduate students and undergraduate students who have made major contributions to the construction project which is the main topic of the thesis are also listed with the dates associated with the project. The institutions are listed in the order of contributions to the project.

Michigan State University, USA

William G. Lynch (Co-PI and Spokesperson), Manyee Betty Tsang (PI and Spokesperson), Rebecca Shane (postdoc, 2011-2014), Giordano Cerizza (Postdoc, 2015-), Jon Barney (undergraduate student, 2011-2013, Graduate student, 2013-), Justin Estee (undergraduate student, 2011-2014, Graduate student, 2014-), Suwat Tangwancharoen (Graduate student, 2011-2016), Zbigniew Chajeccki (postdoc), Fei Lu (postdoc), Pierre Morfouace, Prabi Palni, Clementine Santamaria (Postdoc, 2015-), John Yurkon (Staff), Corinne Anderson (undergraduate student, 2012-), Kraig Andrews (undergraduate student), Ben Brophy (undergraduate student), Peter Chan (Summer undergraduate student), Jimmy Dunn (undergraduate student), Ed Ersoy (undergraduate student), Jon Gilbert (undergraduate student), Han Setiawan (undergraduate student, 2013-), David Witalka (undergraduate student), Rachel Hodges (Graduate student), Juan Manfredi (Graduate student), Jack Winkelbauer (Graduate student), Mike Young (Graduate student).

Kyoto University, Japan

Tetsuya Murakami (Japanese PI and Spokesperson), Nori Nakatsuka (Graduate student), Masanori Kaneko (Graduate student 2014-)

RIKEN, Japan

Hidetada Baba (Staff), TadaAki Isobe (Spokesperson), Mizuki Kurata-Nishimura (Postdoc 2013-), Hiroyoshi Sakurai (Staff), Daisuki Suzuki (Staff), Atsushi Taketani (Staff)

Texas A&M University, USA

Sherry Yennello (Co-PI), Bob Olsen (Staff), Alan McIntosh (Postdoc 2010-2013), Matt Chapman (undergraduate student)

Korea University, South Korea

Byungsik Hong (Faculty), Genie Jhang (Graduate student, 2013-), JungWoo Lee (Graduate student, 2014-)

Institute of Nuclear Physics, Poland

Jerzy Lukasik (Staff), Piotr Pawloski (Staff), Kristof Pelzar (Staff), Pawel Lasko (Graduate Student)

Tsinghua University, China

Rensheng Wang (Graduate student), Zhang Yan (Graduate student 2015-), Zhigang Xiao (Faculty)

Western Michigan State University, USA

Mohamed ElHossieny (Graduate student), Michael Famiano (CoPI), Charlie Snow (undergraduate student), Steve Dye (undergraduate student),

Beijing Normal University, China

Yaofeng Zhang (Lecturer)

Rare Isotope Science Project, South Korea

Hyosang Lee (Staff), Young Jin Kim (Staff)

University of Liverpool, UK

Marielle Chartier (Faculty), William Powell (Graduate student), Jaime Norman (undergraduate student)

TABLE OF CONTENTS

LIST OF TABLES	xi
LIST OF FIGURES	xii
Chapter 1 Particle Observation	1
1.1 A brief history of visual particle detectors	1
1.2 Proportional counter	5
1.3 Time Projection Chamber	14
1.4 $S\pi$ RIT Time Projection Chamber	16
1.5 Choice of gas	20
Chapter 2 Descriptions of SPiRIT TPC	30
2.1 The design and construction of the field cage of the $S\pi$ RIT TPC	30
2.1.1 Conductive painted components	31
2.1.2 Side walls	33
2.1.3 Front wall	36
2.1.4 Exit window	39
2.1.5 Cathode	42
2.1.6 Field cage assembly	43
2.1.7 Electrostatics of field cage	52
2.2 The design and construction of the pad plane of the $S\pi$ RIT TPC	59
2.2.1 Pad plane assembly	59
2.2.2 Pad response function	68
2.3 The design and construction of the wire planes of the $S\pi$ RIT TPC	74
2.3.1 Wire winding and tension measurement	74
2.3.2 Wire plane circuit board	76
2.3.3 Wire plane assembly	81
2.4 The design and construction of the enclosure of the $S\pi$ RIT TPC	88
2.5 The design and construction of the voltage step down of the $S\pi$ RIT TPC	89
2.6 The design and construction of the target mechanism of the $S\pi$ RIT TPC	94
2.7 Overall design assembly of the $S\pi$ RIT TPC	97
2.8 Electronics	104
2.9 Planned trigger system	108
2.10 Gas handling system	115
Chapter 3 Gating grid	119
3.1 Purpose of the gating grid	119
3.2 Simulation of gating grid	124
3.2.1 Single wire plane and a conducting plane	124
3.2.2 Superposition of the electric field	127

3.2.3	Monopolar gating grid	129
3.2.4	Bipolar gating grid	134
3.3	Gating grid driver	137
3.3.1	Design criteria	138
3.3.2	Conceptual design	138
3.3.3	Gating grid driver prototype 1	140
3.3.4	Gating grid driver prototype 2	146
3.3.5	Gating grid driver prototype 3	150
3.3.6	Gating grid driver prototype 4	152
3.3.6.1	Basic design	152
3.3.6.2	Tests and optimization of version 4 gating grid driver	153
3.3.6.3	Measurements and optimization fo the Induced signals on the pads using the GET TPC readout electronics	163
3.3.7	Gating grid driver test	169
Chapter 4	Conclusions	174
4.1	Conclusions	174
BIBLIOGRAPHY	176

LIST OF TABLES

Table 1.1:	List of variables.	5
Table 1.2:	Design parameters of the S π RIT TPC.	17
Table 2.1:	Properties of wire planes of the S π RIT TPC.	74
Table 2.2:	Radii of round corners of the votlage step down.	93
Table 2.3:	Configuration options for AGET [1]	107
Table 3.1:	Dissociation and ionization energy of gases [2]	122
Table 3.2:	The effect of tuning the gating grid driver with Cn and Cp. Rp = 0.95 Ω , Rn = 1.05 Ω	163
Table 3.3:	Negative peak height of the induced signal from the transition of the gating grid driver	164

LIST OF FIGURES

Figure 1.1:	A positron track was photographed from a cloud chamber under the magnetic field of 15000 gauss [3].	2
Figure 1.2:	A bubble chamber picture. The dark lines are tiny bubbles formed along the paths of charged particles under a strong magnetic field [4].	4
Figure 1.3:	Landau distribution	7
Figure 1.4:	Basic structure of a proportional chamber [5]	8
Figure 1.5:	Range of operation for gas-filled detector [5].	8
Figure 1.6:	Simple structure of multiwire proportional chambers [5]	10
Figure 1.7:	Crossection diagram of MWPC	11
Figure 1.8:	Electric field of a multiwire proportional chamber. All wires has potential of 1 V and the outer electrodes has the potential of 0 V. The calculation shows the result for $d = 40 \mu\text{m}$, $s = 1 \text{ mm}$, $L = 8 \text{ mm}$ [6].	12
Figure 1.9:	The two cathode planes are divided into strips parallel and orthogonal to the wires; coordinate x parallel to the sense wires and coordinate y orthogonal to the sense wires. [7].	13
Figure 1.10:	A schematic shows the operation of PEP-4 TPC [8]	14
Figure 1.11:	The reconstructed tracks from a 200 GeV per nucleon Au-Au collision using the STAR TPC [8]	16
Figure 1.12:	An exploded view of S π RIT TPC. More information is available in Section Design and construction of the S π RIT TPC.	17
Figure 1.13:	Operation of the TPC [9]	18
Figure 1.14:	The first Townsend coefficient as a function of electric field strength [10].	21
Figure 1.15:	The first Townsend for noble gases [11].	22

Figure 1.16:	Gas amplification (gain) for different mixtures as a function of anode voltage.	24
Figure 1.17:	Drift velocity of an electron in P-10 gas as a function of the ratio of electric field [12].	25
Figure 1.18:	Drift velocity of an electron in P-10 gas as a function of the fraction of Methane [13].	26
Figure 1.19:	Longitudinal diffusion for P-10 [13].	27
Figure 1.20:	Transverse diffusion for P-10 [13].	27
Figure 1.21:	(a) Electron drift lines in the plane perpendicular to the anode wire. (b) A Spreading out of the electrons along the anode wire due to the $\mathbf{E} \times \mathbf{B}$ effect.	28
Figure 1.22:	Lorentz angle for P-10 with magnetic field of 0.5 T. The angles between the electric field and magnetic field are 0, 15 ,30, 45, 60, 75 and 90 degrees [13].	29
Figure 2.1:	3 dimensional design of the field cage of the $S\pi$ RIT TPC without the exit window polyamide sheet.	31
Figure 2.2:	Prepare the side support for being painted with the copper-silver epoxy paint. Kapton tape is used to mask off the areas that do want the paint to go over.	32
Figure 2.3:	The front window frame was painted with the conducting paint was an epoxy with silver coated.	32
Figure 2.4:	Drawing of a side wall PCB of the field cage. There are holes for the LASER calibration components. The fixtures for the laser ports are not shown in this figure.	33
Figure 2.5:	After the walls were assembled, the interior has 50 strips and 49 strips for the exterior. The strip on the top sinks into the top perimeter and the one at the bottom sinks into the cathode.	34
Figure 2.6:	Side wall of the field cage was laid on the flat surface for 10 hours to cure	35
Figure 2.7:	Solder thin copper pieces on the side walls to connect the strips on the PCBs.	35

Figure 2.8:	The front side of the field cage consists of two PCBs and the window frame which is glued to the two walls. Green: the window frame gas two gas channels which are used to fill the gas into the TPC from the bottom. Purple: The removable inserted window is screwed on the window frame from the inside of the field cage.	36
Figure 2.9:	Exploded view of the front side of the field cage. Shown in the drawing are two gas channels for filling the gas into the TPC.	37
Figure 2.10:	After position the window frame and boards, the boards were attached to the window frame firmly with the brass screws.	37
Figure 2.11:	Inserted removable window of the field cage	38
Figure 2.12:	The inserted window is put on the front wall of the field cage. The copper fingers provide electrical connections to the strips on the walls.	38
Figure 2.13:	The strips on a thin PPTA are connected to the strips on the window frame by copper finger.	40
Figure 2.14:	Exit window of the S π RIT TPC consists of three polycarbonate frames.	41
Figure 2.15:	Exit window	41
Figure 2.16:	Round aluminum edge was attached to the edge of the cathode to reduce a sharp angle.	42
Figure 2.17:	Circuit diagram for the electrical connections of the cathode	43
Figure 2.18:	Assembling the front and side walls of the field cage.	44
Figure 2.19:	Assemble both side walls of the field cage.	45
Figure 2.20:	Apply the bead of Araldite 2013 epoxy to the corner pieces of the back window frame.	45
Figure 2.21:	Back window frame was attached to the wall of the field cage.	46
Figure 2.22:	Glue excess area on the top perimeter has been masked off with plastic and a Kapton tape.	47
Figure 2.23:	Place to the wall of the field cage slowly on the groove filled with beads of Araldite 2013.	47
Figure 2.24:	Wall of the field cage was screwed to the top perimeter.	48

Figure 2.25:	Field cage was placed on the support for checking and cleaning the epoxy.	48
Figure 2.26:	Move the field cage to the flat surface to cure for 10 hours.	49
Figure 2.27:	Prepare the cathode for gluing.	49
Figure 2.28:	To define the potential on each strip, a chain of 10-M Ω resistor was soldered between in the strips	50
Figure 2.29:	Wires were soldered along the strip at the corner for better electrical connections between the strips on corner pieces and the wall. Silver epoxy was applied on the wire at the middle of the strip on the corner pieces to provide a better connection.	50
Figure 2.30:	Insert 1 k Ω resistors along the strips.	51
Figure 2.31:	Copper fingers were used to connect the conductive strips on the exit window to ones on the wall.	52
Figure 2.32:	Diagram shows the resistor network of the S π RIT TPC.	53
Figure 2.33:	Electric field in the drift volume of the TPC and R_p as a function of $\frac{V_{gg}}{V_{cath}}$	56
Figure 2.34:	Potential calculation of the field cage is performed by ANSYS. R_p is 7 M Ω for the V_{cath} and V_{gg} of -6 kV and -110 V, respectively.	57
Figure 2.35:	The strips on the front window frame are slightly different from the rest of the field cage.	58
Figure 2.36:	Electron drift lines near the front window of the S π RIT TPC.	58
Figure 2.37:	Cross-sectional view of the pad plane circuit board [9].	60
Figure 2.38:	Unit cell on the beam right side is a 180 degree rotation of that of the beam left side. Numbers indicate the channel which the signal from the pad is registered to the AGET.	61
Figure 2.39:	Pad plane	62
Figure 2.40:	Top plate with inner surface upwards. There are 384 rectangular holes for Samtec connector feedthroughs.	63

Figure 2.41: Ribs of the top plate	63
Figure 2.42: Gasget gluing	64
Figure 2.43: Stamping metal piece for gluing gasket	65
Figure 2.44: Complete gasket gluing process	66
Figure 2.45: Gluing pattern for the pad plane	66
Figure 2.46: Pad-plane PCB is put to the position by the vacuum table.	67
Figure 2.47: The flatness of the top plate using FARO laser position scanner.	68
Figure 2.48: Values of parameter K_3 as a function of an anode wire pitch s , an anode-cathode separation h and the radius of an anode wire r_a [14]	71
Figure 2.49: Value of K_3 for $\frac{h}{s} \leq 1.0$ [14]	72
Figure 2.50: Pad response function for S π RIT TPC with $w = 8$ mm (red) and $w = 12$ mm (blue)	73
Figure 2.51: Wire-winding machine	75
Figure 2.52: The schematic of the setup for measuring a wire tension.	77
Figure 2.53: measurement of the tension of anode wires: (a) the anode wires do not vibration when the frequency does not match the fundamental frequency. (b) When the applying frequency matches the fundamental frequency of the anode wire, the wire vibrates with a maximum amplitude.	77
Figure 2.54: The printed circuit board (PCB) for anode wires: 26 pads are connected to the high voltage by 26 of 10 M Ω resistors (blue). Each pad is connected to an external ground by 1 nF capacitor (brown).	78
Figure 2.55: Printed circuit board for ground plane	78
Figure 2.56: Printed circuit board for gating grid plane	79
Figure 2.57: Gluing the ground board	79
Figure 2.58: Gluing the anode board to a acrylic spacer	80

Figure 2.59:	Fill the gap on the anode board	80
Figure 2.60:	Anode boards were mounted on the TPC	81
Figure 2.61:	Wire comb assembly	82
Figure 2.62:	Using EZpoxy 83 to hold the wires in place and maintain the tension	83
Figure 2.63:	Wire frame with leveling blocks	83
Figure 2.64:	Solder wires onto the conductive pad on the anode board	84
Figure 2.65:	Connect the anode board to the MHV connector	85
Figure 2.66:	Insulate the anode plane connections	86
Figure 2.67:	Solder adjacent ground boards	87
Figure 2.68:	Layers of a transmission line	87
Figure 2.69:	Transmission line is connected to the gating grid board	88
Figure 2.70:	Enclosure of the S π RIT TPC with the motion chassis	89
Figure 2.71:	Drawing of the bottom plate of the S π RIT TPC	90
Figure 2.72:	Pour Ezpoxy 84 at the center of the bottom plate	90
Figure 2.73:	Polycarbonate sheet was glued to the bottom plate by vacuuming gluing technique.	91
Figure 2.74:	After 24 hours curing time, the covers have been taken off and the bottom plate was cleaned.	92
Figure 2.75:	Conductive paint was applied at the center of the polycarbonate sheet.	92
Figure 2.76:	Copper rods and standoffs were attached to the polycarbonate sheet by 0-80 screws.	93
Figure 2.77:	A quarter round corner was produced by welding.	94
Figure 2.78:	Design model of the target mechanism for the S π RIT TPC.	95
Figure 2.79:	A target can be adjusted in y direction by positioning the fixture on the target frame.	95

Figure 2.80:	A target frame can be moved in z direction via the Z-motion control	96
Figure 2.81:	The x position of the target can be adjusted from the X-motion control.	96
Figure 2.82:	Actual target mechanism	97
Figure 2.83:	Top plate with the cover plate was rotated by 90 degrees.	98
Figure 2.84:	Insert window and fingers were put on the window frame of the field cage.	99
Figure 2.85:	Four people lift the field cage and set it on the set screws on the top plate.	100
Figure 2.86:	Springs were attached to the bottom of the field cage to provide an electrical connection between the cathode and conductive surface on the voltage step down.	101
Figure 2.87:	Top plate with the field cage attached has been rotated to the position for assembling to the enclosure.	101
Figure 2.88:	Top plate was lowering while people at each corner align the top plate assembly with the enclosure.	102
Figure 2.89:	The $S\pi$ RIT TPC without a target mechanism	103
Figure 2.90:	The target mechanism is installed onto the $S\pi$ RIT TPC.	104
Figure 2.91:	The laser alignment techniques was used to align to the center of a target to the center of the entrance window.	104
Figure 2.92:	GET conceptual design [1]	105
Figure 2.93:	GET system is mounted on the $S\pi$ RIT TPC	106
Figure 2.94:	AsAd motherboard	107
Figure 2.95:	Planned cooling system for the $S\pi$ RIT TPC.	108
Figure 2.96:	Trigger timing structure for the gating grid driver. The diagram is not in the correct scale.	109
Figure 2.97:	Planned trigger timing diagram. The modules labeled F in the diagram are the FIFO.	110

Figure 2.98: Connection between the scintillators and electronic modules	111
Figure 2.99: Trigger timing	112
Figure 2.100: A veto signal (blue) occur more than 4 μ s before the T-StartScint. The trigger system generate the normal TTL-Open (yellow), TTL-Close (green).	113
Figure 2.101: There is no generation of TTL-Open (yellow) and TTL-Close (green) when the T-StartScint (purple) and T-Veto (blue) are simultaneous present.	114
Figure 2.102: When a veto signal presents after the event trigger, TTL-Open (yellow) closes and the TTL-Close starts.	114
Figure 2.103: The delay output from G&D2 passes to the start of G&D4 to assure that the TTL-Open (yellow) and TTL-Close (green) are not simultaneous present.	115
Figure 2.104: Position of gas input and output on the S π RIT TPC.	116
Figure 2.105: Planned gas handling system for the S π RIT TPC	117
Figure 2.106: Planned gas handling system for the S π RIT TPC	118
Figure 3.1: Ionized electrons drift into the multiplication region and multiply at the anode wires.	121
Figure 3.2: Formation of polymers from free radical molecules [2]	122
Figure 3.3: Accumulation of negatively charged polymers on the surface of an anode wire [15]	123
Figure 3.4: Polymers deposit on the surface of an anode wire in CO ₂ /Isobuthane [15]	123
Figure 3.5: Grid of wires parallel to a conducting plane [11]	125
Figure 3.6: Wire plane configuration of the S π RIT TPC. The pitch of anode plane (s_1) is 4 mm. The pitch of the ground (s_2) and gating grid (s_3) are 1 mm. The distance from the conducting plane (pad plane) to the anode (y_1), ground (y_2) and gating grid (y_3) is 4, 8 and 14 mm, respectively. The distance from the cathode to the pad plane $y_p = 509.5$ mm.	127

Figure 3.7:	A wire is polarized by an external electric field. Electric fields are pointing upward [11].	131
Figure 3.8:	Drift lines of ionized electrons ($y_1 = 4$ mm, $y_2 = 8$ mm, $y_3 = 14$ mm, $s_1 = 4$ mm, $s_2 = s_3 = 1$ mm)	132
Figure 3.9:	Transparency, T , of the gating grid with $V_{cathode} = 6$ kV. Black triangle : Garfield simulation; Red line: Analytical solution using Equation 3.11.	133
Figure 3.10:	Operation of bipolar gating grid ($z_1 = 4$ mm, $z_2 = 8$ mm, $z_3 = 14$ mm, $s_1 = 4$ mm, $s_2 = s_3 = 1$ mm). (b) Electrons terminate at the positive wires of the gating grid.	135
Figure 3.11:	(a) Transparency of bipolar gating with the presence of magnetic field; (b) The closing voltage of a gating grid increases linearly with the magnetic field.	137
Figure 3.12:	conceptual design of the gating grid driver for $S\pi$ RIT TPC	140
Figure 3.13:	Circuit diagram of the gating grid driver prototype 1	141
Figure 3.14:	Discharging signal of the gating grid driver prototype 1 on the bread board. There are some slow oscillation on the signal.	141
Figure 3.15:	Testing the prototype 1 PCB with a standard capacitor of 11.6 nF and an operating voltage of ± 30 V. Blue signal is a discharging signal from the positive side of the capacitor. There is a negative lobe after the discharge which indicates that the circuit is under damped.	143
Figure 3.16:	Matching the data to the simulation from PSPICE	145
Figure 3.17:	Discharging signals of the gating grid using the gating grid driver prototype 1	145
Figure 3.18:	Discharging signal from the oscilloscope (operating voltage of ± 75 V, resistance of the system of 4.8Ω)	146
Figure 3.19:	Readout signal from the prototype of GET Electronics	146
Figure 3.20:	Circuit diagram of the gating grid driver prototype 2	147

Figure 3.21:	Signals from the oscilloscope shows the discharging from the positive side (blue) and negative side (purple) of the standard capacitor of 22 nF. The two signals discharge at a different rate and have a fluctuation at the beginning as indicated in red circle.	148
Figure 3.22:	Adjust the discharging rate on the negative side to match the signal on the positive side.	149
Figure 3.23:	Green: the TTL trigger signal; Purple: Gate signal for driving N-mosfet switch; Blue: Gate signal for driving P-mosfet switch	149
Figure 3.24:	Circuit diagram of the gating grid driver prototype 3	150
Figure 3.25:	The signal from the oscilloscope shows the time of charging a 22 nF capacitor to the original voltage of ± 12 V. Blue: signal from the positive side of the capacitor; Purple: signal from the negative side of the capacitor.	151
Figure 3.26:	The gating grid driver prototype 3 has been tested with a standard capacitor of 16.5 nF. The operating voltages are -40 and -180 V. It has a turn-on delay time of 100 ns. When the gating grid is open, the positive (yellow) and negative (blue) sides of the capacitor are shorted through the mosfet switches and provide to the common voltage of -110 V.	152
Figure 3.27:	Circuit diagram of the gating grid driver prototype 4	154
Figure 3.28:	The circuit board is tested without connecting to a standard capacitor. The gating grid driver shorts two power supplies together at 45 ns after it is triggered. Blue: discharging signal from the positive side. Green: discharging signal from the negative side.	155
Figure 3.29:	Printed circuit board of the gating grid driver prototype 4. The colored circles indicate the conductive pads which can put the adjusting components, R_p , R_n , C_p and C_n on. R_n is mounted on the other side of the board so it is not visible in this picture.	155
Figure 3.30:	Test the gating grid driver prototype 4 with operation voltages of -40 and -180 V. the values of C_p and C_n are 100 pF. (a) When the gating grid is closed, alternating wires have the voltages of -40 and -180 V. Once it opens, the two power supplies are shorted together and give the common voltage of -110 V. (b) the opening time of the gating grid is 250 ns.	158
Figure 3.31:	There is a induced signal on the pad when the gating grid opens. . .	159

Figure 3.32:	Transition of the gating grid from closed to open and back to closed state in SPICE simulation. $C_p=C_n=100$ pF and $R_p = 0.95 \Omega$, $R_n = 1.05 \Omega$	160
Figure 3.33:	(a) Transition of the gating grid from closed to open state in SPICE simulation, $C_p= 600$ nF and $C_n=100$ pF and $R_p = 0.95 \Omega$, $R_n = 1.05 \Omega$. (b) The same as (a) with different capacitor values $C_p= 100$ nF and $C_n=100$ pF and $R_p = 0.95 \Omega$, $R_n = 1.05 \Omega$	161
Figure 3.34:	The dependence of X and B as a function of C_n-C_p	162
Figure 3.35:	Test the gating grid driver with a standard capacitor of 26 nF and vary C_p and C_n to see the effect from the SPICE simulation. The green line indicates the common voltage level.	163
Figure 3.36:	Test the gating grid driver with the $S\pi$ RIT TPC by varying C_p and C_n . The size of the negative peak is increasing with C_n	164
Figure 3.37:	Using $C_p = 1000$ pF and $C_n = 440$ pF, the negative peak is reduced from 800 to 105 ADC channels.	165
Figure 3.38:	Induced signals are readout by AGET Electronics. In this configuration, C_p and C_n are 1000 and 490 pF, respectively.	166
Figure 3.39:	Top panel: the induced signal comes from the transition of the gating grid. Bottom panel: the external signal which is used to cancel the noise is sent thru the ground plane.	167
Figure 3.40:	Use an external signal (red) which has the opposite polarity if the noise (black) to cancel it. The blue line shows the superposition of those two signal. It has a small negative peak of 50 ADC channels.	168
Figure 3.41:	A schematic of the commissioning experiment setup of the $S\pi$ RIT TPC[74].	170
Figure 3.42:	Transparency of the gating grid of the $S\pi$ RIT TPC as a function of the common voltage of the gating grid for $V_{cathode} = -6632$ V.	171
Figure 3.43:	Transparency of the gating grid of the $S\pi$ RIT TPC as a function of the offset voltage (ΔV_g) of the gating grid for $V_{cathode} = -6632$ V.	173

Chapter 1

Particle Observation

1.1 A brief history of visual particle detectors

In the world of sub-atomic particles, physicists put tremendous time and effort to study properties of particles and the interactions between them. Many theories has been proposed to explain the physics of particles and their interaction. Individual sub-atomic particles are too small to directly observed by us so physicists detect them with various types of detectors such as scintillators, semiconductor detectors and gas detectors. In their simplest form, none of those techniques enables scientists to directly see the paths of all particles coming out from a source or a reaction. If the numbers of particles are large or the reaction is complex, the missing information is too important to allow scientists to make solid conclusions about the physics that is being studied.

In 1912, a cloud chamber was invented by Charles Thomson Rees Wilson [16]. The device is a sealed chamber containing a vapor of water or alcohol. The idea is to allow water or alcohol vapor to reach a saturated point in the container and then lower the pressure. This will produce a supersaturated condition. If a charged particle transverses the chamber, the vapor will condense, following interactions of energetic particles with the cloud chamber gas, into droplets along the track of a charged particle. The particle track can be photographed. This is a breakthrough of scientific instrument because the path of sub atomic particles from a reaction can be observed for the first time. In the presence of a magnetic field, positively

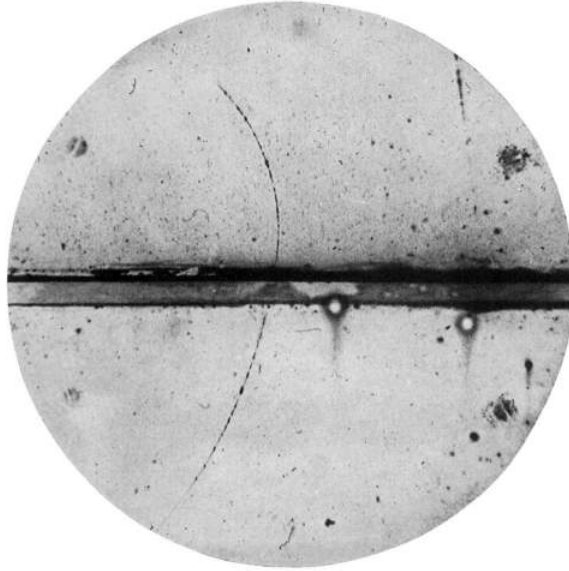


Figure 1.1: A positron track was photographed from a cloud chamber under the magnetic field of 15000 gauss [3].

and negatively charged particles can be distinguished as they curve in opposite directions. In 1932, Carl Anderson found a particle that has a positive charge but has the mass of a free electron by using a cloud chamber under the magnetic field of 15000 gauss, leading to the discovery of a positron [3]. In Figure 1.1, the positron track in the middle was photographed from a cloud chamber. This type of chamber also allows physicists to study electromagnetic showers and nuclear reactions.

The performance of the cloud chamber has two main limitations. Few paths of particles were observed due to the low density of gas and the detection rate of particles was too low to use in conjunction with the new accelerators constructed in 1950s. In 1952, Donald Glaser tried to improve the performance of the cloud chamber [17, 18]. Glaser's idea is to replace the gas with liquid. The chamber was filled with liquid slightly below its boiling point at a certain pressure under a constant magnetic field. Then, the pressure was reduced below the vapor pressure of the liquid. If charged particles transverse the chamber, they ionize atoms and cause the liquid to boil along their paths. Therefore, one can see the

bubbles along the particles's trails as demonstrated in Figure 1.2. Invention of the cloud and bubble chambers played an important role in high energy physics. Many particles has been discovered from bubble chamber pictures such as discovery of Ω^- (1964) [19] and discovery of "charmed" quark (1974) [20, 21]. However, the performance was limited to only visible trails of particles. Some rare processes that occur with low probabilities may be missed due to the long time frame of detection which limits the total number of events that can be observed. In the late 1960s, George Charpak developed multiwire chambers [22, 23] (see Section 1.2) which allows physicists to precisely detect high energy particle reactions at a much higher rate and also measure the energy of a particle at the same time. With the help of readout electronics, physicists are able to record hundreds of events within a second. Typically, multiwire chambers consists of several wire planes with different orientations which are used to determine the trails of particles with high precision. In multiwire chamber, Each wire works as a detector. When read out with high speed electronics and analyzed with high speed computers, the data handling capacity tremendously increased. In 1974, David Nygren introduced a new gas detector called a Time Projection Chamber (TPC) [24] which simplifies the measurement of thousands of sub-atomic particles from a single event while measuring their properties with high accuracy. It employs many of the techniques pioneered with the multiwire chamber and also has an electronic readout system. The TPC is explicitly designed to reconstruct 3-dimensional tracks of particles. The details about the TPC will be discussed in Section 1.3.

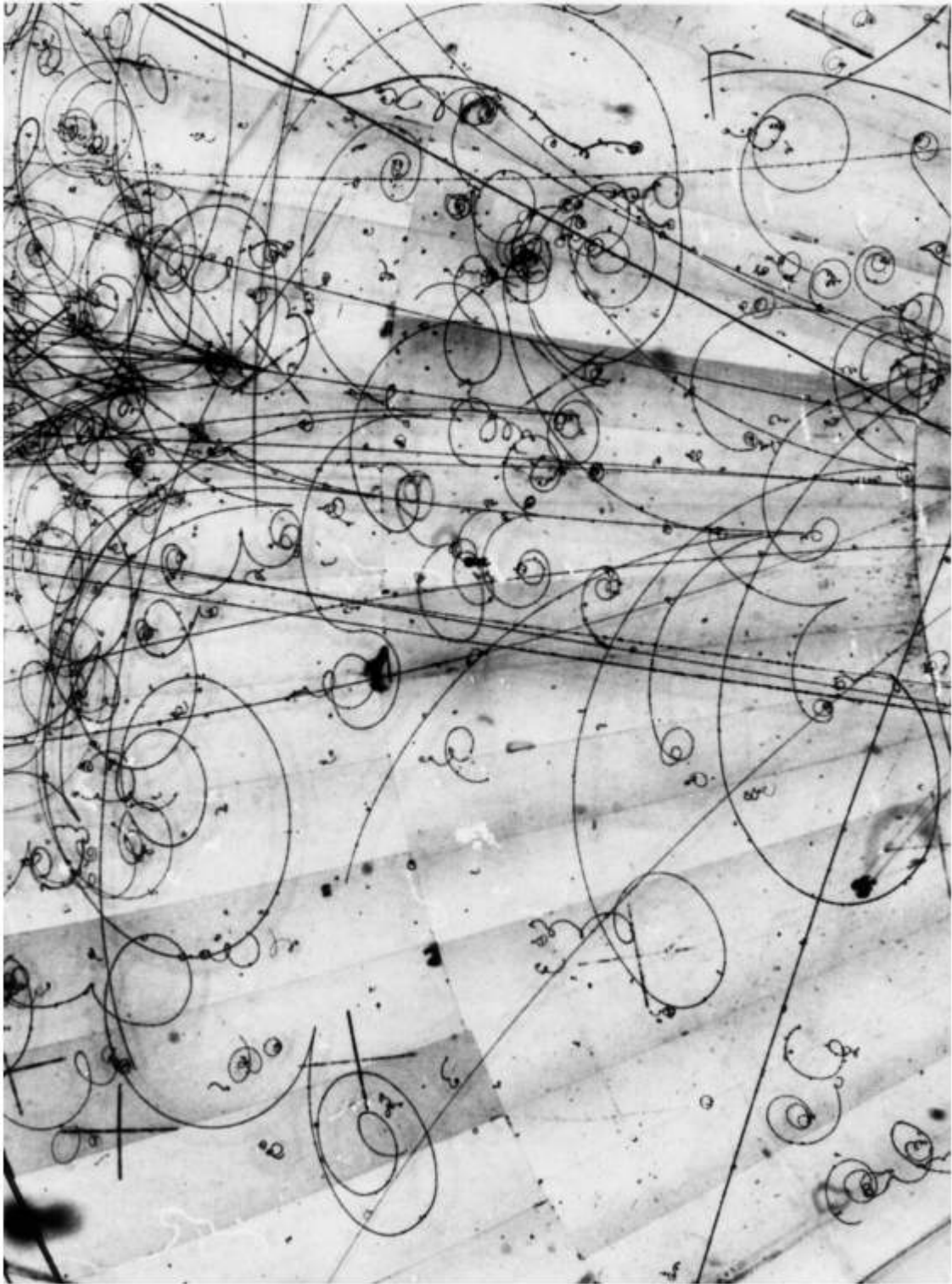


Figure 1.2: A bubble chamber picture. The dark lines are tiny bubbles formed along the paths of charged particles under a strong magnetic field [4].

1.2 Proportional counter

To understand the properties of any gas detector, one needs to consider how a fast charged particle interacts with the gas. The most important interactions are the Coulomb interactions between the charge of the fast particle and the charge of the electrons bound to the atoms in the gas. These interactions transfer energy to the electrons and knocks them off of their atoms. The Coulomb force between the incident charged particle and the atomic electrons decreases inversely as the square of the impact parameter. Integrating over the impact parameter leads to the Bethe-Bloch equation,

$$-\frac{dE}{dx} = Kz^2 \frac{Z}{A} \frac{1}{\beta^2} \left[\frac{1}{2} \ln \frac{2m_e c^2 \beta^2 \gamma^2 T_{max}}{I^2} - \beta^2 - \frac{\delta(\beta\gamma)}{2} \right]. \quad (1.1)$$

Table 1.1: List of variables.

Symbol	Definition
M	Incident particle mass
E	Incident particle energy
T	Kinetic energy
m_e	Electron mass
r_e	Classical electron radius
N_A	Avogadro's number
ze	Charge of incident particle
Z	Atomic number of medium
A	Atomic mass of medium
K	$4\pi N_A r_e^2 m_e c^2$
I	Mean excitation energy
δ	Density effect correction
γ	$1/\sqrt{1 - \beta^2}$

The list of variables is shown in Table 1.1. β is the speed of the projectile in the unit of the speed of light c . Here T_{max} is the maximum kinetic energy which can be passed on a

free electron in a single collision. T_{max} is given by

$$T_{max} = \frac{2m_e c^2 \beta^2 \gamma^2}{1 + 2\gamma m_e/M + (m_e/M)^2}. \quad (1.2)$$

The Bethe-Bloch equation correlates the mean energy loss per unit length or "stopping power" of the particle in the detector gas to its charge and its velocity [25]. The fluctuation of the energy loss by ionization of a charged particles was theoretically described by Landau in 1944 [26]. The distribution of energy loss in thin media is given by

$$f(\lambda) = \frac{1}{\sqrt{2\pi}} \exp \left[\frac{-1}{2} (\lambda + e^{-\lambda}) \right]. \quad (1.3)$$

λ is the reduced energy variable written by

$$\lambda = \frac{\Delta E - \Delta E_{mp}}{\xi}, \quad \text{where} \quad \xi = K \frac{Z}{A} \frac{\rho}{\beta^2} X. \quad (1.4)$$

ΔE is the actual energy loss. ΔE_{mp} is the most probable energy loss. ξ is the average energy loss. X is the thickness of the media. Figure 1.3 shows the characteristic shape of Landau distribution. The long tail at very large energy loss corresponds to an event which one or more energetic electrons, usually called delta electrons, have been produced [27].

Combining this with measurements of other quantities, such as the radius of curvature of the particle in a magnetic field or the particles total energy can allow one to determine what type of particle it is, such as a pion, or the nucleus of light nuclear isotope. Thus, a key quantity one wants to measure is the energy loss in the detector gas. Particles with energies less than that for minimum ionization can be distinguished by their energy loss in gas. This energy loss is deposited into the gas, where some of it goes to unbinding the electron from the

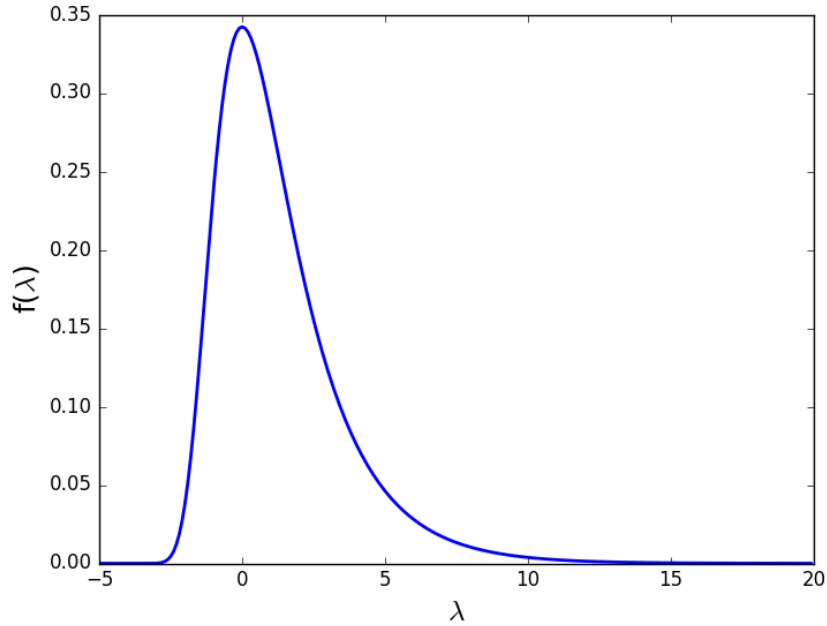


Figure 1.3: Landau distribution

gas (ionization potential) and the rest goes to the kinetic energy of the electrons. These fast primary electrons lose energy in the gas, following the Bethe-Bloch equation, and eventually most of the energy loss of the incident particle is converted to total ionization. At typical value of the energy per ionized electron in P-10 gas is about 26 eV [28, 29]. For a total energy loss of ΔE , the number of secondary electrons is $\frac{\Delta E}{26\text{eV}}$. One can therefore determine the energy loss by counting these secondary electrons.

The basic idea of a multiwire proportional chamber was based on proportional counters, which has been developed around 1940s. Figure 1.4 shows a basic structure of a single wire proportional counter. It has a cylindrical geometry. A voltage difference is applied between the more negative cathode tube and the more positive anode wire located at the center of the tube to create a high electric field where gas amplification occurs [5].

The modes of operation of the proportional counter is shown in Figure 1.5. At low values of the voltage, the field strength is not sufficient to prevent the recombination of the original

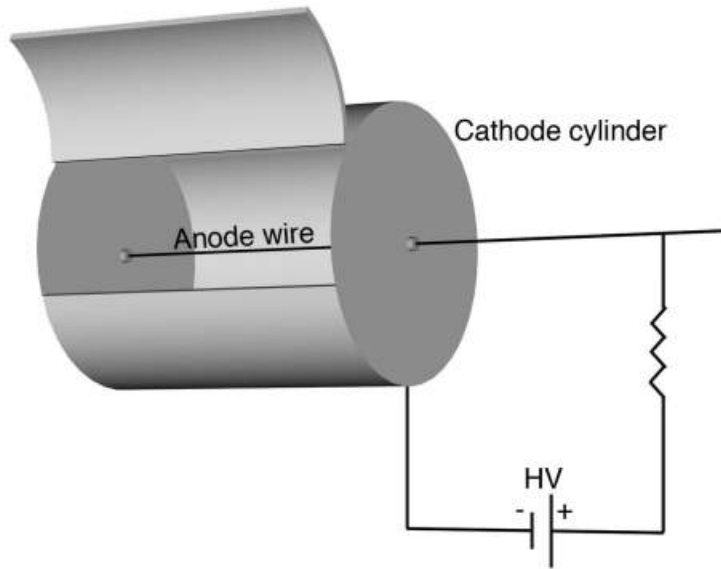


Figure 1.4: Basic structure of a proportional chamber [5]

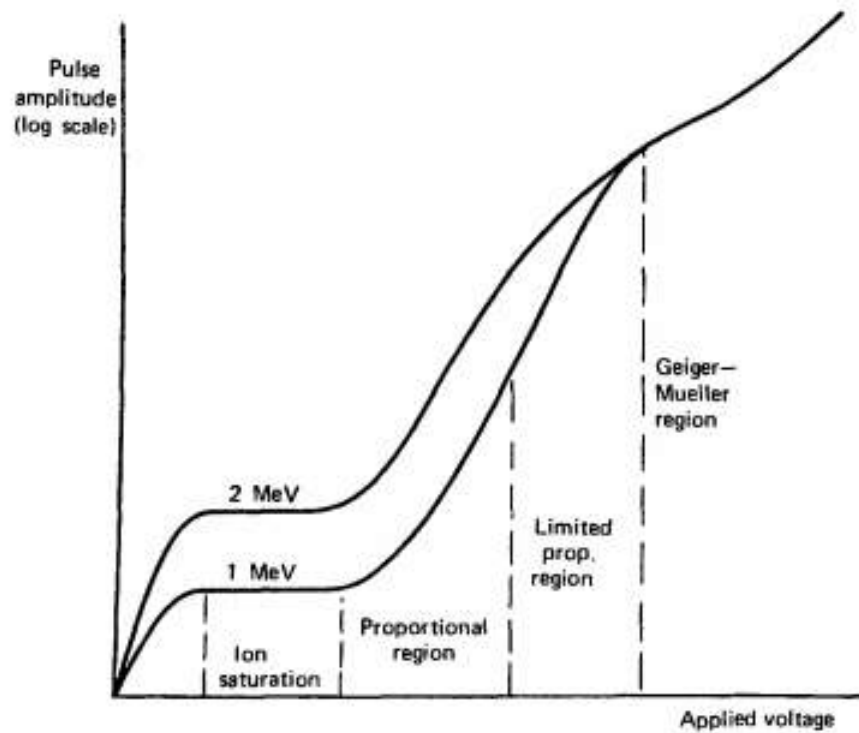


Figure 1.5: Range of operation for gas-filled detector [5].

pairs. Therefore, the collected charge is less than it should be. As the voltage increases, the recombination process is suppressed and the system is in the ion saturation state where the constant amplification is achieved. In the saturation range, the collected charges is nearly

equal to the charge of the original ion pairs. If the voltage is further increased, the collected charge begin to multiply. At a certain range of voltages, the gas multiplication is linear. This region is called proportional region. Here, the collected charges will be proportional to the original ion pairs. If we keep increasing the voltage, then non-linearity of gas multiplication will occur. This non-linear effect is related to positive charges produced in the secondary ionization process. The cloud of these positive charges move very slowly comparing to the speed of electrons towards to the cathode. If the density of the positive charges is sufficiently high, they form a space charge that can significantly distort the electric field in the volume. Since the gas multiplication depends on the magnitude of the electric field, the non-linear effect starts to be observed. From this point, the collected charges increase non-linearly with increasing number of the original ion pairs. This region is called limited proportionality. For further increasing applied voltage, the Geiger-Mueller region is reached. In the Geiger-Mueller mode, the space charge created by the positive ions becomes dominant. Avalanches will proceed along the wire until sufficient number of positive charges has been reached to reduce the electric field below the point that the gas multiplication can hold. There will be no information reflecting the number of the original ion pairs [10]. In this case, the mode of operation that is useful to determine the energy loss are the ion saturation and proportional modes. Both are widely used in nuclear and particle physics. If one wants to track particles through the gas, however, one needs to sample the ionization in small volumes of the gas, where few electrons are produced; thus the signals in ion chamber mode prove to be too small to measure accurately. For this reason, the proportional mode is preferred for tracking.

To achieve proportional mode, one needs to have the large electric field possible near a small radius wire at an elevated electrostatic potential as in a proportional chamber. For small wires of order of 20 μm diameter, one can multiply each of the electrons produced in

the incident ionization by a factor of 1000-10000 [30], increasing the ratio of the signal from the ionization relative to the electronic noise in the electronics amplification system that samples this ionization.

To use a proportional counter to track a trajectory of a particle, it is possible to stack proportional chambers but, it would be a challenge mechanically. Also, there was a belief that having multiwire in the same gas chamber may not work properly due to a large capacitance in the structure. Moreover, non-screened wires may cause the signal to spread [27].

In 1968, Charpak and collaborators introduced a multiwire proportional chamber (MWPC) which consists of thin equally spaced wires sandwiched between two cathode planes. Figure 1.6 demonstrates a schematic cross-section of such a structure. Typically, the distance between a plane of wires to the cathode is about three or four times larger than the wire spacing for proper operation [27]. In the MWPC, each wire works as an individual detector. The detected signals were readout by an electronic system. The MWPC is the first visual particle detector that has electronic readout. This allowed the data taking capacity of experiments to greatly increase.

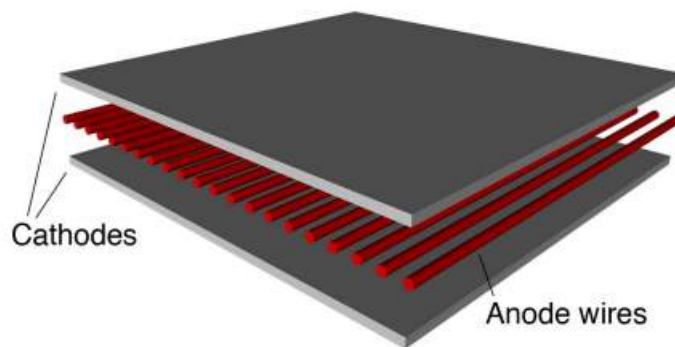


Figure 1.6: Simple structure of multiwire proportional chambers [5]

Figure 1.7 shows an infinite plane of wires of radius a , spacing s and the distance from the wire plane to cathode L . The coordinate system has been center on one wire. We assume

that all wires have the same charge q per unit length. The potential for a thin wires with equal spacing [27] can be expressed by

$$V(x, y) = \frac{CV_0}{4\pi\epsilon_0} \left\{ \frac{2\pi L}{s} - \ln \left[4 \left(\sin^2\left(\frac{\pi x}{s}\right) + \sinh^2\left(\frac{\pi y}{s}\right) \right) \right] \right\} \quad (1.5)$$

$$E(x, y) = \frac{CV_0}{2s\epsilon_0} \left(1 + \tan^2\left(\frac{\pi x}{s}\right) \tanh^2\left(\frac{\pi y}{s}\right) \right)^{1/2} \left(\tan^2\left(\frac{\pi x}{s}\right) + \tanh^2\left(\frac{\pi y}{s}\right) \right)^{-1/2}. \quad (1.6)$$

V_0 is the potential on the wire and capacitance per unit length C is given by

$$C = \frac{2\pi\epsilon_0}{\frac{\pi L}{s} - \ln\left(\frac{2\pi a}{s}\right)}. \quad (1.7)$$

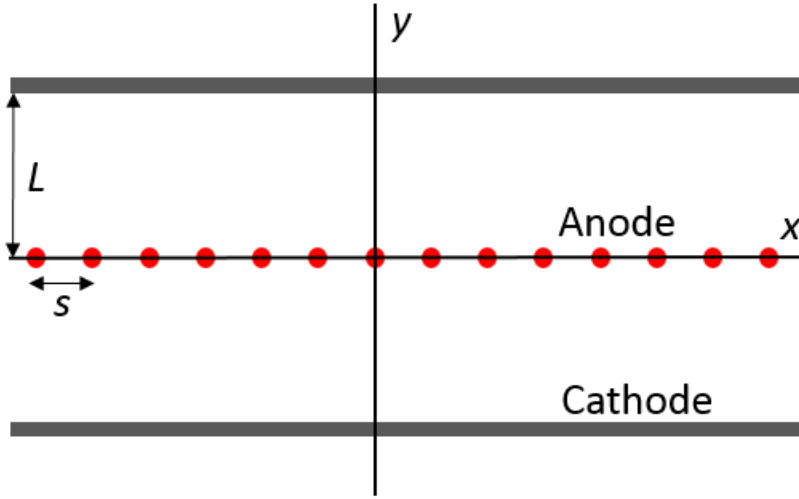


Figure 1.7: Crosssection diagram of MWPC

Early multiwire proportional counters were constructed with thin cathode windows above and below the anode wire plane. They were used to detect charged particles that passed through one cathode, through the anode wire plane and out the other cathode. When a

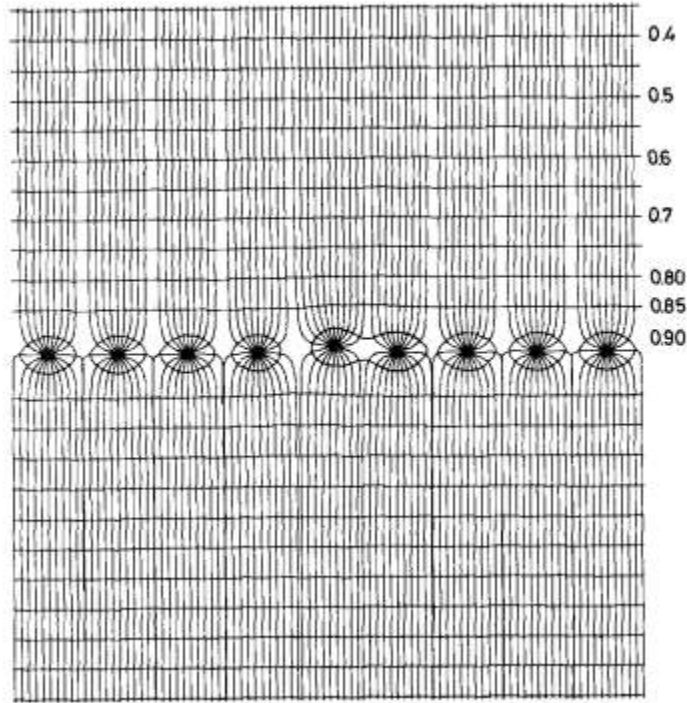


Figure 1.8: Electric field of a multiwire proportional chamber. All wires has potential of 1 V and the outer electrodes has the potential of 0 V. The calculation shows the result for $d = 40 \mu\text{m}$, $s = 1 \text{ mm}$, $L = 8 \text{ mm}$ [6].

charged particle transverses the chamber, it ionizes the gas atom or molecule and a primary ion pair is produced. The electrons drift along the electric field lines in the opposite direction of the field towards the nearest wire where the multiplication occurs. The voltage that applies to the wire is crucial as discussed in Section 1.2. By putting a preamplifier on each wire, one can determine which wire is closest to the ionization allowing the position of the ionization to be measured with an accuracy comparable to the wire spacing. However, at high anode voltages, sparks on the wire often damaged the preamps.

To improve the spatial resolution of the MWPC, Breskin et. al. introduced the cathode plane that is equipped with strips parallel and orthogonal to the sense wires instead of a single cathode plane [7]. With this detector, each cathode strip is connected to the input of a preamplifier , which holds the cathode at a virtual ground while measuring the image

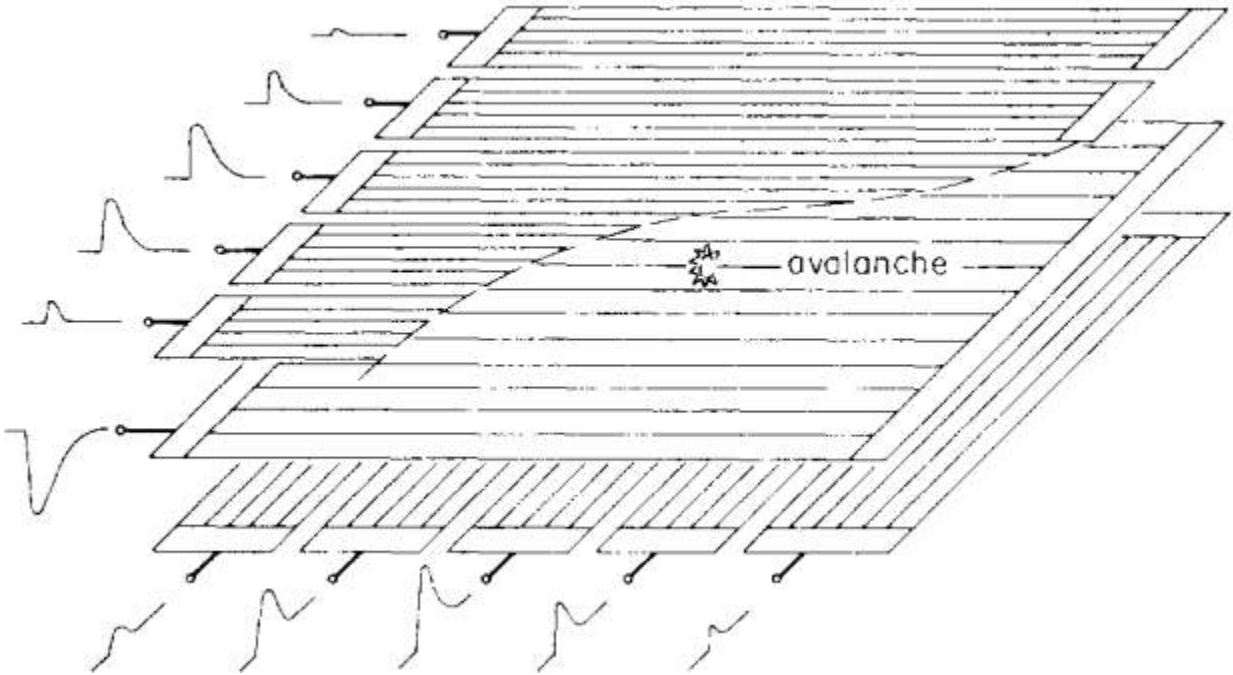


Figure 1.9: The two cathode planes are divided into strips parallel and orthogonal to the wires; coordinate x parallel to the sense wires and coordinate y orthogonal to the sense wires. [7].

charges induced on it by the motions of the electrons and ions near the anode wires. Sparking typically did not damage preamplifiers attached to the cathode. Also, the ionization is typically on one or two of the wires. With this design, one can apply the central of gravity technique to obtain the location of interaction in two dimensions with an accuracy better than the spacing of the anode wires. In Figure 1.9, the signal is the largest on the cathode strips nearest to where the avalanche occurs and decreases with distance from the avalanche. The point of interaction can be obtained by calculating the center of gravity of the signal which is expressed by

$$x = \frac{\sum(Q_i - b)x_i}{\sum(Q_i - b)}. \quad (1.8)$$

Q_i is the charge collected on the i^{th} strip. x_i is the coordinate of the i^{th} strip. b is a

small correction to the noise [5]. There are also further developments on a cathode design to improve spatial resolution of the MWPC [31] and data acquisition techniques to achieve high quality results[32, 33].

1.3 Time Projection Chamber

A Time Projection Chamber (TPC) is a gas-filled detector that provides a 3-dimensional track of particle moving through the volume. The TPC plays a crucial role in the studies of high track density environment and particle identification by energy loss [34].

The first TPC was invented by David Nygren at the Lawrence Berkeley Laboratory (LBL) in the late 1970s. The first application was the study of 29 GeV positron-electron collision in PEP-4 detector as seen in Figure 1.10 [8].

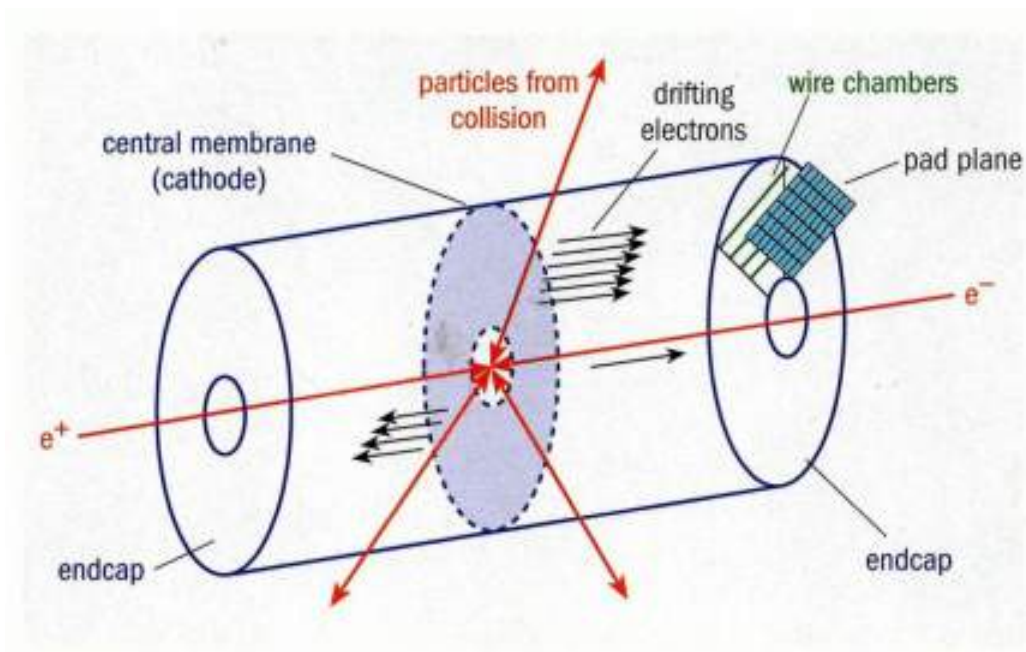


Figure 1.10: A schematic shows the operation of PEP-4 TPC [8]

When a charged particle transverse the TPC, it ionizes the gas atoms or molecules along the trajectory. The liberated electrons drift in the electric field towards the detection region

which consists of wire planes and pad plane as shown in Figure 1.10. To measure the position of the particle trail with high precision, the electric field needs to be uniform throughout the drifting region. In addition, there is a high magnetic field applied in parallel with the electric field. With the presence of magnetic field, it provides the possibility to obtain the momentum of the particle from the curvature and also minimizes the lateral diffusion of electrons in directions perpendicular to the electric and magnetic fields. For a typical TPC, such as S π RIT TPC, diffusion is reduced by more than an order of magnitude. At the anode wires, electrons are multiplied and induce image charges on the pad plane nearby which is at ground potential, and segmented into electrically distinct pads, each connected to its own preamplifier. These induced signals are readout via the preamplifiers and the rest of electronic readout system. The position of the induced image charges on the pad plane determine the particle's trajectory in two dimensions. The third dimension is obtained from the drift time to the pad plane from where the ionization occurs to the anode wires.

One of the major detectors for relativistic heavy-ion collisions is a TPC. The TPC can provide the 3-dimensional picture of hundreds or thousands of particle tracks from a single collision. Few other detector can handle such a huge multiplicity. In Figure 1.11, thousands of particle tracks are reconstructed from the Solenoidal Tracker at RHIC (STAR) TPC [8].

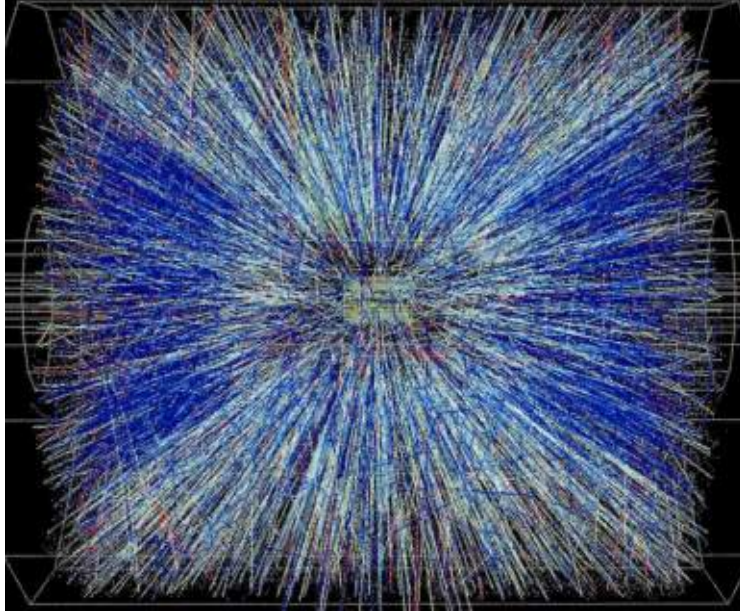


Figure 1.11: The reconstructed tracks from a 200 GeV per nucleon Au-Au collision using the STAR TPC [8]

1.4 S π RIT Time Projection Chamber

The SAMURAI Pion-Reconstruction and Ion-Tracker Time Projection Chamber (S π RIT TPC) [9] has been constructed at Michigan State University as part of an international collaboration to constrain the symmetry energy term in the nuclear equation of state (EOS) at twice supra saturation density region. The detector will be used in conjunction with superconducting SAMURAI dipole magnet of the SAMURAI spectrometer [35, 36] at RIKEN, Japan [37, 38, 39].

Figure 1.13 illustrates the operation of the TPC for a positive particle traversing the chamber. When a charged particle passing through the active volume of the TPC, it ionizes the gas. The ionized electrons drift along the electric field as shown in black arrows in the Figure to the anode wires and get multiplied there. The image charges induced on the pads provide a projection of the particle trajectory on the horizontal plane (x, z). Here the positive particle bends to beam left (counter-clockwise). A negative particle would bend to

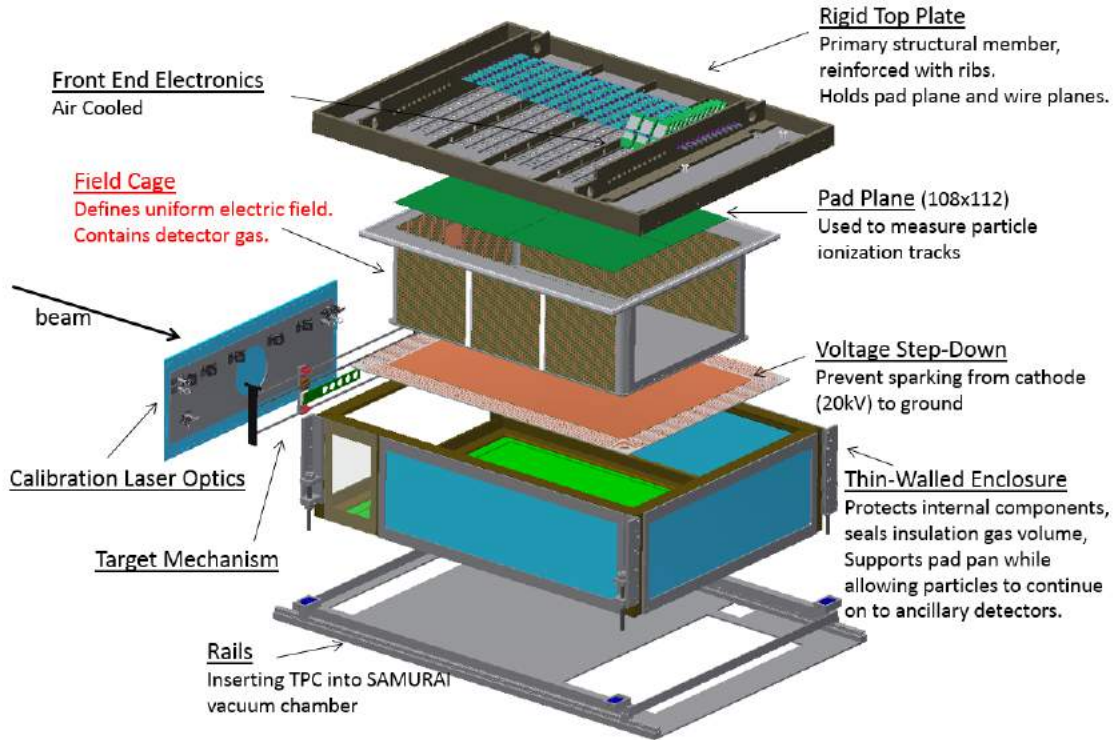


Figure 1.12: An exploded view of S π RIT TPC. More information is available in Section Design and construction of the S π RIT TPC.

Table 1.2: Design parameters of the S π RIT TPC.

Pad	12 mm x 8 mm
Gas gain	1270
Number of pads	12096 (112 x 108)
Electric field	142 V/cm
Drift length	50 cm
Drift velocity	5.5 cm/ μ s
Pressure	760 Torr
Multiplicity limit	200
Gas mixtures	P-10 (90% Ar + 10% CH ₄)
Range of particle detection	π , $Z = 1 - 8$

beam right (clockwise). If the direction of the magnetic field is reversed, as in the case of the S π RIT TPC, the directions of the tracks are reversed from counter clockwise-to clockwise for positive particles. The vertical components (y) of the particle trajectory is obtained from

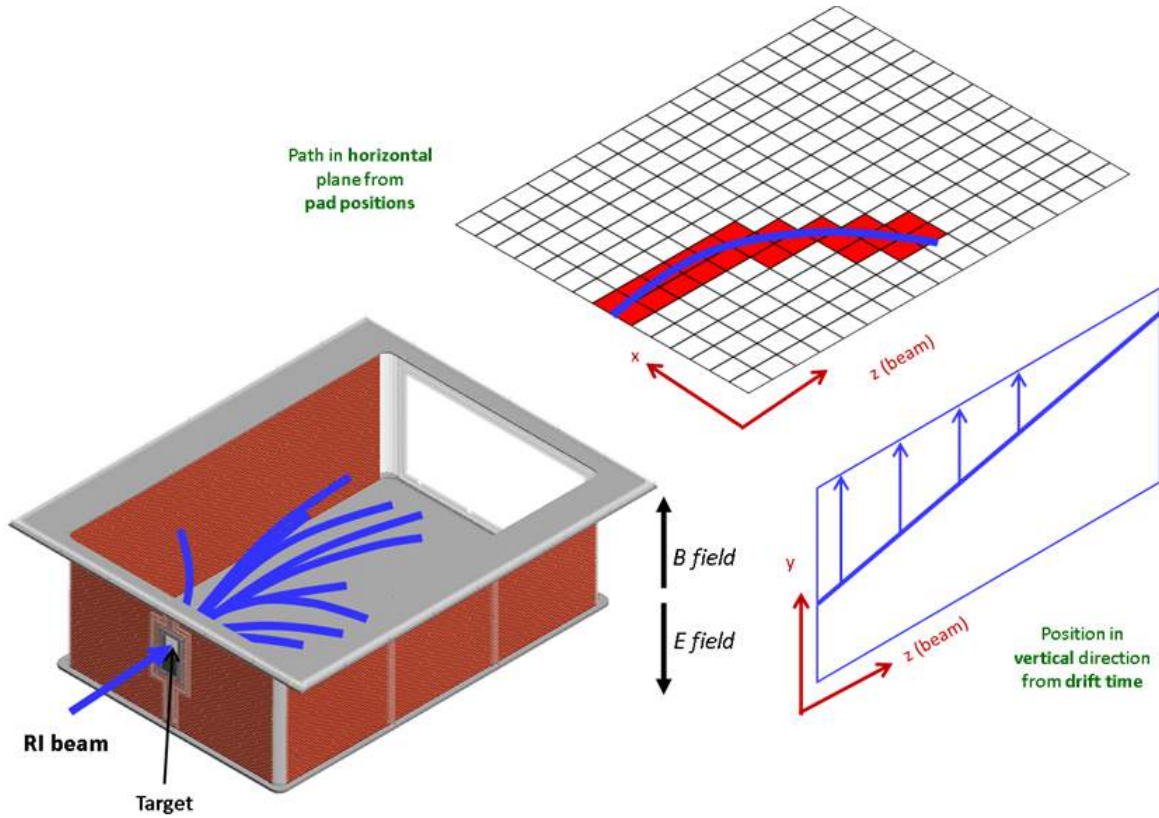


Figure 1.13: Operation of the TPC [9]

the arrival time of electrons.

The $S\pi$ RIT TPC has adopted some design parameter from the EoS TPC [40], which operates with similar magnet geometry and has requirements for pion-track reconstruction. Figure 1.12 shows an exploded view of the $S\pi$ RIT TPC. The detector is a rectangular box. The outer enclosure has the dimension of 2.06 m long x 1.50 m wide x 0.74 m high (see Section 2.4). The field cage is designed to have a drift length of 50.9 cm. The walls of the field cage have 6 mm wide copper strips with 4 mm gap between them. One important feature of the $S\pi$ RIT TPC is to have a thin wall. This allows light charged particles to exit the gas volume and interact with a scintillator trigger array that samples from multiplicity of the particles that exit the field cage (see Section 2.9). The construction details and properties of the field cage is available at Section Field cage of the $S\pi$ RIT TPC. The arrangement of

the pad and wire planes resemble that of the EoS TPC [40] (see Section 2.3). Signals from the pads in the $S\pi$ RIT TPC are readout by the Generic Electronic for TPCs (GET) which will be discussed in Section 2.8. The P-10 gas mixtures will be used in the $S\pi$ RIT TPC experiment. The gas properties is discussed in Section 1.5.

In the design of the $S\pi$ RIT TPC, we decided to employ the multiwire drift chamber technology instead of more recently developed technologies such as Gas Electron Multipliers (GEMs) [41] and Micromesh gaseous structure chambers (Micromegas) [42]. Micromegas use a thin metal mesh instead of anode wires. The mesh is supported a small distance above the pads. There is a simple wire plane above the Micromegas providing strong electric field in which the avalanche forms. GEMs are made of plastic foils which are metal coated on both sides with 50 - 100 μm diameter holes in them. The metal coatings are biased to a few hundred volts to create a strong electric field in the holes. Electrons drifting through the holes create avalanche as much as that of around anode wires [8]. When a MICROME GAS gas amplifier is employed, the electrons are directly deposited on the sense pads of TPC. This is often the case with a GEM gas amplification technology is used. However, there are examples of where a GEM is used as an additional gas amplification stage before a multiwire proportional counter readout as used in the $S\pi$ RIT TPC. Barring this latter option, both GEMS and MICROME GAS technologies have an intrinsic spatial resolution in the pad plane coordinates that is limited to the pitch of the pads on the pad plane, which is typically of the order of 5-10 mm. As discussed in Section 1.3, muliwire proportional counter readout technologies as employed in the $S\pi$ RIT TPC have induced charges in many pads that have be used to interpolate the track to a factor of 10 less than the pad pitch, which is much more precise, as discussed in Section 2.2.

1.5 Choice of gas

Avalanche multiplication can occur in any gas [27]. Some gases or gas mixtures may have different properties such as low working voltage, high gain operation, good proportionality, fast recovery, etc. Therefore, the choice of gas depends on the individual experiment requirement, which the TPC is designed [43].

After ionization, electron and ions created by a moving charged particle drift in the opposite directions to the anode and cathode respectively. Many subsequent collisions between electrons and the gas atoms or molecules occur during the drift of these charges. Electrons and ions have dramatically different mobilities in the gas, in particular ions have drift velocities in the gas that are typically 3 orders of magnitude smaller than are the electron drift velocities in the same region of the detector [44, 45]. If the electric field is very strong, as in the vicinity of the anode wires of the TPC, free electrons that are accelerated by the applied electric field between collisions with the gas. For low fields the electronic velocity is randomized between collisions. In analogy with the drift of electrons through conductors, the electrons on average drift in a directions of the electric field with a drift velocity that is proportional to the electric field and inversely proportion to the gas density or essentially the gas pressure. In case of sufficiently high electric fields, the electrons may achieve sufficiently high kinetic energy between collisions with the gas molecules so that they have enough energy to ionize neutral gas molecules during the next collisions, increasing of the local density of free electrons and ions. Typically, the threshold field for this secondary ionization is of the order of 10^6 V/m for typical gases [10].

All electrons, including those produced by the secondary ionization will be subsequently accelerated by the electric field and further ionize the molecules in the gas, leading to a

rapid increase in the number of electrons moving towards the anode. If n is the number of electrons at a given position, after the path dx , the increase in number can be expressed by

$$dn = n\alpha dx \tag{1.9}$$

where α is the first Townsend coefficient which has the unit of $1/[\text{Length}]$. The inverse of α is the mean free path for an electron in this gas and this electric field to suffer ionizing collision producing one additional electron. The positive ion created in the ionization may collide with the cathode surface and liberate an electron from the surface of an electrode. The success rate of emitting an electron from the surface of an electrode is described by the second Townsend coefficient [46]. The first Townsend coefficient is zero for the electric field below the threshold and gradually increases with increasing field strength above the threshold as shown in Figure 1.14.

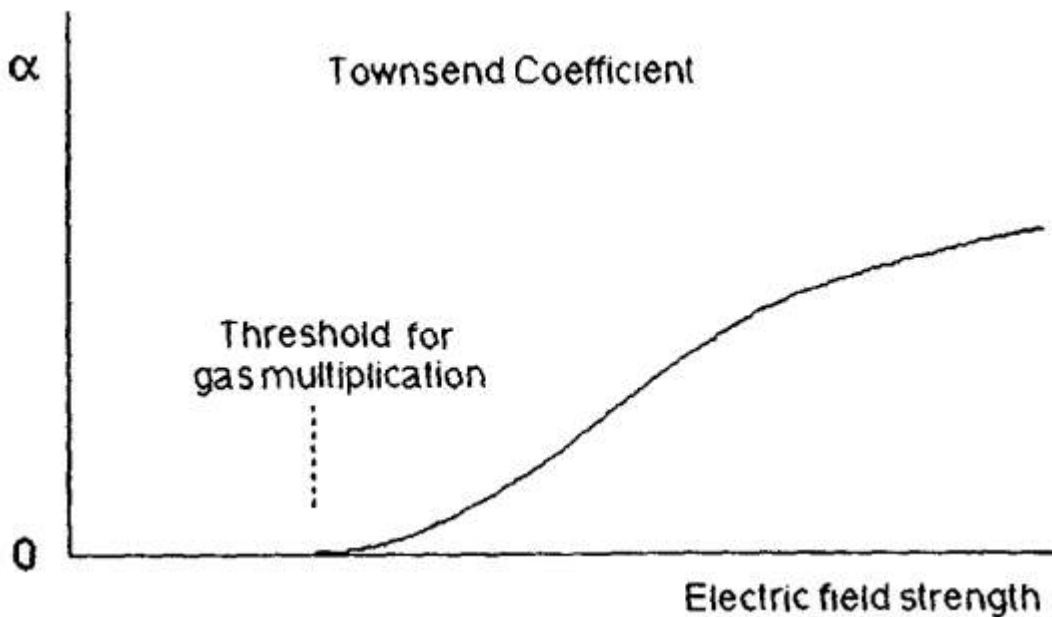


Figure 1.14: The first Townsend coefficient as a function of electric field strength [10].

Figure 1.15 shows the first Townsend coefficient for various noble gases. Normally, com-

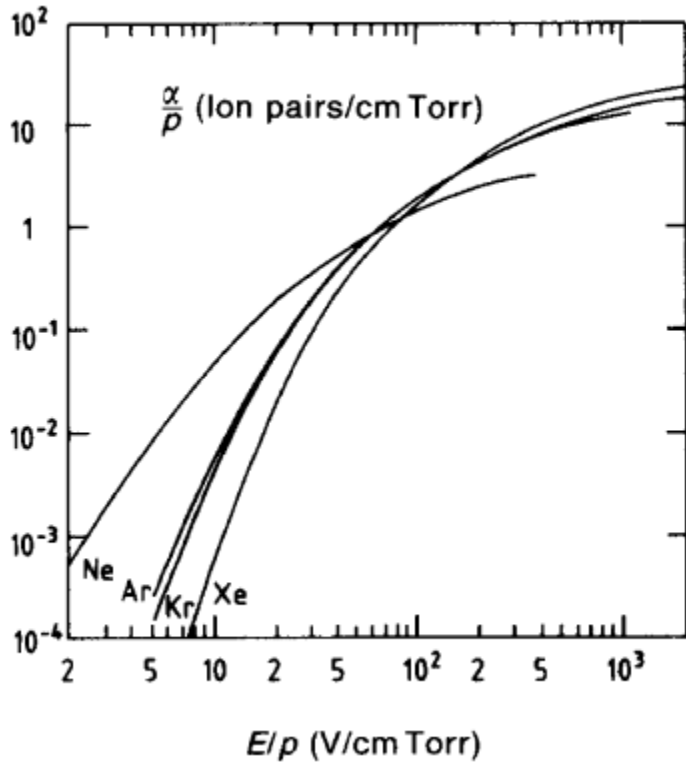


Figure 1.15: The first Townsend for noble gases [11].

plex molecules have a higher threshold ($E/p \geq 10$) for the avalanche multiplication to occur than noble gases [27]. Therefore, noble gases are often used as a main component in gas-filled detector when high gas amplification is desired. Xenon or Krypton is much more expensive. In general, Argon is a more affordable choice [47]. However, using a pure noble gas can be a problem. The excited noble gases can only return to ground state by radiation process. For Argon, the minimum energy for an emitted photon is 11.6 eV [48]. For the S π RIT TPC this energy is well above the work function of the cathode made of aluminum (4.08 eV) [49]. Therefore, these photons can excite electrons from the cathode and side walls leading to the emission of electrons from remote surfaces of the gas containment vessel and a delocalization of the ionization. This is typically countered by the addition of molecular gas additives to the counter gas to quench these emitted photons as discussed below.

When Argon is ionized, the electrons will drift to the anode and the Argon ions will migrate to the cathode where the ions are neutralized. The neutralization can lead to the emission of photons or to the emission of another electron from the metal surface. Indeed, if the photon emission is not suppressed, it can result in a permanent discharge in the gas detector even at a moderate gas gain.

Complex molecules containing large amount of non-radiative excited states allows a wide range of photon absorption. For example, methane is an efficient absorber in the range of 7.9 to 14.5 eV [50] which covers the range in energy of the photons emitted by Argon. However, the addition of excessive quenching gases or poor choice of quenching gases can be a problem. In particular, large molecules tend to form polymers which ionized and these polymers tend to attach to the surface of anode wires or the surface of the cathode. This will reduce the performance of the detector (see Section 3.1).

The amplification factor, G , can be obtained by integrating Equation 1.9 between S_{min} where the avalanche starts and the wire radius a :

$$G = \frac{n}{n_0} = \exp\left[\int_{S_{min}}^a \alpha(s) ds\right] = \exp\left[\int_{E_{min}}^{E(a)} \frac{\alpha(E)}{dE/ds} dE\right]. \quad (1.10)$$

n and n_0 are the final and initial number of electron in the avalanche [11].

In Figure 1.16, gas gain for different mixtures are obtained from GARFIELD simulation [51]. The P-10 gas (Argon 90% + Methane 10%) will be used for the first S π RIT TPC experiment. Later in this Section, we will discuss the properties of the P-10 gas.

In the presence of electric field, electrons drift along the field with a drift velocity, v_d . The drift velocity depends on the pressure and temperature. The contamination in the gas such as water or oxygen can affect the drift velocity as well [52]. Figure 1.17 demonstrates the

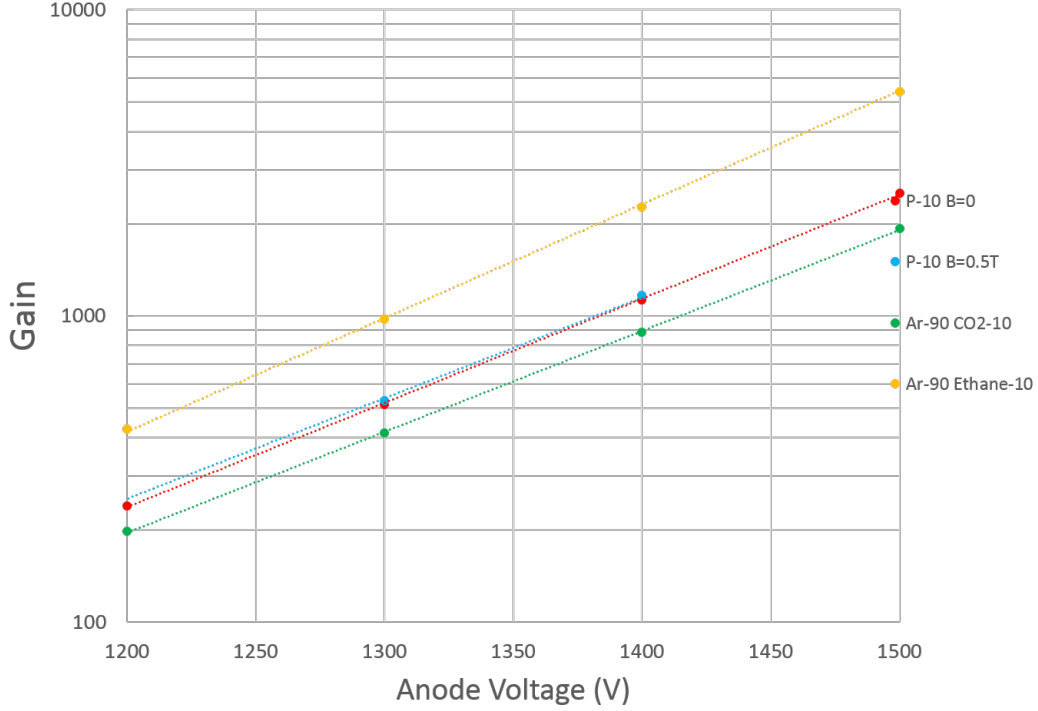


Figure 1.16: Gas amplification (gain) for different mixtures as a function of anode voltage.

drift velocity of electron in P-10 gas as a function of the ratio of electric field E and pressure p . There is a peak of the drift velocity at $E/p = 0.14$ V/cm/mbar which corresponds to the electric field of 142 V/cm for an atmospheric pressure. The drift velocity at the peak is 5.5 cm/ μ s. If one operates a gas detector so that the drift velocity is near this peak, the drift velocity will be less sensitive to changes in the gas density, which is given by the temperature and pressure, and to variations in the electric field. In the S π RIT TPC, the drift velocity is important for the operation of the gating grid. Since the S π RIT TPC has the drift length of 50.9 cm which is the distance from the cathode to pad plane. If the drift velocity is 5.5 cm/ μ s, the gating grid needs to open for 9.25 μ s after triggered by a candidate event to allow all ionized electrons pass through the grid to the anode plane located at 1 cm above the gating grid. The current design of the gating grid driver can open the gating grid in 350 ns corresponding to 1.9 cm of drift length. Some ionized electrons created from the

candidate event located within 1.9 cm below the gating grid will not pass through the grid after the grid is opened.

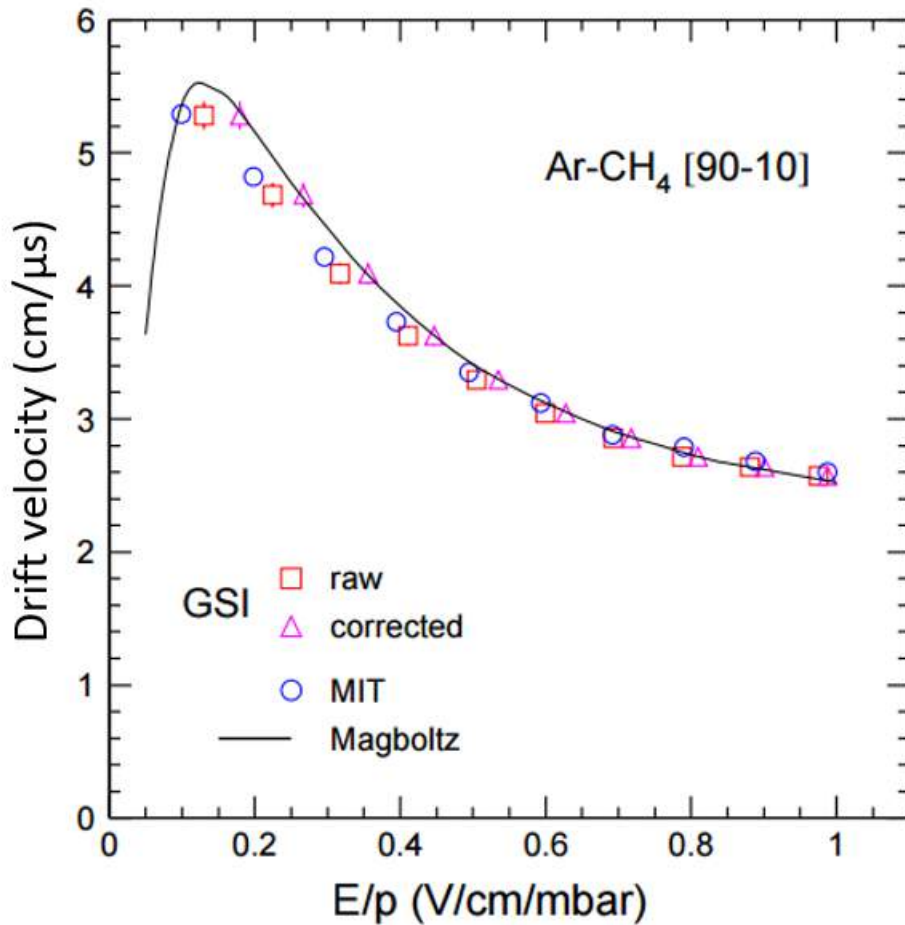


Figure 1.17: Drift velocity of an electron in P-10 gas as a function of the ratio of electric field [12].

The drift velocity increases with the percentage of Methane for the P-10 mixtures as shown in Figure 1.18. In addition, the diffusion also plays an important role in the spatial resolution. Electrons and ions moving along the electric field scatter off the atoms and molecules of the gas. This causes variation in the velocity along the electric field which leads to a spatial diffusion in the direction parallel to the electric field and a lateral diffusion perpendicular to the electric field. The longitudinal and transverse diffusions for P-10 as a function of electric field are shown in Figure 1.19 and 1.20. In the calculation, the electric

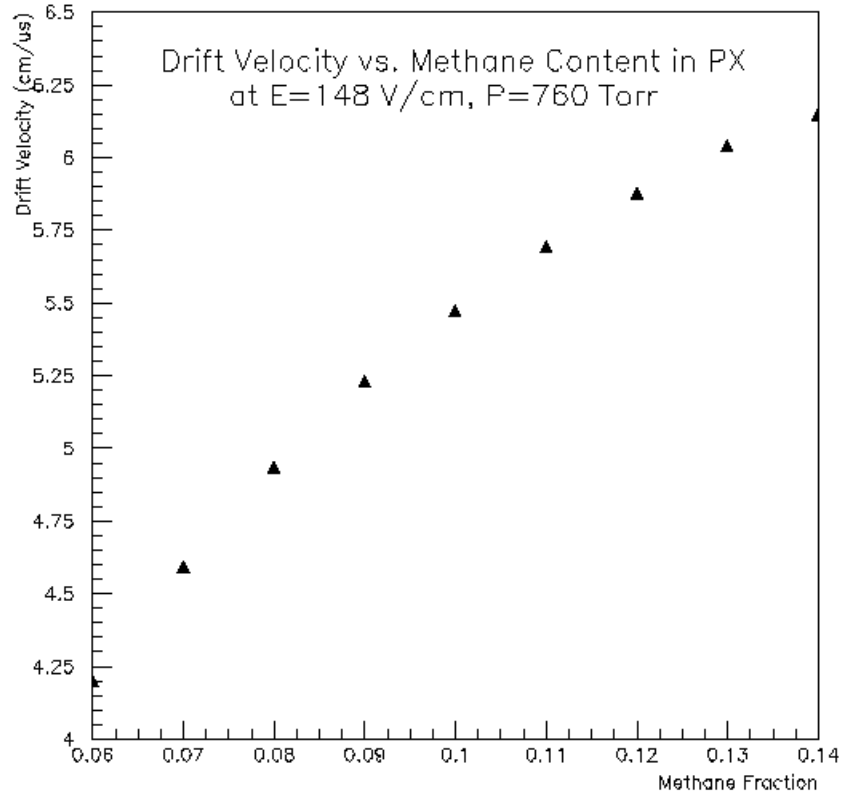


Figure 1.18: Drift velocity of an electron in P-10 gas as a function of the fraction of Methane [13].

field \mathbf{E} is parallel to magnetic field \mathbf{B} . The transverse diffusion decreases with increasing magnetic field. In the track reconstruction of the TPC, the longitudinal diffusion causes an uncertainty of the position where the ionization occurs in y -direction (vertical) while the transverse diffusion causes an uncertainty of the position in (x,z) plane. The latter effect can be suppressed by introducing a magnetic field parallel to the main electric field of the TPC.

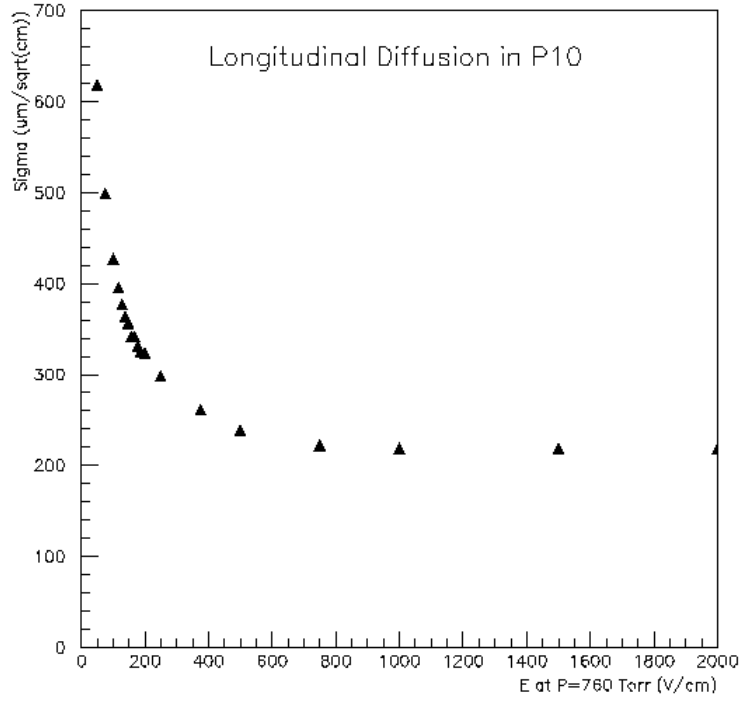


Figure 1.19: Longitudinal diffusion for P-10 [13].

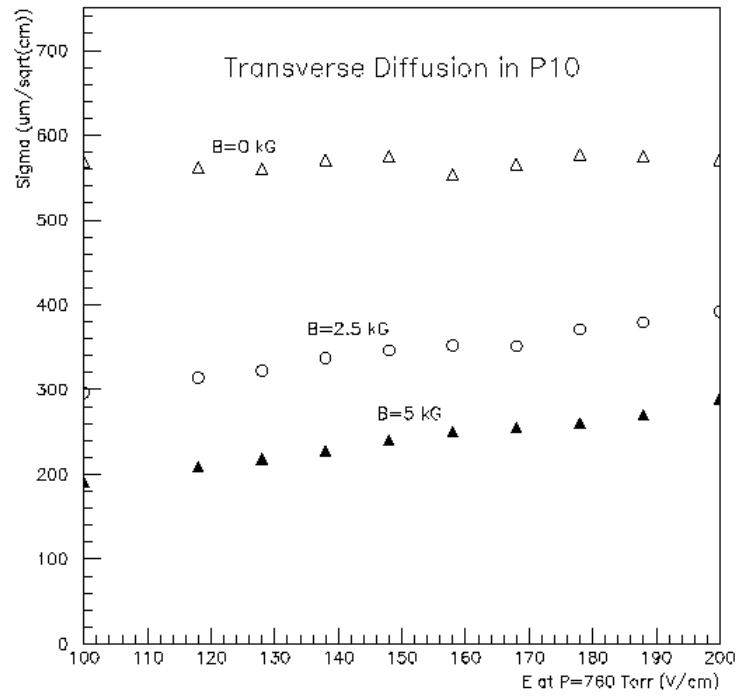


Figure 1.20: Transverse diffusion for P-10 [13].

The angle of the drifting electron makes with the electric field is defined as Lorentz angle. The Lorentz angle is one of important properties of P-10. It can help to understand the effect of $\mathbf{E} \times \mathbf{B}$ on the transport of electrons near the anode wires. The misalignment of the electric and magnetic fields near the anode wires can result in distortion of electron drift lines which affect the position resolution and arrival time [53, 54, 55]. Consider the drift lines in the plane perpendicular to the anode wires as shown in Figure 1.21(a).

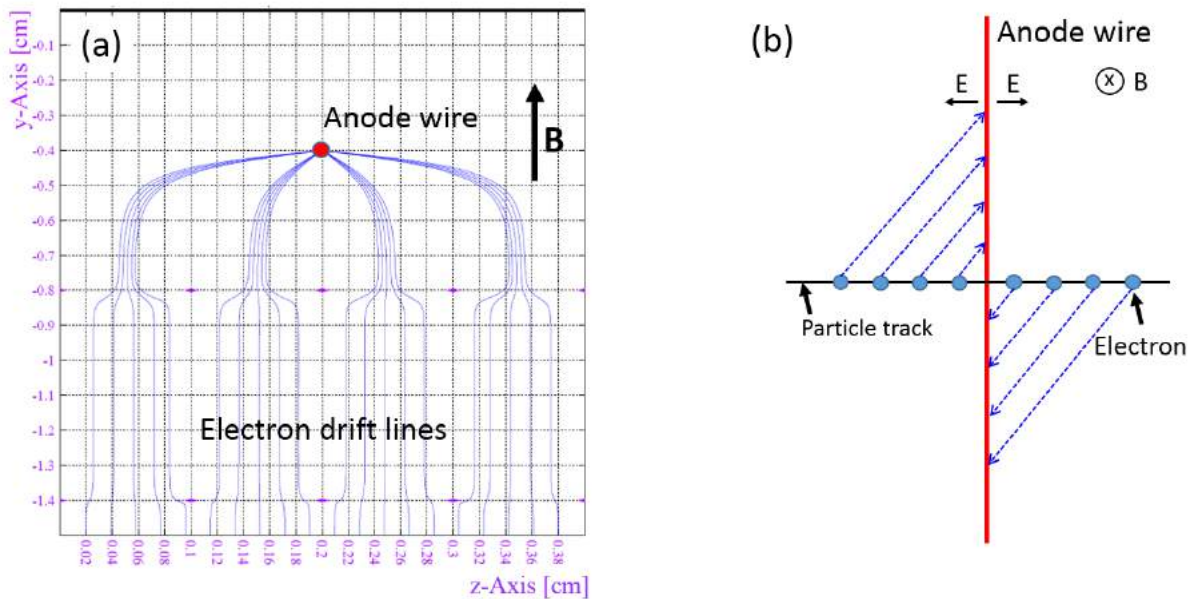


Figure 1.21: (a) Electron drift lines in the plane perpendicular to the anode wire. (b) A Spreading out of the electrons along the anode wire due to the $\mathbf{E} \times \mathbf{B}$ effect.

The electron trajectories that start at z values further from the wire have portions where they are nearly horizontal, i.e. perpendicular to the magnetic field. These trajectories are more influenced by the $\mathbf{E} \times \mathbf{B}$ drift velocity than those closer to the anode wire. The effects of the $\mathbf{E} \times \mathbf{B}$ drift velocity or Lorentz angle are clearly seen in Figure 1.21(b) which shows the projection of these trajectories on the plane perpendicular to the magnetic field. The horizontal line is the ionization track of the original particle. The dashed line show the projection of the electron drift lines. Trajectories originating far to the left are deflected

upwards and those originating further to the right are deflected downwards. The $\mathbf{E} \times \mathbf{B}$ field spreads out the charge from the original track along the wire worsening the spatial resolution of the charge distribution along the wire. The drift lines coming from regions along the track have a smaller Lorentz angle correction. Therefore, the charge will not be shifted as much along the wire. Alternatively, one can understand this effect by considering the electrons originating further away from the wire experience a much weaker electric field comparing to those closer to the wire, the electric field lines for those electrons originating further away are nearly perpendicular to the magnetic field and the Lorentz angle is large. When those electrons drift closer to the wire, the effect of the $\mathbf{E} \times \mathbf{B}$ drift velocity and the Lorentz angle decreases reflecting the high electric field as shown in Figure 1.22.

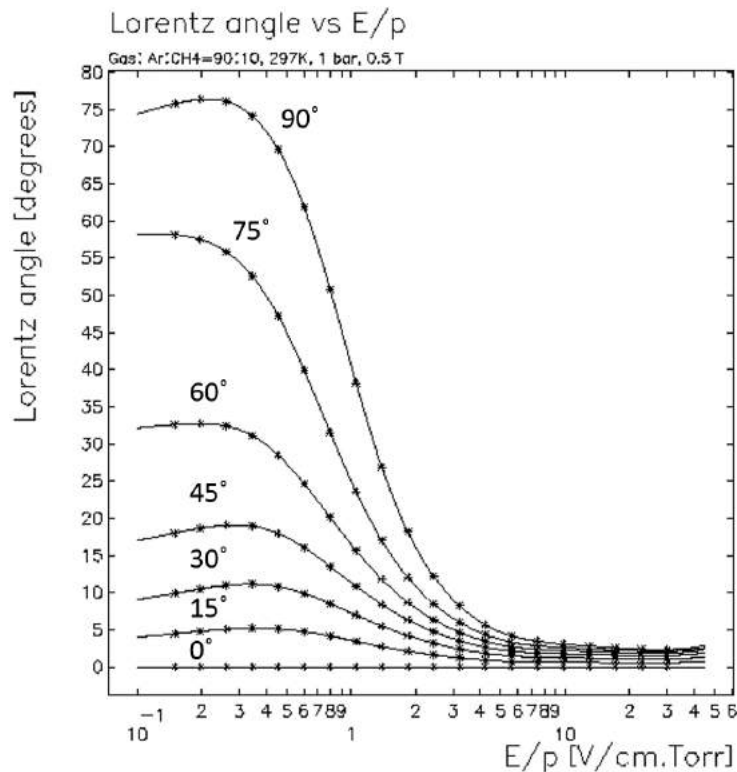


Figure 1.22: Lorentz angle for P-10 with magnetic field of 0.5 T. The angles between the electric field and magnetic field are 0, 15, 30, 45, 60, 75 and 90 degrees [13].

Chapter 2

Descriptions of SPiRIT TPC

2.1 The design and construction of the field cage of the S π RIT TPC

The field cage of the S π RIT Time Projection Chamber (TPC) is a rectangular box with the interior dimensions of 144.64 cm in the horizontal z direction of the beam, by 96.61 cm in the horizontal x direction perpendicular to the beam and 51.10 cm in the vertical y direction perpendicular to the beam. The field cage is a gas-tight volume filled with P-10 gas. Figure 2.1 is 3-dimensional design of the field cage without a polyamide sheet on the exit window. The field cage consists of five main parts which are a top perimeter, side walls, a front wall, an exit window and a cathode. The side and front walls are made of 1.6-mm thick halogen-free G10 printed circuit boards. G10 is a fiber glass-epoxy laminate consisting of layers of fiber glass with an epoxy binder. The exit window is constructed of a polycarbonate frame and a 125- μ m thick polyamide sheet with the dimensions of 39 by 81 cm. The entrance window has a 4- μ m PPTA (poly p-phenylene terephthalamide) foil with the dimensions of 6 by 7 cm. The four vertical corners which are made of halogen-free G10 and constructed from quarter sections of a 4-inch diameter G10 tube. This makes the corners rounded avoiding the high electric field gradients that would be associated with angle at the corner. The details of each part of the field cage will be discussed later in this section.

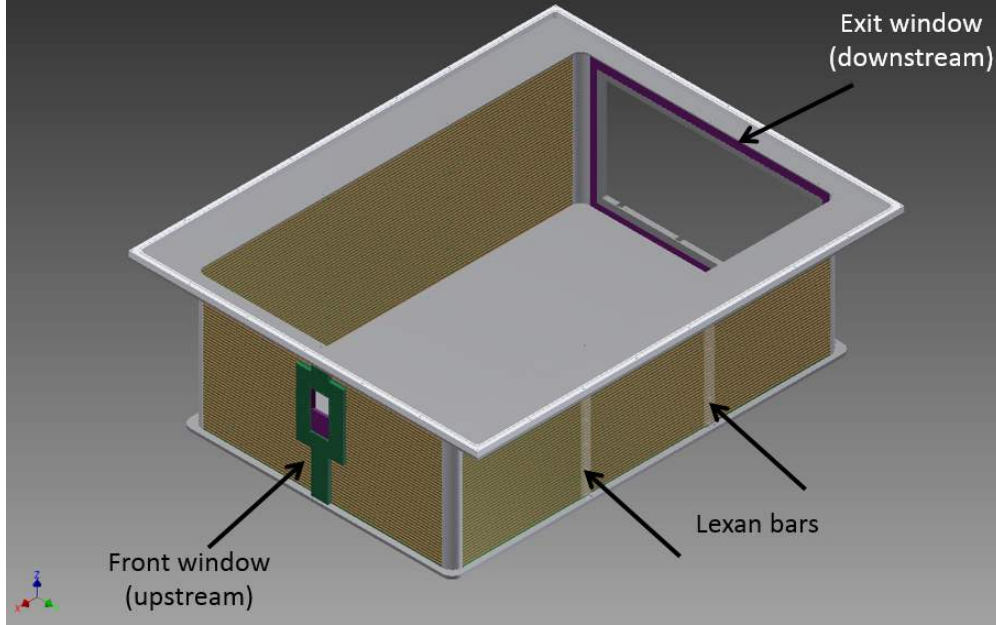


Figure 2.1: 3 dimensional design of the field cage of the $S\pi$ RIT TPC without the exit window polyamide sheet.

2.1.1 Conductive painted components

To provide a uniform field inside the field cage, the corner pieces, side supports, exit and front window frames need to have strips that extend over the insulating surfaces on these pieces to match the conducting equipotential surfaces on the walls. We use the CHO-SHIELD 610 conductive spray coated epoxy paint to provide a conductive surface on those components. It is a two-component epoxy spray paint with silver coated copper flakes embedded in it, which formed a conductive epoxy surface when cured. In Figure 2.2, we show the insulating polycarbonate side support bars just before they were painted. Here, the clear polycarbonate surfaces are covered by 4 mm wide Kapton tape, which was used to mask the insulating surfaces that should not be spray painted by the conducting epoxy. This Kapton tape had a acrylic adhesive that could be readily removed by cleaning with ethyl alcohol. Similar techniques were used for all of the other insulating surfaces.

In Figure 2.3, one can see how the front window frame was painted with the conductive

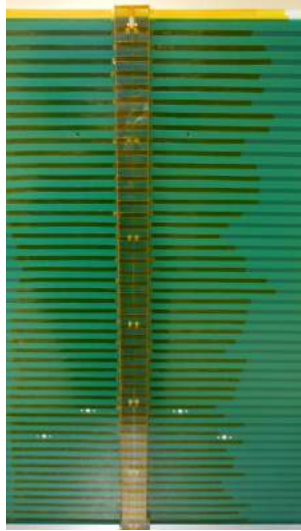


Figure 2.2: Prepare the side support for being painted with the copper-silver epoxy paint. Kapton tape is used to mask off the areas that do not want the paint to go over.



Figure 2.3: The front window frame was painted with the conducting paint was an epoxy with silver coated.

epoxy paint. After the epoxy paint cured, the frame was unmasked and cleaned carefully with ethanol. The same procedures were used to create necessary conductive surfaces on the three other surfaces. All conductive surfaces were checked for continuity. The painted conductive strips matched the electrode surfaces on the neighboring circuit boards on the field cage walls to better than a mm.

2.1.2 Side walls

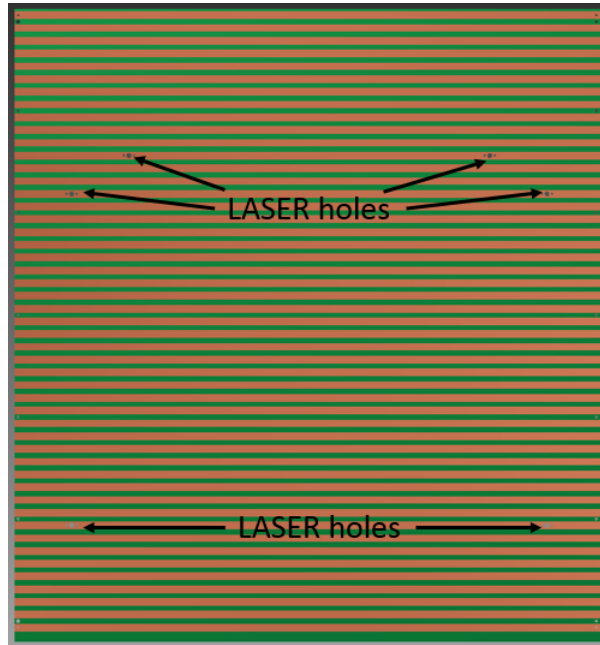


Figure 2.4: Drawing of a side wall PCB of the field cage. There are holes for the LASER calibration components. The fixtures for the laser ports are not shown in this figure.

Most of the side walls of the field cage are formed of 1.6-mm halogen-free G10 printed circuit boards. Each side wall was formed of 3 PCBs; the side wall contained 6 such PCB in total. The dimensions of each PCB are 46.3 by 49.6 cm. There are 6-mm wide copper strips and 4 mm gaps between the strips which correspond to a 1-cm pitch on the interior and exterior of the field cage as shown in Figure 2.5. The 4 mm gap between conducting strips was chosen to allow the operation at higher possible Electrostatic drift fields. There are vias, shown larger than scale on the drawing, which connect the inside and outside strips that are at the same electrostatic potential. In Figure 2.4, there are holes for mounting the LASER calibration components. These laser holes have been equipped with quartz windows and mounting fixtures to hold fiber optics connections for a calibration laser. While the laser systems has been tested, they have not yet been mounted on the $S\pi$ RIT TPC.

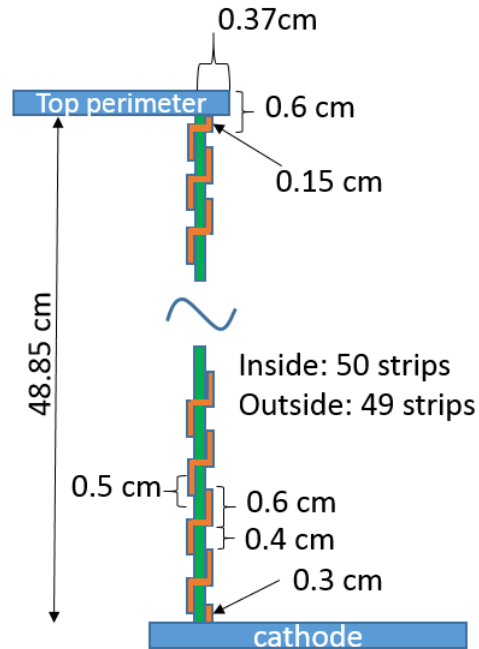


Figure 2.5: After the walls were assembled, the interior has 50 strips and 49 strips for the exterior. The strip on the top sinks into the top perimeter and the one at the bottom sinks into the cathode.

The technique for gluing the field cage is the following. To assemble the side walls, the regions where the walls were glued to the side supports were first sanded by using a 220-grit sandpaper. A Kapton tape with acrylic adhesive was used to mask off areas to where glue should be applied. In addition, a 6-inch wide plastic pieces were taped on both sides of the walls to provide more protection for the PCBs. Then, 3-mm beads of Araldite 2013 epoxy were applied on the side supports. Then, 2-56 brass screws were inserted through the boards and into the side supports. Positioning has been done carefully to prevent excess movement and smearing of the glue. Then, the PCBs and side supports were pressed together and the screws were tightened that both positioned and secured the PCBs and circuit boards while the glue hardened. Then, excess glue on both sides is cleaned with ethanol. Finally, the side wall was undisturbed on the flat surface for 10 hours to cure as shown in Figure 2.6. Each side wall consists of three PCBs. To minimize handling while the glue is hardening, we glued

each side in two steps, first PCB 1 and 2 were glued and after the glue sets, the third PCB was attached to have a complete side wall.

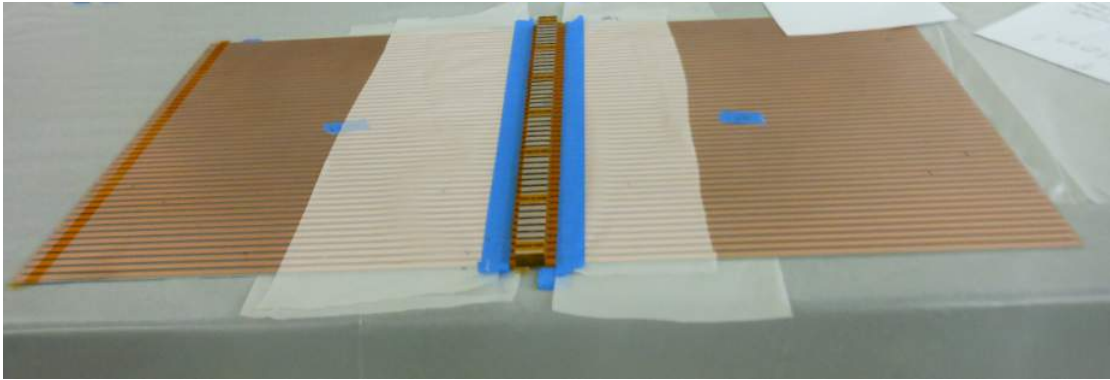


Figure 2.6: Side wall of the field cage was laid on the flat surface for 10 hours to cure

After the epoxy cured, we soldered thin copper pieces on the interior of the field cage to connect all the strips on the neighboring PCBs. On the exterior of the field cage, wires were also soldered on the walls to ensure a well defined electrical potential on the outside of the support bars and around the curved corners of the field cage. This also ensured electrical continuity between the painted strips on the side supports and PCBs. This process will be discussed in details on Section 2.1.6.

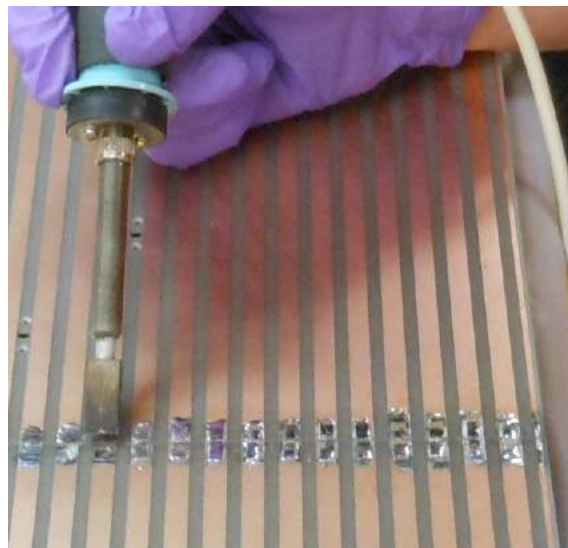


Figure 2.7: Solder thin copper pieces on the side walls to connect the strips on the PCBs.

2.1.3 Front wall

In the mechanical drawing in Figure 2.8, the front wall of the field cage is shown. It consists of two PCB walls, a window frame (green) and a removable window (purple). The removable window is screwed on the window frame as shown in Figure 2.9. On the window frame, there are two gas channels which are used to reroute the filling gas from the filling connection at the top of the field cage through the window frame to the bottom of the field cage. This is desirable because the gas connections can present a point where sparks can occur, thus it is better that these connections are made at the top where the voltage is low. These gas channels were made gas tight during the gluing process.

The procedure for assembling the front wall is similar to that of the side wall. First of all, all glue regions were prepared by using a 220-grit sandpaper. The glue excess areas were masked off. The glue beads were applied along side of the gas channels on the window frame. The glue bead on the inside of the channels needs to be much smaller (1 mm) than that of the outside of the channels (3 mm) so that the excess glue will not fill the gas channel.

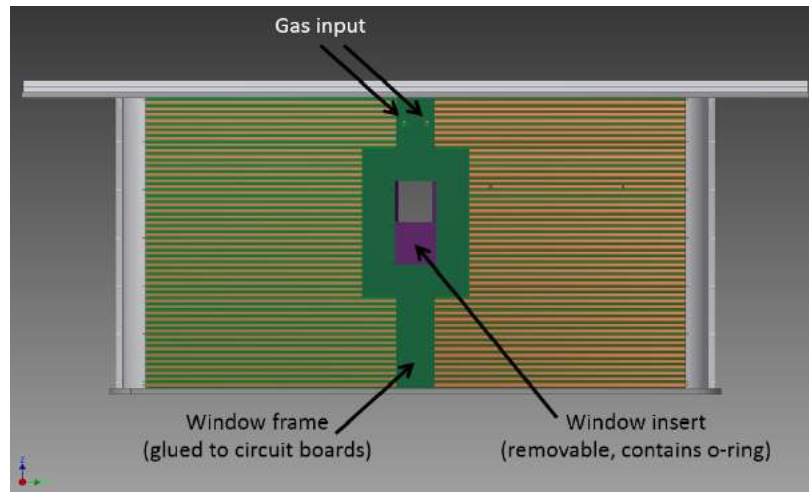


Figure 2.8: The front side of the field cage consists of two PCBs and the window frame which is glued to the two walls. Green: the window frame gas two gas channels which are used to fill the gas into the TPC from the bottom. Purple: The removable inserted window is screwed on the window frame from the inside of the field cage.

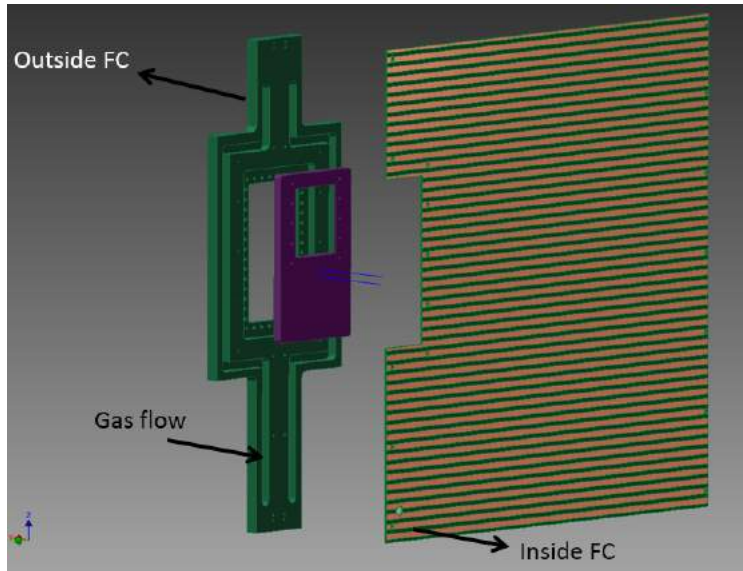


Figure 2.9: Exploded view of the front side of the field cage. Shown in the drawing are two gas channels for filling the gas into the TPC.

In Figure 2.10, the boards were slowly position and lower over the window frame. The window frame was screwed to the walls. After cleaning the excess glue, the front wall was carefully flipped over and laid on the flat surface for 10 hours to cure.

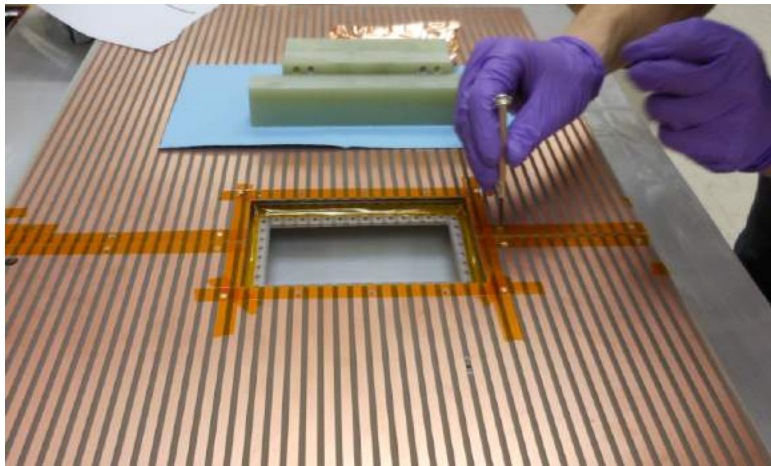


Figure 2.10: After position the window frame and boards, the boards were attached to the window frame firmly with the brass screws.

The purple piece in Figure 2.9 represents the removable window of the field cage to which the actual window is glued. It has the dimensions of 9.9 cm wide, 16.9 cm long



(a) Front side of an inserted window



(b) Back side of an inserted window

Figure 2.11: Inserted removable window of the field cage



Figure 2.12: The inserted window is put on the front wall of the field cage. The copper fingers provide electrical connections to the strips on the walls.

and 0.9525 cm thick and is constructed from polycarbonate. In Figure 2.11(a), the thin ($4 \mu\text{m}$) PPTA foil forming the beam entrance window is shown. It has the dimensions of 5.73 by 7.0 cm. This allows the beam, produced and scattering particles to pass into the field

cage for detection by the TPC. The copper fingers as seen in Figure 2.11 provide electrical connections to the conductive strips on the wall as demonstrated in Figure 2.12. The strips on the inserted window on the exterior were also connected to the strips on a thin PPTA foil by copper fingers as shown in Figure 2.13. Aluminum conductive strips were evaporated onto the window using the large NSCL evaporator. The exterior side of the window has an o-ring seal, which is compressed by screws that are screwed into the window from outside the field cage. Should the window be broken, the window frame can be removed and the window replaced.

One should note that the conductive strips on the interior of the window are aligned with the interior field cage strips, but are 8 mm wide and separated by 1 mm from the neighboring strips, unlike the case of the field cage strips, which are 6 mm wide with 4 mm gaps. This choice is optimized for the P10 filling gas of initial TPC operation, where the field cage electric field will have a low value of 130 V/cm. Also, one should note that the conductive strips on the outside of the window are aligned with those on the inside, unlike the case of the field cage. Thus there is a shift in these external strips on the outside of the window. This change is required to ensure that there are no sparks through the window to a voltage differential between inside and outside strips that are different electrostatic potential while being only separated by the window thickness 4 μm .

2.1.4 Exit window

The exit window and window frame of the S π RIT TPC were constructed out of three polycarbonate frames as shown in Figure 2.14. The purple frame was glued and screwed permanently to the field cage. The outer dimensions of this frame (purple) are 49.6 by 90.96 cm and the inner dimensions are 43.45 by 84.76 cm. On this side of the exit window frame, there are



Figure 2.13: The strips on a thin PPTA are connected to the strips on the window frame by copper finger.

holes for 2-56 screws. These are used to attached the frame to the corner pieces. The other two pieces (gray) were combined to make the removable downstream window. These two pieces were glued together. The 125 μm kapton window was stretched and glued to the inner surface of the of the removable window frame as seen in Figure 2.15. The aluminum conductive strips on the PPTA were evaporated onto them with a large evaporator setup on the NSCL detector laboratory. Aluminum conducting epoxy was sprayed on the outer window frames to continue the conducting strips on the outside of the removable window to the edge of the window frame. Small circuit boards that matched the 6 mm strips and 4 mm gaps were pressed onto the outside of the exit window as a pressure contact. Wires leading from these contacts were soldered to the side panes of the TPC field cage to make electronic continuity between all of the strips that are suppose to be at the same potential. On the inside of the field cage, continuity of the inner conducting strips was ensured by flexible beryllium copper fingers. To ensure that that these fingers make a positive contact on the strips on the inner window, copper strips were glued with silver epoxy to the strips

on the inner side of the window. The finger contacts made contact with these copper strips when the rear window is screwed onto the field cages and the o-ring is compressed that seals the window.

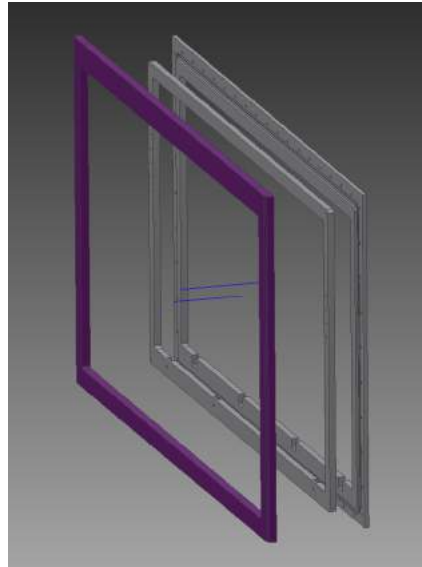


Figure 2.14: Exit window of the $S\pi$ RIT TPC consists of three polycarbonate frames.



Figure 2.15: Exit window

2.1.5 Cathode

The cathode of the $S\pi$ RIT TPC is constructed of the aluminum honeycomb which is bonded to the field cage by Araldite 2013 epoxy. The cathode is a rectangular solid with the dimensions of 101.6 cm wide, 149.86 cm long and 1.54 cm high. The upper surface of the cathode is a solid aluminum sheet, while the lower is perforated so as to allow the cathode to be placed in a vacuum, should the TPC be evacuated and later refilled with an explosive counter gas, when used as an active target. The four corners of the cathode are rounded to reduce sparking at a high voltage (5-20 kV). In Figure 2.16, an aluminum round edge was attached to the edge of the cathode to further reduce the possibility of sparking. Since the work function of aluminum can be lower than the energy of the LASER originally purchased for calibration, the inner surface of the cathode was coated by graphite at the center area of 96.4 by 144.45 cm to minimize the production of photo-electrons by scattered laser light.



Figure 2.16: Round aluminum edge was attached to the edge of the cathode to reduce a sharp angle.

The cathode of the $S\pi$ RIT TPC is connected to the external power supply, voltage step

down and field cage. There are two sets of 50 resistors with the resistance of $100\text{ M}\Omega$ used as voltage divider to define the voltage in the field cage. Between each neighboring pair of strips, there are two resistors, each with 100 Mohm , making the resistance between neighboring strips to be 50 Mohms . Thus, the total resistance of the field cage is about $R_{FC}=2.5\text{ G}\Omega$. The voltage step down has 7 resistors with individual resistance of $100\text{ M}\Omega$ for a total resistance of $R_{VSD} = 700\text{ M}\Omega$. In Figure 2.17, the circuit diagram shows how the components are connected. The beginning of the resistance network is connected to a conductive surface of the voltage step down. The Voltage step down design, discussed in section 2.5, has an upper conductive surface which is shorted by a spring loaded contact to the under side of the cathode. This upper surface is capacitively coupled through a polycarbonated insulating sheet to the TPC enclosure. The corresponding capacitance to ground is $C_{VSD} = 7.09\text{ nF}$. When combined with R_{Line} , this capacitance makes a low pass filter that effectively filters out noise from the cathode power supply. The cathode is connected to the power supply via a resistor of $R_{Line} = 10\text{ M}\Omega$.

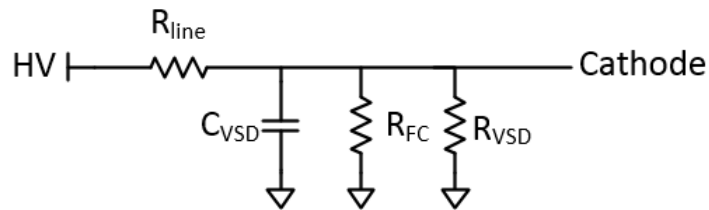


Figure 2.17: Circuit diagram for the electrical connections of the cathode

2.1.6 Field cage assembly

In this section, the design and assembly of the TPC field cage are more clearly described. Careful planning is required as the epoxy sets up on about 2-3 hours depending on temper-



Figure 2.18: Assembling the front and side walls of the field cage.

ature. So all assembly procedures were practiced without glue and timed before the final assembly was undertaken. Prior to gluing, regions that should not be glued on the side and front walls are masked off by the plastic sheets and Kapton tape. First, the side and front walls were assembled as discussed in Sections 2.1.2 and 2.1.3. Then a corner section was attached to each of these walls and to the back window frame as shown in Figure 2.20. After these pieces were glued, the full assembly of the field cage was performed. In Figure 2.18, the process illustrated for the TPC side panels. Here this work is initially done on a table and then transferred to precision surface plate. Blocks are used to support the walls, allowing access to the bottom of the walls to remove the excess epoxy. In both Figures 2.18 and 2.19, the person in the foreground is applying the Araldite 2013 epoxy, while the other were applying a 3-mm bead of Araldite 2013 epoxy on the corner piece. Once it is done, the third person brought the side wall and attach to the front wall. After all strips on the front and side walls have been aligned, the front and side walls were screwed together and then we repeat the same process for the other side wall as seen in Figure 2.19.

The next step is to glue the back window frame to the field cage wall. In Figure 2.20,



Figure 2.19: Assemble both side walls of the field cage.

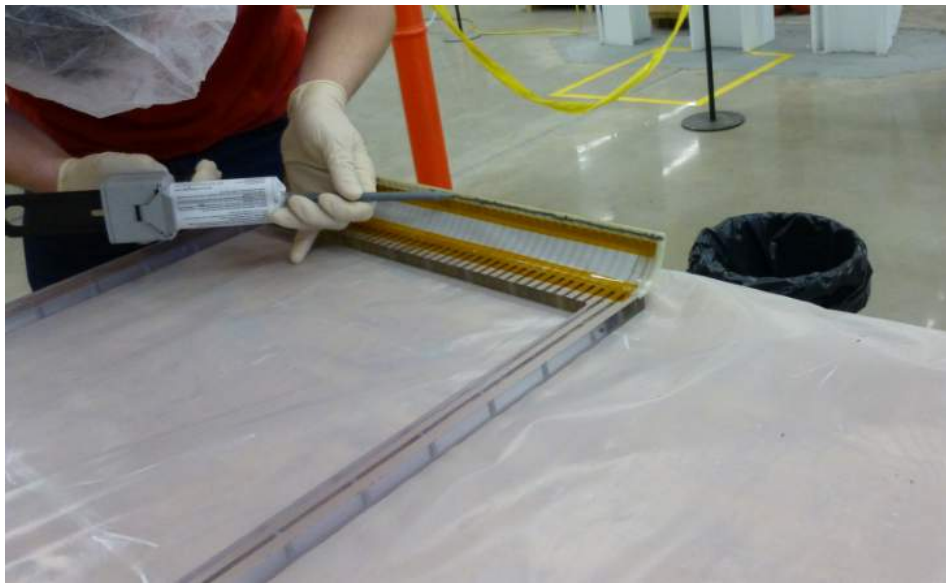


Figure 2.20: Apply the bead of Araldite 2013 epoxy to the corner pieces of the back window frame.

a 3-mm bead of Araldite 2013 epoxy was applied to the corner piece of the back window frame where it attaches to the side panels. After the epoxy beads were applied, the back window frame was assembled to the rest of the wall as shown in Figure 2.21. We checked the alignment of all strips and clean the excess glue. Then the wall was left to cure for 10

hours.



Figure 2.21: Back window frame was attached to the wall of the field cage.

After the epoxy on the wall cured, the next task is to glue to the wall to the top perimeter. The regions on the top perimeter that will be glued were prepared by a 220-grit sandpaper and cleaned with Ethanol. All area that should not be glued but could accumulate excess glue was masked with plastic and a Kapton tape. Then 3-mm beads of Araldite 2013 were put on the groove as shown in Figure 2.22. The cathode was screwed to the walls without epoxy because it is easier to move the wall and position it to the groove on the top perimeter. In addition, the cathode provides rigidity and prevents the wall from deforming.

In Figure 2.23, the wall with the cathode was lower slowly over the groove of the top perimeter. It is important that the wall went into the groove properly. Then the field cage was move to the side of the flat table so that we can screw the wall to the top perimeter from the bottom as seen in Figure 2.24 and it is true for the other side.

After the wall was screwed to the top perimeter, the field cage has been transfer to the supports for checking and cleaning the epoxy from inside and outside as shown in Figure



Figure 2.22: Glue excess area on the top perimeter has been masked off with plastic and a Kapton tape.



Figure 2.23: Place to the wall of the field cage slowly on the groove filled with beads of Araldite 2013.

2.25. Once it is done, the field cage has been placed on the flat surface plate again to cure for 10 hours as shown in Figure 2.26.

After the epoxy cured, the next step is to glue the cathode. First of all, the cathode

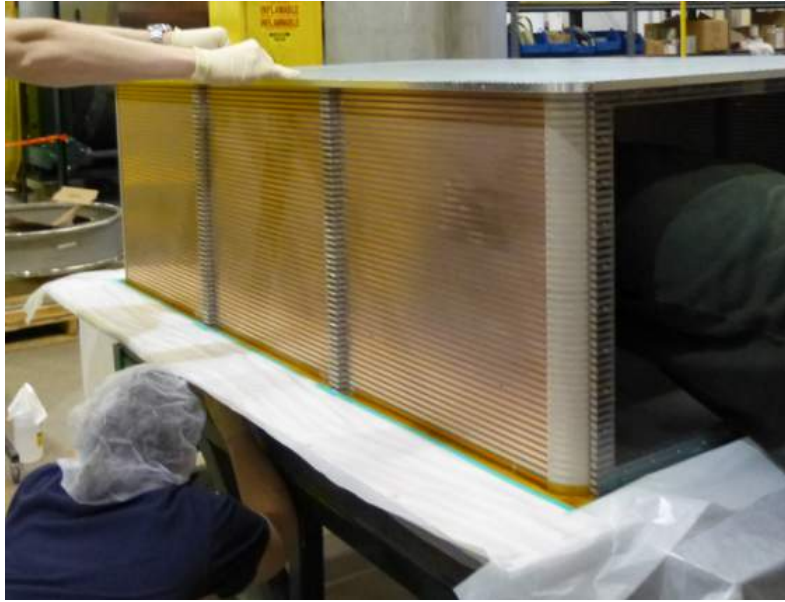


Figure 2.24: Wall of the field cage was screwed to the top perimeter.



Figure 2.25: Field cage was placed on the support for checking and cleaning the epoxy.

was removed from the field cage and prepared for gluing. 3-mm beads of Araldite 2013 were applied into the groove on the cathode as shown in Figure 2.27. Then the rest of the field cage was fit into the groove and screwed down. The excess glue was cleaned and the field cage was left to cure for 10 hours.

Once the mechanical assembly of the field cage is done, the chain of 10-M Ω resistors,



Figure 2.26: Move the field cage to the flat surface to cure for 10 hours.



Figure 2.27: Prepare the cathode for gluing.

described in Section 2.1.6 was soldered on the wall to define the potential on each strip as seen in Figure 2.28. For the interior of the field cage, in Figure 2.29, each strip at the corner was connected across the corner via a wire. Silver conductive epoxy was applied between the wire and painted conductive epoxy strip on the corner to provide a better electrical

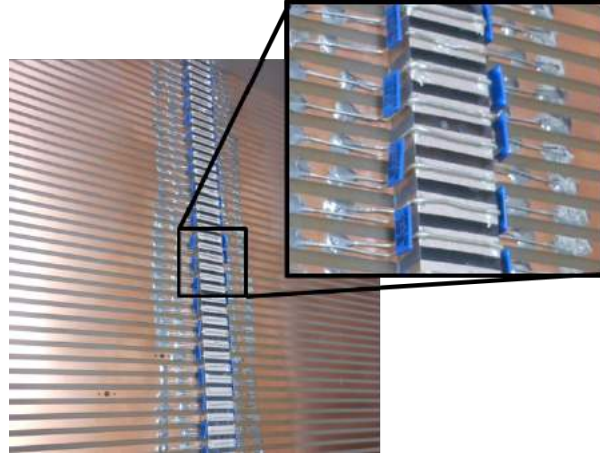


Figure 2.28: To define the potential on each strip, a chain of $10\text{-M}\Omega$ resistor was soldered between in the strips

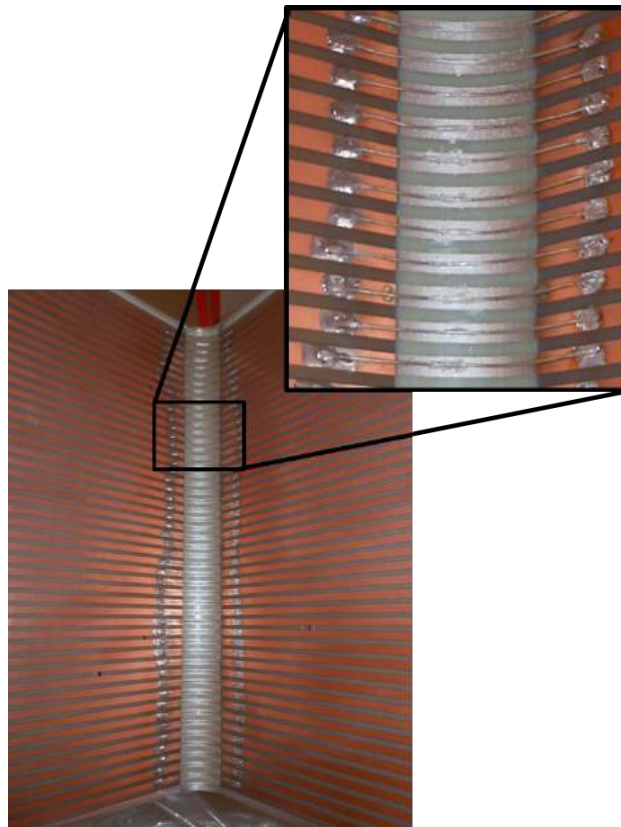


Figure 2.29: Wires were soldered along the strip at the corner for better electrical connections between the strips on corner pieces and the wall. Silver epoxy was applied on the wire at the middle of the strip on the corner pieces to provide a better connection.

connection. Then, $1\text{ k}\Omega$ resistors were inserted on the front corner on the beam left side along the strips by using silver epoxy as shown in Figure 2.30. These $1\text{ k}\Omega$ resistors are used

for two main reasons. First, we can check whether we have a good connection for inside and outside on each strip when the exit window is attached to the TPC. The total resistance on each strip between the exit window and wall should be in the order of $k\Omega$ if the strip has a good electrical connection. In addition, if the magnetic field suddenly quenches, having a resistor can minimize the magnetic force on the field cage because it will reduce the induced current on the strip loop. In Figure 2.31, copper fingers were used to connect the exit window to the field cage. The assembly of the TPC will be discussed in Section 2.7.



Figure 2.30: Insert $1\text{ k}\Omega$ resistors along the strips.

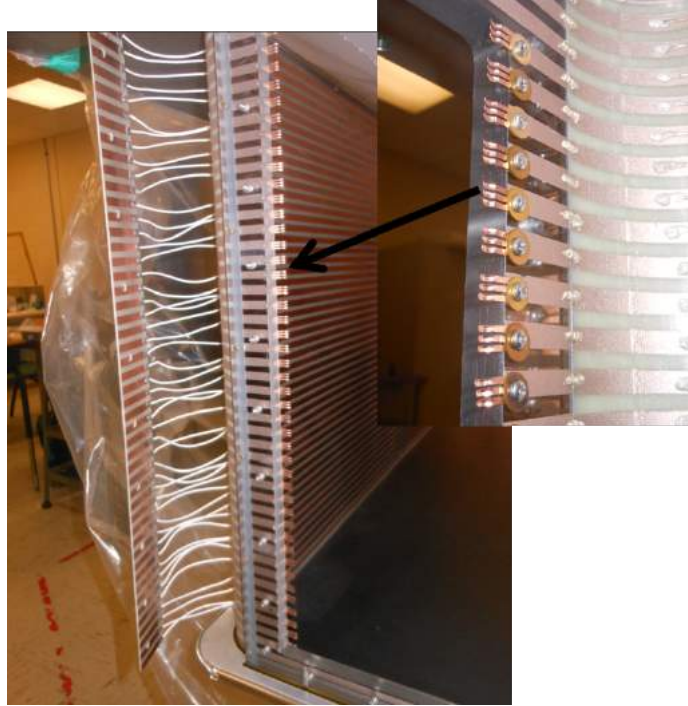


Figure 2.31: Copper fingers were used to connect the conductive strips on the exit window to ones on the wall.

2.1.7 Electrostatics of field cage

If the electric field inside the drift volume is distorted, it will affect electron trajectories from the point of ionization to the multiplication region of the TPC. The tracking algorithms assume the electric field to be parallel to the magnetic field. When that is not true, the trajectories may not be vertical as assumed in the tracking algorithm and also the drift times, which are proportional to the electric field, may be different than expected. Either can result in the complicated reconstruction of the track and large possible uncertainties in the reconstructed momenta of the produced particles in the nuclear reactions. To achieve the best reconstruction of a particle track, having a uniform electric field inside the drift volume is important. As mention in Section 2.1.6, we use a resistor chain to gradually step down the voltage from the cathode to the gating grid and maintain a uniform vertical electric field in the drift region. As shown in Figure 2.32, $10\text{ M}\Omega$ resistors, R , were soldered between the

strip from the cathode to the top perimeter on beam left and beam right sides of the TPC. As all strips at the same height are electrically connected, the two resistor $10\text{ M}\Omega$ resistor chains are in parallel leading to a resistance of $5\text{ M}\Omega$ between two neighboring strips on the inside of the field cage. Another resistor, R_p , was connected from the top perimeter to ground (Top plate).

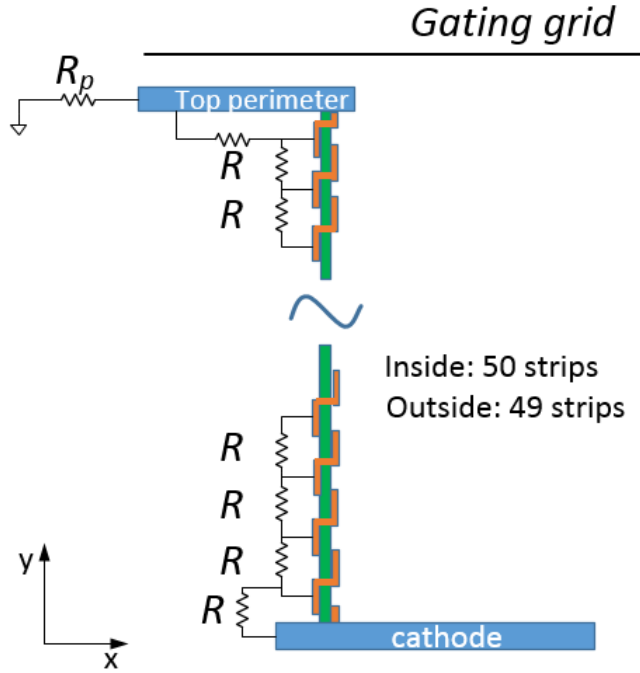


Figure 2.32: Diagram shows the resistor network of the SπRIT TPC.

The effective resistance between the cathode to ground can be written as

$$R_{eff} = 49R + R_p. \quad (2.1)$$

The voltage on each step can be obtained by

$$V_n = \frac{V_{cath}(R_p + (50 - n)R)}{R_{eff}} \quad ; n = 1, 2, 3, \dots, 50, \quad (2.2)$$

where V_{cath} is the voltage of the cathode and V_n is the voltage on the n^{th} step. For $n = 1$,

V_n is equal to V_{cath} . The value of the R_p is adjustable to ensure that the electric field from cathode to gating grid is uniform. In the S π RIT TPC, the distance between cathode and gating grid, $|y_{gg} - y_{cath}|$, is 49.614 cm and the distance between top perimeter and gating grid, $|y_{gg} - y_{tp}|$, is 0.614 cm. Therefore, the distance between top perimeter and cathode, $|y_{tp} - y_{cath}|$, is 49.0 cm. An electric field can be divided into two region. E_1 is an electric field between top perimeter and gating grid and E_2 is an electric field between cathode and top perimeter which can be expressed by

$$E_1 = \frac{V_{gg} - V_{tp}}{|y_{gg} - y_{tp}|} \quad (2.3)$$

$$E_2 = \frac{V_{tp} - V_{cath}}{|y_{tp} - y_{cath}|} \quad (2.4)$$

In general, E_1 and E_2 are not the same since the distance between the top perimeter and gating grid does not have the same pitch as the rest of the field cage. Therefore, an adjustable resistor, R_p , may not have the same value as ones on the strips. The electric field in these regions have to be matched to achieve a uniform electric field from the cathode to the gating grid. We need $E_1 = E_2$. Therefore, the expression for R_p can be written as

$$R_p = \frac{49R}{f(V_{gg}, V_{cath}) - 1} \quad (2.5)$$

where

$$f(V_{gg}, V_{cath}) = \frac{y_{gg} - y_{cath}}{y_{gg} - y_{tp} + (y_{tp} - y_{cath}) \frac{V_{gg}}{V_{cath}}} \quad (2.6)$$

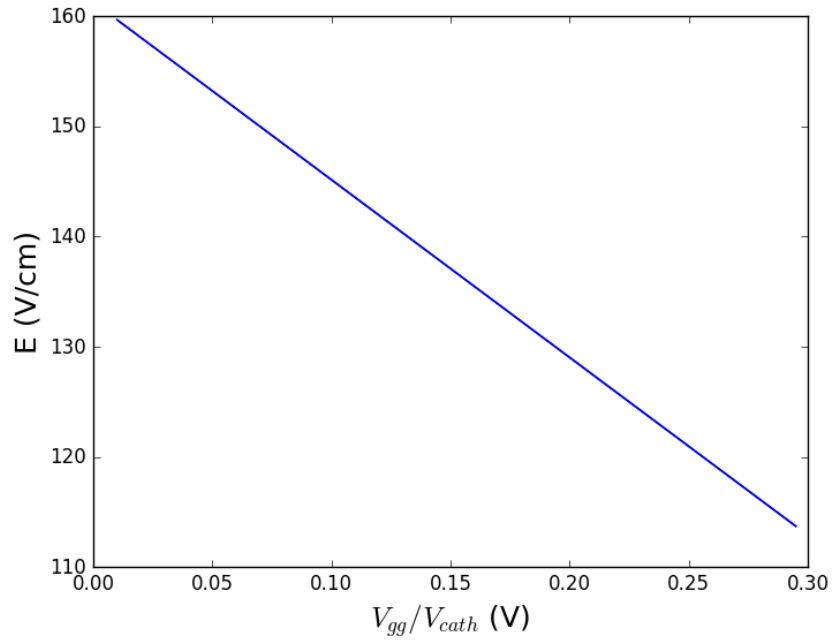
In Equation 2.5, R_p depends on the ratio of V_{gg}/V_{cath} . Figure 2.33(a) shows the electric

field in the drift volume of the TPC as a function of V_{gg}/V_{cath} for $V_{cath} = -8$ kV. The values of R_p needed to adjust the voltages on the strips as a function of V_{gg}/V_{cath} for V_{cath} is shown in Figure 2.33(b). Once we know the strength of the electric field which can be expressed by Equation 2.7, we can use the ratio V_{gg}/V_{cath} for V_{cath} to determine the value of R_p .

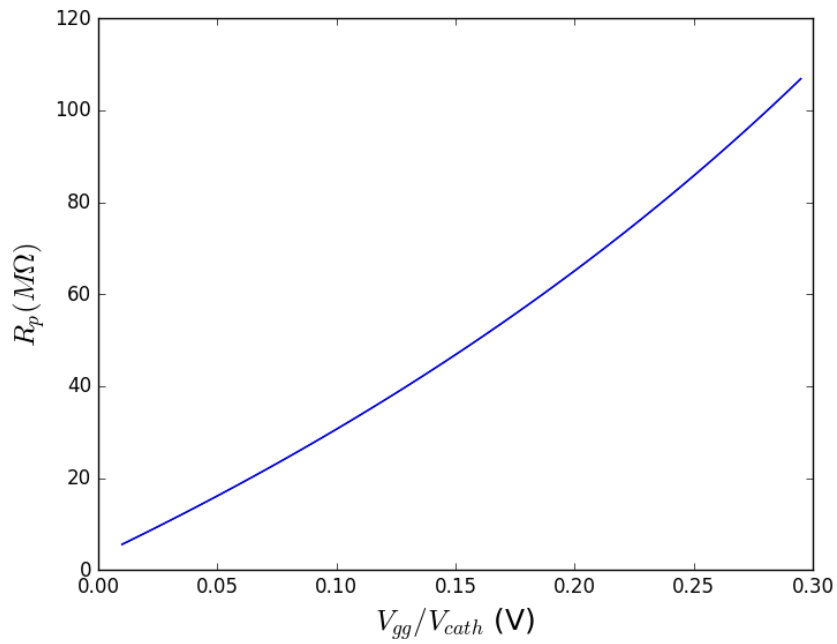
$$E_{TPC} = \frac{V_{gg} - V_{cath}}{|y_{gg} - y_{cath}|} \quad (2.7)$$

Once R_p is known, all voltages on the strips can be determined. Figure 2.34 shows the equipotential lines inside and outside the field cage of the S π RIT TPC performed by ANSYS® "Maxwell". The calculation shows that adjusting the voltages according to the formula gives a uniform electric field in the drift volume. The voltage on each strip is obtained from the Equation 2.2.

In the S π RIT TPC the strips on the upstream window are slightly different from the rest of the field cage as seen in Figure 2.35, described in Section 2.1.3. Figure 2.36 illustrates the electron drift lines near the front window of the S π RIT TPC. Ideally, the electric field inside the TPC should be uniform everywhere. In reality, the electric field of the TPC is defined by the voltages on the cathode, gating grid plane and the strips on the wall of the field cage. In the area close to the wall or front window of the TPC, the electric field deviates from uniformity due to the transverse component of the electric field. The deviation of electric field cause the distortion of electron drift lines. Typically, the vertical component of the position where the ionization occurs is obtained from the time that an electron drifts upward to the anode wire. The distorted drifting electrons take longer time to reach the anode wire and the position in the horizontal plane that these electrons reach is different from the original position. These effects lead to very complicated correction of the track



(a) Electric field in the drift volume as a function of $\frac{V_{gg}}{V_{cath}}$ for $V_{cath} = -8$ kV



(b) R_p as a function of $\frac{V_{gg}}{V_{cath}}$

Figure 2.33: Electric field in the drift volume of the TPC and R_p as a function of $\frac{V_{gg}}{V_{cath}}$.

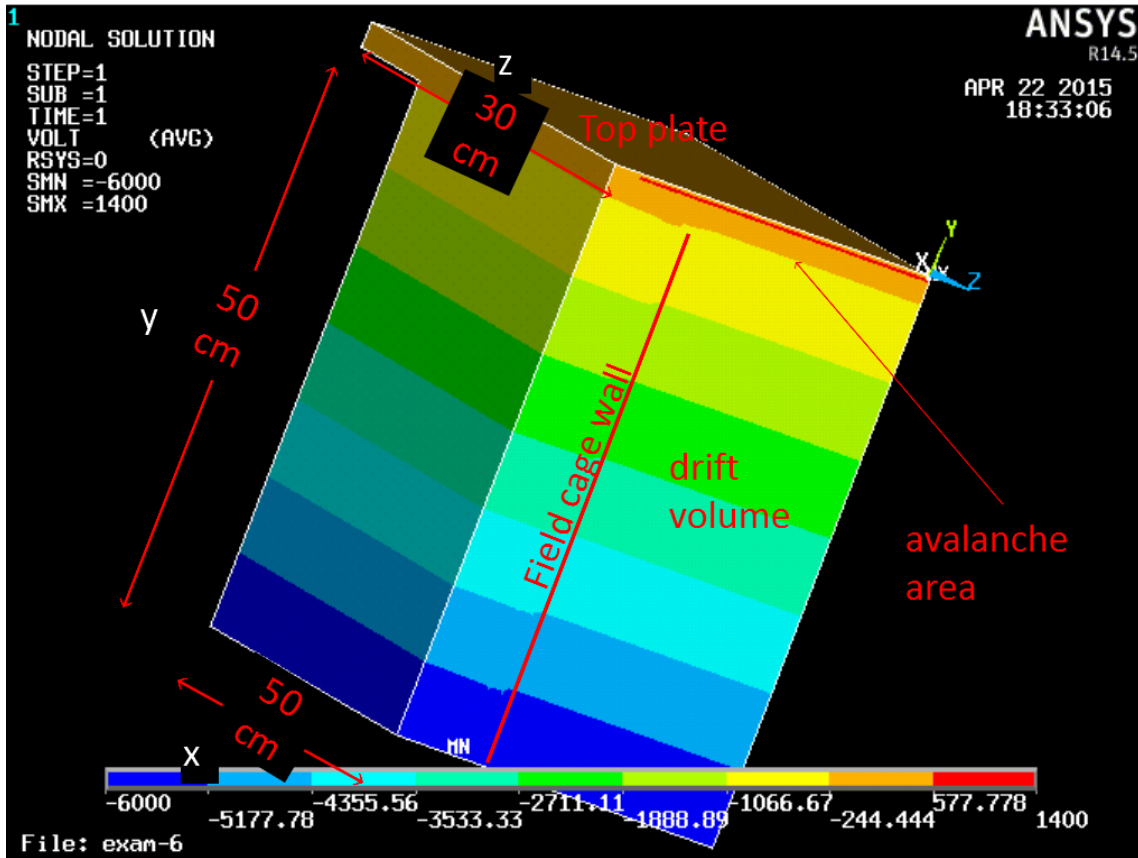


Figure 2.34: Potential calculation of the field cage is performed by ANSYS. R_p is $7 \text{ M}\Omega$ for the V_{cath} and V_{gg} of -6 kV and -110 V , respectively.

reconstruction procedures. In particular, the electric field lines in this calculation are bent away from the front window and end up displaced about 1 mm towards the interior of the field cage. However, this transverse electric field disturbance decreases exponentially with the distance from the window [11]. For the $S\pi$ RIT TPC, the calculation from Garfield [51] shows that at the distance of 2.3 cm from the window, the electric field is uniform and the electron drift lines become a straight line. One should not that near the window, the ionization from a central heavy ion collision will be very large and the track density will be very high. For typical events, it is likely that this region may be very difficult to analyze, which may limit the impact of this region on the final experimental analyses.

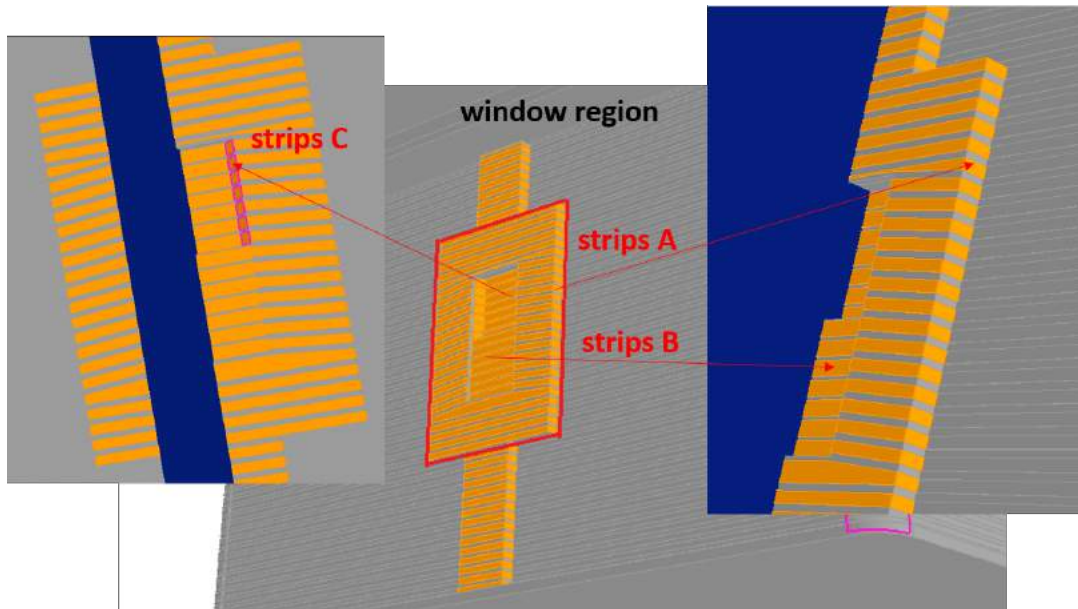


Figure 2.35: The strips on the front window frame are slightly different from the rest of the field cage.

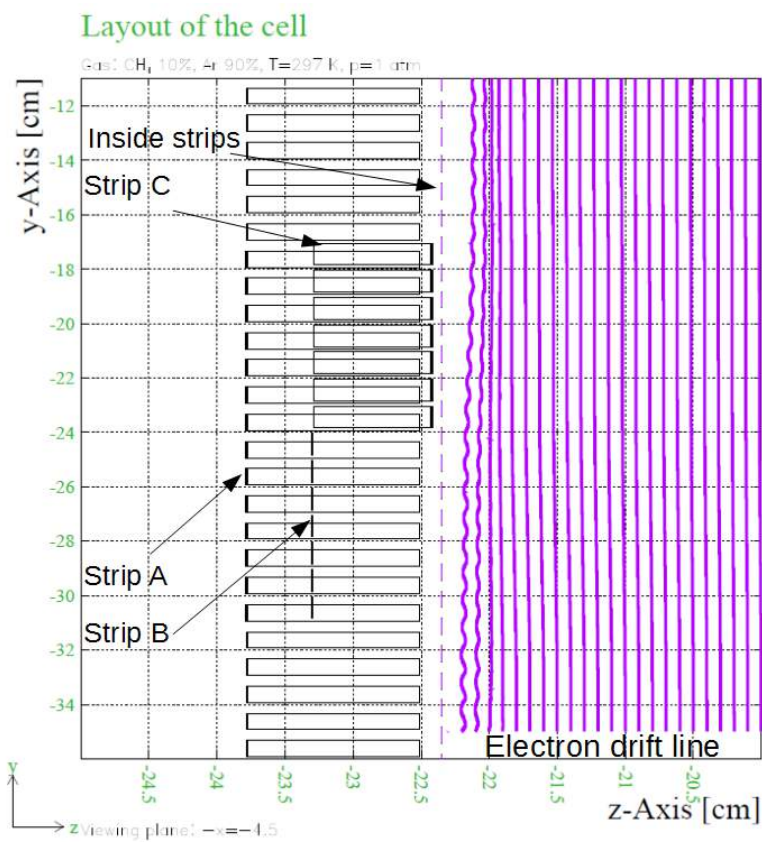


Figure 2.36: Electron drift lines near the front window of the S π RIT TPC.

2.2 The design and construction of the pad plane of the S π RIT TPC

2.2.1 Pad plane assembly

The motion of ions close to the anode wires and the requirement that the pad plane and its pads remain at ground potential causes image charges to move between the conducting pads and the attached Generic Electronics for TPCs (GET) electronics. The pad plane for the SPiRIT TPC has 12096 rectangular copper pads of $\Delta x = 8$ mm by $\Delta z = 12$ mm arranged in 112 rows and 108 columns. Here the rows go in the x direction transverse to the beam and the columns go in the z direction parallel to the beam. The long dimension of the pad are aligned with the beam direction [9]. In a typical experiment, the beam lies along the z-axis and ideally, the electric and magnetic field lie exactly along the y-axis. The pad plane lies in the x-z plane. The circuit boards for the pad plane is a 6-layered board in which ground layers separate the charge-sensitive pads, traces and readout connections. In Figure 2.37, we illustrate the PCB construction. In this Figure, the gray layers illustrate the various G10 thickness. The pads, the ground layers and signal layers are indicated in the Figure. As shown in the Figure, the signal layers are shielded from the charge sensitive pads by the ground layers. This is done to minimize cross-talk between large signals in one pad into other signal line where the interesting signals from pions, for example, may much smaller.

The pad plane is made from four separate halogen-free G10 PCBs. This is important because halogen atoms are extremely electronegative and would capture ionized electrons coming from the tracks. Each PCB contains 3024 pads, which were grouped into 48 unit cells of 63 pads each. Signals from these 63 pads were sent by 63 traces to 63 electronic

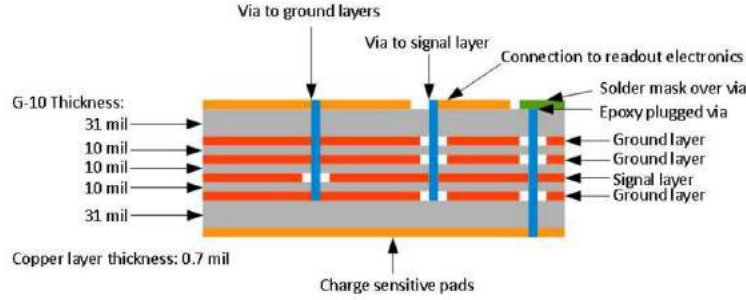


Figure 2.37: Cross-sectional view of the pad plane circuit board [9].

readout channels of the GET readout electronics via the traces in the pad plane and some short cables that take the signals to the ASAD readout boards, discussed in Section GET electronics. In Figure 2.39, a unit cell is connected to two separate 44-pin Samtech connectors on the other side of the PCB. One of these Samtec connectors handles 32 of the 63 signals and the other one carries the other 31 of the signals. One of the connector has 32 channels connected to the pad while the other connector has 31 channels connected to the pads. The unit cell on the beam right side is a 180 degree rotation of one on the beam left side as shown in Figure 2.38.

The PCBs collect the charge from the amplification region. They also transmit the charge to the electronics. In addition, they form part of the gas containment barrier between the field cage and the air outside of the TPC. It is extremely important that the pad plane is flat to within about $100 \mu\text{m}$, rigid and leak tight. These PCBs are glued on the top plate by a multi-stage gluing process. During this gluing process, the top plate is removed from the TPC and turned upside down. The TPC has a rotation mechanism that allows it to be rotated about its center of gravity. Hold the top plate into position while the pad plane is glued and later while the wire planes are attached. The top plate was bolted to the rotation mechanism, upside-down with its inner surface upwards. In Figure 2.40, the center area of the top plate has 384 rectangular connector feedthrough holes for the Samtech connectors

9	12	14	20	23	25	27	
5	7	1	18	31	29	33	
0	2	3	16	30	32	28	32 Channels
4	6	8	13	24	21	26	
48	50	52	10	15	17	19	Beam left
41	43	46	54	57	59	61	
36	37	39	49	65	67	63	31 Channels
34	38	40	51	64	66	62	
42	44	47	53	55	58	60	Center
<hr/>							
60	58	55	53	47	44	42	
62	66	64	51	40	38	34	
63	67	65	49	39	37	36	31 Channels
61	59	57	54	46	43	41	
19	17	15	10	52	50	48	Beam right
26	21	24	13	8	6	4	
28	32	30	16	3	2	0	32 Channels
33	29	31	18	1	7	5	
27	25	23	20	14	12	9	

Figure 2.38: Unit cell on the beam right side is a 180 degree rotation of that of the beam left side. Numbers indicate the channel which the signal from the pad is registered to the AGET.

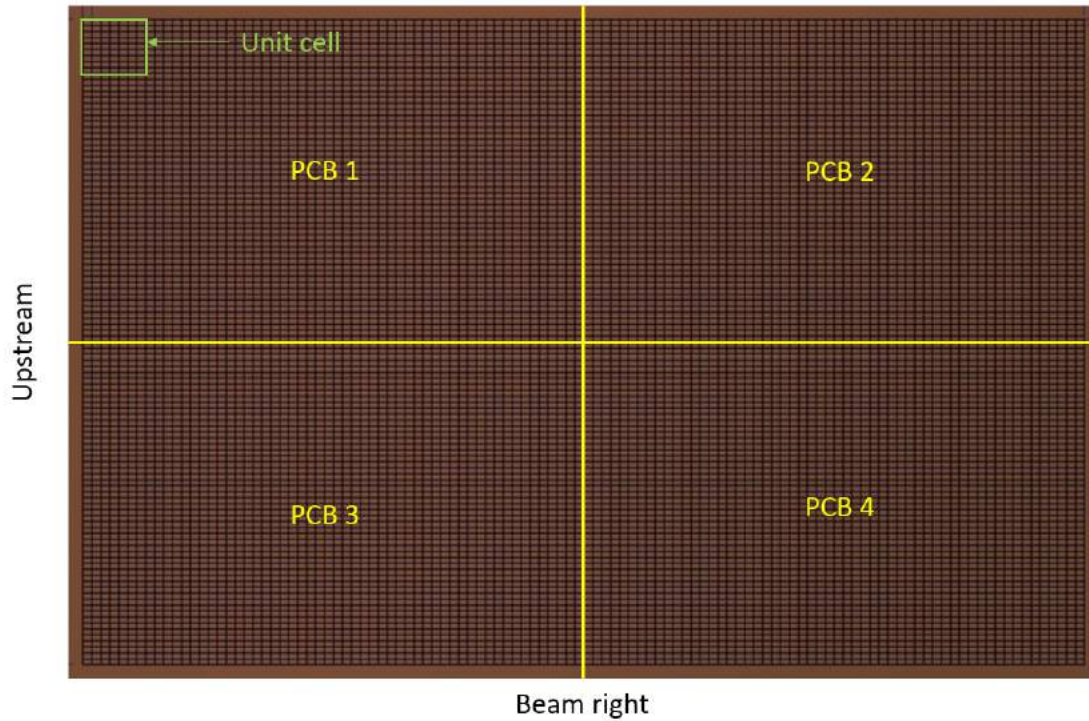


Figure 2.39: Pad plane

which will be attached to the PCBs on the other side. One unit cell will use 2 Samtech connectors. The top plate has ribs on the opposite (outside) surface, shown in Figure 2.41, that largely prevent the top plate from bending along the edges of the top plate. These ribs also largely force all points on the top plate at a given value of z to lie in a straight line.

This design, however, does allow opposing corners of the top plate to both be displaced up or down relative to the other corners. In practice, these corners could be out of plane by as much as 2 mm depending on the flatness of the floor which supported the top plate and rotation mechanism assembly. To avoid complications from this, we jacked up the corners of the rotation mechanism to make the top plate as flat as possible. During the gluing process, we have to preserve the flatness of the pad plane and the pad plane need to be rigidly glued. In addition, we need to avoid the glue on the electrical connectors on the other side of the pad plane. If there is a leak, we need some solutions to fix it. Therefore, we decided to

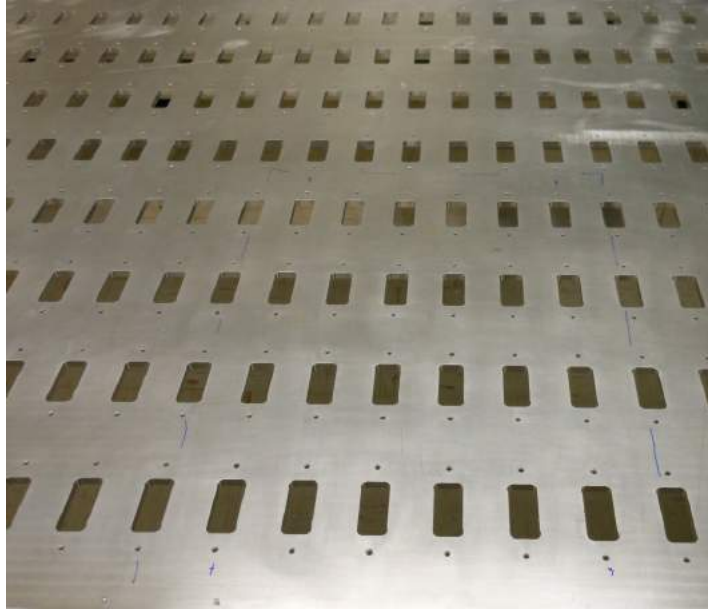


Figure 2.40: Top plate with inner surface upwards. There are 384 rectangular holes for Samtec connector feedthroughs.

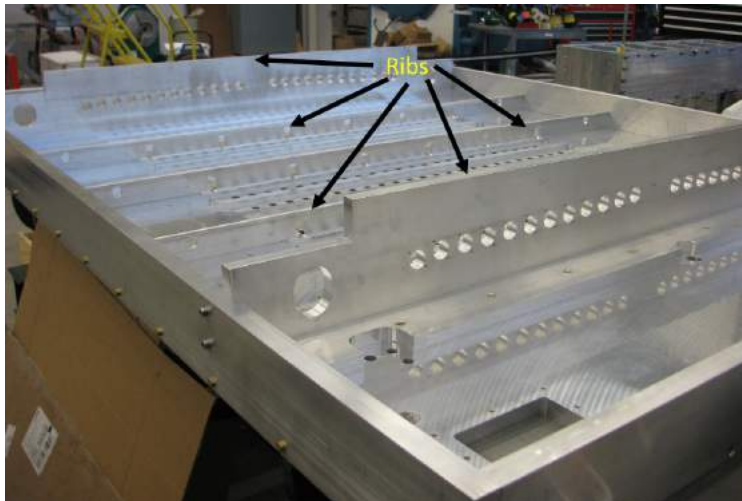
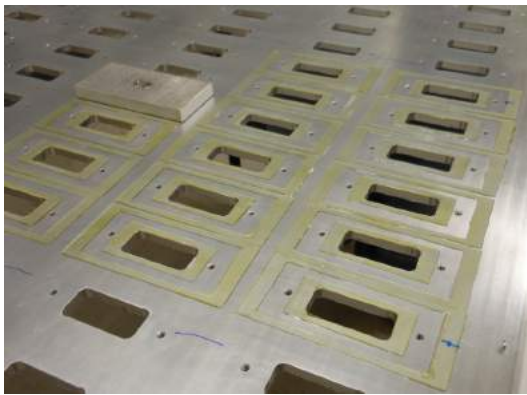


Figure 2.41: Ribs of the top plate

employ gaskets that will be glued to the top plate and to the pad plane and hold the pad plane flat and rigid. Then we need a way to inject glue to correct for leaks. After the top plate was reasonably leveled, the polycarbonate gaskets will be glued on the top plate. As shown in Figure 2.42, each connector feedthrough hole on the top plate has 2 gasket pieces glued around the hole. The bigger gasket has the outer dimensions of 3.000" by 1.375" and

the inner dimensions of 2.500" by 1.125". The smaller gasket has the outer dimensions of 1.75" by 0.80" and the inner dimensions of 1.25" by 0.55". The bigger gasket is large enough to go around the area for one connector while the smaller gasket is large enough to go around the connector feedthrough hole but not cover the screw holes for holding the connector. The stamping metal piece as seen in Figure 2.43 is used to put the gasket to the correct position. The big and small gaskets were hold to the metal by a little drop of water. One needs to check that the gasket will not drop when we turn the metal piece upside down. Continuous threads of EZpoxy 83 were applied along the middle of gasket edges. Then, the metal piece with the gaskets attached to it was placed on the top place and put a little bit pressure on the metal piece. After lifting the stamping piece up, the gaskets should stay on the top plate around the hole. We repeated the procedure 24 times as seen in Figure 2.42(a) to make one section of gasket gluing (Figure 2.42(b)). Then, put the 14" x 9.5" metal plate with neoprene foam and Teflon lining on top of the glued pieces. We put some weight to provide a uniform pressure to the metal plate and leave for 24 hours for the epoxy to cure.



(a) Use a stamping piece to put the gasket to the correct position



(b) A complete section of gasket gluing

Figure 2.42: Gasget gluing

After the polycarbonate gaskets were glued on the top plate as seen in Figure 2.44, each of the four PCBs forming the pad plane were separately glued. When in place ,the horizontal

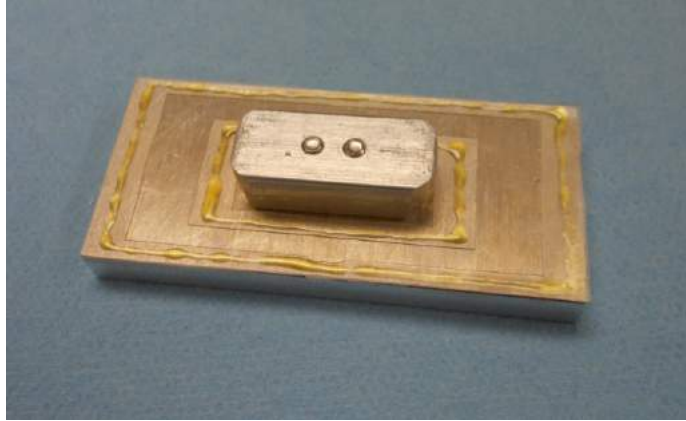


Figure 2.43: Stamping metal piece for gluing gasket

position of each PCB was defined by two dowel pins in the top plate. The following procedure was used to glue the pad plane to the top plate. First, the pad plane was put into its correct position, as defined by the dowel pins. Then a precision vacuum plate was put on top of the pad plane and the vacuum was applied. The precision vacuum table was attached to a precision alignment jig that could fix the horizontal and vertical position and orientation of the vacuum table, but allowed it to be removed and replaced accurately. A precision vacuum table was mounted on an alignment fixture and then lowered onto the PCB which pulled it flat. Then, the PCB plus table was raised to the correct height. After checking at the position of the PCB was correct, both table and PCB were removed. The PCB firmly held in place by vacuum pressure. Then, thin extruded lines of Araldite 2013 epoxy were applied to the gasket surfaces as shown in Figure 2.45 that should lie under the PCB. These were applied with sufficient thickness so that some glue would bond the top plate directly to the gasket and pad plane, but insufficient glue so as to fill the space between the inner and outer gaskets surrounding a connector feedthrough hole. This is believed to be important because the Araldite 2013 displays a greater adhesion between the aluminum top plate and the polycarbonate gasket than does the EZpoxy 83. Then the vacuum table with a PCB were

returned to the alignment fixture above the gluing surfaces and lowered to the correct height. They were then held flat by a vacuum table during the gluing process. It was necessary to apply some weight to the vacuum table to get the pad plane to the correct height (see Figure 2.46). This need for extra weight was not anticipated.

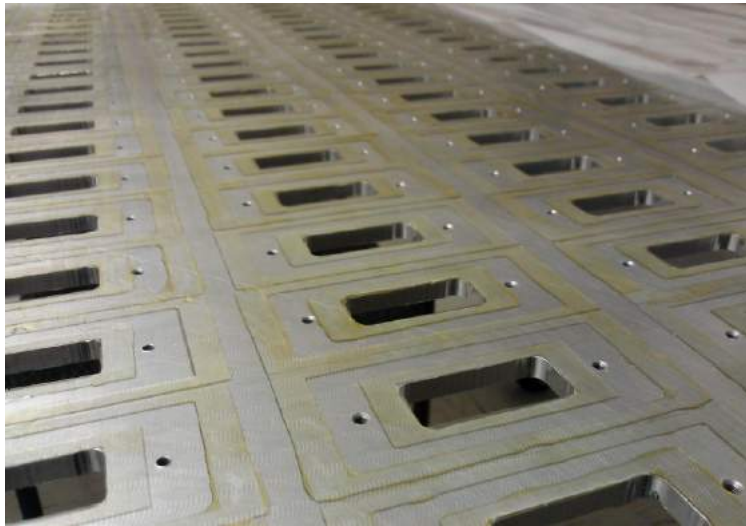


Figure 2.44: Complete gasket gluing process

After the PCBs were glued, the top plate attached to the rest of the enclosure and the top



Figure 2.45: Gluing pattern for the pad plane

plate was subsequently tested to see whether it was gas-tight by applying a small positive pressure to the inside surface of the top plate. Methane gas was injected into the enclosure and the leak rate of Methane gas was detected with the INFICON hydrocarbon leak detector. About a half of the 384 feedthrough holes had a detectable leak. Most were minor. These leaks were plugged by injecting EZpoxy 83 through one of the screw hole and thereby filling the volume between the two gaskets surrounding each feedthrough holes. The possibility that this would be needed was anticipated and motivated to two gasket design. After this final gluing operation, the TPC was gas-tight.



Figure 2.46: Pad-plane PCB is put to the position by the vacuum table.

A FARO laser position sensor was used to determine the flatness of the top plate prior to the mounting the wire planes. The result from the laser position measurement indicates that the distance between the pad plane and the anode wires is constant within $125 \mu\text{m}$. The measurements indicated that the pad plane was slightly closer to the anode wires at the center of the pad plane. This may be due to the weight applied during the gluing of the pad plane to the top plate, which may have distorted the top plate while gluing. In Figure 2.47,

the flatness measurement of the top plate after gluing the pad plane is shown. The top plate is flat within 5 mils (0.13 mm). This discrepancy was within our design specifications.

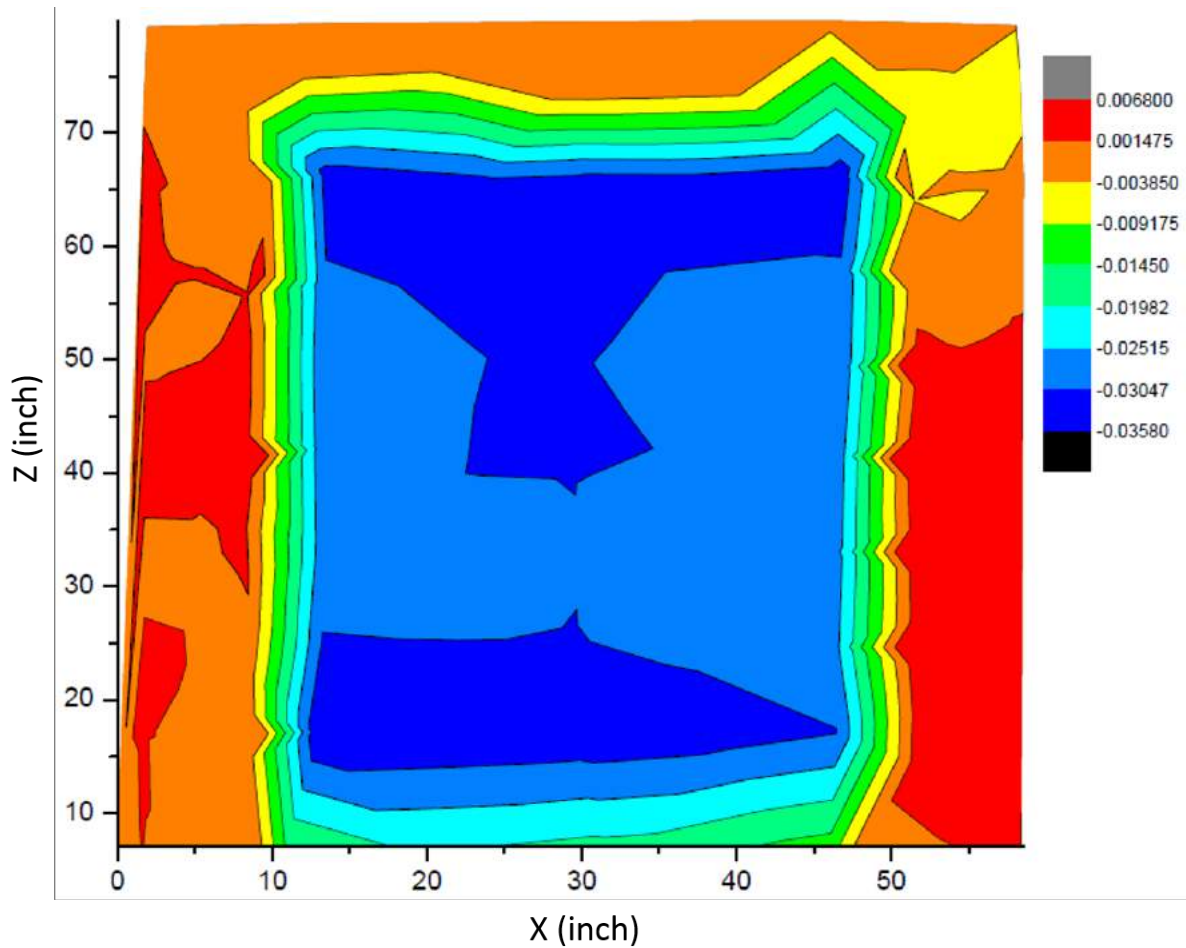


Figure 2.47: The flatness of the top plate using FARO laser position scanner.

2.2.2 Pad response function

For the TPC, dE/dx and particle tracking are the main measurements. The accuracy of dE/dx depends on the gain stability and the energy resolution. The distribution of induced charge on the pad plane and electron diffusion in the drift region affect the resolution of the particle tracking. The pad response function (PRF) includes the relationship between the induced signal on the pad and the position of a track traveling parallel to the length

of the pad. The width of PRF is an important parameter that influences the resolution of the TPC [56]. The induced charge distribution on the pad plane can be explained by Gatti charge distribution [57, 58]. It is a semi-empirical formula calculating the charge distribution on the cathode plane according to the amplification geometry. The arrangement of the system is approximated by an enclosed cathode-anode-cathode consisting of the ground plane, anode plane and the pad-plane which is also at ground potential. Within this region, the initial unmultiplied secondary electronic charge is small and the much larger charges of the electronics and ions produced by the avalanche are equal and opposite. The image charges on the ground and anode plane are largely in response to this avalanche. Therefore, the sum of all signals within the gas and on the electrode surfaces at any given time is zero. The sum of cathode signals are therefore equal to the sum of negative signals of the anode. This can be express by

$$I_{c1}(t) = \frac{1}{2}I_c(t) = -\frac{1}{2}I_w(t). \quad (2.8)$$

Where I_{c1} is the charges induced on the one of the cathode plane (pad plane), I_c is the charges induced on both cathode planes (i.e. ground plane and pad plane) and I_w is the charges induced on the anode plane. The charges on an infinitesimal cathode strip can be obtained by firstly defining the cathode charge distribution:

$$dI_{c1}(t, \lambda) = I_c(t)\Gamma(\lambda)d\lambda \quad (2.9)$$

$$\int_{-\infty}^{\infty} \Gamma(\lambda)d\lambda = \frac{1}{2} \quad (2.10)$$

Where $\lambda = \frac{x}{h}$ is the distance of the infinitesimal strip from the avalanche position in

the cathode plane x which is normalized to the anode-cathode separation h . The charge distribution can be represented by a single-parameter semi-empirical expression known as Gatti function:

$$\Gamma(\lambda) = K_1 \frac{1 - \tanh^2 K_2 \lambda}{1 + K_3 \tanh^2 K_2 \lambda} \quad (2.11)$$

The parameter K_1 and K_2 are defined by K_3 :

$$K_1 = \frac{K_2 \sqrt{K_3}}{4 \arctan \sqrt{K_3}} \quad (2.12)$$

$$K_2 = \frac{\pi}{2} \left(1 - \frac{\sqrt{K_3}}{2} \right) \quad (2.13)$$

The values of K_3 are illustrated in Figure 2.48 for $\frac{h}{s} > 1.0$. Here, $h=4$ mm is the spacing between the anode wire plane and the nearby ground plane or pad plane cathodes and $s=4$ mm is the spacing between anode wires. For the smaller values of $\frac{h}{s} (\leq 1.0)$, K_3 has a different value for the configurations that the anode wires are parallel or perpendicular to the length of the pads on the pad plane [58, 14] as seen in Figure 2.49(a) and (b). Note that $\Gamma(\lambda)$ represents the charge distribution on the single cathode plane from a single avalanche. For S π RIT TPC with $\frac{h}{s} = 1.0$, the corresponding values of K_3 are 0.625 and 0.550 for parallel and perpendicular configurations, respectively. Note that the values of K_3 from both configurations should be of assistance of estimation. The parallel configuration is useful for determining the coordinate of the track relative to the long 12mm dimension of the pads and the perpendicular configuration is useful for determine the coordinate of the track relative to the shorter 8 mm dimension of the pad.

The value of K_3 used in the SpiRITROOT was obtained from extrapolating the function

in Figure 2.48 with the expression:

$$K_3 = \left(A \times \frac{s}{h} + B\right) \cdot \left(C \times \frac{s}{r_a} + D + E \times \frac{s^2}{r_a^2}\right) \quad (2.14)$$

Where s is the anode wire pitch, h is the distance between the anode plane and the pad plane and r_a is the radius of the anode wire. The Equation 2.14 gives the value of $K_3 = 0.7535$.

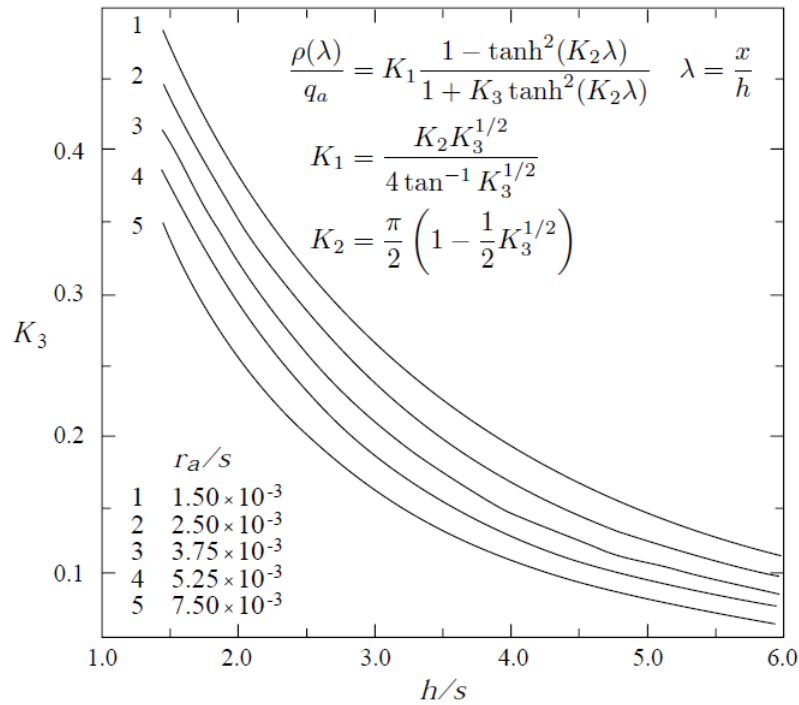
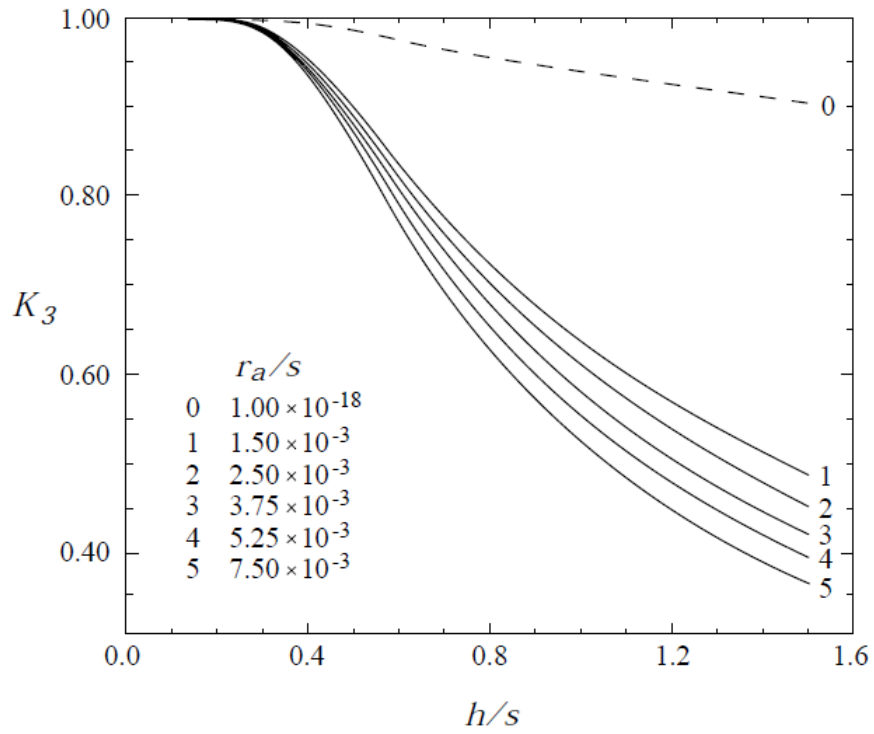


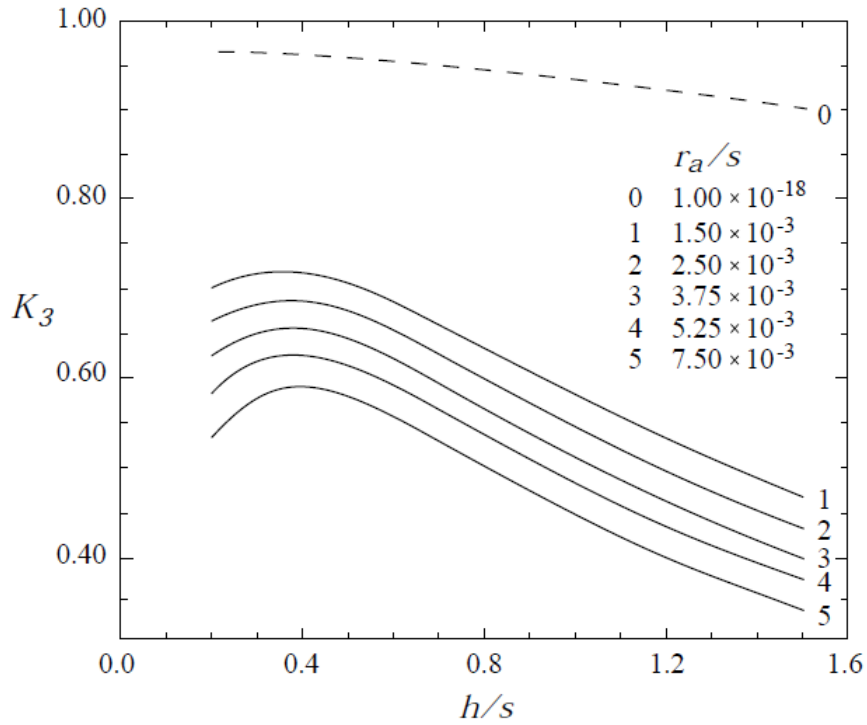
Figure 2.48: Values of parameter K_3 as a function of an anode wire pitch s , an anode-cathode separation h and the radius of an anode wire r_a [14]

For the strip with finite width w centered at position λ one can calculate the signal by the expression:

$$I(t, \lambda, w) = \int_{\lambda-w/2}^{\lambda+w/2} dI(t, \lambda') d\lambda' = I_c(t) \int_{\lambda-w/2}^{\lambda+w/2} \Gamma(\lambda') d\lambda' = I_c(t) P_0(\lambda) \quad (2.15)$$



(a) Values of parameter K_3 as anode wires are perpendicular to the pad plane.



(b) Values of parameter K_3 as anode wires are parallel to the pad plane.

Figure 2.49: Value of K_3 for $\frac{h}{s} \leq 1.0$ [14]

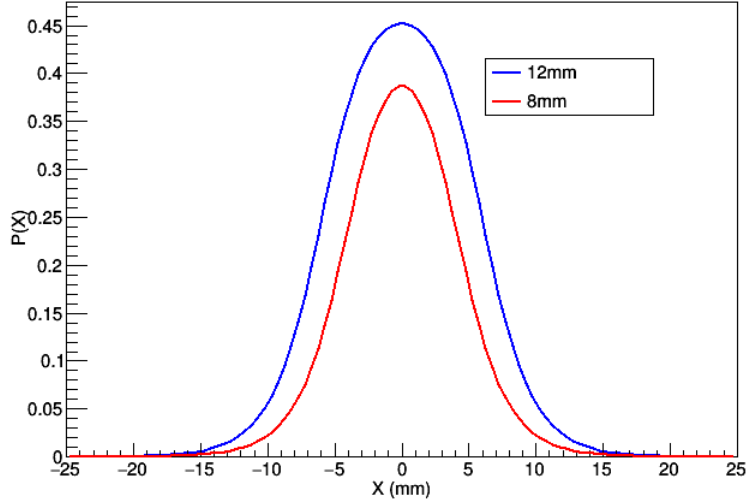


Figure 2.50: Pad response function for S π RIT TPC with $w = 8$ mm (red) and $w = 12$ mm (blue)

$$P_0(\lambda) = \frac{K_1}{K_2\sqrt{K_3}} \left(\arctan \left[\sqrt{K_3} \tanh K_2 \left(\lambda + \frac{w}{2h} \right) \right] - \arctan \left[\sqrt{K_3} \tanh K_2 \left(\lambda - \frac{w}{2h} \right) \right] \right) \quad (2.16)$$

$P_0(\lambda)$ is the pad response function (PRF). The pad response function provides the information on what fraction of total cathode signals is induced in the strip. As the width w increases the PRF approaches the maximum value of $\frac{1}{2}$. This means that any pad can read up to 50% of the total charge. For S π RIT TPC, the width of the pad is 8 mm is in the direction parallel to the wire and 12 mm is in the direction perpendicular to the wire. The PRFs of both widths are shown in Figure 2.50. The PRF of the width of 8 mm shows that 39% of the total charge is collected at the central strip while it is 45% for the width of 12 mm. The two adjacent pads for the width of 8 mm collect 5.5% of the total charge each and it is 2.4% for the width of 12 mm. In both cases, the sum of the collected charges from the central and adjacent pads are 50%. For the track measurement, an effective pad response function $P_{eff}(\lambda)$ can be used as well. $P_{eff}(\lambda)$ can be constructed by a superposition of Gaussian curves and it is sufficient [11].

2.3 The design and construction of the wire planes of the S π RIT TPC

The multiplication region of the S π RIT TPC consists of three wire planes which are anode, ground and gating grid planes. The arrangement of the three wire planes are resembled that of EOS Time Projection Chamber (EOS TPC) [40].

2.3.1 Wire winding and tension measurement

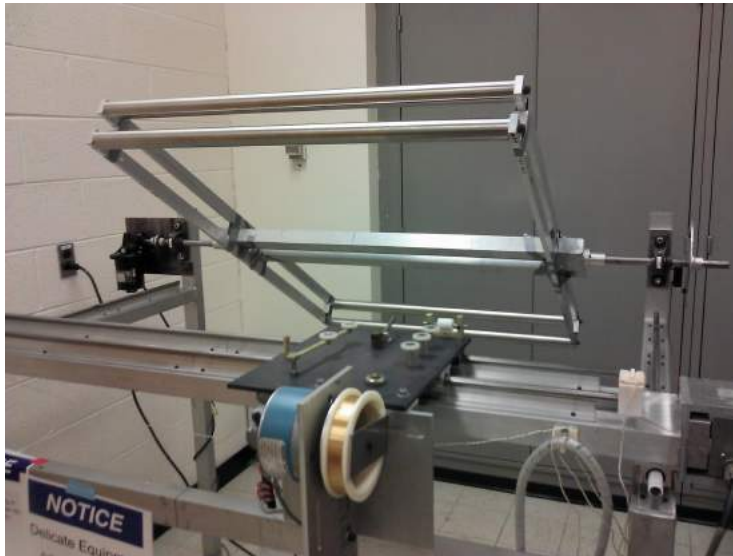
All three wire planes of the S π RIT TPC have been fabricated from the wire-winding machine in the clean room at the National Superconducting Cyclotron Laboratory (NSCL) at Michigan State University (see Figure 2.51). The machine provides a precise pitch and a well-defined tension on each wire. The machine fabricates two frames of wires at a time as seen in Figure 2.51(a). The tension and properties of each wire plane are shown in Table 2.1.

Table 2.1: Properties of wire planes of the S π RIT TPC.

	Anode	Ground	Gating grid
Material	Gold- plated tungsten	BeCu	BeCu
Diameter (μm)	20	76	76
Tension (N)	0.5	1.2	1.2
Max. Current (mA)	600	1000	1000

To perform the wire-winding process, first of all, two identical wire frames are firmly mounted on the wire-winding machine. Then, a wire is run through the pulley system as shown in Figure 2.51(b) and attached to the middle bar below the wire frames. The tension for the wires is defined by the combination of springs. Note that one needs to run

a wire-winding machine with a proper speed so that the wire does not break during the process. After the wire winding process is complete, all wires are held in place with fast curing Hardman 04001 epoxy. Then the wires between both ends of the wire frames are cut. Finally, the wire frame has detached from the machine and moved to a clean box and transported to the TPC.



(a) Wire-winding machine



(b) Spring tension system

Figure 2.51: Wire-winding machine

Tension on the wires is crucial. To avoid the gravitational sagging effect, a sufficient tension is necessary. For the S π RIT TPC, the tension for anode, ground and gating grid wires are 0.5, 1.2 and 1.2 N, respectively. To measure the tension of the wires on the frames, the string resonance technique is used to verify the tension of each wire plane. For the system that both ends of a string are fixed, the fundamental vibration mode of the string of length L can be expressed [59, 60] by

$$f = \frac{1}{2L} \sqrt{\frac{T}{\mu}}. \quad (2.17)$$

Where f is a resonance frequency, μ is mass per unit length and T is a wire tension. The tension of a wire can be calculated by

$$T = 4\mu L^2 f^2 \quad (2.18)$$

For the test setup in Figure 2.52, a frequency oscillator is used to feed the sinusoidal current to the wire. A strong earth magnet is placed at 1cm under the wire. The force generated between the current and the magnetic field pull the wire back and forth in the horizontal plane with a frequency f . The fundamental vibration loop is observed while the frequency is changing. When the amplitude of the wire loop reaches the maximum, the frequency is recorded. The tension of the wire can be obtained from Equation (2.18).

2.3.2 Wire plane circuit board

The PCBs for all three wire planes were made of Roger 4003. The area of the wire plane is divided into 14 sections. This allows some sections of the anode to operate at the reduced gas gain for an analysis of heavier particles. Each PCB for the anode has 26 conductive

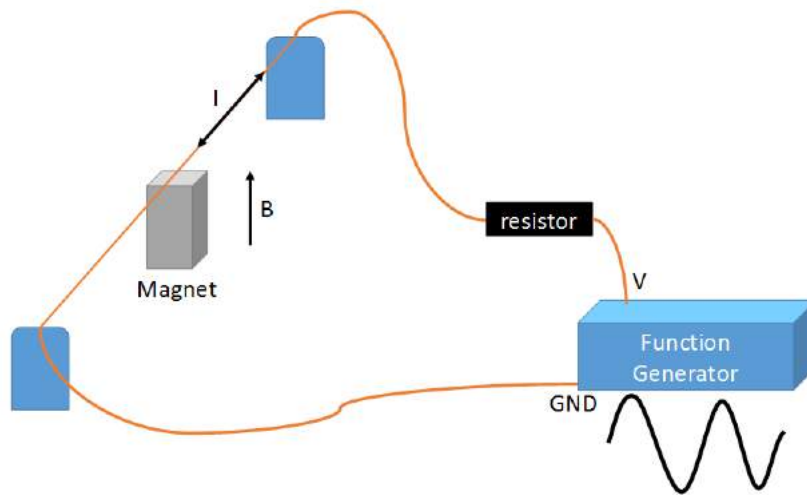
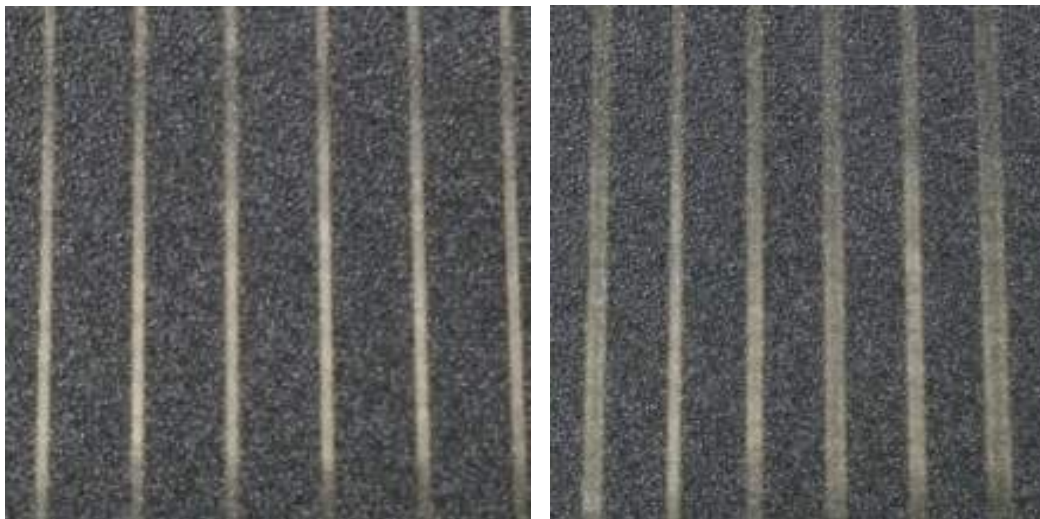


Figure 2.52: The schematic of the setup for measuring a wire tension.



(a) anode wires when they are not resonance (b) anode wires at a resonance frequency

Figure 2.53: measurement of the tension of anode wires: (a) the anode wires do not vibration when the frequency does not match the fundamental frequency. (b) When the applying frequency matches the fundamental frequency of the anode wire, the wire vibrates with a maximum amplitude.

pads with the pitch of 4 mm for the center of the pad. Each pad is connected to the high voltage via a 10 M Ω resistor and to external ground via a 1 nF capacitor as demonstrated in Figure 2.54. The PCBs for the ground plane has 104 conductive pads with the pitch of 1 mm each board. All the pads are connected to the pad named "GND" on the board as shown in Figure 2.55. The PCBs for the gating grid plane has the same number of pads and pitch as the ground board. The pads on the gating grid board are connected to the pad named "POS" on the top side and "NEG" on the bottom side of the board alternatively as seen on Figure 2.56.



Figure 2.54: The printed circuit board (PCB) for anode wires: 26 pads are connected to the high voltage by 26 of 10 M Ω resistors (blue). Each pad is connected to an external ground by 1 nF capacitor (brown).



Figure 2.55: Printed circuit board for ground plane

All boards were glued to the aluminum spacer to bring up the top surface of the board to

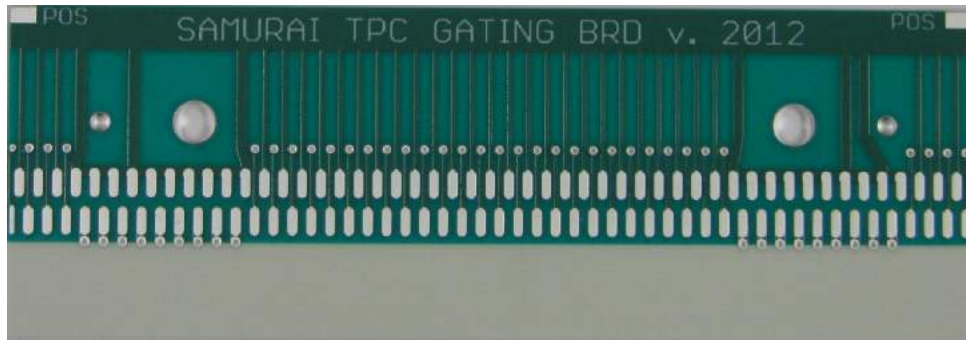


Figure 2.56: Printed circuit board for gating grid plane

the height of 4 mm, 8 mm and 14 mm from the pad plane for the anode, ground and gating grid boards, respectively. Each spacer and PCB were aligned by the dowel pins. Gluing the gating grid and ground boards has the same procedure. First of all, we put the kapton tape on the PCBs to provide a protection from the epoxy. Then, EZpoxy 83 was apply on the aluminum spacer. When it is done, the PCBs were attached to the spacer as seen in Figure 2.57. Note that we need to make sure that the dowel pins do not extent past the top of the circuit board. After all PCBs were attached to the spacers, A uniform pressure was applied to the boards and leave for 24 hours to cure.

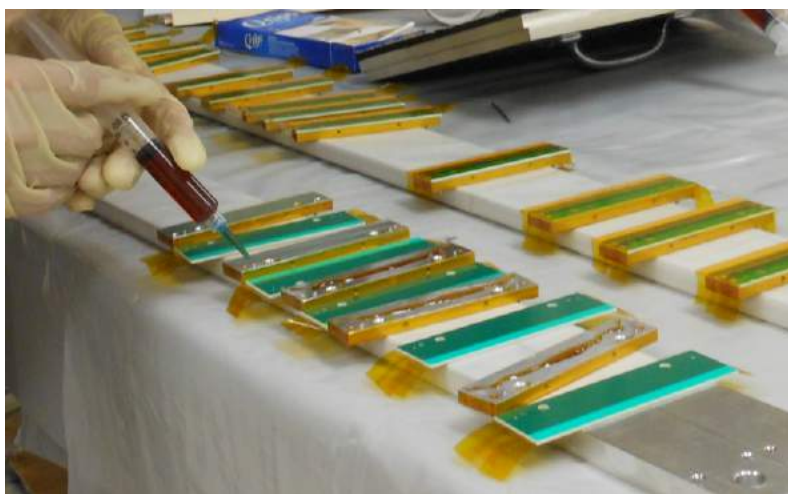


Figure 2.57: Gluing the ground board

Gluing an anode board the spacer has a few more steps than the gating grid and ground

board gluing. Since the anode board has electrical components on it. We need to prevent the component from shorting to the spacer. Therefore, we first glued the anode board with resistors and capacitors on it to the acrylic spacer with EZpoxy 83 as seen in Figure 2.58 to provide an insulation. The acrylic spacer has the hole where the electrical components were placed on. After the epoxy cured, we covered all electrical components with Ezpoxy 83 to provide another insulation as seen in Figure 2.59. Finally, the anode board were glued to the aluminum spacer.

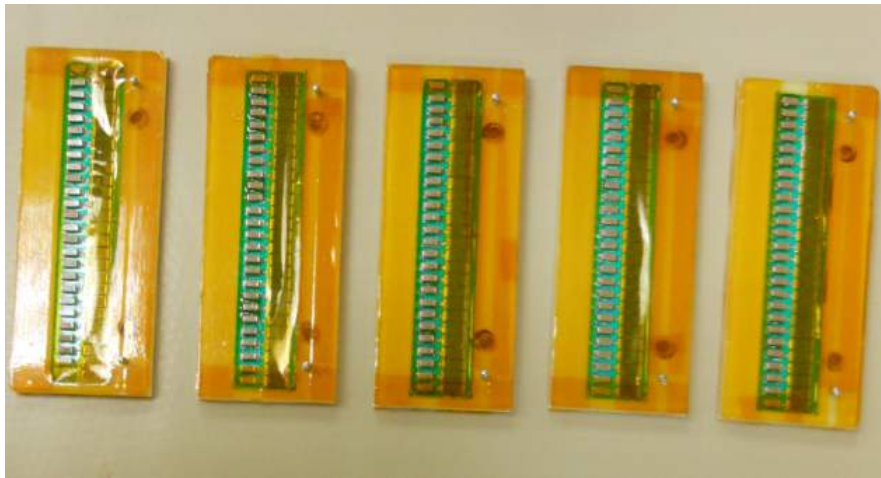


Figure 2.58: Gluing the anode board to a acrylic spacer

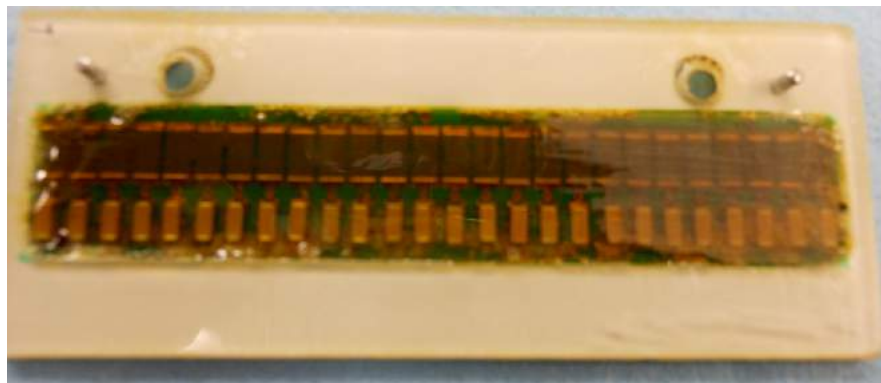


Figure 2.59: Fill the gap on the anode board

2.3.3 Wire plane assembly

The wire plane has been assembled from anode, ground and gating grid planes, respectively. Note that all process has been done in the clean environment. For the anode plane, first of all, the PCBs glued to the aluminum spacers were put on the top plate on both sides as seen in Figure 2.60. All PCBs were aligned to the position by the dowel pins and fixed to the TPC with non-magnetic screws since the TPC typically run under a strong magnetic field. The height from the top surface of the anode board to the pad plane has been checked to be 4 mm. After all anode boards were mounted to the TPC properly and accurately, the wire comb assembly was mounted onto the top plate and align wire combs by using square flange holes as shown in Figure 2.61. The height of the wire combs can be adjusted by using an additional spacer which could bring the combs up to the height of the gating grid and ground planes.

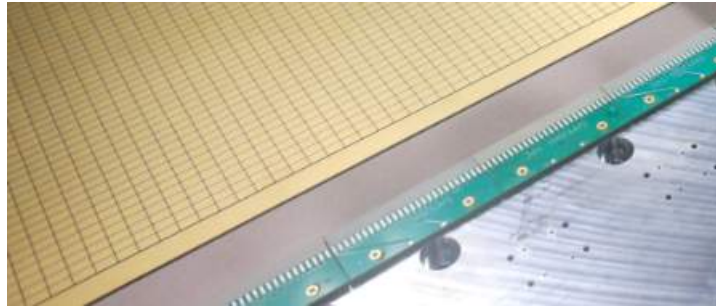


Figure 2.60: Anode boards were mounted on the TPC

Then, the wire frame with anode wires has been transported to the TPC. Note that the maximum number of wires that the wire frame can have is half of the whole wire plane of the TPC. The wire frame has the leveling blocks attached to the four corners of the frame with screws protruding 2-3 cm. These block were used to adjust the height of the wire frame as seen in Figure 2.63. Before, we transport the wire frame to the top plate. One needs to check that the leveling screws on the frame extend enough to be well above the wire combs

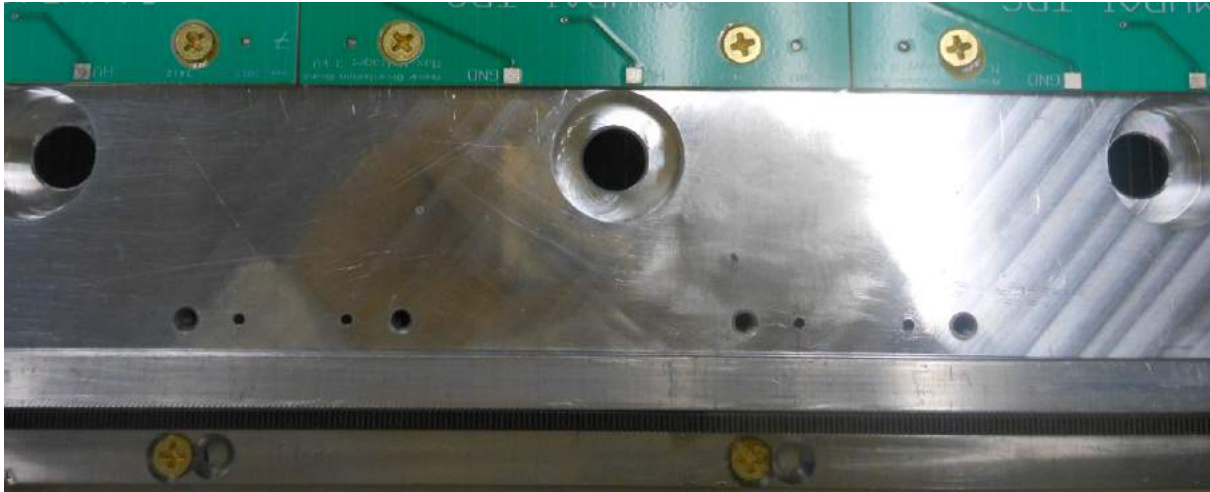


Figure 2.61: Wire comb assembly

assembly. After that, the wire frame was moved on to the top of the top plate. The height of the wire frame was adjusted to be roughly the same and then align the wires to the combs. The wires should be roughly vertically centered in the wire comb valleys and slightly to one side of the soldering pads. In this case, when the frame is pushed down laterally, then the wires are centered in the pad. After we check the alignment, the wire frame are lowered down slowly until the wires are in the combs with the correct pitch and centered in the pad. Note that we need to make sure that all wires touch the pad. To check the connection, we can use a voltmeter to check whether the pad is short to the frame. If only some pads short to the frame, the wire frame should be lowered down slowly until all pads short to the frame. Before solder the wires, we need to hold all wires firmly in place by applying EZpoxy 83 on the white area of the circuit board as show in Figure 2.62. In this procedure, it is a good idea to have two person working together. The first person uses a syringe lay epoxy bead over the white area on the circuit board. The second person uses the syringe with an angled tip and removes excess epoxy and make sure that the epoxy does not go over the solder pad. Once the epoxy has cured, the wires will be soldered onto the pad as demonstrated in Figure

2.64.

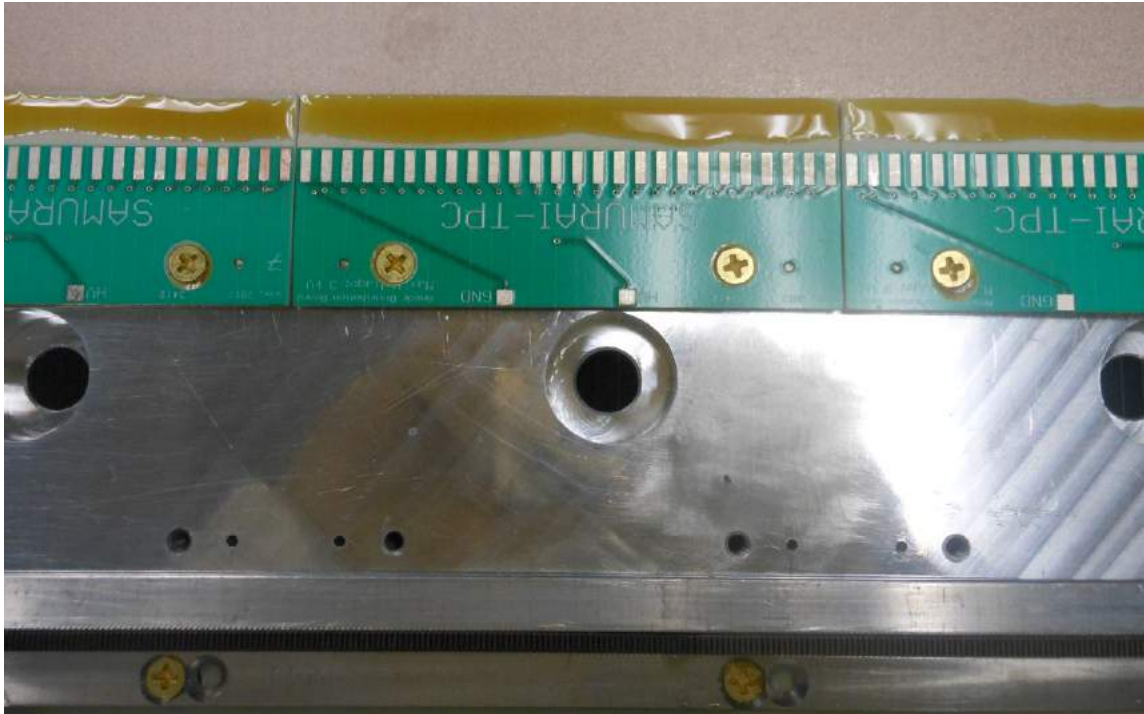


Figure 2.62: Using EZpoxy 83 to hold the wires in place and maintain the tension

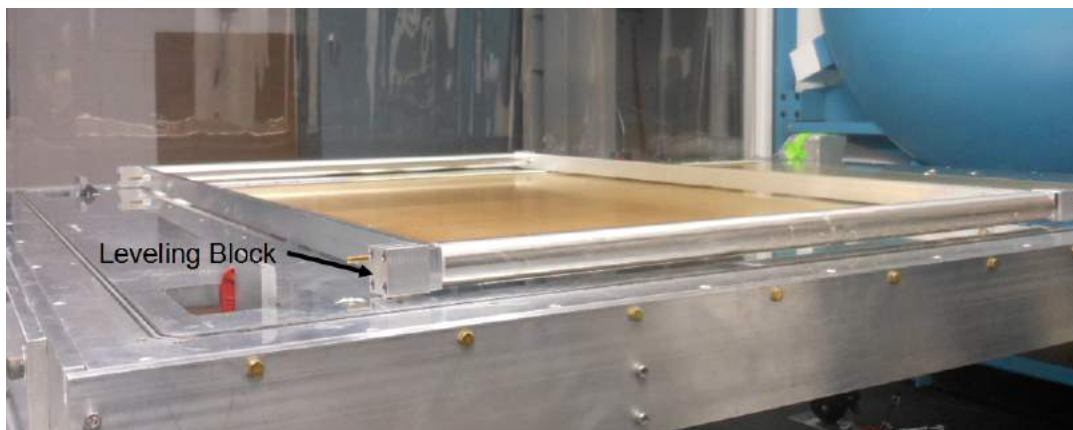


Figure 2.63: Wire frame with leveling blocks

Once soldering is done, the excess wire will be cut off. To prevent the cut wire from swing around the wire plane, we place a piece of tape over the wires about 3" from the solder joints and cut from the frame. Then, the wire frame is carefully lifted off and put the tape over both sides of the cut wires. The procedure for the wire plane assembly up to this point will

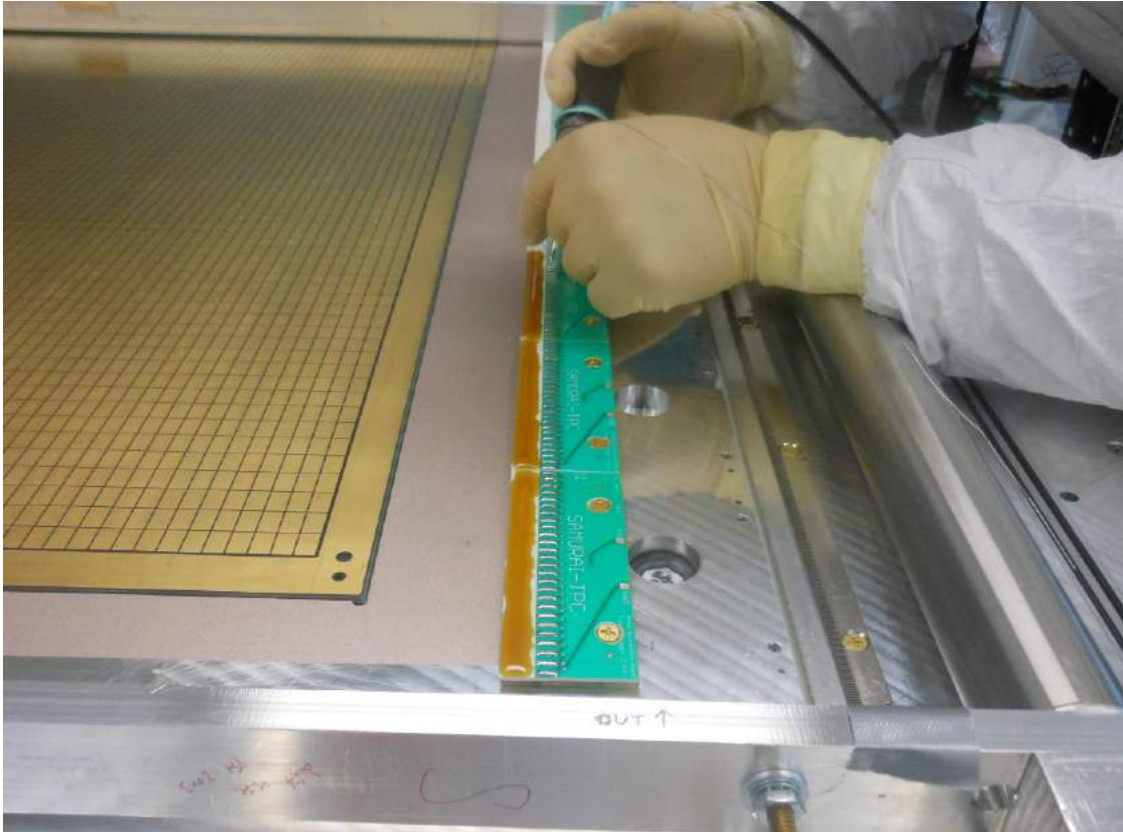


Figure 2.64: Solder wires onto the conductive pad on the anode board

be the same for the gating and the ground planes. Note that the pitch of the gating grid and ground wires are 1 mm. The distance from the pad plane for the ground and gating grid planes are 6 and 14 mm, respectively. After that wires were cut off, we need to test the electrical connection on the circuit board. For anode board, every wire is connected to "HV" pad. If we use a multimeter, it should read 10 M Ω between the "HV" pad and the other end of the wire. For the ground wires, one need to ensure that all wires are connected to the ground pad. For the gating grid wires, there are two sets of wires interlaced with every other. Ensure that one set of wires is connected to the "POS" pad and the other set of wires is connected to the "NEG" pad. Once the connections are tested. The wires were cut as close to the solder joints as possible.

Then, the electrical feedthrough connectors were mounted onto the top plate. Anode



Figure 2.65: Connect the anode board to the MHV connector

boards are connected to MHV connectors which go near the filled board with BNC connectors in between as seen in Figure 2.65. To prevent the anode solder joints from sparking to the ground wires, another layer of EZpoxy 83 was applied over the solder joints. Also, some EZpoxy 83 was put over the MHV connectors and some Araldite 2013 on the soldered wires to provide an additional insulation as shown in Figure 2.66. Note that the wire plane assembly procedure is to do one plane at a time.

For ground boards, the "GND" pads are connected on the adjacent boards and the "GND" pad on the most downstream board was soldered to the BNC connector near the downstream end of each row as seen in Figure 2.67. For gating grid boards, we soldered the "POS" to "POS" and "NEG" to "NEG" pads on the adjacent boards. There are two transmission lines added to the gating grid section each side of the pad plane. The transmission



Figure 2.66: Insulate the anode plane connections

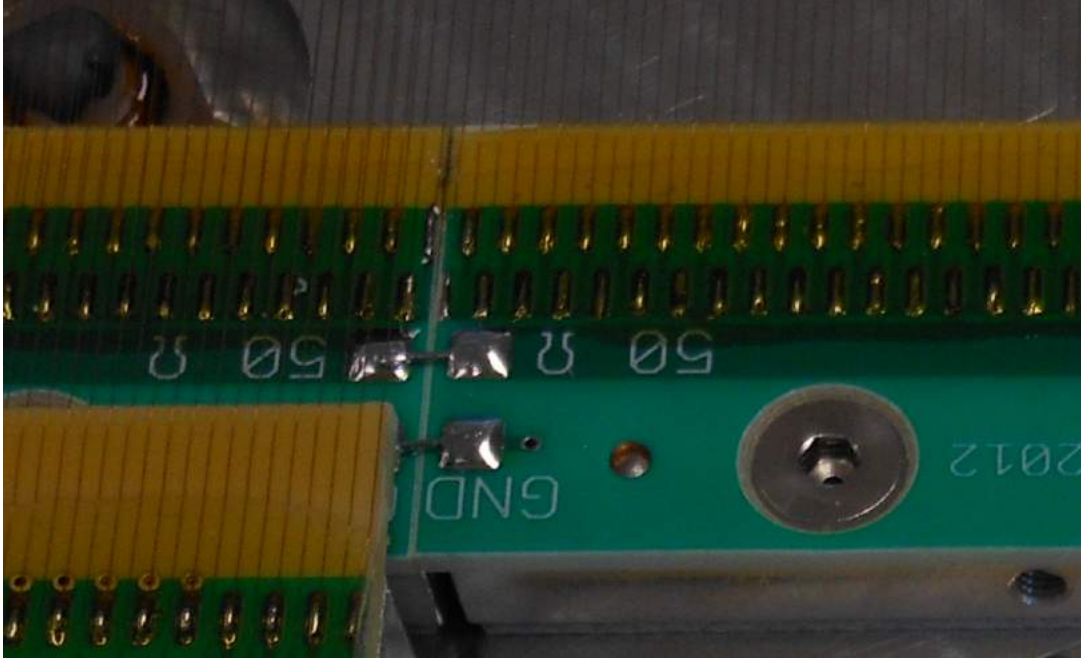


Figure 2.67: Solder adjacent ground boards

line is made of alternative layers between EZpoxy 83 and Copper ribbon cables. Each ribbon cable inside the transmission line has the Copper wire extends to connect to the positive or negative polarities of each gating grid board as seen in Figure 2.68 and 2.69. Once all gating grid boards are connected to the transmission line, the two ends of the transmission line were soldered to the dual lemo connector near the downstream end of each row.

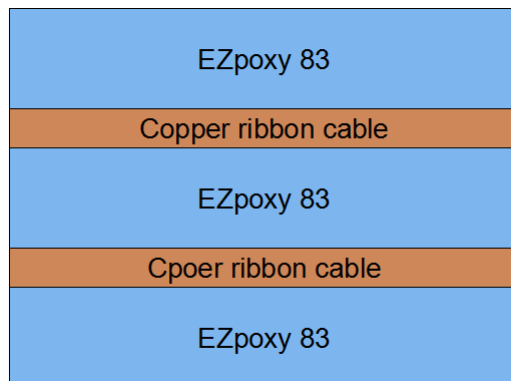


Figure 2.68: Layers of a transmission line

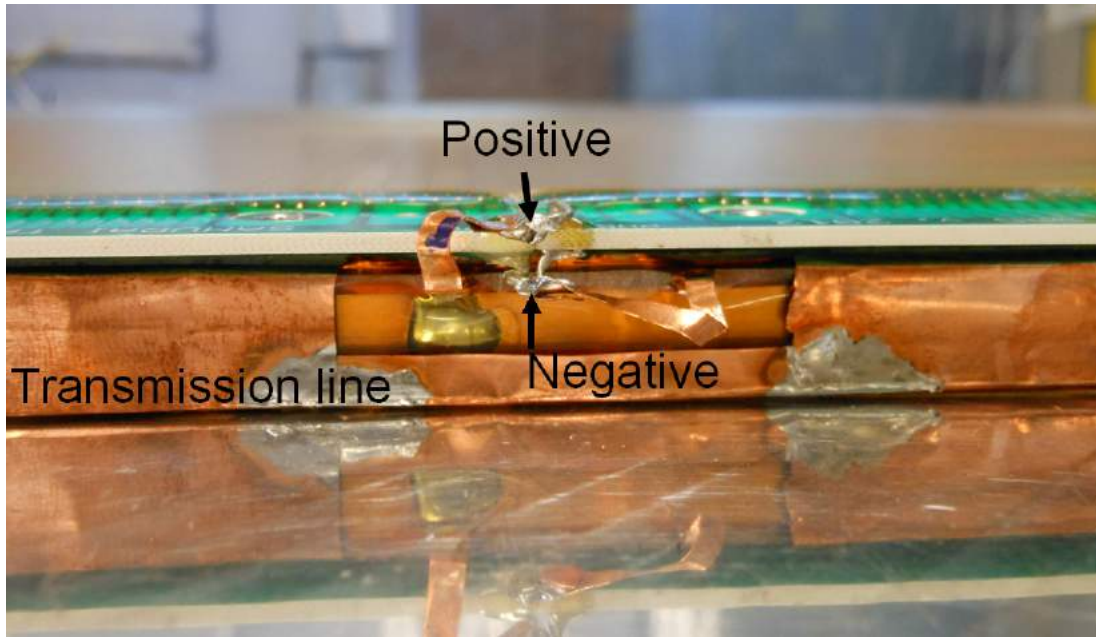


Figure 2.69: Transmission line is connected to the gating grid board

2.4 The design and construction of the enclosure of the $S\pi$ RIT TPC

The enclosure of the $S\pi$ RIT TPC is a rectangular box with the dimensions of 206 cm long, 150 cm wide and 74 cm high. The walls on the enclosure were made of thin aluminum so that the particles from nuclear reactions can pass through. We can use the particle multiplicities that go through the enclosure on the side and downstream of the TPC to generate a trigger for the electronics. In Figure 2.70, the motion chassis can be attached to the enclosure on the upstream and downstream sides. This allows the TPC to be moved and rotated. There are two clear polycarbonate windows on the left and right sides. The windows were put on the the enclosure with the o-ring so that the volume remains gas-tight and we can see the field cage and the target mechanism through this windows.

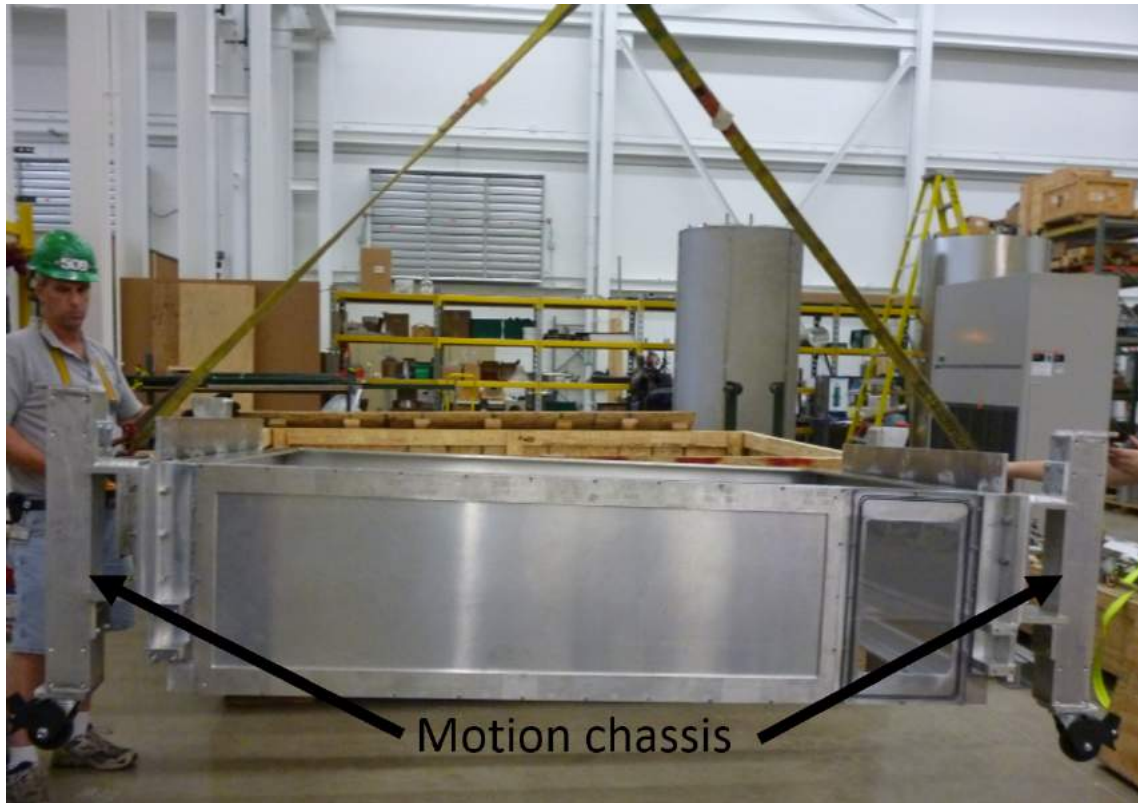


Figure 2.70: Enclosure of the $S\pi$ RIT TPC with the motion chassis

2.5 The design and construction of the voltage step down of the $S\pi$ RIT TPC

In typical experiment, the cathode can be biased up to 20 kV. We need to prevent it from sparking to the components nearby. The voltage step down was assembled on the bottom plate of the enclosure. It allows 20 kV from the cathode at the bottom of the field cage to step down to ground over 8 copper rings on the bottom plate.

The bottom plate is an aluminum plate with the dimensions of 142.24 cm wide, 195.90 cm long and 1.27 cm high. The plate has been cut down at the center by 126.87 cm wide, 174.88 cm long and 0.63 cm deep as show in Figure 2.71.

For the assembly of the voltage step down, first of all, the bottom plate was laid on the

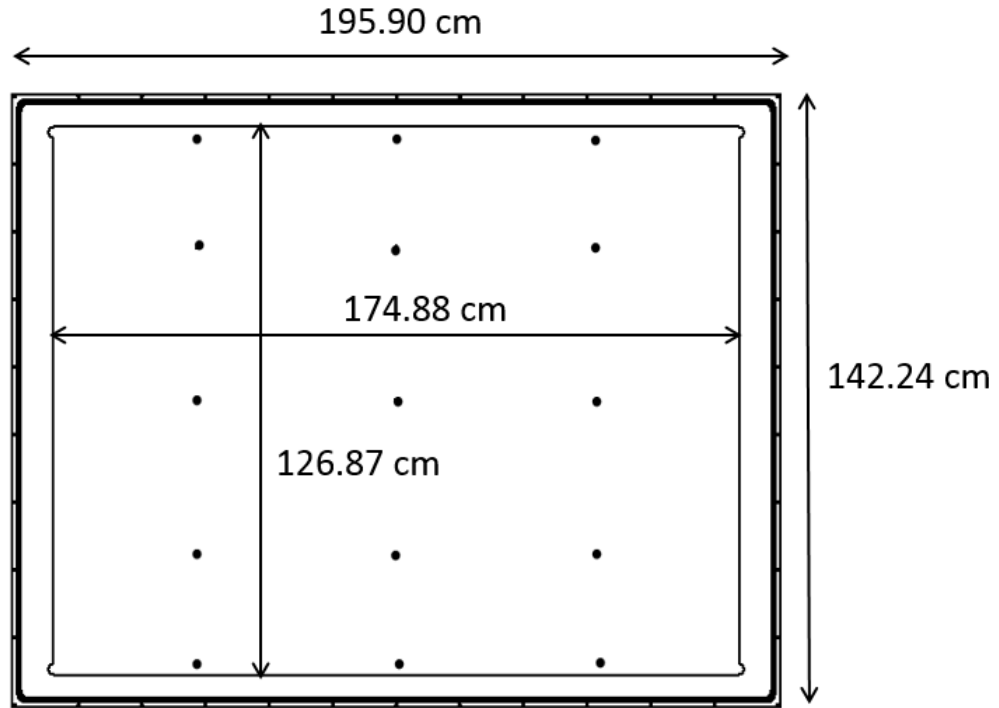


Figure 2.71: Drawing of the bottom plate of the $S\pi$ RIT TPC

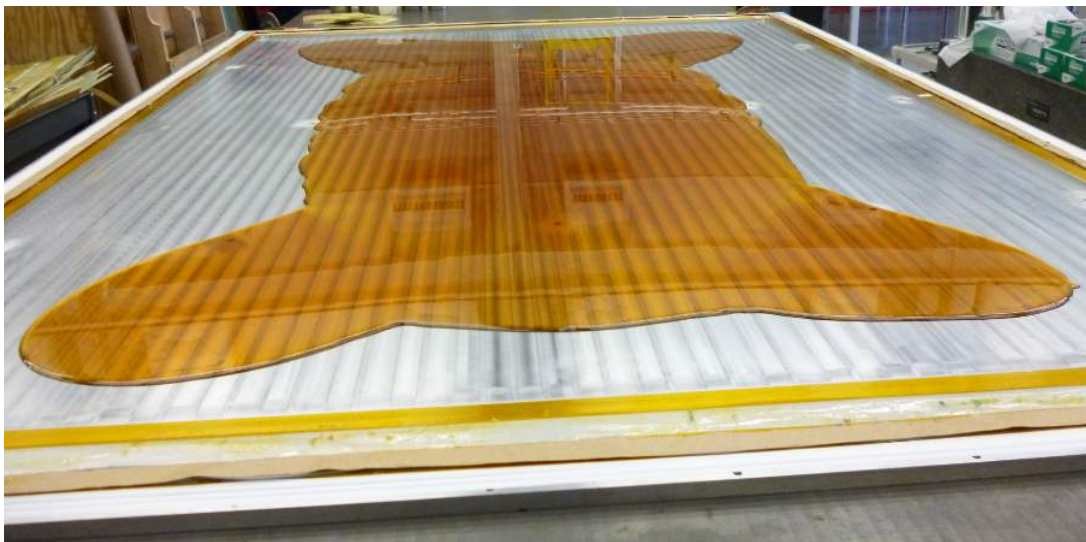


Figure 2.72: Pour Ezpoxy 84 at the center of the bottom plate

flat surface and glue excess area was protected with plastic and a Kaptop tape. To provide an insulation surface, a polycarbonate sheet of 1/4" (0.63 cm) thickness was used to cover the bottom plate. In Figure 2.72, we used Ezpoxy 84 to glue a polycarbonate sheet to the

bottom plate. The Ezpoxy has been poured at the center of the plate and then we slowly put a polycarbonate sheet over the area. To glue evenly over a large surface area, we use vacuuming gluing technique. The procedure is to put the sealant tape around the area that we need to glue and cover it with a breather cloth over the polycarbonate and a vacuum plastic over the sealant tape. Then we pumped it down so that the polycarbonate sheet was pressed down with even pressure to the plate as shown in Figure 2.73. Then we left it to cure for 24 hours. After it cured, the covers have been taken off for cleaning. Figure 2.74 shows the bottom plate after gluing process.



Figure 2.73: Polycarbonate sheet was glued to the bottom plate by vacuuming gluing technique.

In Figure 2.75, after successful gluing, a conductive paint was applied at the center of the polycarbonate which will be at the same voltage of the cathode on the field cage. The next step is to install copper rings onto the the polycarbonate. The voltage step down consists of 8 copper rings, each of which was formed from 4 straight copper rods on standoffs. The long and short rods are 145.31 and 97.31 cm long, respectively. The rods and standoffs were

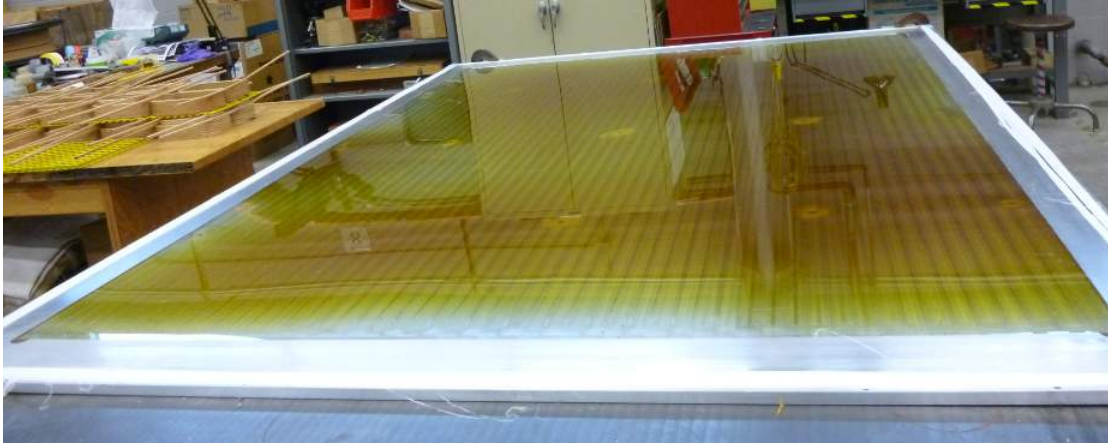


Figure 2.74: After 24 hours curing time, the covers have been taken off and the bottom plate was cleaned.



Figure 2.75: Conductive paint was applied at the center of the polycarbonate sheet.

fixed on the polycarbonate sheet by 0-80 screws as show in Figure 2.76. 4 quarter round corners were produced by welding as shown in Figure 2.77.

The radii of rings can be seen in Table 2.2. Once 8 copper rings was complete, 100 M Ω resistors were soldered between the rings. This allows the voltage on the cathode to step

Table 2.2: Radii of round corners of the voltage step down.

Ring	Radii (cm)
1 (inner most)	4.55
2	5.97
3	7.39
4	8.81
5	10.24
6	11.56
7	12.88
8	14.20

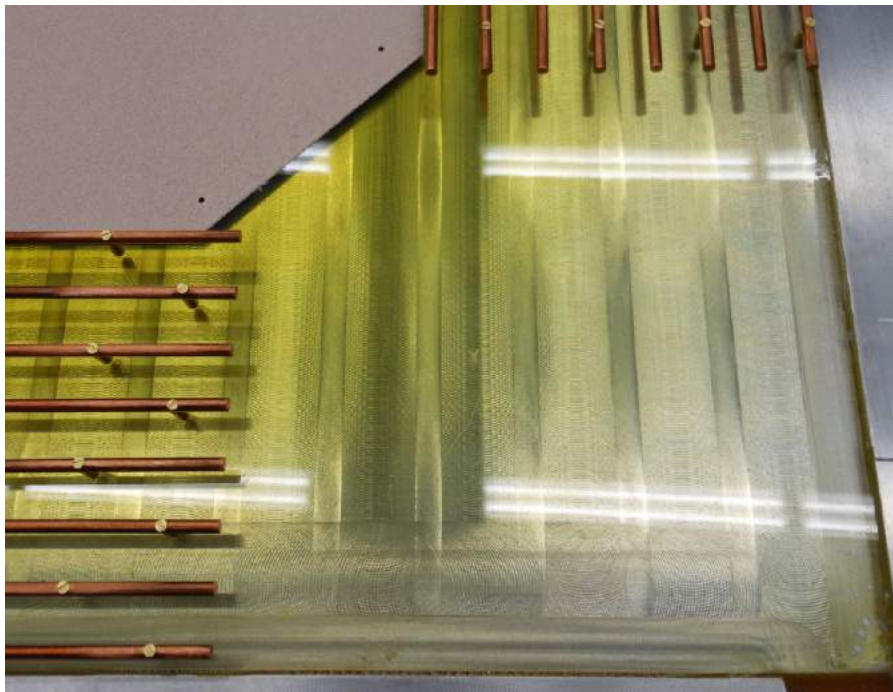


Figure 2.76: Copper rods and standoffs were attached to the polycarbonate sheet by 0-80 screws.

down gradually to ground on the enclosure. Then the bottom plate with the voltage step down was mounted to the enclosure. To test the voltage step down, dry nitrogen gas was introduced to the enclosure and 20 kV was slowly introduced to the inner most ring. There is no sparking observed during the test.



Figure 2.77: A quarter round corner was produced by welding.

2.6 The design and construction of the target mechanism of the $S\pi$ RIT TPC

A target position for the $S\pi$ RIT TPC is placed outside the detector. In Figure 2.78, the target mechanism for the $S\pi$ RIT TPC has been designed to be able to adjust the target position in x , y and z directions. The target frame has five available slots allowing an experiment to have multiple targets and also has two fixtures for adjusting the position in y direction as shown in Figure 2.79.

In Figure 2.80, the Z-motion control has two angle motion controls as indicated in yellow and gray. Inside the box on the target frame structure, the gray gear is designed to have a thread. Therefore, when the yellow gear is rotated, it drives the gray one and the box will move back and forth in the z direction. To keep the target frame rigid and avoid bending just a center part of the frame, an aluminum support bar is introduced on the structure to

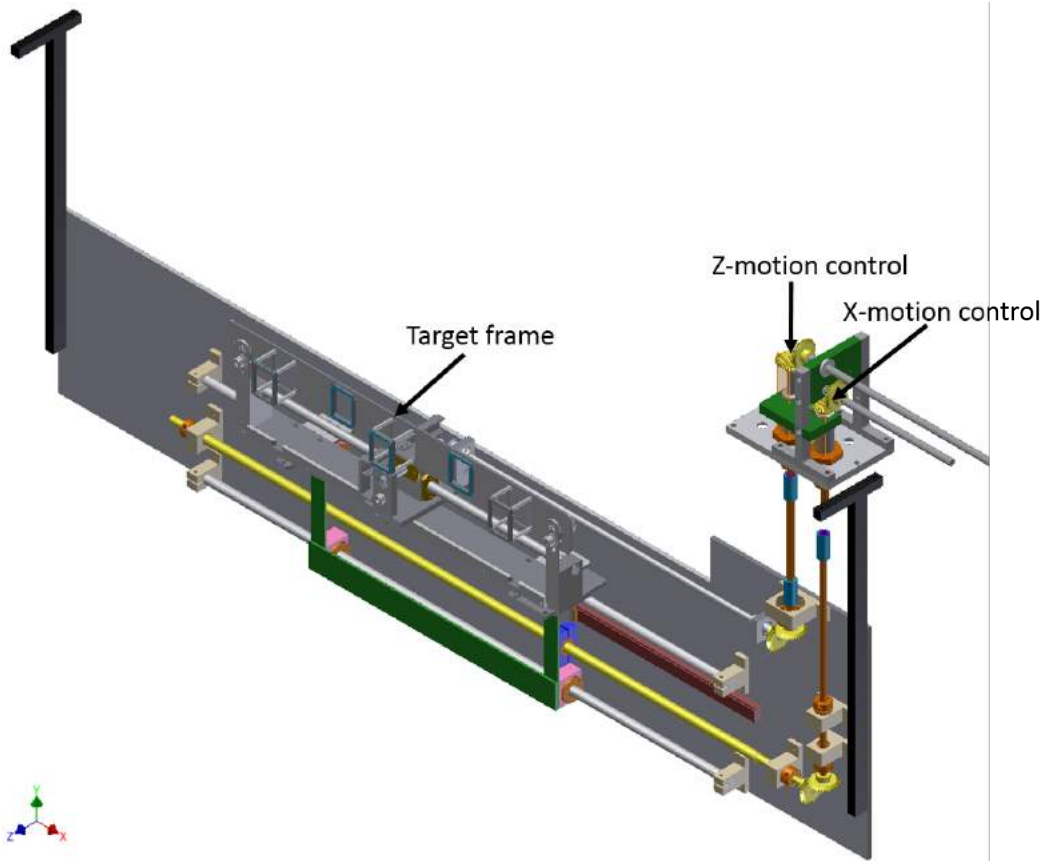


Figure 2.78: Design model of the target mechanism for the $S\pi$ RIT TPC.

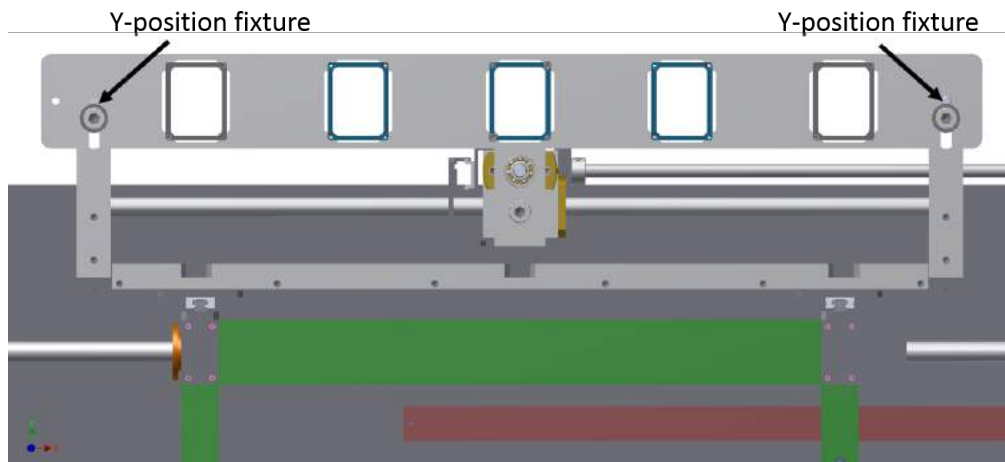


Figure 2.79: A target can be adjusted in y direction by positioning the fixture on the target frame.

assure that the whole target frame is moving at the same time.

A similar idea was applied to the X-motion control as well. In Figure 2.81, when the

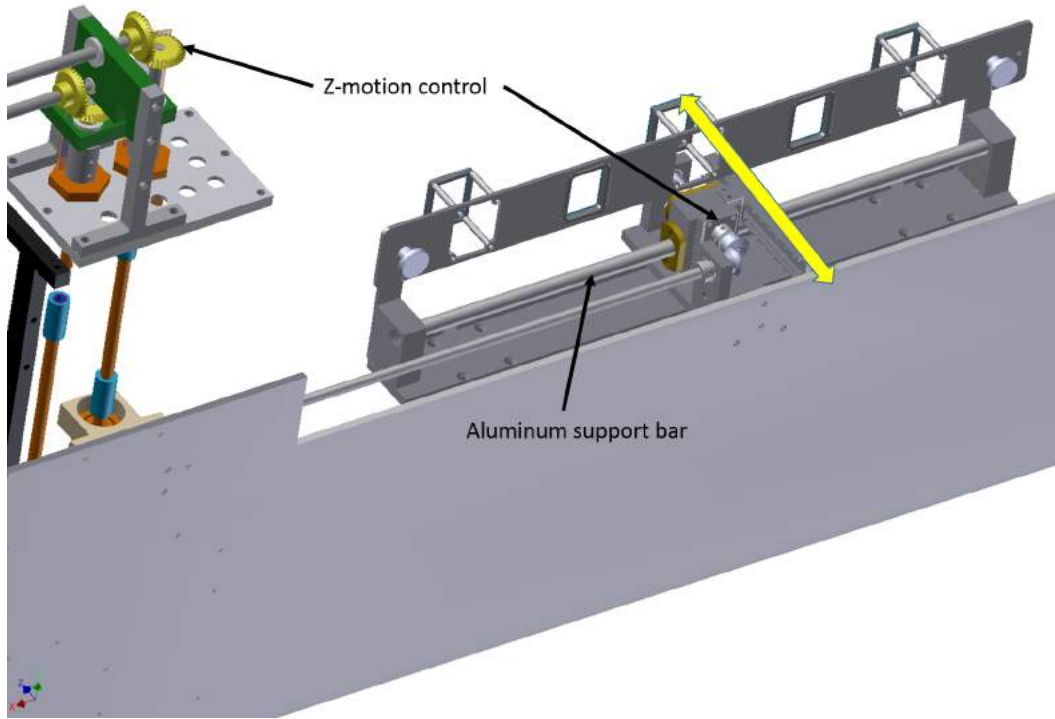


Figure 2.80: A target frame can be moved in z direction via the Z-motion control

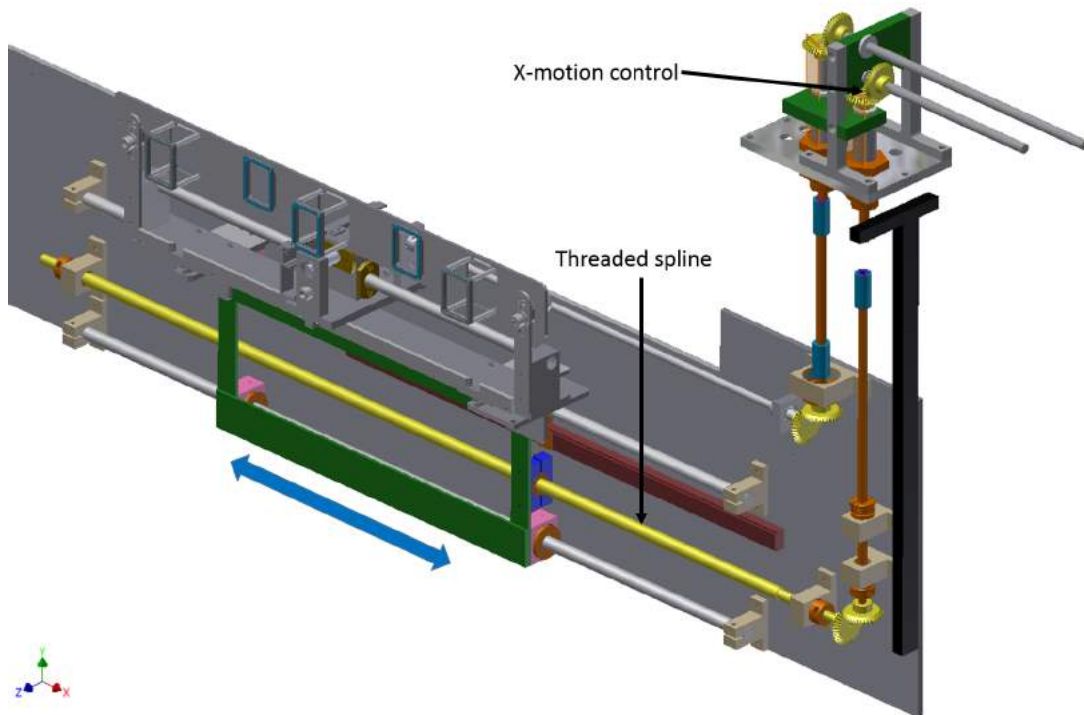


Figure 2.81: The x position of the target can be adjusted from the X-motion control.

angle motion control is turning, it drives the threaded spline (yellow) and the target frame will move in the x direction. The actual target mechanism can be seen in Figure 2.82.



Figure 2.82: Actual target mechanism

2.7 Overall design assembly of the $S\pi$ RIT TPC

The assembly of the TPC will start from attaching the field cage to the top plate. There is a lexan ring between the field cage and the top plate. The ring has O-rings on both sides to ensure that the volume remains gas-tight after assembly. To provide a protection for the wire planes, a cover plate was put over the lexan ring with set screws and was tightened with wing nuts. The top plate with a cover was rotated by crane to the position that the pad plane is perpendicular to the ground as seen in Figure 2.83. Clamps were inserted around a lexan ring to secure the O-ring. One should note that the cover plate must be loosened slightly to fit in the clamps. After insert all clamps, all but six wing nuts were removed from the set screws.

To prepare the field cage for the assembly, the field cage was set on a stable support so that upstream and downstream ends are in a correct orientation with respect to the top plate. Top perimeter should rest on a clean surface. Prior to attaching the field cage to the



Figure 2.83: Top plate with the cover plate was rotated by 90 degrees.



Figure 2.84: Insert window and fingers were put on the window frame of the field cage.

top plate, the upstream window and copper electrode fingers were put on the window frame as shown in Figure 2.84. To attach the field cage to the top plate, the remaining wing nuts and cover plate were removed. This operation must be done in the clean room. As in Figure 2.85, two people were stationed at top perimeter and other two people at the cathode. All four people lifted the field cage. The two people on the top perimeter guided the perimeter onto the set screws while the other two provide support. The guilders attached 2 or 3 wing nuts to set screws at the top while the other two continue to support. For each hole, the set screws were removed and a nylon spacer was inserted. Then screw on a final screw and a nylon washer to tighten the top plate onto the field cage. In Figure 2.86, springs were attached to the bottom of the field cage. This provides an electrical connection between the cathode and conductive surface of the voltage step down and make the surface to have the same potential as the cathode.



Figure 2.85: Four people lift the field cage and set it on the set screws on the top plate.

After the field cage was attached to the top plate, the exit window was put on the field cage. Then the top plate with the field cage attached on it has been rotated to the position as shown in Figure 2.87. The enclosure was moved underneath the top plate with a correct orientation. Some additional weights may put on the top plate to ensure that it is level. Then slowly lower the crane and people were stationed at each corners to align the top plate assembly with the enclosure as demonstrated in Figure 2.88.

Once the top plate and enclosure were aligned, the motion chassis were removed from the top plate. Then we screwed the top plate to enclosure properly. Two people on opposite corners were gradually tightening screws a little each time around the top plate until the gap between them is less than 5 mils. Once it is done, the $S\pi$ RIT TPC without a target



Figure 2.86: Springs were attached to the bottom of the field cage to provide an electrical connection between the cathode and conductive surface on the voltage step down.



Figure 2.87: Top plate with the field cage attached has been rotated to the position for assembling to the enclosure.



Figure 2.88: Top plate was lowering while people at each corner align the top plate assembly with the enclosure.

mechanism is shown in Figure 2.89.

Finally, a target mechanism will be installed onto the detector. Almost all components of the target mechanism structure was assembled together as demonstrated in Section 2.6. The structure of the target mechanism was attached to aluminum bars of the motion control feedthroughs from square flanges on the top plate as shown in Figure 2.90. A laser alignment technique was used to align the center of a target to the center of the entrance window of the S π RIT TPC. The laser cross will be pointing at the center of the entrance window. In Figure 2.91, a grid paper was put on the target frame. The position of the laser cross on the grid paper is used to show how much offset we have from the center of the entrance window.



Figure 2.89: The S π RIT TPC without a target mechanism



Figure 2.90: The target mechanism is installed onto the S π RIT TPC.

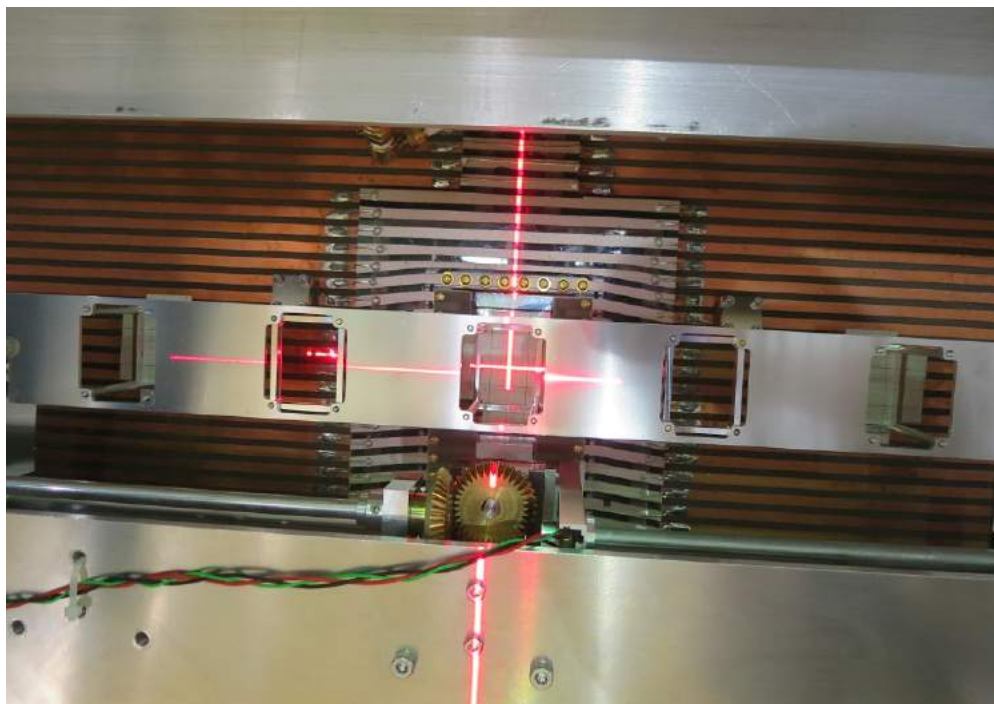


Figure 2.91: The laser alignment techniques was used to align to the center of a target to the center of the entrance window.

2.8 Electronics

Signals from the pads in the S π RIT TPC are read out by the Generic Electronic System for TPCs (GET), which is a reconfigurable and scalable medium sized system up to 30k

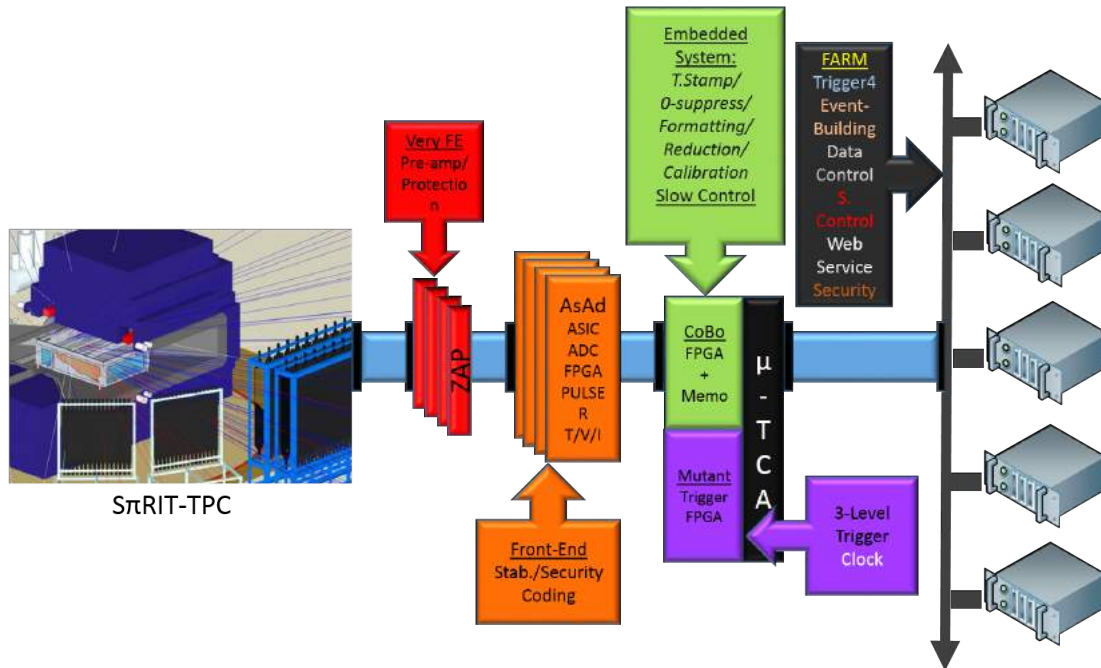


Figure 2.92: GET conceptual design [1]

electronic channel [1]. Figure 2.92 shows the GET hardware architecture. Signal from the pads are sent via the protection circuit cards, ZAP and short cables to the AGET chips on an AsAd (Asic and Adc) motherboard. Each AGET chip can service 64 pads and contains a Preamp (PA), a Switched Capacitor Array (SCA) with a maximum of 512 time buckets at 1 to 100 MHz, multiplexer and inspection functions. The physical AsAd motherboard can be seen in Figure 2.94. Data from an AsAd board is read out by a Concentration board (CoBo), which resides in a μ TCA crate. Each CoBo receives inputs from 4 AsAd boards or up to 1024 pads. Therefore, the S π RIT TPC needs a total of 12 CoBos and 48 AsAd boards to read out all pads as shown in Figure 2.93.

Each AGET allows the gain and filter to be configured. The configuration options of an AGET are shown in Table 2.3. Currently, the gain/channel for the S π RIT TPC is set to be 0.12 pC, which provides a similar gain setting for the Front End Electronics (FEE) cards of the STAR TPC [61]. Each channel has a discriminator which allows for selective readout

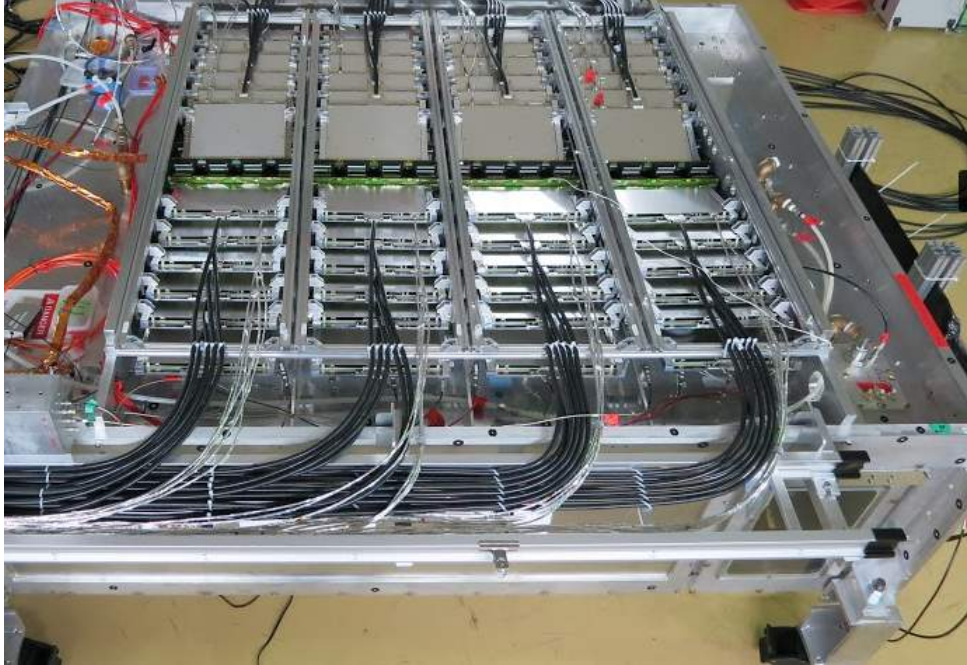


Figure 2.93: GET system is mounted on the $S\pi$ RIT TPC

of live channels. The 12 bit ADC samples on the AsAd boards give an effective 10.5 bit resolution.

Each CoBo is furnished with a Xilinx Virtex 5 FPGA chip, which is coupled to fast memory with a double buffer architecture. The functions of the CoBo are to configure its 4 AsAd cards, (2) collect ADC outputs and perform data reduction, time stamping, formatting functions and (3) transfer data at 1 Gb/s to the 10 Gb/s μ TCA switch. GET uses Gigabit Ethernet via TCP/IP and embedded LINUX and VxWorks. The maximum event rate for the system can be 500 events per second. For the first $S\pi$ RIT TPC experiment, the anticipated rate is less than 100 events per second.

The plan for the cooling system for the electronics is to use the air at the room temperature and blow over the AsAd boards via the plastic tunnels as shown in Figure 2.95. The plastic tunnel has been punched holes at which the position of each hole is right over each AsAd. Note that the size of the hole is important. If it is too small, the temperature of



Figure 2.94: AsAd motherboard

Table 2.3: Configuration options for AGET [1]

Parameter	Value
Polarity of detector signal	Positive or Negative
Number of channels	64
External Preamplifier	Yes
Input dynamic range	120 fC; 1 pC; 10pC
Gain	Adjustable/channel
Output dynamic range	2 V p-p
I.N.L	<2 %
Peaking time	69, 117, 232, 501 or 1024 ns
Power consumption	<10 mW/channel
Number of SCA Time bins	512
Sampling frequency	1 MHz to 100 MHz
Readout frequency	20 MHz to 25 MHz
SCA Readout mode	512 cells; 256 cells; 128 cells

the flowing air will be high due to the adiabatic process. Figure (result) shows that without the air cooling the temperature of the electronics rises up to 40°C. With the air cooling, the temperature is slightly increase and stable at 37°C.

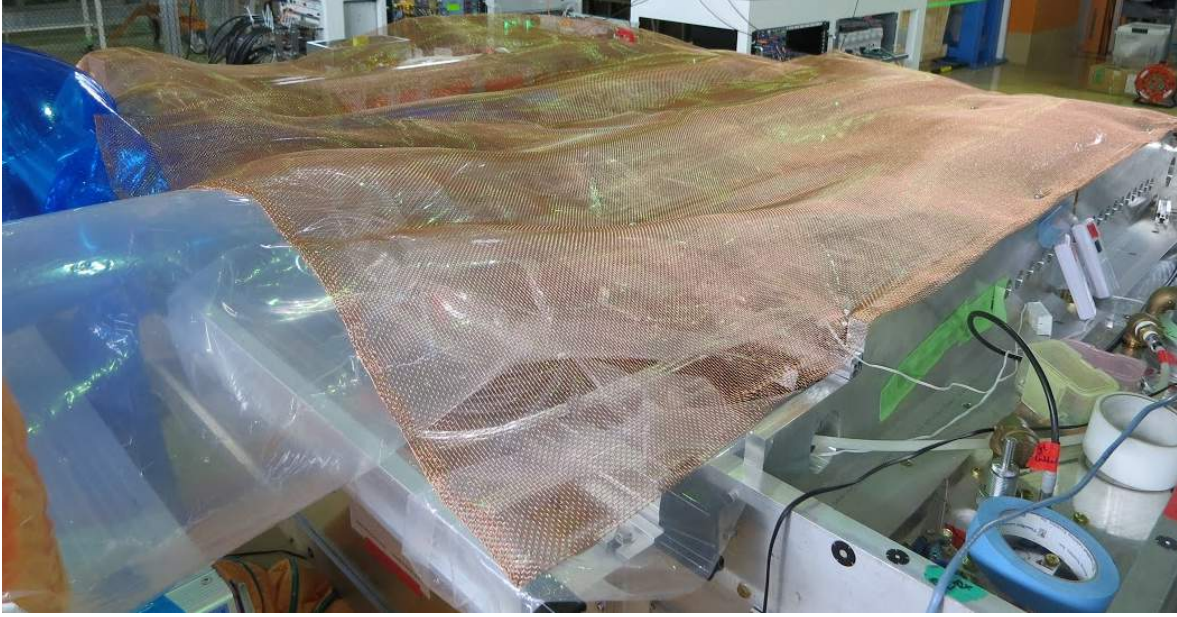


Figure 2.95: Planned cooling system for the $S\pi$ RIT TPC.

2.9 Planned trigger system

The structure of the trigger timing for the $S\pi$ RIT TPC is as follows. There will be at least one beam timing scintillator upstream. The flight path between the timing scintillator and target is 215 cm. The distance between the target and veto scintillators is 187 cm. At downstream of the TPC, there will be a wall of multiplicity scintillators as the veto scintillators (Krakow arrays). This wall is 150 cm wide, which is the same width of the TPC. Along both sides of the TPC, there are rows of scintillator multiplicity paddles (Kyoto array). In addition, there is an active collimator that is 10 cm upstream of the target.

Each of these elements of the trigger has a delay to produce a logic signal and it takes time for these signals to propagate along cables to the trigger logic. These signals will be combined to make the subsequent TTL signal that starts the gating grid driver. Each scintillator takes 3 ns to generate the light and another 3 ns for the light to propagate to the photomultiplier tube (PMT), avalanche photo diode (APD) or Multi-Pixel Photon Counter (MPPC). The

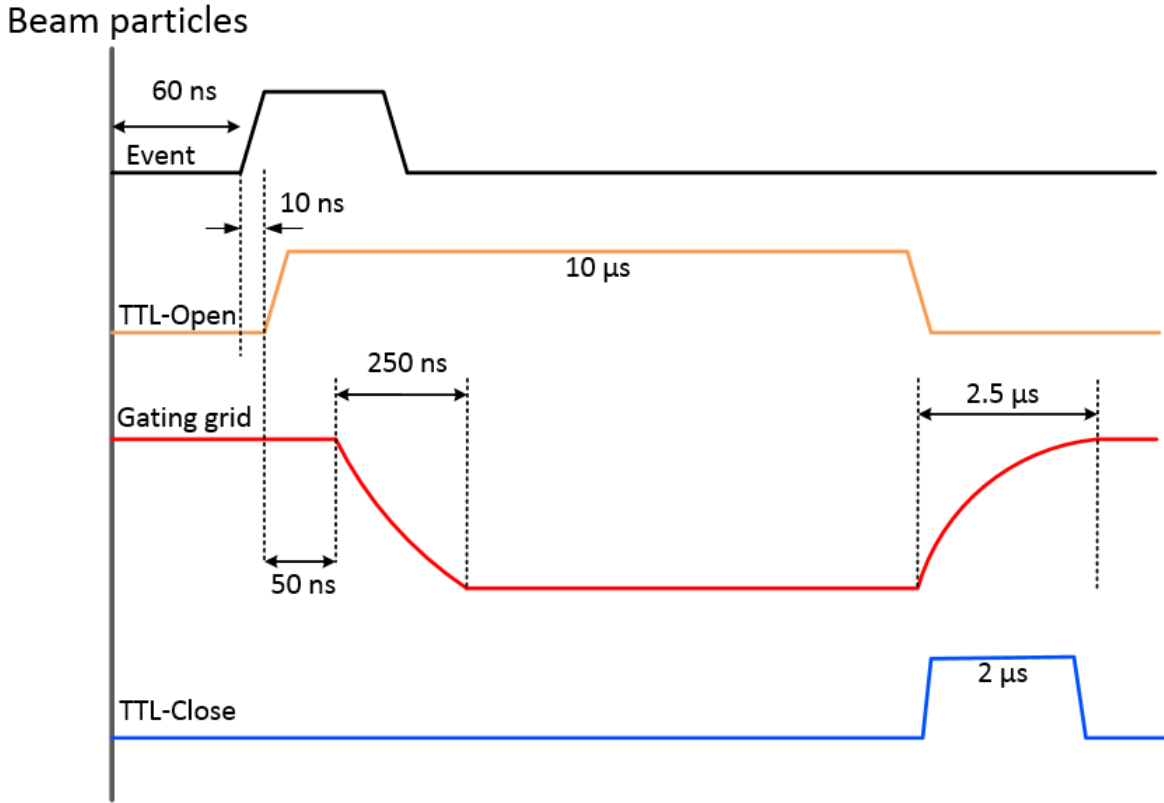


Figure 2.96: Trigger timing structure for the gating grid driver. The diagram is not in the correct scale.

start signal is read out by a PMT, which takes 25 ns and discriminated by a constant fraction discriminator, which takes 15 ns. There can be a logic signal from the start in 46 ns after the beam hits the start scintillator. Adding times from the light generation and propagation times to the wavelength shifter (12 ns), amplification and discrimination times, a logic signal from the veto scintillator, active collimator or multiplicity paddles in about 40 ns after charged particles hit these scintillators. We have to add the time differences in propagation times for the particles to hit the scintillators and the electronic propagation delay times from the scintillators to the trigger electronics. The latter depends on the placement of the electronics. In Figure 2.96, once the logic signal reaches the gating grid driver (GGD), the chip on the board takes 10 ns to generate the TTL signal (TTL-Open) to open the gating

grid for 10 μ s. At the end of the TTL-Open, another TTL signal (TTL-Close) will be sent to the GGD to close the gating grid within 2.5 μ s. Closing time of the gating can be in order of millisecond without the TTL-Close signal.

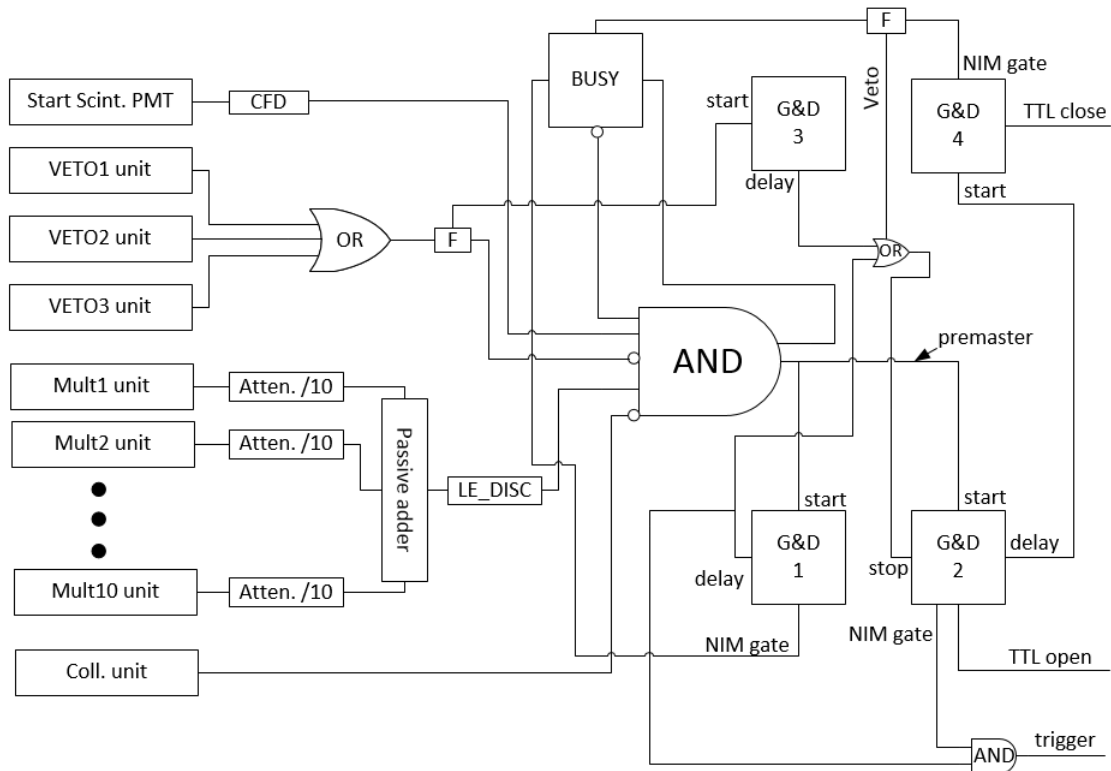


Figure 2.97: Planned trigger timing diagram. The modules labeled F in the diagram are the FIFO.

Figure 2.97 show a trigger diagram and VETO, Mult and Coll units are demonstrated in Figure 2.98. According to the diagram, if a wide NIM signal from the active collimator was present, it will result in rejection of this event. Therefore, there is no premaster, TTL-open, TTL-close and trigger. In Figure 2.99, the time signal for the multiplicity scintillator, T-Mult and start scintillator, T-StartScint have widths of 10 ns. The signal from the active collimator, T-Coll have a width of 100 ns which would prevent the generation of the premaster, TTL-Open, TTL-Close and trigger signals. The premaster signal comes from the large AND in the middle of the digram, which is shown with five possible inputs. It is likely that

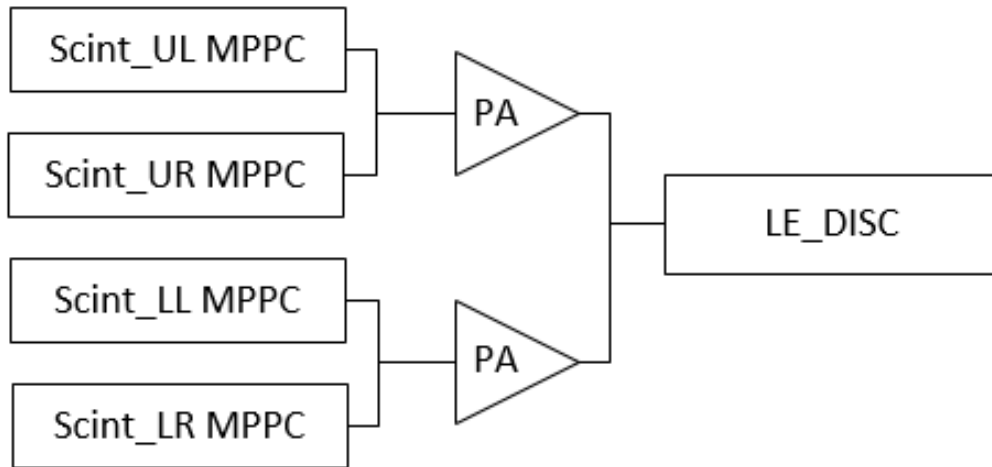


Figure 2.98: Connection between the scintillators and electronic modules

the T-Mult and T-StartScint would never be used at the same time; either T-StartScint or T-Mult would be used. If T-StartScint is used, then one gets a premaster if the circuit is not busy and there is T-StartScint with no T-Veto and T-Coll. If the T-Veto is present, $4\text{-}\mu\text{s}$ wide NIM signal, it would prevent the generation of the premaster, TTL-Open, TTL-Close and trigger signals. Also, it would keep the gating grid close until the charge from this beam pulse is absorbed on the gating grid.

The premaster output serves as the start for G&D1 and G&D2. The TTL signals from these gate generators are generated about 22-25 ns later, which is approximately 102 ns after beam velocity particles hit the veto wall when the trigger is the start scintillator. G&D2 generates the TTL-Open signal. The TTL-Open generated by G&D2 requires both the premaster as a start and the OR of G&D1 delay signal or a delayed T-Veto as a stop. We set G&D1 to require only a start from the premaster and it will generate a delayed output $11\ \mu\text{s}$ later. If there is no T-Veto from a random event in the meantime, this delayed stop from G&D1 will stop G&D2 and the width of the TTL-Open will be about $11\ \mu\text{s}$ and the gating grid will open. At the same time that the TTL-Open is stopped by the delayed signal

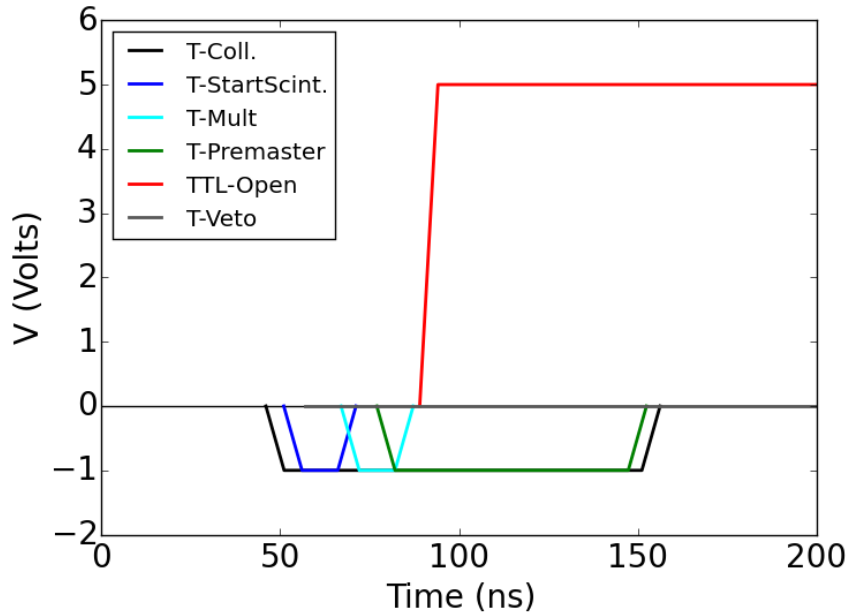


Figure 2.99: Trigger timing

passing through the OR, the delayed output of the G&D2 will trigger G&D4 and generate the TTL-Close signal, which will close the switches to recharge the gating grid. The delay time between the delayed output of G&D2 and the start of G&D4 is necessary to assure that the TTL-Open is returned to zero before the TTL-Close starts. Otherwise, this will short two power supplies through four mosfet switches with potentially disastrous results.

If there is a beam particle from the later beam pulse that hit the veto less than $11 \mu s$ after the event that triggered the premaster, the ionization of the beam particle will reach the gating grid in $2.27\text{-}4.09 \mu s$. If this ionization is not blocked by the time it reaches the gating grid, it may cause the anode wires to spark. Therefore, the T-Veto from the beam particle will pass to G&D3, which will generate a delayed output $2.27 \mu s$ or later. This delayed output goes through the OR and stops G&D2 earlier. The gating grid will start the close at about $2.27 \mu s$ after the arrival of the T-Veto signal. This $2.27 \mu s$ delay may need to be adjusted to make sure that the gating grid is fully closed before the ionization from this

beam pulse pass through the gating grid.

A prototype trigger circuit was constructed to test the circuit in Figure 2.97. A pulser was used to generate two NIM signals which were used to simulate the response of the circuit to an event defined by a T-StartScint NIM timing signal of 10 ns length from the start scintillator and a T-Coll timing signal of $4.09 \mu\text{s}$ length from the OR of the veto paddles. This test circuit was generated using 1 level adapter NIM module, one 4-fold logic FIFO, one Phillip Scientific 5-fold coincidence module and two Lecroy222 gate generators.



Figure 2.100: A veto signal (blue) occur more than $4 \mu\text{s}$ before the T-StartScint. The trigger system generate the normal TTL-Open (yellow), TTL-Close (green).

Figure 2.100 shows the case for a valid event. A T-Veto signal, shown in blue, occurs more than $4 \mu\text{s}$ before the T-StartScint, (top line in purple). Therefore, the trigger generators generate the normal TTL-Open (yellow), TTL-Close (green). The length of the TTL-Open is defined by the width of the timing gate from G&D1.

When the T-Veto and T-StartScint are simultaneous, it prevents a premaster and the subsequent generation of either TTL-Open, TTL-Close or trigger as shown in Figure 2.101. Figure 2.102 shows the case where the projectile-like residue arrives the veto while the gating



Figure 2.101: There is no generation of TTL-Open (yellow) and TTL-Close (green) when the T-StartScint (purple) and T-Veto (blue) are simultaneous present.



Figure 2.102: When a veto signal presents after the event trigger, TTL-Open (yellow) closes and the TTL-Close starts.

grid is open. After an adjustable delay defined by the arrival of the veto signal and by the length of G&D3, the TTL-Open (yellow) closes earlier than $11 \mu\text{s}$ and TTL-Close (green) starts. In Figure 2.103, there is no TTL-Close (green) generated for this event. The length of the delay from G&D3 need to be adjusted with the beam for such events so that the TTL-

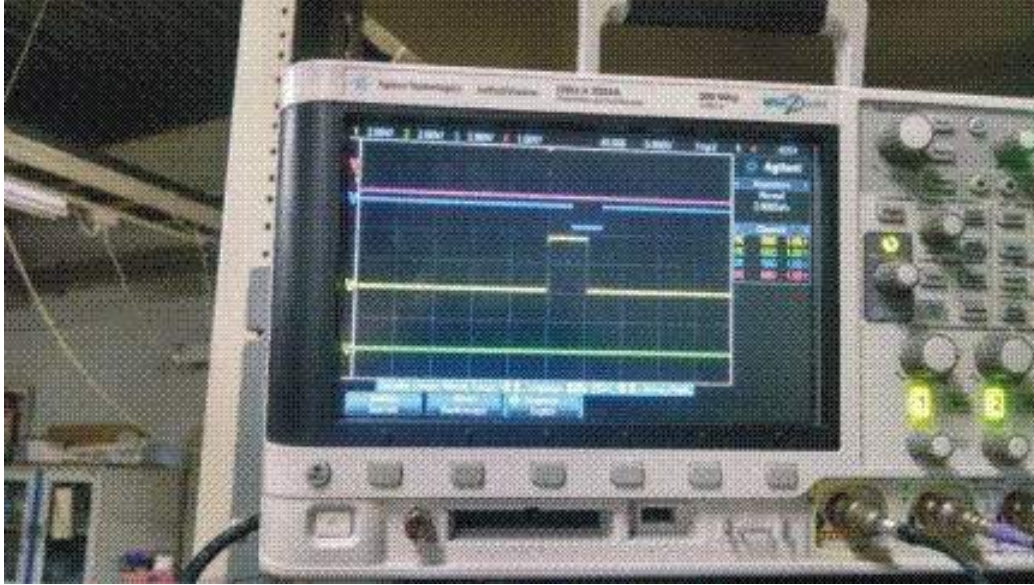


Figure 2.103: The delay output from G&D2 passes to the start of G&D4 to assure that the TTL-Open (yellow) and TTL-Close (green) are not simultaneous present.

Open closes at the right time to prevent beam ionized particles from entering the anode plane. In the meantime, it allows some time for the previous event to be fully collected before the gate is closed. The delay output from G&D2 passes to the start of G&D4 so that the TTL-Open and TTL-Close are never simultaneous present.

2.10 Gas handling system

The $S\pi$ RIT TPC uses P-10 gas (90% Ar, 10% methane). The properties of the P-10 gas is discussed in Section(Choice of gas). Figure 2.105 shows the planned gas handling system which will be used in the first experiment of the $S\pi$ RIT TPC. The detector is operated at the room temperature (20°C) and 1 atm.

The procedure for handling the gas is as follows. The gas from the P-10 cylinder is fed to the field cage of the TPC via the mass flow controller. Since the exit window of the $S\pi$ RIT TPC is made of a 75 micron-thick Kapton sheet, the differential pressure between

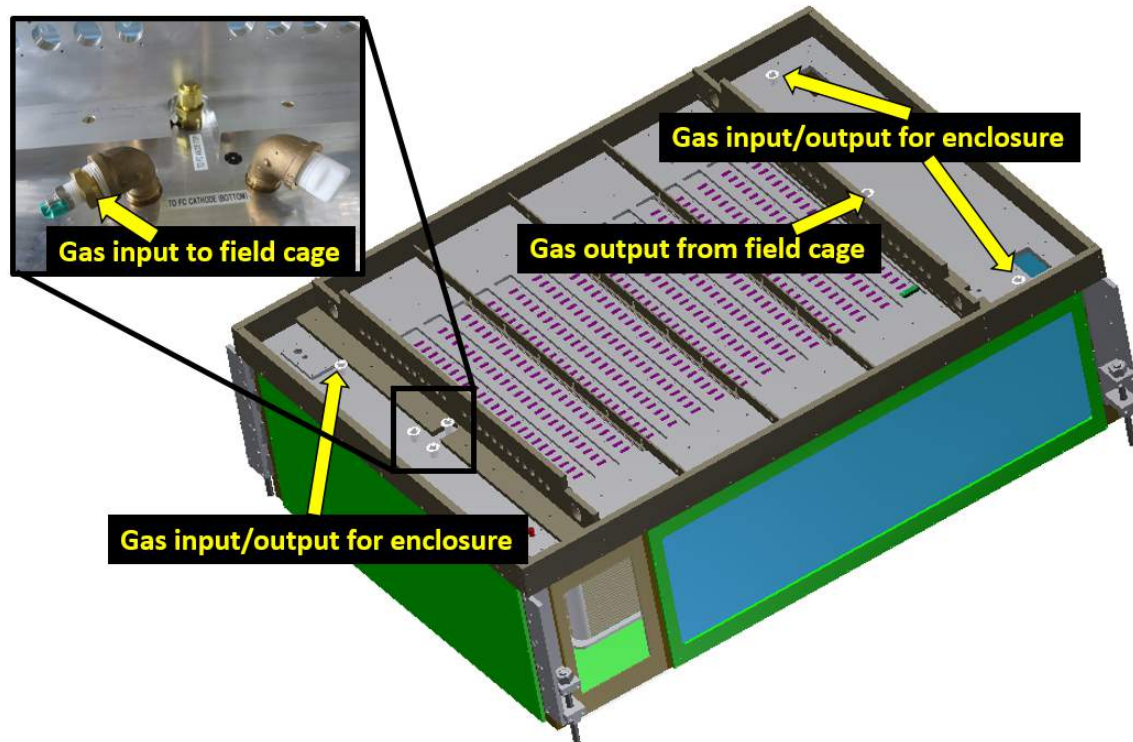


Figure 2.104: Position of gas input and output on the S π RIT TPC.

the volume inside the field cage and the outside should not exceed 1.2 atm. Therefore, the maximum flow rate that we could run is 1000 cm³/minute. Before the gas input of the field cage, there is a pressure gauge for monitoring the pressure of an input gas. In Figure 2.104, the gas flows into the top channels on the front window and fill the volume from the bottom. The excess gas will exit the field cage on the downstream side. From the gas output of the field cage, we either connect to the gas input of the enclosure so that the whole volume of the detector is filled with P-10 gas or connect a different gas line such as Nitrogen to the gas input of the enclosure. The latter allows the TPC to have two different gases. The schematic diagram from using two types of gas is shown in Figure 2.106. The last section is to connect the gas output of the enclosure to the bubbler to prevent the contamination of gas. At the gas output of the enclosure, there are humidity and oxygen monitors to check the condition of the volume inside.

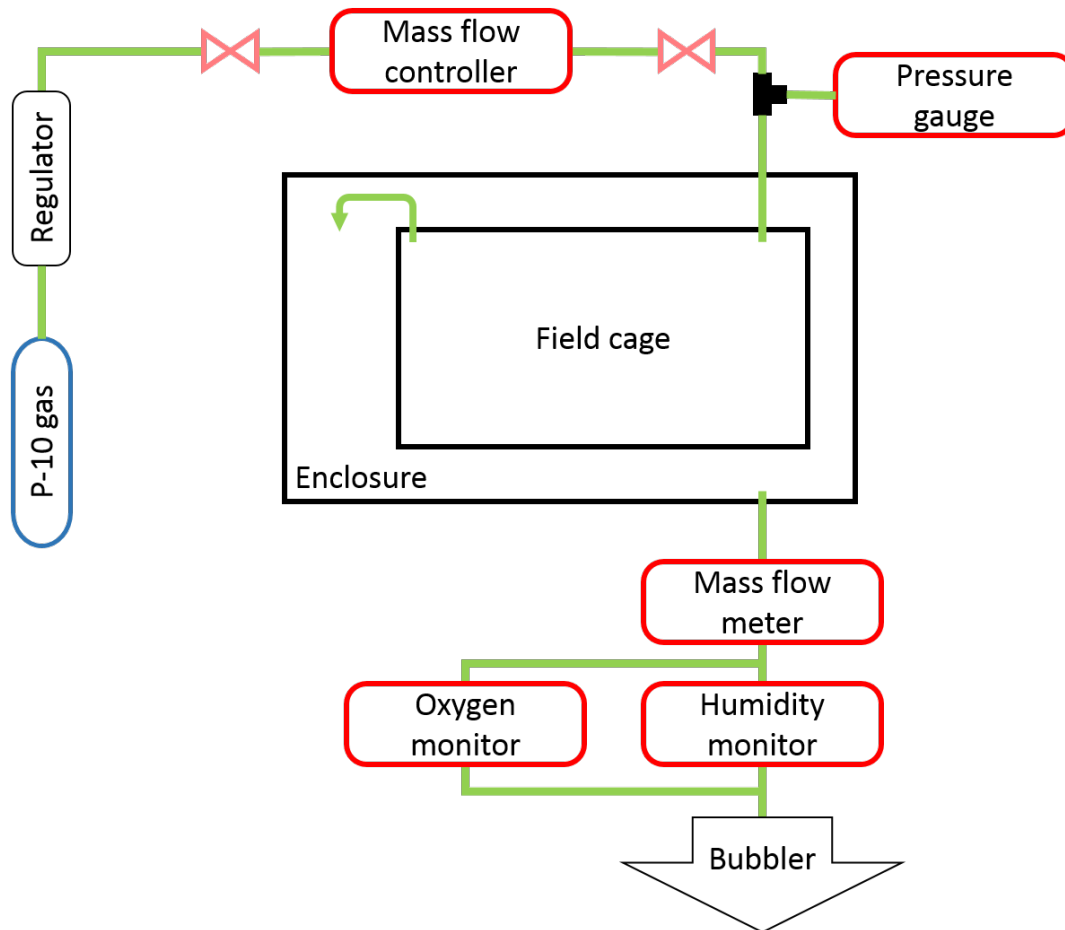


Figure 2.105: Planned gas handling system for the S π RIT TPC

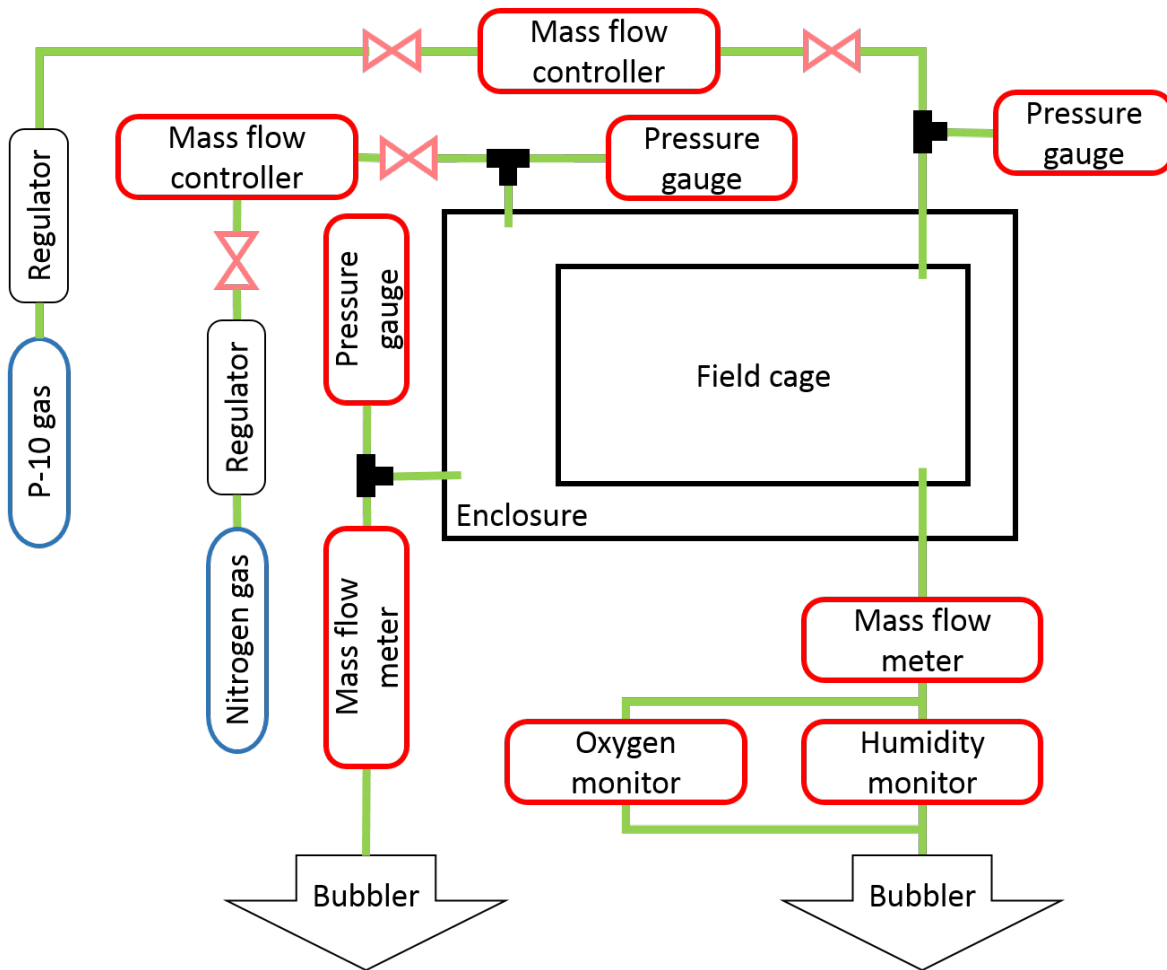


Figure 2.106: Planned gas handling system for the SπRIT TPC

Chapter 3

Gating grid

3.1 Purpose of the gating grid

A gating grid is used to control the passage of electrons and ions in the TPC. In a typical experiment, the gating grid is kept closed except when externally triggered by an interesting event. When the gating grid is closed, no electron or positive ions pass between the drift volume and the region containing the anode plane where gas amplification occurs. When it is opened, the gating grid will be transparent to drifting electrons allowing them to pass essentially without loss from the drift region to the anode wires. The gating grid serves two functions: 1. It prevents unwanted electrons going into the avalanche region and the back flow of the positive ions from the avalanche region into the drift volume [62]. Preventing these positive ions from entering the drift region will have the effect of minimizing the space-charge effects from such positive ions, which can distort the drift field in the detector and adversely [63, 64]. 2. An addition gating grid minimizes the deposition of polymers on the anode wires and prevents aging of the anode wires [65, 66].

In typical operation of the S π RIT TPC, charged particles produced in heavy-ion collisions ionize the gas inside a reaction chamber filled with P-10 gas (90% Argon, 10% Methane). Ideally, the ionized electrons drift along the parallel electric and magnetic fields towards a multi-layered set of wire planes as illustrated in Figure 3.1. As discussed in Section 1.4, the drift time of these electrons to the anode plane provides the vertical (y) location of

the ionization track and the horizontal (x and z) locations of the ionization at the pad plane provides the horizontal locations of the ionization track. Unfortunately, there can be horizontal components of the electric or magnetic fields that add to the vertical components, discussed in Section 2.1.7. These can distort the Cartesian reconstruction of the tracks from the electronic signals measured at the pad plane of the TPC. Such electric field distortion can arise if the positive ions produced near the anode wires are allowed to drift along the dominantly vertical electric and magnetic fields back into the drift volume. The positive ions drift slowly and it is possible that the build-up of those space charges in the drift regions of the TPC can lead to horizontal components of the electric field that could significantly change the direction of the electronic drift velocity away from vertical and lead to rate dependent problems in the reconstruction of the momenta of the detected particles [67]. This can be avoided if positive ions are captured on the gating grid before they can go to the drift region.

A second problem that the gating grid can reduce is the aging of the anode wires due to deposition of polymers on the wires, caused by impurities in the counter gas or by negatively charged polymers produced from the methane during the primary ionization or from the avalanche [15]. Ionization of such molecules in the gas can result in the removal of electrons from the molecules or in the breakup of covalent bonds of the gas molecules. Table 3.1 shows that the ionization energy for simple electron removal from a molecule is typically 2-5 times larger than a covalent bond. When a covalent bond breaks, there is a possibility to form a charged radical molecule. If such molecules are close to the anode and are negatively charged, they can be attracted towards the anode surface due to the high electric field near the anode wire as illustrated in Figure 3.2. These molecules can be deposited to form an irregular polymer coating on the anode surface. Blinov et al. [15] performed a test on the polymer deposit on the surface of an anode wire with various types of gas mixtures. The

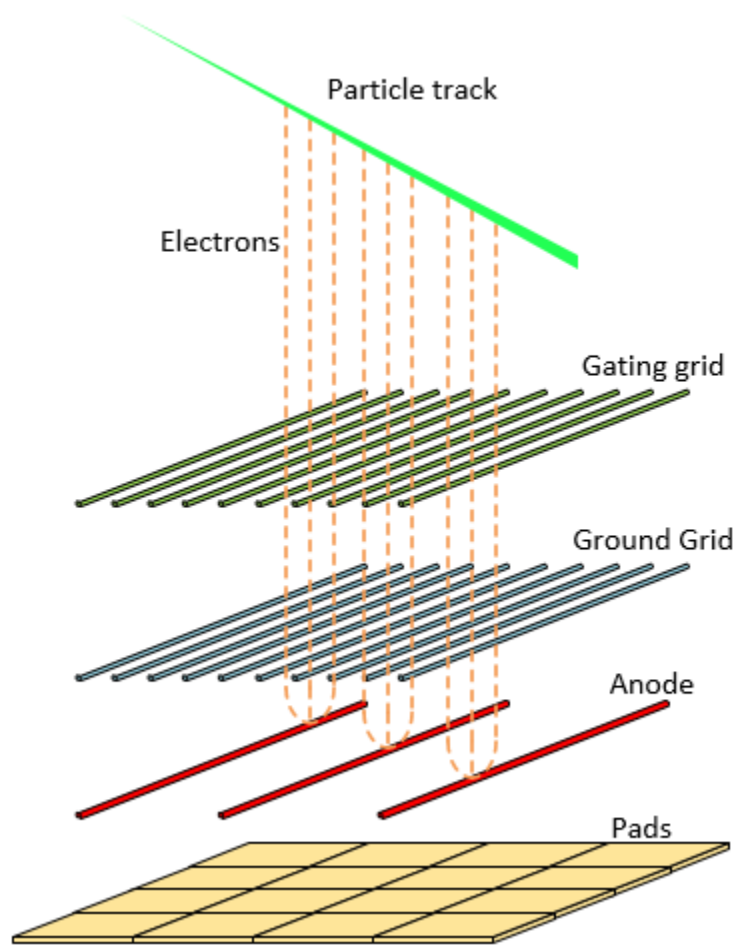


Figure 3.1: Ionized electrons drift into the multiplication region and multiply at the anode wires.

study shows that charged polymers tend to accumulate on the tips of the rough surface of the anode wire as shown in Figure 3.3. Once the first layer sticks to the metal surface, polymers can continue to accumulate, preferentially on the highest points, where the electric field is greatest. The possibility of building up of the polymers increase; the growth at the high points looks like the growth of "hair". An example for polymer accumulation can be seen in Figure 3.4. This polymer coating increases the effective wire diameter, reducing the gas gain. If these polymers are not controlled, the performance of the TPC will deteriorate after the wire chambers have been used for some time.

Table 3.1: Dissociation and ionization energy of gases [2]

	Dissociation (eV)	Ionization (eV)
Ar	-	15.8
Xe	-	12.1
H ₂	4.5	15.6
N ₂	9.7	15.5
O ₂	5.1	12.5
Ethanol	≥3.2	10.5
Iso-propanol	≥3.2	10.2
DME	≥3.2	9.98
C ₆ H ₆	≥3.6	11.5
H ₂ O vapor	4.8	12.6
Methylal	≥3.2	10.0
CO ₂	7.8	13.8
Iso-buthane	≥3.2	10.6
CH ₄	4.3	12.6

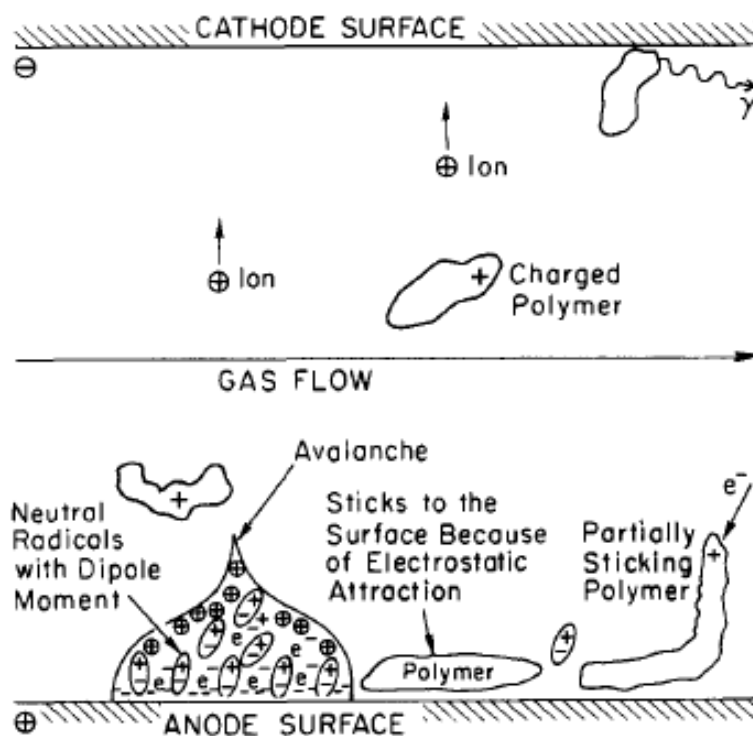


Figure 3.2: Formation of polymers from free radical molecules [2]

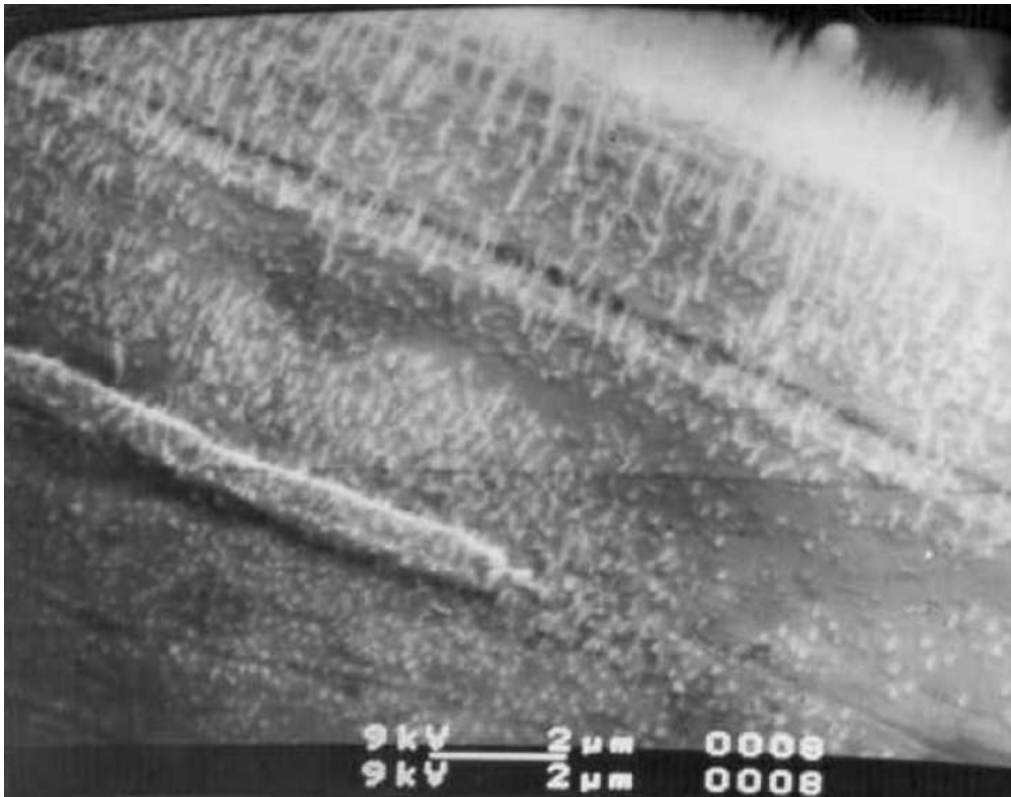


Figure 3.3: Accumulation of negatively charged polymers on the surface of an anode wire [15]

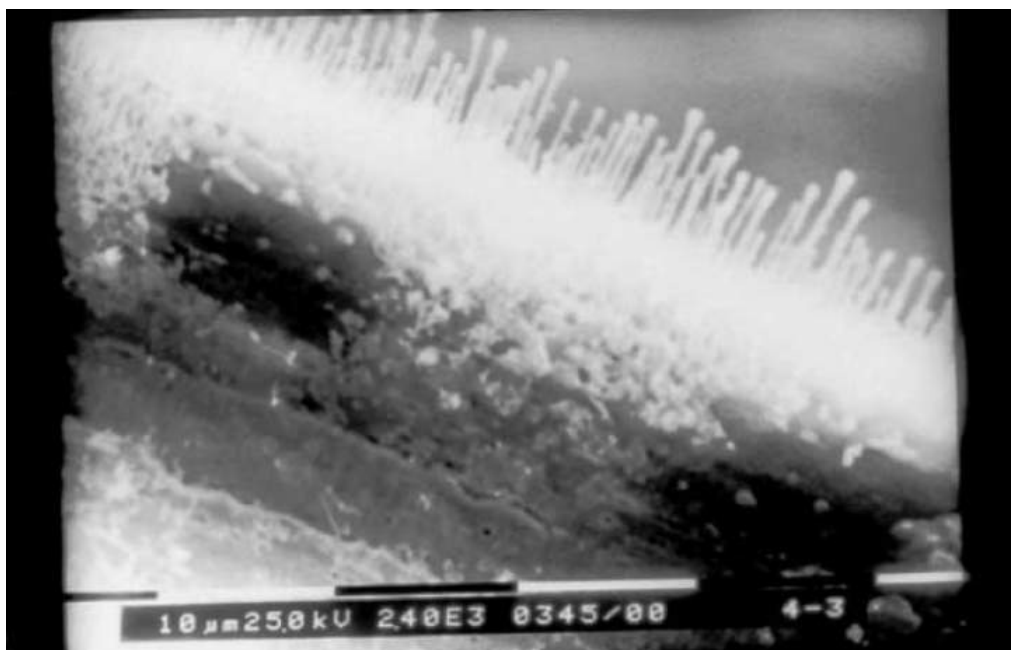


Figure 3.4: Polymers deposit on the surface of an anode wire in CO₂/Isobutane [15]

A possible solution to these problems is to use a gating grid. This will minimize the accumulation of the charged polymers and also prevent the positive ions from drifting into the drift volume and distorting the field.

3.2 Simulation of gating grid

3.2.1 Single wire plane and a conducting plane

To study a behavior of a gating grid, we neglect any effect of the magnetic field and consider how to control the passage of charges through the gating grid with the use of electric fields alone. We start with a grid of wires parallel to a conducting plane. In Figure 3.5, the $x - z$ plane is coincident with a conducting plane. The wires is oriented along the y axis and the z axis is perpendicular to the plane. Neighboring wires in the gating grid are separated from each other by the pitch s .

The electrostatic potential mainly depends on y and z coordinates due to the symmetry along the z direction. Using complex variable techniques in which the both electrostatic potential and the electric field are analytic functions in the complex plane. The standard coordinate system for TPC has the z axis along the beam axis, the x axis is horizontal that y axis is vertical. This would make the (y, z) plane to be the plane in which complex variable techniques would be applied. Since y and z are not the usual variables for complex variables, it is convenient for the calculating the properties of the gating grid to make a change of coordinate system as follows. For the following discussion, we retain the y direction to be vertical, but make the x direction to lie along the beam axis. The z direction in this new coordinate system is horizontal perpendicular to the beam axis. In this new coordinate system, the potential depends only on x and y ; it does not depend on z . The conducting

plane has zero potential ($y = 0$). In these complex variable techniques, the potential in the charge free region is an analytic function of the complex position $x + iy$ corresponding to the Cartesian coordinate (x, y) . The electric field at complex position U for a line source at complex position U' running in the z direction perpendicular to the plane is $E = \frac{\lambda}{2\pi\epsilon_0(U-U')}$. Due the presence of the conducting surface represented by the pad plane, for full electric field includes the field from the surface charge on the ground plane, which can be represented by an image charge of $-\lambda$ at position \bar{U} [11].

If one further solves for the complex potential of a single wire with line charge density of λ at $U' = x' + iy'$, one obtains

$$\phi(U) = -\frac{\lambda}{2\pi\epsilon_0} \ln \frac{(U - U')}{(U - \bar{U}')} \quad (3.1)$$

where $U = x + iy$ is the coordinate of a general point and \bar{U} is the complex conjugate of U' . By adding the contribution of each wire, the total potential can be written as

$$\phi(U) = -\frac{\lambda}{2\pi\epsilon_0} \sum_{k=-\infty}^{k=+\infty} \ln \frac{(U - U'_k)}{(U - \bar{U}'_k)}. \quad (3.2)$$

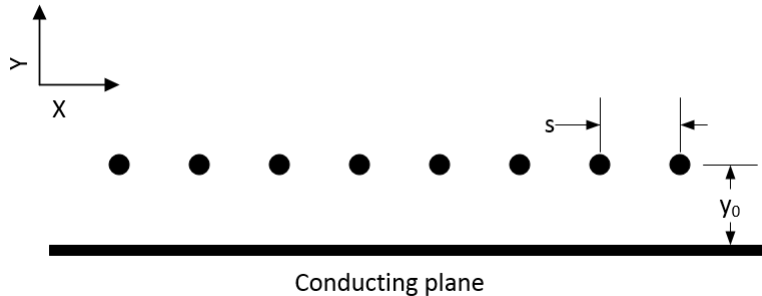


Figure 3.5: Grid of wires parallel to a conducting plane [11]

The corresponding real potential [11], $V(x, y) = \mathbf{Re} \phi(U)$, is

$$V(x, y) = -\frac{\lambda}{4\pi\epsilon_0} \ln \frac{\sin^2[(\pi/s)(x - x_0)] + \sinh^2[(\pi/s)(y - y_0)]}{\sin^2[(\pi/s)(x - x_0)] + \sinh^2[(\pi/s)(y + y_0)]} \quad (3.3)$$

where x_0 and y_0 correspond to the coordinates of the midpoint between two wires at the center of the wire plane. The electric field calculated from the Equation 3.3 is given by:

$$E_x(x, y) = \frac{\lambda}{2s\epsilon_0} \left[\frac{1}{A_1} - \frac{1}{A_2} \right] \sin \left[\frac{2\pi}{s}(x - x_0) \right],$$

$$E_y(x, y) = \frac{\lambda}{2s\epsilon_0} \left(\frac{\sinh[(2\pi/s)(y - y_0)]}{A_1} - \frac{\sinh[(2\pi/s)(y + y_0)]}{A_2} \right), \text{ where} \quad (3.4)$$

$$A_1 = \cosh \left[\frac{2\pi}{s}(y - y_0) \right] - \cos \left[\frac{2\pi}{s}(x - x_0) \right],$$

$$A_2 = \cosh \left[\frac{2\pi}{s}(y + y_0) \right] - \cos \left[\frac{2\pi}{s}(x - x_0) \right].$$

The potential of a wire grid at a distance that is much larger than the pitch can be approximated by the following equations.

$$V(x, y) = \frac{y\lambda}{\epsilon_0 s} \text{ for } y < y_0, \quad y_0 - y \gg \frac{s}{2\pi}$$

$$V(x, y) = \frac{y_0\lambda}{\epsilon_0 s} \text{ for } y_0 < y, \quad y - y_0 \gg \frac{s}{2\pi} \quad (3.5)$$

Thus, the potential created by one plane of wire in Equation 3.3 at a distance $d \gg s/2\pi$ behaves like a sheet of charge with a surface charge density $\sigma = \lambda/s$. Near the surface of the wire, the potential is evaluated at $(x - x_0)^2 + (y - y_0)^2 = r^2$. Then, the potential of the wire grid can be approximated by

$$V(\text{wire grid}) = \frac{\lambda y_0}{\epsilon_0 s} \left(1 - \frac{s}{2\pi y_0} \ln \frac{2\pi r}{s} \right). \quad (3.6)$$

3.2.2 Superposition of the electric field

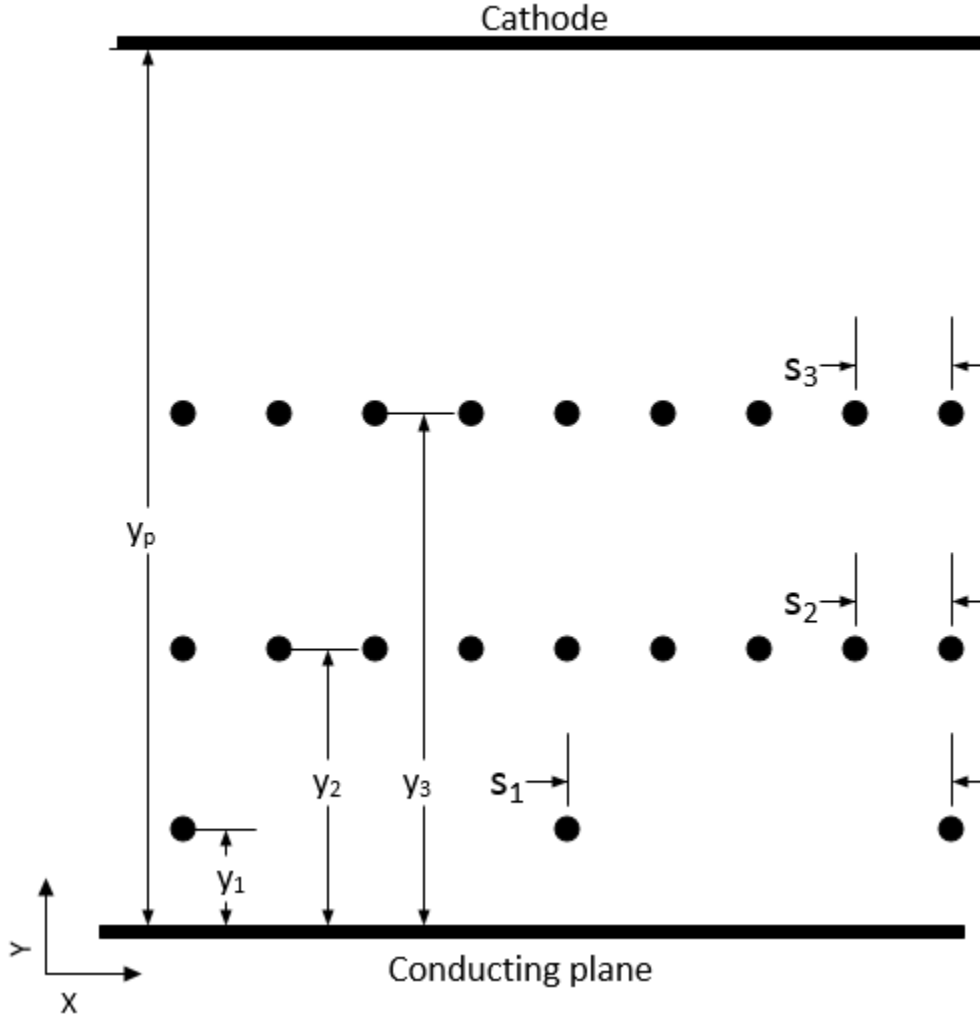


Figure 3.6: Wire plane configuration of the SπRIT TPC. The pitch of anode plane (s_1) is 4 mm. The pitch of the ground (s_2) and gating grid (s_3) are 1 mm. The distance from the conducting plane (pad plane) to the anode (y_1), ground (y_2) and gating grid (y_3) is 4, 8 and 14 mm, respectively. The distance from the cathode to the pad plane $y_p = 509.5$ mm.

In SπRIT TPC, there are three planes of wires as shown in Figure 3.6. y_1 , y_2 and y_3 represent the distance from the conducting plane (pad plane) to the anode, ground and gating grid planes, respectively. The ground and gating grid planes have the pitch of 1 mm and the anode plane has the pitch of 4 mm. To calculate the field properties of the TPC, we superimpose the contribution from all wire planes by using Equation 3.5 and 3.6. Then,

the potential of the wire plane can be expressed by

$$\begin{aligned}
V_a &= \frac{\lambda_a}{\epsilon_0 s_1} \left(y_1 - \frac{s_1}{2\pi} \ln \frac{2\pi r_a}{s_1} \right) + \frac{\lambda_z y_1}{\epsilon_0 s_2} + \frac{\lambda_g y_1}{\epsilon_0 s_3} + \frac{\sigma_p y_1}{\epsilon_0} \\
V_z &= \frac{\lambda_a y_1}{\epsilon_0 s_1} + \frac{\lambda_z}{\epsilon_0 s_2} \left(y_2 - \frac{s_2}{2\pi} \ln \frac{2\pi r_z}{s_2} \right) + \frac{\lambda_g y_2}{\epsilon_0 s_3} + \frac{\sigma_p y_2}{\epsilon_0} \\
V_g &= \frac{\lambda_a y_1}{\epsilon_0 s_1} + \frac{\lambda_z y_2}{\epsilon_0 s_2} + \frac{\lambda_g}{\epsilon_0 s_3} \left(y_3 - \frac{s_3}{2\pi} \ln \frac{2\pi r_g}{s_3} \right) + \frac{\sigma_p y_3}{\epsilon_0} \\
V_p &= \frac{\lambda_a y_1}{\epsilon_0 s_1} + \frac{\lambda_z y_2}{\epsilon_0 s_2} + \frac{\lambda_g y_3}{\epsilon_0 s_3} + \frac{\sigma_p y_p}{\epsilon_0}.
\end{aligned} \tag{3.7}$$

V_a , V_z , V_g and V_p are the potential of the anode, ground, gating grid and cathode, respectively. λ_a is the charge per unit length of the anode wire. λ_z is the charge per unit length of the ground wire and λ_g are the charge per unit length of the gating grid wire. r_a is the radius of the anode wire. r_z is the radius of the ground wire. r_g is the radius of the gating grid wire. σ_p is the surface charge density of the cathode.

To simplify the Equation 3.7, we define a surface charge density σ for each wire plane as λ/s . Then, we can rewrite these equations as

$$\begin{pmatrix} V_a \\ V_z \\ V_g \\ V_p \end{pmatrix} = A \begin{pmatrix} \sigma_a \\ \sigma_z \\ \sigma_g \\ \sigma_p \end{pmatrix} \tag{3.8}$$

where A is the matrix of the potential coefficients. The inverse of A is the capacitance matrix.

Once it is known, we can obtain the induced charge on each electrode as in Equation 3.9.

$$\begin{pmatrix} \sigma_a \\ \sigma_z \\ \sigma_g \\ \sigma_p \end{pmatrix} = A^{-1} \begin{pmatrix} V_a \\ V_z \\ V_g \\ V_p \end{pmatrix} \quad (3.9)$$

According to Equation 3.7, A can be written as

$$A = \frac{1}{\epsilon_0} \begin{pmatrix} y_1 - \frac{s_1}{2\pi} \ln \frac{2\pi r_a}{s_1} & y_1 & y_1 & y_1 \\ y_1 & y_2 - \frac{s_2}{2\pi} \ln \frac{2\pi r_z}{s_2} & y_2 & y_2 \\ y_1 & y_2 & y_3 - \frac{s_3}{2\pi} \ln \frac{2\pi r_g}{s_3} & y_3 \\ y_1 & y_2 & y_3 & y_p \end{pmatrix} \quad (3.10)$$

From this matrix and, more accurately from its inverse, we can determine the transmission of electrons and ions through various grids.

3.2.3 Monopolar gating grid

Within the active volume of the S π RIT TPC there is a constant electric field directed downwards towards the cathode. The electrons ionized in the gas drift upwards along electric and magnetic fields towards the gating grid. Depending on the voltages on the grid wires, these electrons will either stop on the wires or pass through the grid towards the ground and anode wire planes.

Those electrons following electric field lines that terminate on a gating grid electrode will stop on this electrode. Those that do not will pass through the gating grid. From Gauss's law, the surface charge on a conductor is given by the electric field normal to its surface.

Thus, the ratio of the surface charge density on the gating grid to the surface charge density on the cathode is equal to the fraction of electric field lines that terminate on the gating grid, and consequently to the fraction of the electrons produced by ionization within the active volume that are captured on the gating grid. Thus, from section 3.2.2, if the ionized electrons follow the electric field lines, the transparency of the gating grid T can be obtained by

$$T = 1 - \frac{\sigma_g^+}{|\sigma_p|} \quad (3.11)$$

where σ_p is the negative surface charge density of the negatively biased cathode and σ_g^+ is the positive charge density of the gating grid. Figure 3.7 illustrates how a wire residing in an external electric field E will be polarized by the field. A surface charge density σ_D will be polarized by the external electric field normal to the surface of the wire. The dependence of the resulting charge density on the wire as a function of angle can be expressed as

$$\sigma_D = 2E\epsilon_0 \cos \theta, \quad (3.12)$$

where θ is the angle between the electric field E and the radius vector from the center to the surface of the wire. In general, the wire can also have a total nonzero linear charge λ in addition to σ_D . Therefore, the total surface charge density is

$$\sigma_w = \frac{\lambda}{2\pi r} + 2E\epsilon_0 \cos \theta, \quad (3.13)$$

where r is the radius of the wire as shown in Figure 3.7. The total charge per unit length can both net positive and net negative contribution distributed non-uniformly over the surface

of the wire. The positive charge density on the gating grid is

$$\sigma_g^+ = \frac{\lambda^+}{s_3} \quad (3.14)$$

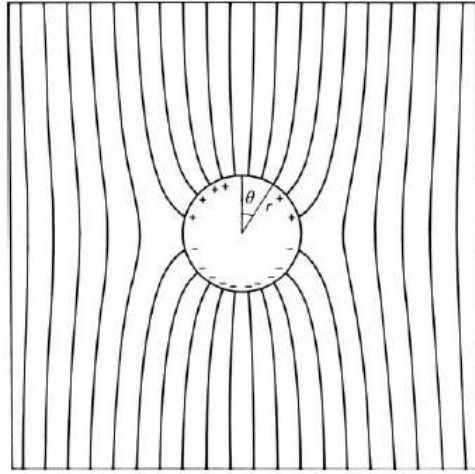


Figure 3.7: A wire is polarized by an external electric field. Electric fields are pointing upward [11].

In order to calculate the transparency of the gating grid T , we only count the positive charges upon which the electric field lines transporting charge terminate. These line charges can be obtained by integrating the surface charge over the region where the charge is positive. These can be obtained from the following equations. When the charge density remains negative overall the entire surface of the wire, we have:

$$\lambda^+ = 0 \quad \text{when} \quad \frac{\lambda}{2\pi r} < -2E\epsilon_0. \quad (3.15)$$

When the charge density is positive over the entire surface of the wire, we have:

$$\lambda^+ = \lambda \quad \text{when} \quad \frac{\lambda}{2\pi r} > 2E\epsilon_0. \quad (3.16)$$

When the charge density positive at small θ_0 , and becomes negative at larger θ_0 , the integral over the angles were the surface charge $\sigma > 0$ yields:

$$\lambda^+ = \frac{\lambda\theta_0}{\pi} + 4Er\epsilon_0 \sin \theta_0 \quad \text{when} \quad -2E\epsilon_0 < \frac{\lambda}{2\pi r} < 2E\epsilon_0, \quad (3.17)$$

$$\theta_0 = \arccos \frac{-\lambda}{4\pi\epsilon_0 Er}.$$

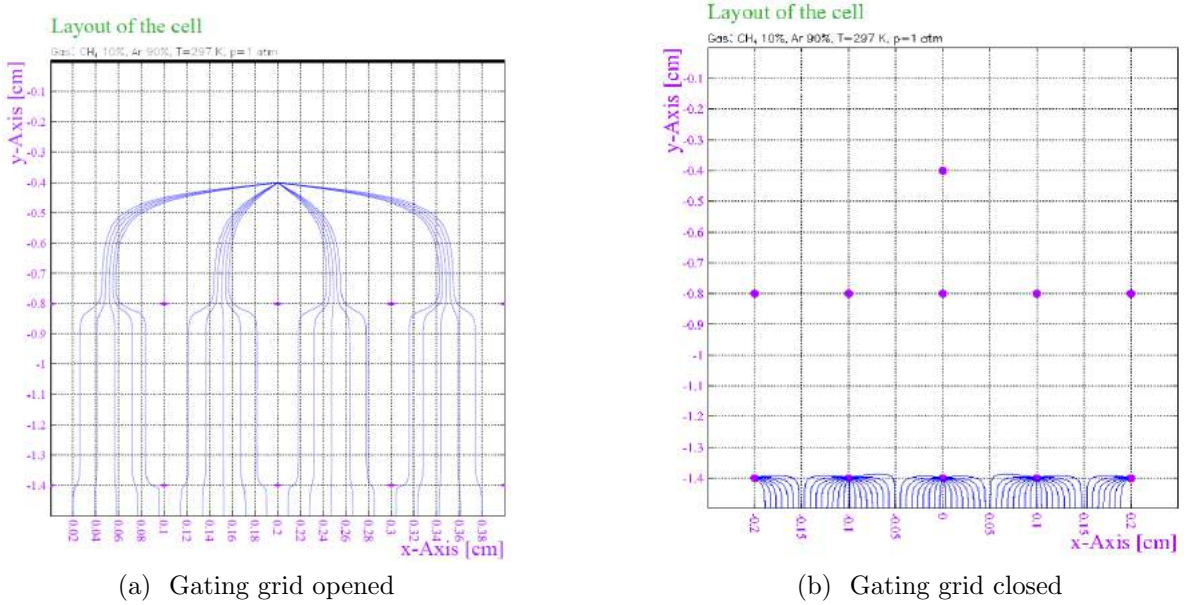


Figure 3.8: Drift lines of ionized electrons ($y_1 = 4$ mm, $y_2 = 8$ mm, $y_3 = 14$ mm, $s_1 = 4$ mm, $s_2 = s_3 = 1$ mm)

Figure 3.8 illustrates the operation of the gating grid in the absence of a magnetic field. The wire planes from the top to the bottom are the gating grid, ground and anode planes, respectively. The ionized electrons are drifting downwards. When the gating grid is opened, as shown in Figure 3.8(a), all ionized electron pass through the anode plane. No electrons pass the grid when it is closed, as illustrated in Figure 3.8(b). For the close state of the gating grid in Figure 3.8, the wires are sufficiently positively biased so that there is net positive charge density on the entire surface of the wire.

These calculations were obtained from GARFIELD, a gas detector simulation program,

which calculates the motion of electrons and ions subject to the electric and magnetic fields and to the scattering with gas atoms and molecules [51, 68]. According to the calculation, the voltage of the gating grid needs to be negative enough depending on the cathode potential to achieve a full transparency, which occurs when there are no regions of net positive charge density on the gating grid wires. Figure 3.9 shows the comparison between the calculation of the transparency of the gating grid from GARFIELD and the analytical solution, given by Equation 3.11. The transparency from GARFIELD calculation agrees with the result from the analytical solution.

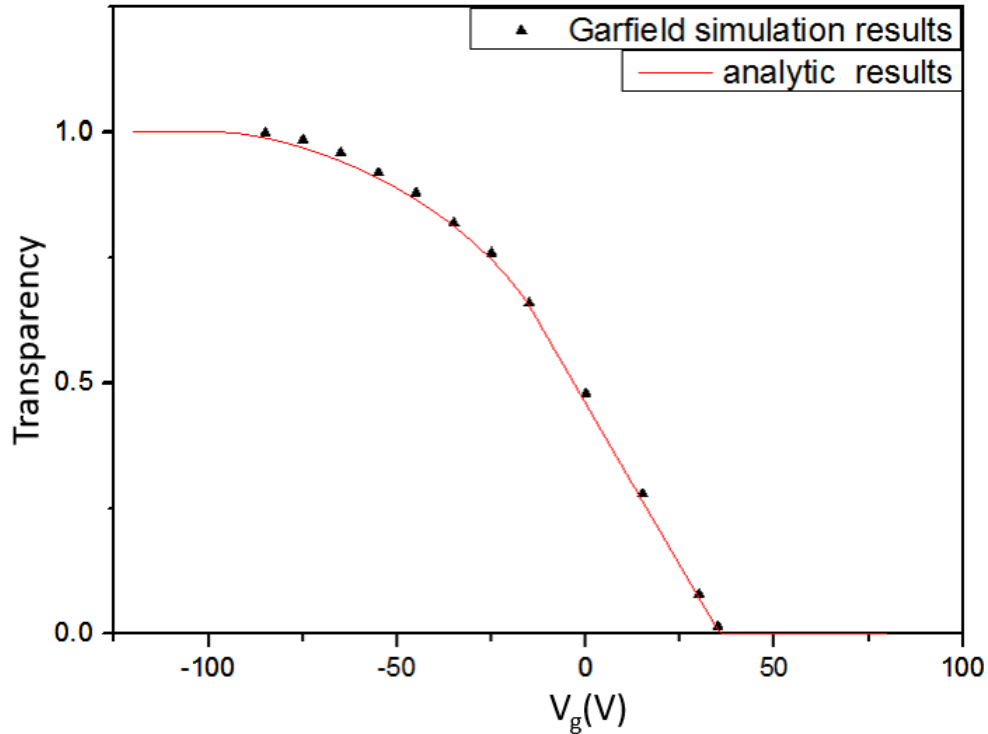


Figure 3.9: Transparency, T , of the gating grid with $V_{cathode} = 6$ kV. Black triangle : Garfield simulation; Red line: Analytical solution using Equation 3.11.

As shown in Figure 3.9, it is possible to regulate the charge transmitted through the gating grid by varying the grid voltage. This "mono-polar" gating grid scheme can be employed to control electrons and ions passing through the gating grid. The device operated in this mode

can be found in Reference [63]. However, as discussed in Section 3.2.4, a bipolar gating grid is more suitable for the S π RIT TPC because it allows the grid to close with minimum noise introduced to the TPC electronics.

3.2.4 Bipolar gating grid

Section 3.2.3 is called monopolar gating grid, because all wires on the gating grid are biased to a common potential. However, few gating grids operate in that mode due to the speed required. For the S π RIT TPC, the transition of the gating grid from close to open state has to occur within a time interval $\Delta T \leq 1 \mu s$. The currents required to change the voltages on the gating grid within this ΔT interval can cause a large disturbance on the anode wires. The induced signal from a poorly designed gating grid can be enormously larger than the data signal. Having the ground grid between the gating grid and the anode plane partially shields the anode and pad plane from the gating grid transition noise. However, this shielding is insufficient to allow the use of a monopolar gating grid for the S π RIT TPC.

An improve design for the gating grid involves closing the gating grid by biasing adjacent wires on the gating grid to two different potentials $V_{average} + \Delta V_g$ and $V_{average} - \Delta V_g$ on the adjacent wires. As the average voltage of the gating grid does not change, the net charge on the gating grid does not change for this method. In the closed configuration, the grid has positive surface charge density every other wire and negative surface charge density on the wire in between. If one sets the voltage difference between the wires, the electron drift lines will terminate at the positive wires closing the gate.

The transparency of the bipolar gating grid can be obtained from Equation 3.11. The positive charge density induced on the wire is expressed by

$$\sigma_{\Delta}^{+} = \frac{-\epsilon_0}{\frac{s_3}{\pi} \ln \frac{\pi r g}{2s_3}}. \quad (3.18)$$

The total charge variation on the gating grid is 0. Therefore, the negative charge density is $\sigma_{\Delta}^{-} = -\sigma_{\Delta}^{+}$. On the positive wire, the total surface charge density is given by

$$\sigma_{bipolar}^{+} = \sigma_{\Delta}^{+} + \frac{\sigma g}{2}. \quad (3.19)$$

The $\frac{\sigma g}{2}$ means that only half plane of the gating grid contributes the positive charge. The transparency of the bipolar gating grid can be obtained from

$$T = 1 - \frac{\sigma_{\Delta}^{+} + \sigma g/2}{|\sigma_p|}. \quad (3.20)$$

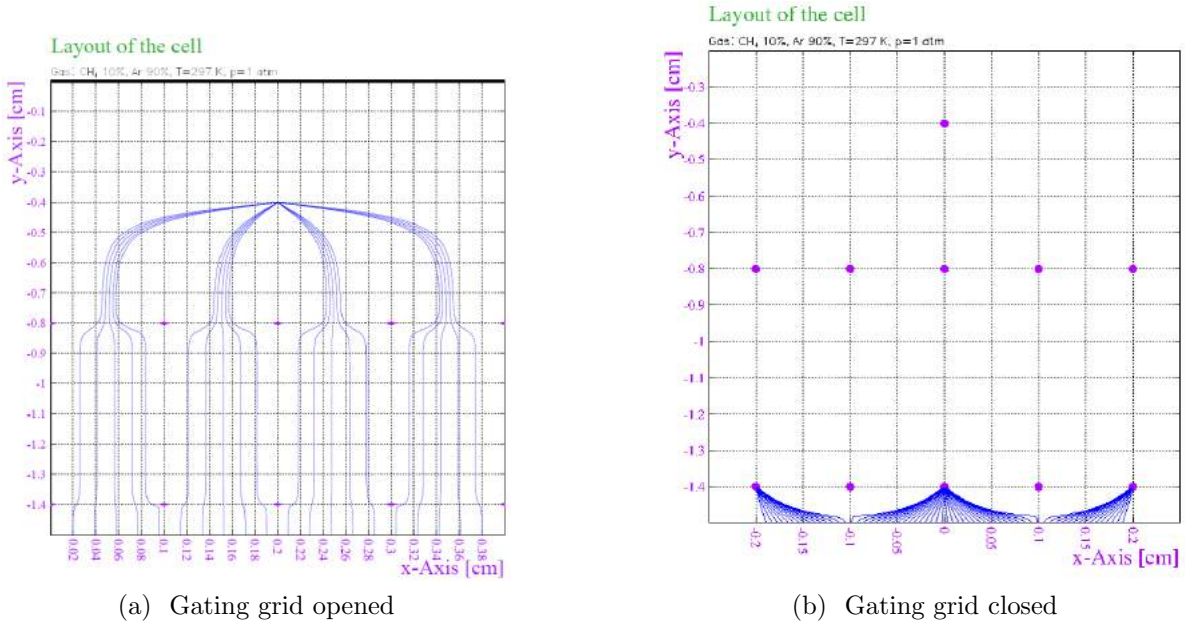


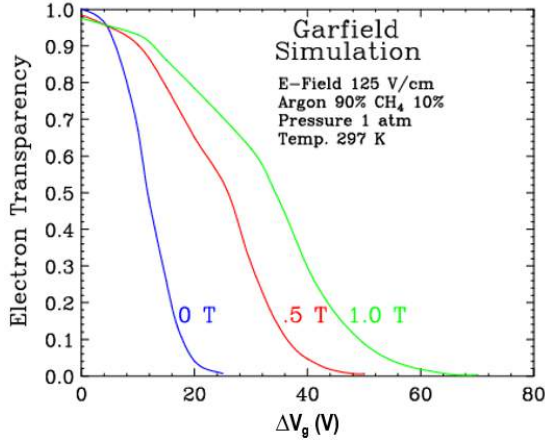
Figure 3.10: Operation of bipolar gating grid ($z_1 = 4$ mm, $z_2 = 8$ mm, $z_3 = 14$ mm, $s_1 = 4$ mm, $s_2 = s_3 = 1$ mm). (b) Electrons terminate at the positive wires of the gating grid.

In Figure 3.10(b), the close state of the bipolar gating grid is different from the configu-

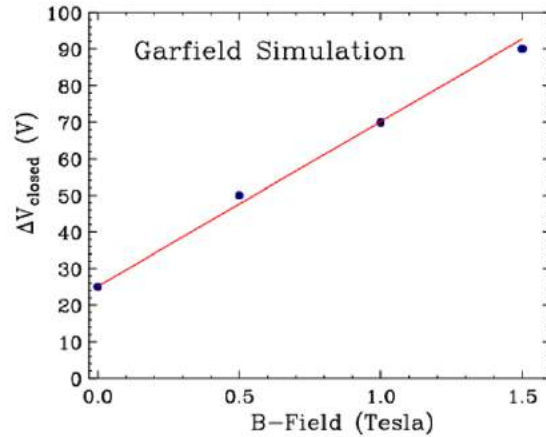
ration in Figure 3.8(b). In Figure 3.8, when the grid is closed, all drifting electrons terminate on the wires that are above the track. However, in the closed state of bipolar gating grid, drifting electrons terminate at the nearest adjacent positively biased wire, thus preventing the transport of electrons through the gating grid. Likewise any positive ion produced at the anode will be driven towards the negatively biased gating grid wires, stopping there.

Next, we will consider the effect of having a magnetic field that is parallel to the main electric field, as is the case in the S π RIT TPC. The behavior of drifting electrons and ions is strongly influenced by the magnetic field. The effects of magnetic field is characterized by the parameter $\omega\tau$ where ω is a cyclotron frequency of the electron and τ is mean time between collisions of the electrons with the gas molecules. It governs the degree to which the magnetic field can influence the trajectory between collisions. When it is small, the motion thermalizes before the effects of the track curvature become important. Thus, small values of $\omega\tau$ lead to small modifications of the trajectories by the magnetic field. This has the consequence that the ion trajectories are similar to what they were without magnetic field. When $\omega\tau$ is large, charged particles can travel a long ways along the curved trajectory dictated by the magnetic field. The mean free path for ion is generally smaller than that for electrons as $\omega\tau$ is very small for ions and can be very large for electrons in some gases. Larger corrections occur for the electrons in the parts of their trajectories where the electric field acts to bend the electron track towards the wire, which is in a direction perpendicular to magnetic field. In this part of the trajectory, the electronic tracks can be bent by the magnetic field in the direction parallel to the wire, diminishing the number of electrons capture on the wire. If one increases the ΔV_g to close the gate, the voltage required to close the gate for ions is largely unchanged, but the electron will require a large voltage to close the gate [11]. Figure 3.11(a) shows the electron transparency of a gating grid with the

presence of magnetic field. In the simulation, the electric field \vec{E} is parallel to the magnetic field \vec{B} . The voltage required to close the gate increases roughly linearly with the magnetic field as seen in Figure 3.11(b). Amendolia et al. study the influence of the magnetic field on the performance of the gating grid and also see that the offset voltages of the gating grid are increasing linearly with the magnetic field strength [69]. In the experiment for the S π RIT TPC, the detector will be operated under the magnetic field of 0.5 T. To completely close the gating grid, we need to apply $\Delta V_g \geq 50$ V. The planned ΔV_g will be 75 V to assure that the gating grid is completely closed.



(a) Electron transparency of a gating grid



(b) Closing voltage as a function of the magnetic field

Figure 3.11: (a) Transparency of bipolar gating with the presence of magnetic field; (b) The closing voltage of a gating grid increases linearly with the magnetic field.

3.3 Gating grid driver

Gating grid driver controls the transition between the closed and open states of the gating grid. In S π RIT TPC, the operation of the gating grid has been designed for a bipolar grid configuration, in which the gating grid will have to same potential for the open state and is biased up or down by ΔV_g in adjacent wires for the closed state.

3.3.1 Design criteria

In a typical experiment, the gating grid is kept closed most of the time unless it is externally triggered by an interesting event. There is a "dead" region below the gating grid at the edge of the active volume, in which ionized electrons will drift into the grid between the time that the event trigger is satisfied and gate is fully opened. The size of the dead region is governed by the electron drift time and the time needed to open the gate. The former is determined by the gas pressure and electric field. It is possible to change the electron drift time by changing the counter gas, but doing that can change the operating parameters of the TPC significantly. If one desires to use P-10 gas, which consists of 90% argon and 10% methane and has a drift velocity of about $5.5 \text{ cm}/\mu\text{s}$, then, the gating grid needs to open as fast as possible ($\leq 500 \text{ ns}$) to reduce the dead region.

As discussed in Section 3.2, large amount of charges brought onto the gating grid within a short time (200 - 300 ns) can potentially cause a large induced signal on the pads which can be considerably larger than the charge ionized by a weakly ionizing particle such as an energetic pion. To avoid this problem, the gating grid has to drain the charge at equal rate on both positive and negative sides so that the average potential of the gating grid remains constant.

3.3.2 Conceptual design

Figure 3.12 shows a conceptual design of the gating grid driver for the $S\pi\text{RIT}$ TPC. The gating grid is connected to the gating grid driver via two low impedance transmission lines (4Ω) which supply voltage to alternating wires. In the $S\pi\text{RIT}$ TPC, the 4Ω transmission lines has been designed and custom made to minimize the noise from the transition of the

gating grid from open to close state and vice versa. The value of the impedance of the transmission cable and thus its size is dictated by the available space in the TPC. In the transmission lines, the currents from the positive and negative polarities of the gating grid flow in opposite directions along adjacent conductors in these transmission lines. The noise from the transition can be reduced as the induced signals from the currents which have the opposite polarities are largely canceled. There are two power supplies connected to the circuit. One of the power sources gives higher potential +HV while the other gives the lower potential -HV. They are connected through two types of mosfet switches (N and P type). N and P-mosfet switched are connected to the +HV and -HV, respectively. The advantage of using a mosfet switch is that when the switch is closed, the internal resistance is lower comparing to other types of switches. This helps in allowing one to tune the resistance across the switches to a lower total resistance value. Also, a mosfet switch has a short turn-on delay time (<100 ns). It allows the gating grid to make a transition quickly.

For the closed state, both mosfet switches are opened. The alternating wires of the gating grid are biased by +HV and -HV. When the gating grid is opened, the two mosfet switches are closed. The two power supplies are connected together by the combined resistance of the two switches. The current flows between the two sides of the gating grid until both sides of the grid reach the average voltage. The gating grid is kept opened long enough to let all electrons from the interesting event to pass through the grid and then the two sides of the gating are restored to their original values, closing the gate. The key challenge is to open the gate quickly without the average voltage of the two side of the gating grid deviating significantly from the average value.

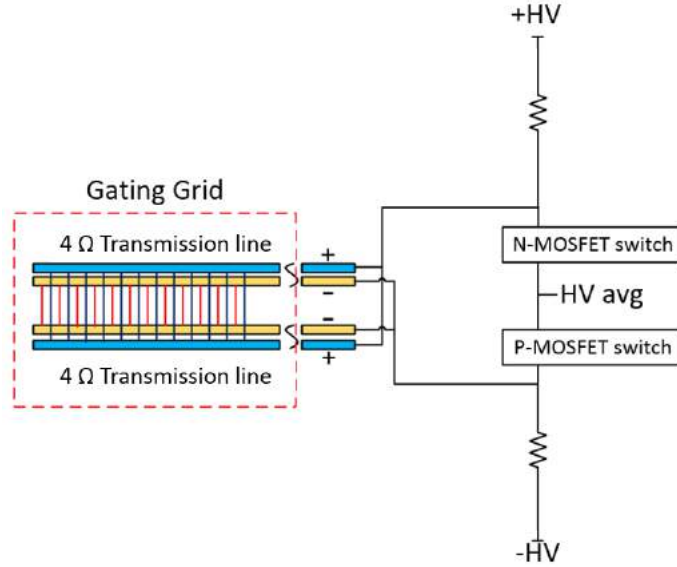


Figure 3.12: conceptual design of the gating grid driver for S π RIT TPC

3.3.3 Gating grid driver prototype 1

In the first prototype, two of BEHLKE mosfet switches (HTS 21-14) are used to control the gating grid operation. Figure 3.13 shows the circuit diagram of the gating grid driver prototype 1. The BEHLKE switches need a DC voltage of 5 V to stabilize them and it is controlled by the external TTL signal. The switches remain opened until it is triggered by the TTL signal. The closing time interval is equal to the width of the TTL signal. Therefore, we are able to decide how long we need to open the gating grid. R1 and R2 in the circuit diagram are used to adjust the impedance between the gating grid driver and the gating grid.

This prototype was first assembled on the bread board and had a resistance of 6 Ω . It was connected to the gating grid via low impedance cables. The capacitance of the gating grid was measured to be 26.5 nF. A voltage of ± 75 V was applied for the first test. The time for decay starts at the time when the gate starts to open.

In Figure 3.14, we show the gating grid signals. The green signal shows the positive

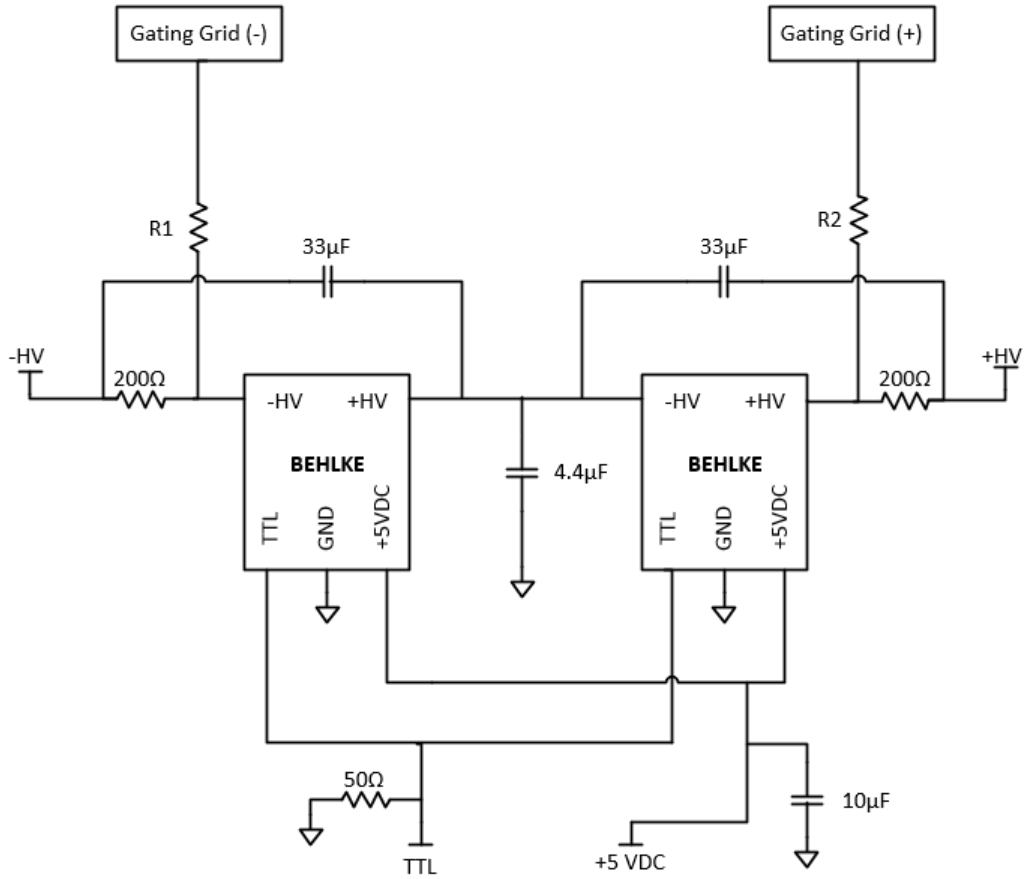


Figure 3.13: Circuit diagram of the gating grid driver prototype 1

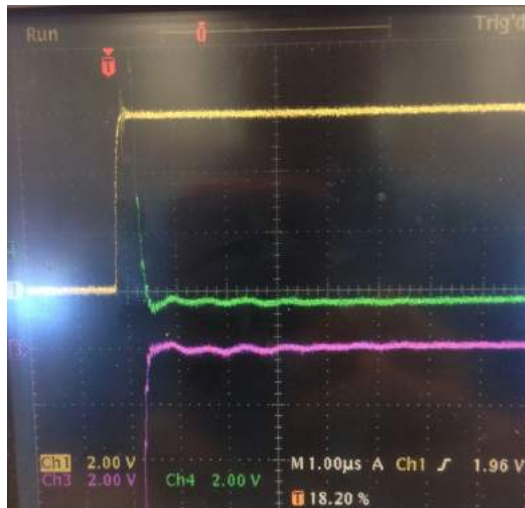


Figure 3.14: Discharging signal of the gating grid driver prototype 1 on the bread board. There are some slow oscillation on the signal.

voltage on the gating grid. The pink signal shows the negative voltage on the gating grid. The scope sensitivity of the pink and green traces is set to 2 V/division, so the ± 75 V initial voltages on the gating grid are off scale. The yellow logic signal shows the TTL trigger signal which triggers the closing of the two BEHLKE switches. These switches begin to close 150ns after the leading edge of this logic signal. The leading edge of the logic signal is about 600 ns before the two gating voltage signals come within 0.4 V of the minimum voltage. This rapid discharge of the gating grid occurs within about $600-150=450$ ns of the leading edge of TTL trigger signal. However, there are slow oscillations that continue on after the opening of the gating grid itself. From Figure 3.11(a), the transparency of the gating grid will be about 80% by the time the gating grid voltages have decreased by $1/e$ of the original voltage of ± 75 V, so the gate will be mostly open about 300 ns after the gating grid switches begin to close. This slow oscillation indicates that the circuit is under damped. One can also see that the oscillation on both the more positive side (green trace) and the more negative side (pink trace) of the gating grid are in phase. This means that there is a common mode oscillation, which must be suppressed. If the positive excursion of the voltage oscillation is large, it may affect the readout data by making noise signal that is comparable to the pion signals, making it difficult to set the thresholds in the readout electronics sufficiently low to trigger on the pion particles.

One period of the slow oscillation comes from the capacitance and inductance of the gating grid and gating grid driver circuit. It is important to try to minimize this inductance, in particular that, which can be attributed to long wires and traces and the utilization of components with large inductances. Therefore, a printed circuit board (PCB) was designed to minimize the inductance and improve grounding of the board. However, it should be noted that the inductance of the gating grid itself is no longer in the circuit for this test.

In Figure 3.15, the PCB was tested with 11.6 nF standard capacitor and an operating voltage of ± 30 V. The resistance of the circuit is 4.8Ω . In this case, it takes 400 ns between the leading edge of the TTL trigger to discharge to the average voltage for the gating grid. Considering that 120 ns of this time occurs between the arrival of the gating grid trigger and the closing of the gating grid switches, the actual discharge takes about 280 ns and the low frequency oscillation is significantly decreased. It should be noted that the inductance of the gating grid is not in the circuit during this test. In addition, there is a negative lobe on the signal after the discharge. This indicates that the circuit is still significantly under damped.

To investigate the slow oscillation, we use a simple model of RLC series circuit to estimate the effective inductance of the circuit. To achieve a critically damped condition to get rid of the negative lobe, R , L and C are related by $R = 2\sqrt{\frac{L}{C}}$.

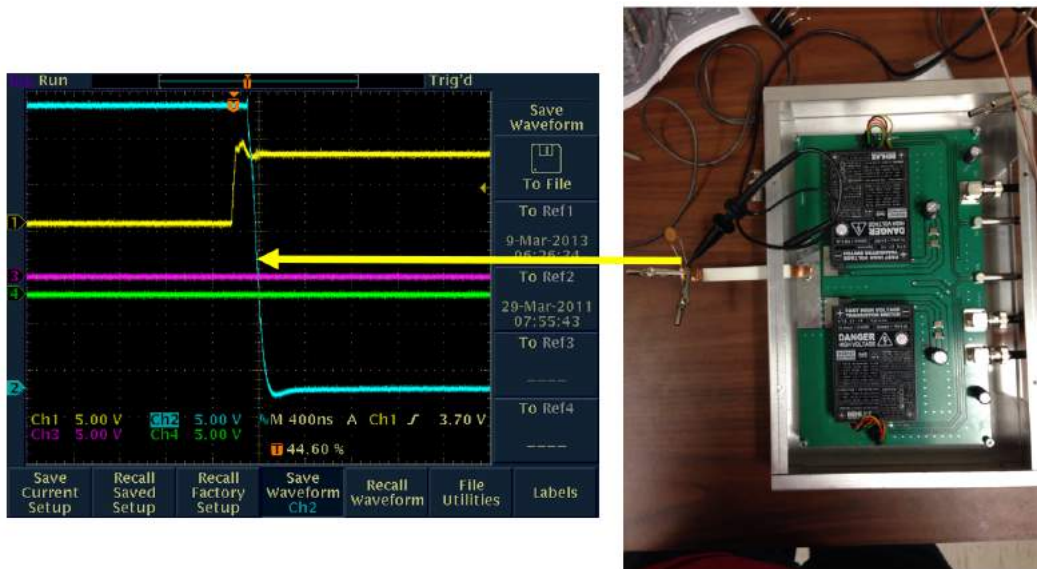


Figure 3.15: Testing the prototype 1 PCB with a standard capacitor of 11.6 nF and an operating voltage of ± 30 V. Blue signal is a discharging signal from the positive side of the capacitor. There is a negative lobe after the discharge which indicates that the circuit is under damped.

We use the SPICE circuit-analysis program to simulate the circuit. SPICE was originally

developed at the University of California, Berkeley by Laurance Nagel. The program provides DC, AC and transient analysis and is used to check the integrity of the circuit designs and to predict circuit performance [70]. For the simulations done in this work, we use the version OrCAD EE PSPICE downloaded from [71]. In the simulation, a resistor, a capacitor and an inductor were connected in series. The resistor represents the resistance of the gating grid driver. The capacitor represents the capacitance of the $S\pi$ RIT TPC. Note that the actual TPC has much more complicated structure. The inductor represents the inductance of the system. By matching the simulation to the data with the actual gating grid, we determine the effective inductance of the PCB to be around 160 nH. The comparison between data and calculation is shown in Figure 3.16. Therefore, with a resistance of 4.8 ohms and a capacitance of 27 nF, one should achieve a critically-damped condition. After adjusting the capacitance value in a bench testing to match this condition, the negative peak disappears and the discharge time increases to 600 ns.

The capacitance of the gating grid is 26.5 nF which is close to the critically-damped condition. The result of testing the PCB with the actual gating grid with an operating voltage of ± 30 V is shown in Figure 3.17. As expected, there is no negative peak and it takes about 600 ns to discharge, however, the voltage declines by 1/3 in about 160 ns, at which time the gate is nearly 80% open. In the test with the bread board and the PCB, there is a 120 ns delay time in opening the gate.

The gating grid driver has been connected to the $S\pi$ RIT TPC and tested with the voltages of ± 75 V. The induced signal on the pads are read out by the prototype of the General Electronics for the TPC (GET). Figure 3.19 shows the induced signal from the pads which is amplified by GET electronics as a function of time bucket. Since the data was taken by using a peaking time of 232 ns and writing time of 50 MHz, one time bucket corresponds

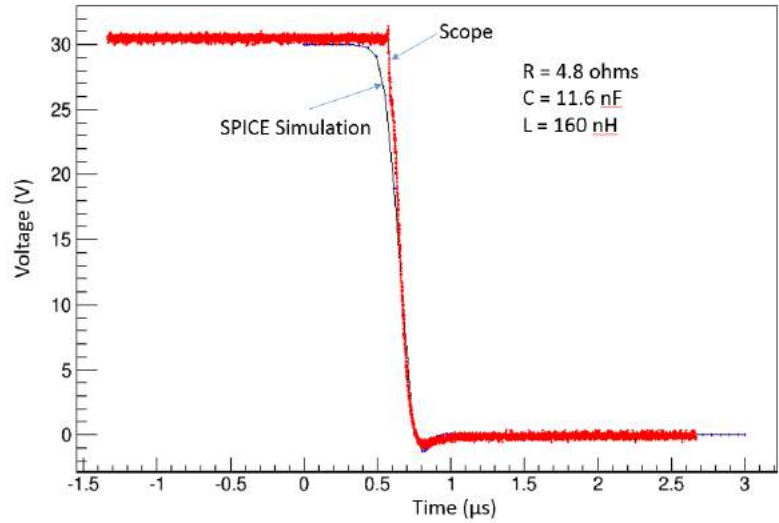


Figure 3.16: Matching the data to the simulation from PSPICE

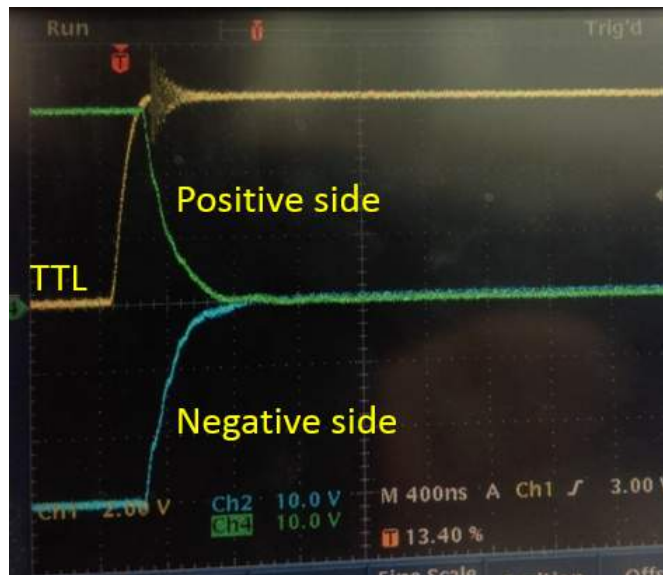


Figure 3.17: Discharging signals of the gating grid using the gating grid driver prototype 1 to 20 ns. The first induced signal occurring between time bucket 125th to 200th comes from the discharging of the gating grid when it is opened while the other negative peak indicates when the gate is closed.

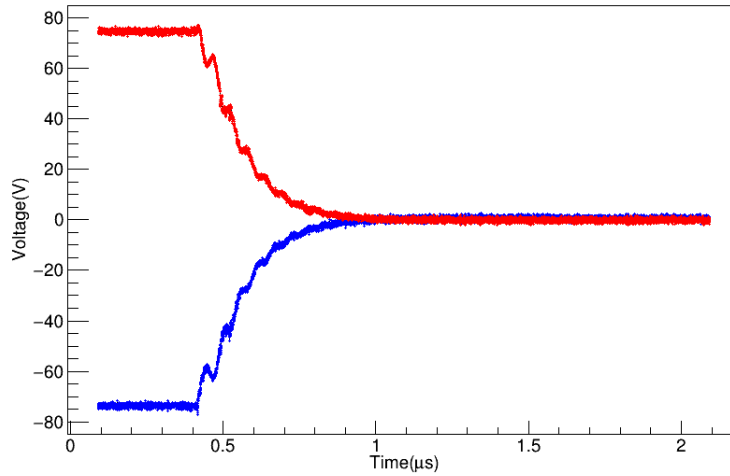


Figure 3.18: Discharging signal from the oscilloscope (operating voltage of ± 75 V, resistance of the system of 4.8Ω)

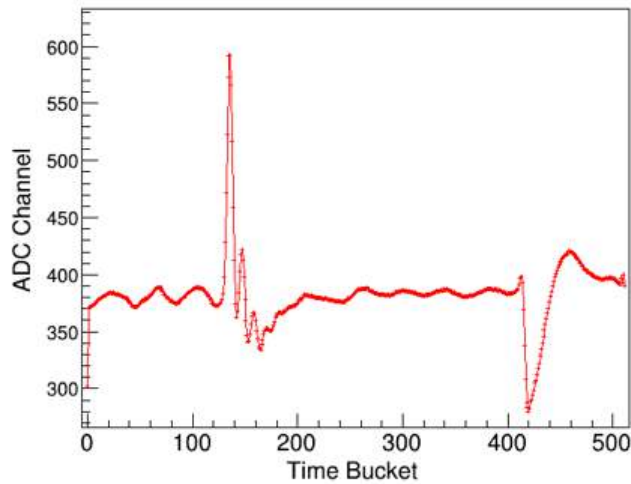


Figure 3.19: Readout signal from the prototype of GET Electronics

3.3.4 Gating grid driver prototype 2

The prototype 1 gating grid driver has the turn-on delay time of 120 ns which is rather long. Ideally, the gating grid would open instantaneously after triggered. We therefore tried to reduce the turn-on delay time as much as possible. In the prototype, the BEHLKE switches were replaced by N-mosfet (IRF640) and P-mosfet (IRF9640) switches which have the same turn-on delay time of 14 ns as shown in Figure 3.20. To drain charges from the gating grid

there is a high frequency noise and it disappears when the capacitor is fully discharged. In addition, the discharge rate of the signals from both sides are different. This comes from the differences between two switches which are related to the internal resistance and capacitance of the switch. In this case, the discharging on the negative side is slower than that of the positive side.



Figure 3.21: Signals from the oscilloscope shows the discharging from the positive side (blue) and negative side (purple) of the standard capacitor of 22 nF. The two signals discharge at a different rate and have a fluctuation at the beginning as indicated in red circle.

To adjust the purple signal to match the blue one, a 10 Ω resistor was added in parallel to R1 (5 Ω) so the resistance on the negative side is 3.33 Ω . This brought two signals to the same discharging rate as shown in Figure 3.22. The gating grid was opened at 100 ns after triggered, slightly faster than the first prototype. The switches fully close when the voltage difference between the gate and source of the mosfet reaches $V_{GS} = 10$ V. Figure 3.23 shows that, this gate driver chip (MCP14E11) requires 100 ns for the gate signal to go from 0 to 12 V which is too long. To optimize this, we need circuit components that are able to generate a 10 V signal faster. In addition, the closing time for the prototype 1 and 2 is around 50 μ s. According to the circuit diagram, when the switches are opened, the capacitor

will be charged via a 200 Ω resistor on each side. This long closing time will decrease the performance of TPC and some of unwanted ionized electrons can go through the gating grid because the potential on the grid has not reached the fully close state.



Figure 3.22: Adjust the discharging rate on the negative side to match the signal on the positive side.

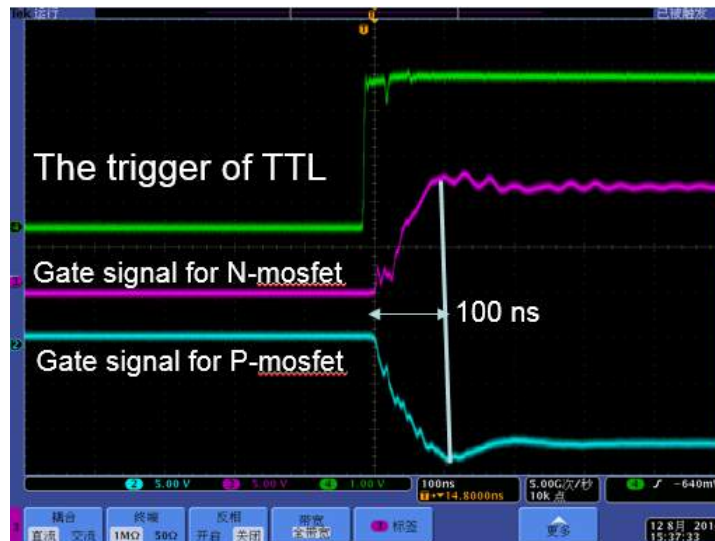


Figure 3.23: Green: the TTL trigger signal; Purple: Gate signal for driving N-mosfet switch; Blue: Gate signal for driving P-mosfet switch

gating grid and short it together. Then the gating grid discharges. At the end of the TTL-1 signal, the two switches open and the two sides are no longer connected together. Then they charge back to their original voltage.

How fast the gating grid recharge depends on whether one supplies a TTL signal through the TTL-2 input. If a TTL signal is sent to the TTL-2 right after the end of the TTL-1 signal, the two switches, N2 and P2, are closed. They connect the +HV and -HV supplies to their respective sides of the gating grid through a switch and a $10\ \Omega$ resistor. If one does not supply a TTL signal to the TTL-2 input, these switches remain open and the gating grids will recharge more slowly through $1\ \text{k}\Omega$ resistors that connect across the positive and negative poles of each switch. A $22\ \text{nF}$ capacitor is connected to the gating grid driver and test at the operating voltage of $\pm 12\ \text{V}$. The closing time of the gating grid driver is the time to recharge the capacitor to the original voltage ($\pm 12\ \text{V}$). It takes $2\ \mu\text{s}$ to charge the capacitor to $\pm 12\ \text{V}$. In the previous prototype, it takes around $50\ \mu\text{s}$ to recharge it.

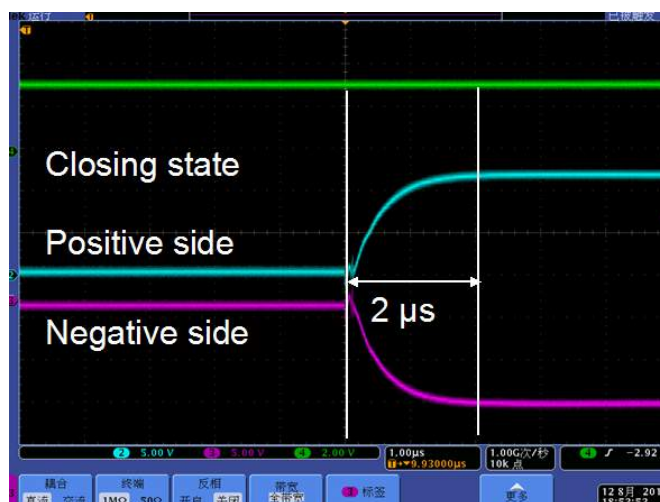


Figure 3.25: The signal from the oscilloscope shows the time of charging a $22\ \text{nF}$ capacitor to the original voltage of $\pm 12\ \text{V}$. Blue: signal from the positive side of the capacitor; Purple: signal from the negative side of the capacitor.

In Figure 3.26, we tested the transition of the prototype by connecting it to a standard

capacitor of 16.5 nF. The operating voltages are -40 and -180 V. When the gating grid driver was triggered by the external TTL (purple), the positive and negative sides of the capacitor were shorted together and had the common voltage of -110 V. This prototype has the turn-on delay of 100 ns which is very similar to the previous ones. Even though we are able to decrease the closing time of the gating grid by introducing another pair of mosfet switches (N2 and P2), the opening time is still too long. This issue is that the gate driver chip which receives the TTL trigger signal and generates a gate signal of ± 10 V for the switches does not respond fast enough for our purposes. To shorten this opening time, the gate driver chip needs to respond quicker and take less time to generate the 10-12 V gate signal.

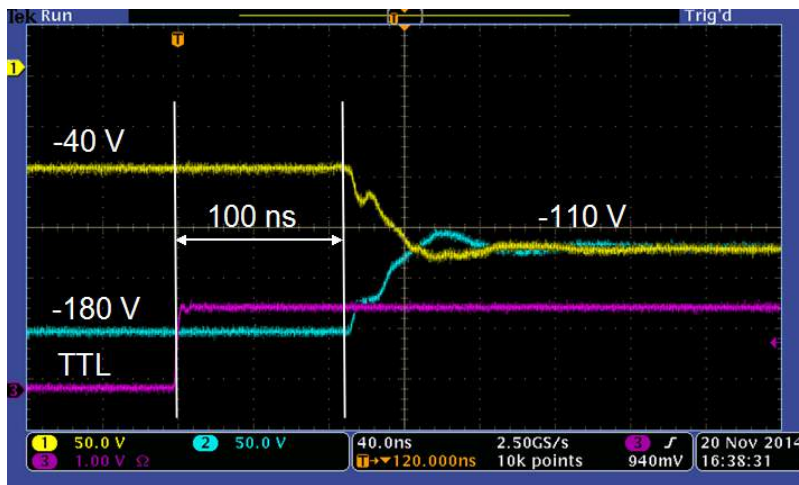


Figure 3.26: The gating grid driver prototype 3 has been tested with a standard capacitor of 16.5 nF. The operating voltages are -40 and -180 V. It has a turn-on delay time of 100 ns. When the gating grid is open, the positive (yellow) and negative (blue) sides of the capacitor are shorted through the mosfet switches and provide to the common voltage of -110 V.

3.3.6 Gating grid driver prototype 4

3.3.6.1 Basic design

To address the slow ramp of the MC14E11 trigger chips in the previous prototype, an improved circuit was developed. In Figure 3.27, the circuit diagram of this new prototype is

shown. It uses the circuit diagram of the prototype 3 but the gate driver chips, MC14E11 were replaced by MIC4420/4429 which can generate the voltage from 0 V to 12 V in 20 ns. In addition, the N-mosfet and P-mosfet switches are driven by the MIC4420 (ND) and MIC4429 (PD), respectively. The gate driver chip is changed to reduce the turn-on delay time of the gating grid driver. In addition, to avoid an unwanted induced signal when the gating grid is opened, the positive and negative wires of the grid needs to be discharged at the same rate. In the previous prototypes, the times required to close the P-mosfet and N-mosfet switches which allow passage of current from both sides are different. The discharging rate of the gating grid corresponds to the RC time constant τ which is defined by R_p , R_n , C_p and C_n in the circuit diagram. The diodes which are connected in parallel to the 1 k Ω resistors in the middle of the circuit diagram are used to hold the gate driving signal stable for a long opening time ($\geq 500 \mu\text{s}$) of the gating grid. In a typical experiment of the S π RIT TPC, the opening time of the gating grid is around 10 μs . Therefore, the diodes are not necessary for the first series of experiments with the P10 filling gas. They could be useful for a much slower gas such as hydrogen or helium.

3.3.6.2 Tests and optimization of version 4 gating grid driver

In Figure 3.28, the gating grid driver prototype 4 has been tested with all power and trigger system without connecting to a standard capacitor or the gating grid. When the TTL signal (yellow) is supplied to the TTL-1 input, the two switches, N1 and P1 are closed. The +HV (-20 V) and -HV (-160 V) supplies are connected through those switches. The switches, N1 and P1, were closed at 45 ns after they were triggered. In this prototype, we therefore reduced the turn-on delay time of the circuit from 120 ns (prototype 1) to 50 ns, however, we can see that the negative switch (in green) opens about 2 ns faster than the positive switch

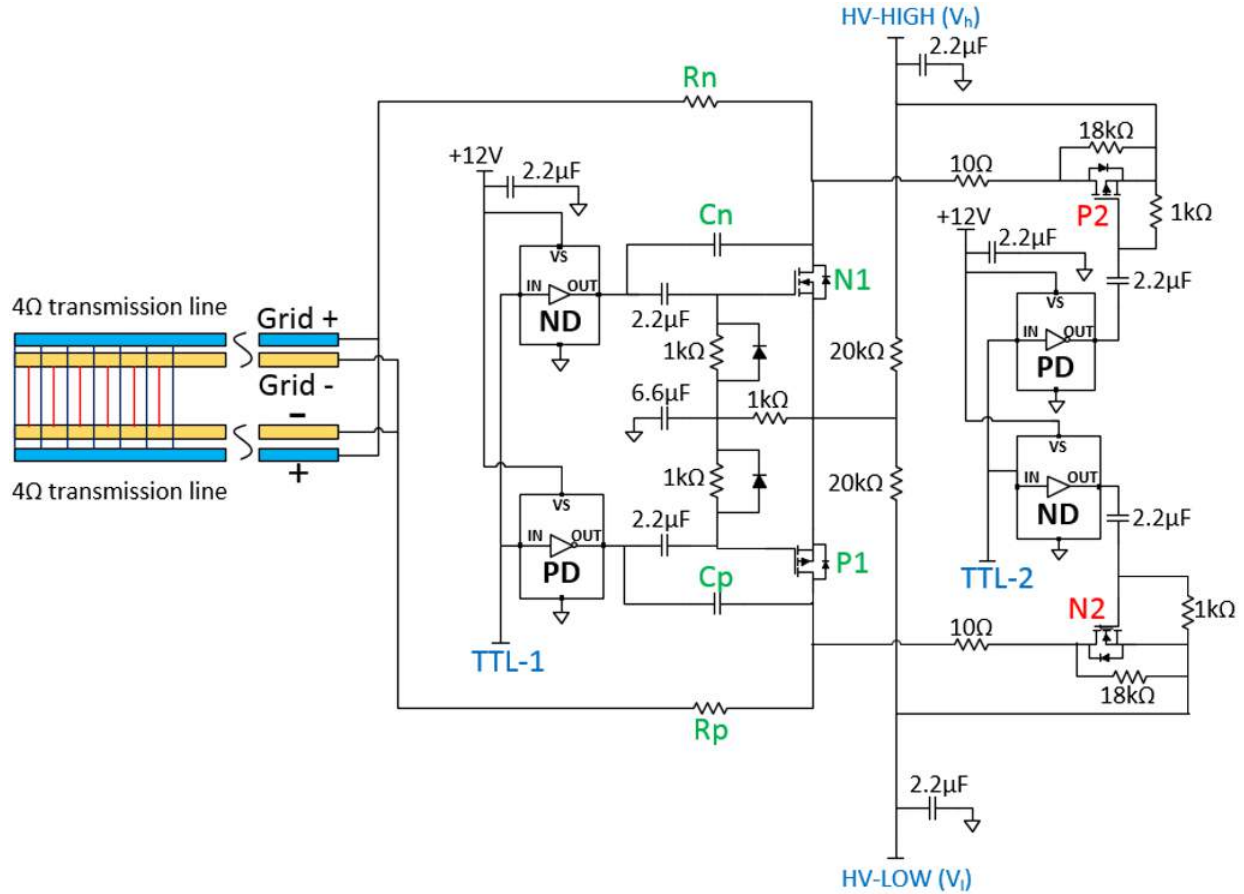


Figure 3.27: Circuit diagram of the gating grid driver prototype 4

(in blue). After closing there is an oscillation with a period of about 3 ns, which is out of phase between the positive and negative sides. Such a fast oscillation would be too fast for the pad electronics to amplify. The pad electronics would only amplify slower Fourier components of the signal with periods at least an order of magnitude longer.

Figure 3.29 shows the PCB of the gating grid driver prototype 4. There are places for adjusting components which are R_p , R_n , C_p and C_n . They are used for matching the discharging rate of the two sides of the gating grid. For the testing, we connect the gating grid driver to the $S\pi$ RIT TPC and run with operating voltages of -40 and -180 V. The values of C_p and C_n are 100 pF. The resistance of the IRF9640 in series with R_p and IRF640 in series with R_n are 1.6 and 1.7 Ω , respectively.



Figure 3.28: The circuit board is tested without connecting to a standard capacitor. The gating grid driver shorts two power supplies together at 45 ns after it is triggered. Blue: discharging signal from the positive side. Green: discharging signal from the negative side.

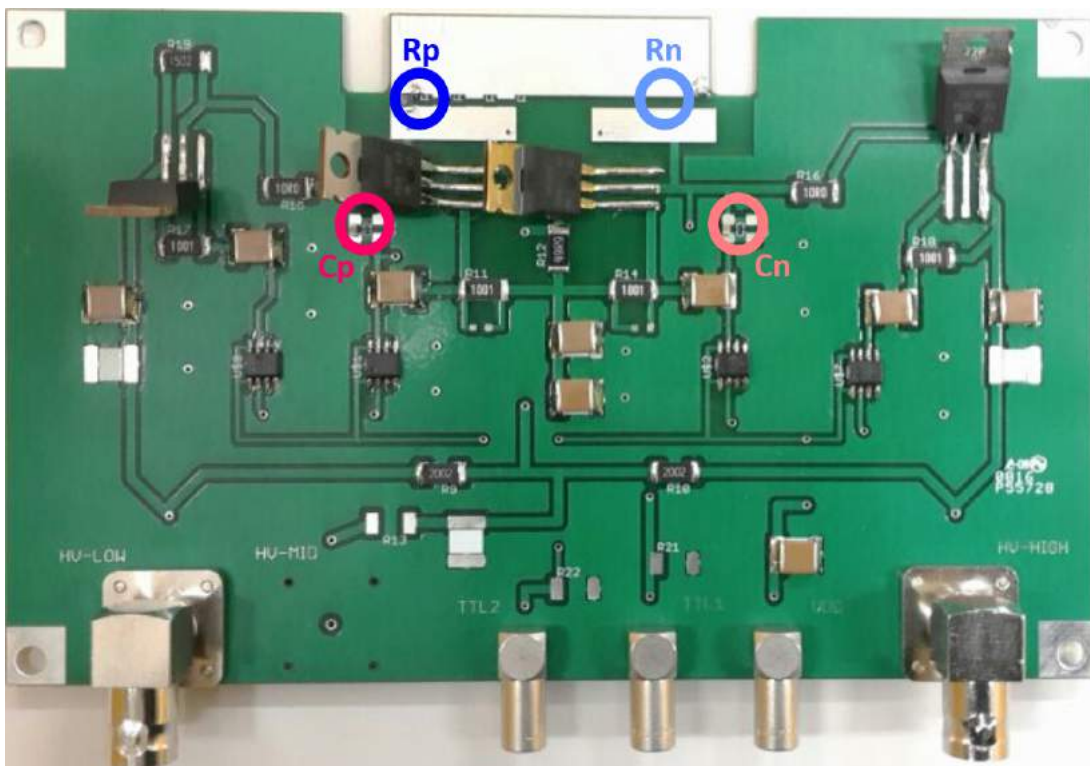
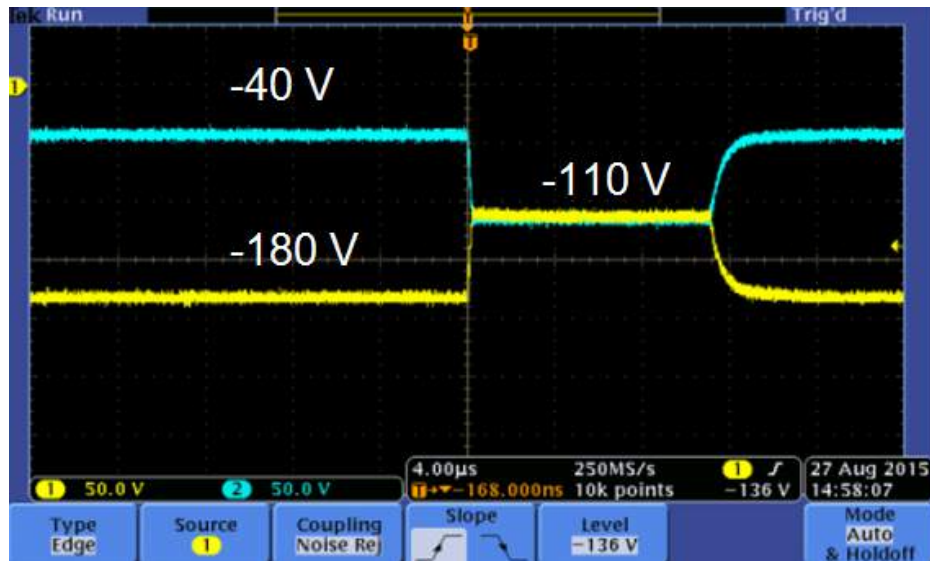


Figure 3.29: Printed circuit board of the gating grid driver prototype 4. The colored circles indicate the conductive pads which can put the adjusting components, R_p , R_n , C_p and C_n on. R_n is mounted on the other side of the board so it is not visible in this picture.

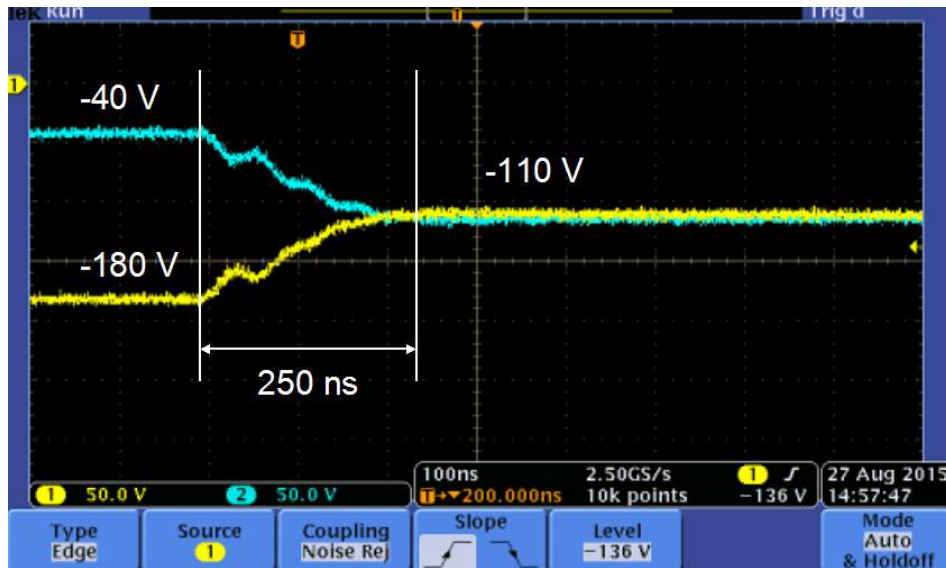
The transition of the gating grid from closed to open state can be seen in Figure 3.30. When the gating grid is closed, the wires are biased to -40 and -180 V, alternatively. Once the TTL signal is sent to the TTL-1 input, the two power supplies are shorted together and provide a common voltage of -110 V. At the end of the TTL-1, another 2- μ s TTL signal is sent to the TTL-2 input to close the gating grid and it takes 2.5 μ s to recharge every wire back to the original voltages. In Figure 3.31, from the readout of the GET Electronics, there is an induced signal detected on the pads. This signal occur during the transition of the gating grid from closed to open state. The signal has a negative peak during the first 450 ns of the transition and then goes to the positive side. The negative signal has the peak height of 800 ADC channels. This induced signal last 1.6 μ s. The maximum of ADC channels that the AGET Electronics can hold is 4096 channels. The negative excursion of this signal is in the direction of the expected signal from real events, which are also negative. We would like to keep the size of the negative peak of the order 1 % of the maximum ADC which corresponds to 50 ADC channels or less. In the typical experiment, the signal from an interesting event also has the negative polarity. It might be possible to accommodate the presence of a negative signal on the pads of a magnitude greater than 50 channels if we decide to skip partial readout and record all of the data on all of the pads for every event. In that case, one could simply record the line shape of the gating grid signal and perform a software subtraction on the data. This is not the ideal option. The GET electronics can be read out in a partial readout mode, which suppresses the readout of channels below a preset threshold. If one could hold the negative excursions of the gating grid pickup signal to less than 50 channels, the threshold could be set above it and only the pads with real data (not gating grid noise) would be read out, reducing the readout time and the size of the data files. This motivated extensive and focused efforts to minimize the negative excursions. Which

such a minimization has the benefit of minimizing the amount of data to be read out, the positive excursions are also important to control. To eliminate the influence of the gating grid pickup noise on the data, however, one would nevertheless want to subtract it from the recorded data. The accuracy of this subtraction is naturally improved if both the negative and the positive excursions of the gating grid noise signal are reduced as much as possible.

This option of partial readout mode motivated optimizing the gating grid noise signal. To study the discharge characteristics of the mosfet switches for the circuit of the prototype 4 and guide out efforts to reduce the gating grid noise, we use a SPICE model of the mosfet switches provided by the manufacturer in the simulation. SPICE (Simulation Program with Integrated Circuit Emphasis) is a computerized circuit simulation program that can be obtained from [71]. N-mosfet model is available at [72] and P-mosfet model is available at [73] <http://www.vishay.com/mosfets/list/product-91086>. In the simulation, the gating grid is replaced by a capacitor of 26.5 nF which approximates the capacitance of the S π RIT TPC gating grid. Figure 3.33 shows the SPICE simulations of the gating grid transitioning from the closed to open and then back to close state. At the beginning of the simulations, the gating grid is closed. Alternate wires represented by the two sides of the capacitor are biased to -40 and -180 V. The N- and P-mosfet switches close at 0.5 μ s. It takes 350 ns for the gating grid to reach the common voltage of -110 V. In this particular simulations, the gating grid closes 4 μ s after opening and it takes 3 μ s to recharge the wire back to the original voltages. We start with the default values of $C_p=C_n=100$ pF and $R_p=R_n=1$ Ω . Figure 3.32 illustrates the SPICE simulation of an ideal circuit. In reality, circuit boards are made of components with imprecise specified values. Resistors can have small inductance values, for example. In addition, the gating grid is more complicated the approximation of a single capacitance of about 26 nF. This demonstrated by the complex noise signals shown in Figure



(a) Transition of the gating grid from opening to closing state



(b) Discharging signals when the gating grid is opened.

Figure 3.30: Test the gating grid driver prototype 4 with operation voltages of -40 and -180 V. the values of C_p and C_n are 100 pF. (a) When the gating grid is closed, alternating wires have the voltages of -40 and -180 V. Once it opens, the two power supplies are shorted together and give the common voltage of -110 V. (b) the opening time of the gating grid is 250 ns.

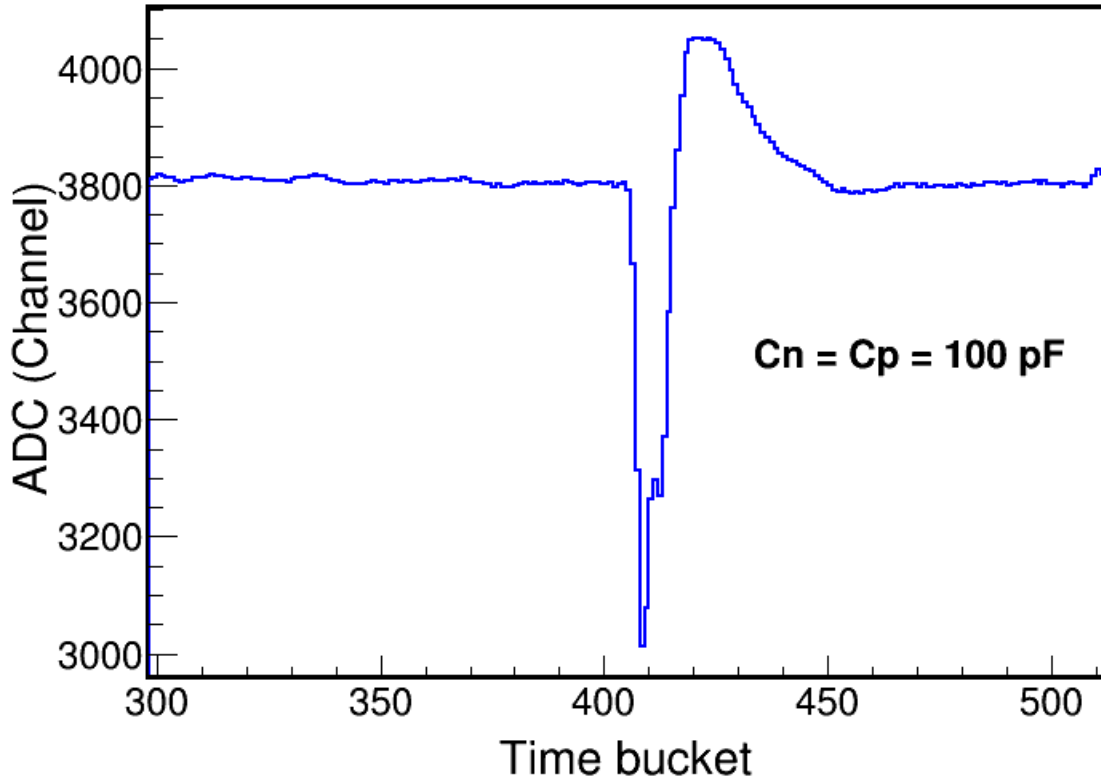


Figure 3.31: There is a induced signal on the pad when the gating grid opens.

3.35 that the spice model does not reproduce. The idea of including the extra capacitors and resistors, C_n , C_p , R_n and R_p associated with the N1 and P1 switches allows adjustment to accommodate real operation of the TPC gating grid. Typically, R_n and R_p control the discharge time while C_n and C_p are adjusted to balance the positive and negative charge.

By changing the values of C_p , C_n , R_p and R_n , one can simulate the situation when the discharge from both positive and negative sides of the wires are not symmetric. Figure 3.33(a) shows the SPICE calculations of the signal from the gating grid transitioning from the closed to open state with $C_p=600$ nF, $C_n=100$ pF and $R_p=0.95$ Ω , $R_n=1.05$ Ω . Here the green line depicts the voltage on the positive side of the gating grid and the red line depicts the voltage on the negative side of the gating grid. In this idealized circuit, the asymmetry of the discharge voltage obtained by adding the positive and negative voltages

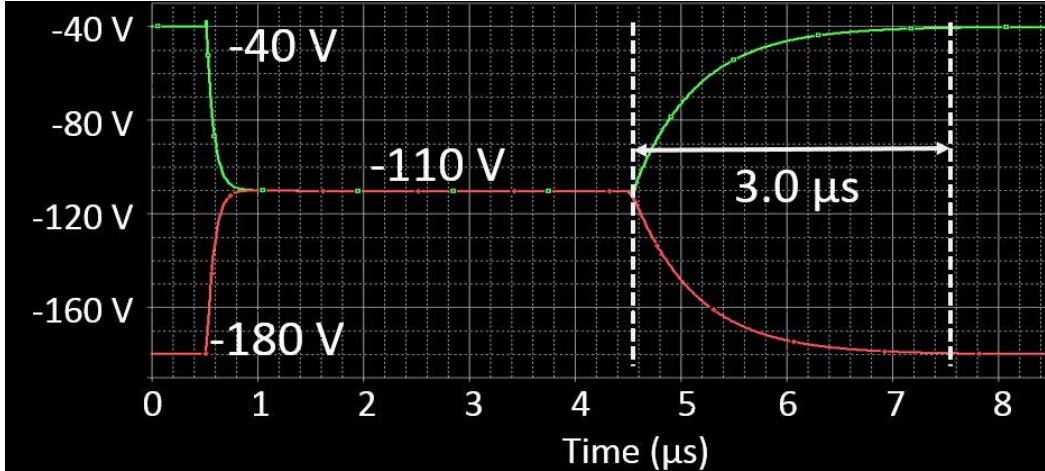
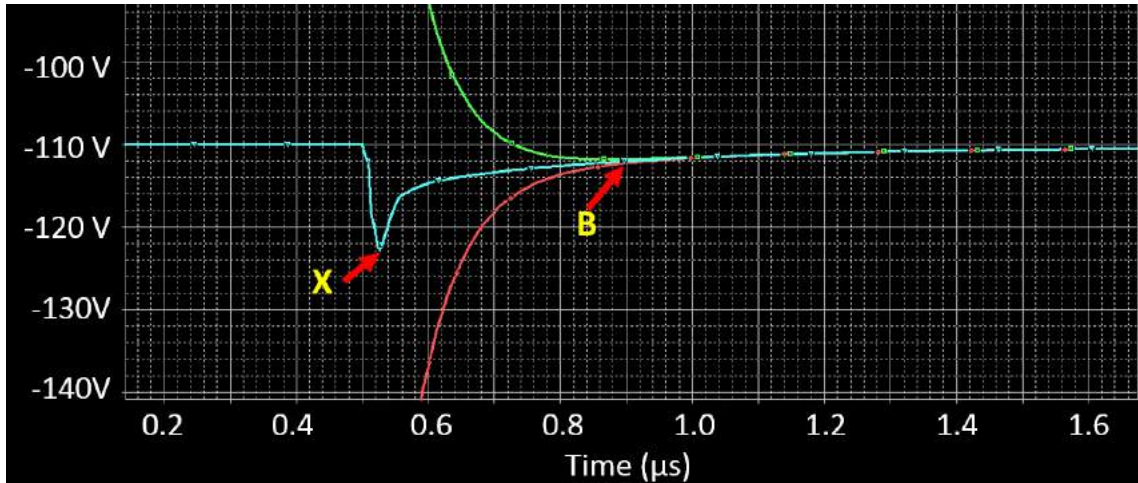
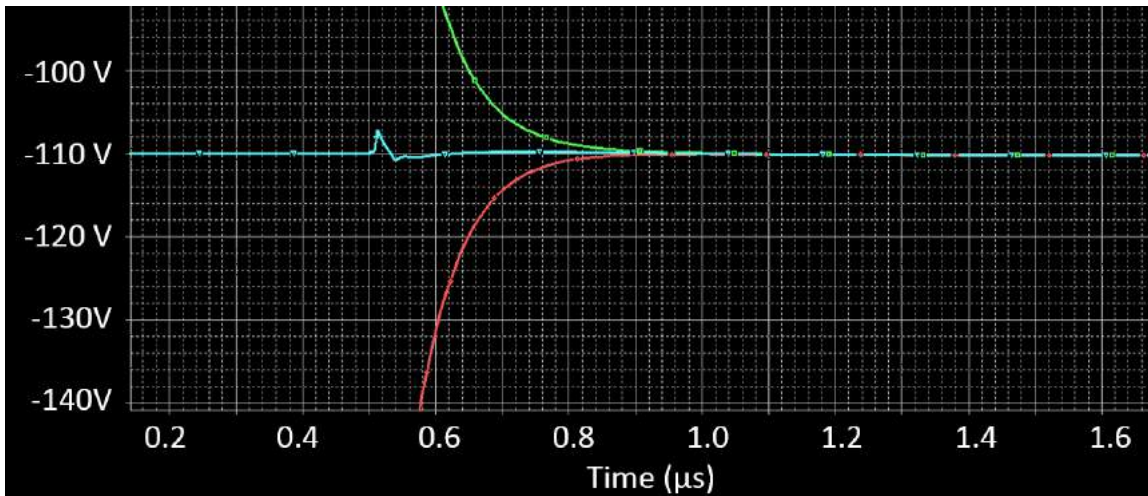


Figure 3.32: Transition of the gating grid from closed to open and back to closed state in SPICE simulation. $C_p=C_n=100$ pF and $R_p = 0.95 \Omega$, $R_n = 1.05 \Omega$.

or obtain the light blue trace. In the SPICE calculations for this circuit, the asymmetry is very small corresponding to an excursion of $X = -13$ V from the common voltage (-110 V) at the minimum. At $0.25 \mu\text{s}$ after opening the gate, the sum of the voltages is $B = -2$ V (1%) from the common voltage of -110 V. To show the effects of tuning the gating grid driver, we vary the values of C_n and C_p in Table 3.2. The plots shown in Figure 3.34 are the dependence of X and B as a function of $(C_p - C_n)$. As expected in the ideal environment of this simulation, the best configuration is when both C_p and C_n have the default values of 100 pF and $R_p=0.95 \Omega$, $R_n=1.05 \Omega$. As shown in Figure 3.33(b) with the best tuned values, the discharge rate is now nearly symmetric and both the X and B values are small at -1 and -0.1 V as shown in Table 3.2. Note that the signals from the $S\pi$ RIT TPC have negative polarity so it is more important to minimize the negative charge in the tuning.

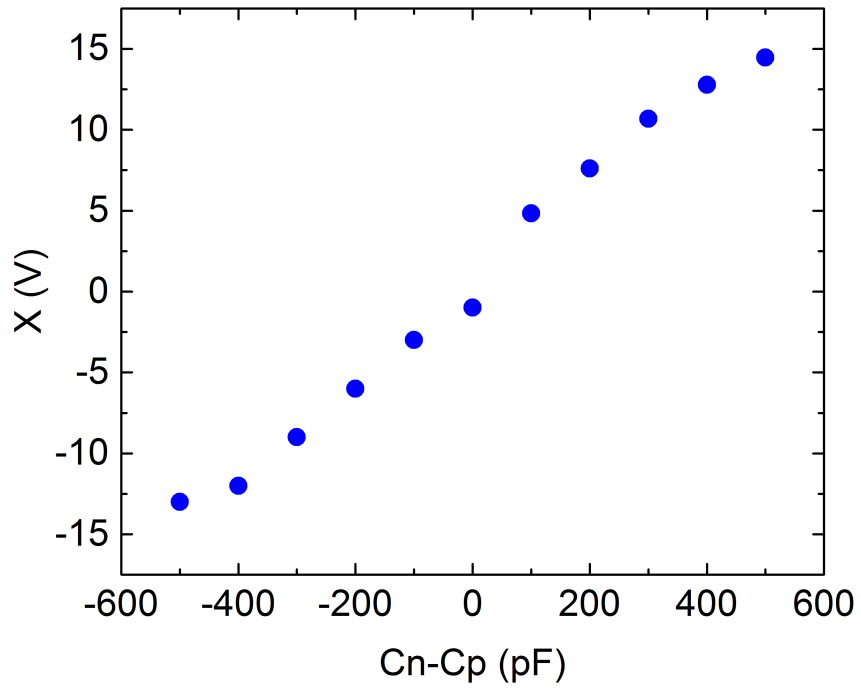


(a)

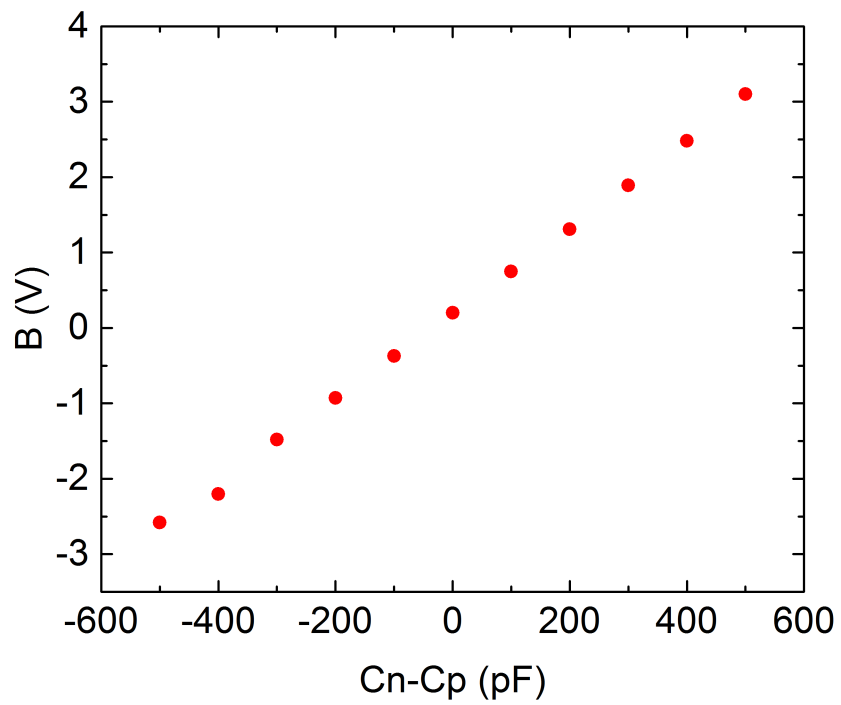


(b)

Figure 3.33: (a) Transition of the gating grid from closed to open state in SPICE simulation, $C_p = 600$ nF and $C_n = 100$ pF and $R_p = 0.95 \Omega$, $R_n = 1.05 \Omega$. (b) The same as (a) with different capacitor values $C_p = 100$ nF and $C_n = 100$ pF and $R_p = 0.95 \Omega$, $R_n = 1.05 \Omega$.



(a) $X(V)$

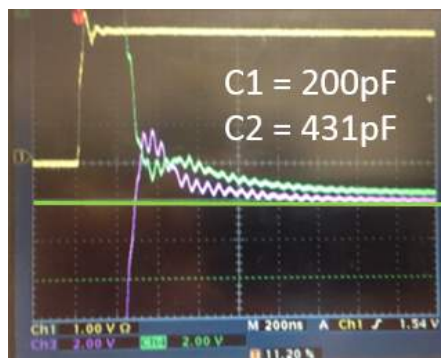


(b) $B(V)$

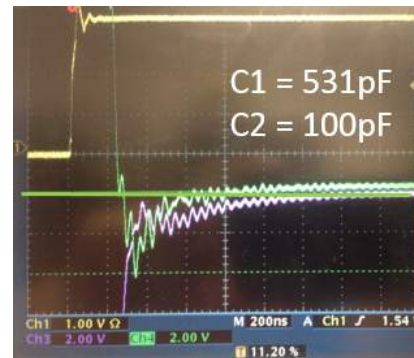
Figure 3.34: The dependence of X and B as a function of $C_n - C_p$.

Table 3.2: The effect of tuning the gating grid driver with C_n and C_p . $R_p = 0.95 \Omega$, $R_n = 1.05 \Omega$.

C_p (pF)	C_n (pF)	$C_n - C_p$ (pF)	X(V) from -110 V	B(V)
100	100	0	-1	0.2
200	100	-100	-3	-0.37
300	100	-200	-6	-0.93
400	100	-300	-9	-1.48
500	100	-400	-12	-2.2
600	100	-500	-13	-2.58
100	200	100	4.84	0.75
100	300	200	7.6	1.31
100	400	300	10.65	1.89
100	500	400	12.78	2.48
100	600	500	14.47	3.1



(a) C_p is less than C_n



(b) C_p is larger than C_n

Figure 3.35: Test the gating grid driver with a standard capacitor of 26 nF and vary C_p and C_n to see the effect from the SPICE simulation. The green line indicates the common voltage level.

3.3.6.3 Measurements and optimization fo the Induced signals on the pads using the GET TPC readout electronics

It is important to assess the influence of the gating grid opening on the readout electronics. To do so, we attached the gating grid driver to the gating grid on the S π RIT TPC and then we opened the gating grid and readout the signal that was induced on the pads during time that the gating grid was opening.

These tests were performed shortly after the readout electronics began to function properly. Thus, the analysis capabilities were limited the exploration of the response of specific selected pads on the pad. Those results are shown in the following.

Table 3.3: Negative peak height of the induced signal from the transition of the gating grid driver

C_p (pF)	C_n (pF)	Peak height (ADC)
100	100	800
100	220	1314
100	270	1724
330	270	751
390	270	415
1000	270	264
1000	330	211
1000	440	105
1000	490	182

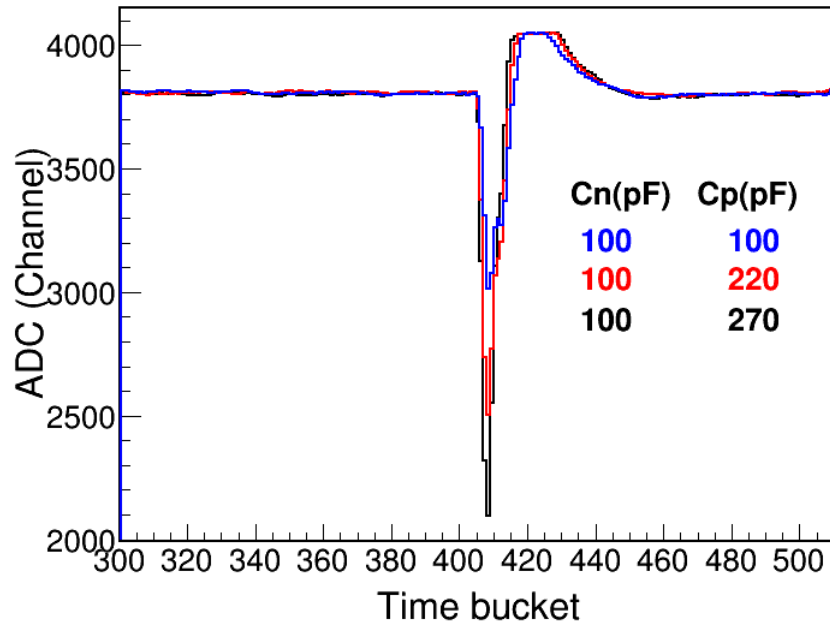


Figure 3.36: Test the gating grid driver with the $S\pi$ RIT TPC by varying C_p and C_n . The size of the negative peak is increasing with C_n .

We tested the gating grid prototype 4 with the $S\pi$ RIT TPC by varying C_p and C_n . The operating voltages are -40 V and -180 V. In Figure 3.36, we show the pulse induced on the pad

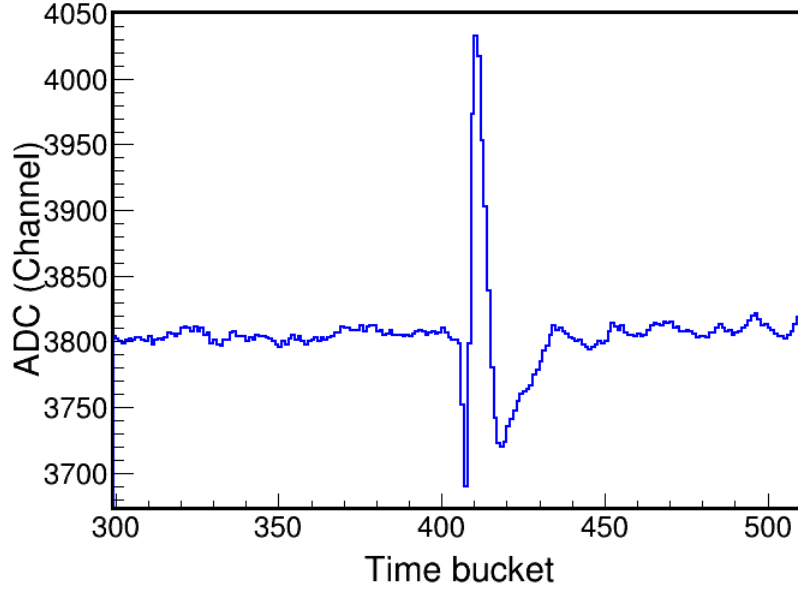


Figure 3.37: Using $C_p = 1000$ pF and $C_n = 440$ pF, the negative peak is reduced from 800 to 105 ADC channels.

for this highest AGET gain range of 120 fC. For results shown below, we show the digitized value for the induced pulse. In this representation, the signal induced by multiplication of electrons near the anode wires would be negative. The amplitude of the negative pulse increases with signal and would be proportional to the dE/dx of the ion that produced this pulse by ionizing the gas somewhere above the pad. The gating grid produces a negative pulse that could be confused with an ionization event. The size of the negative peak of this gating grid noise pulse is increasing with C_n . More detailed result can be seen in Table 3.3. The peak height of the negative signal decreases when C_p is larger than C_n . By adjusting the capacitance of C_p and C_n , the negative peak at 800 ADC channels was reduced to 105 ADC channels for $C_p = 1000$ pF and $C_n = 440$ pF.

In Figure 3.37, we show GET data from the pads for this choice of $C_p = 1000$ pF and $C_n = 440$ pF. As discussed previously, the negative peak has been reduced to 105 ADC channels. There are two places that this signal occur. It would be an added complication to

cancel both negative signals at the same time. On the other hand, the induced signal for $C_p = 1000$ pF and $C_n = 490$ pF has positive peak at the beginning and then go to a negative peak as seen in Figure 3.38. We chose to test whether this type of pulse could be canceled by injecting a external pulse on the ground plane. Given the available equipment, the pulse shown in Figure 3.38 was easier to replicate and try to cancel the negative signal with an external positive signal.

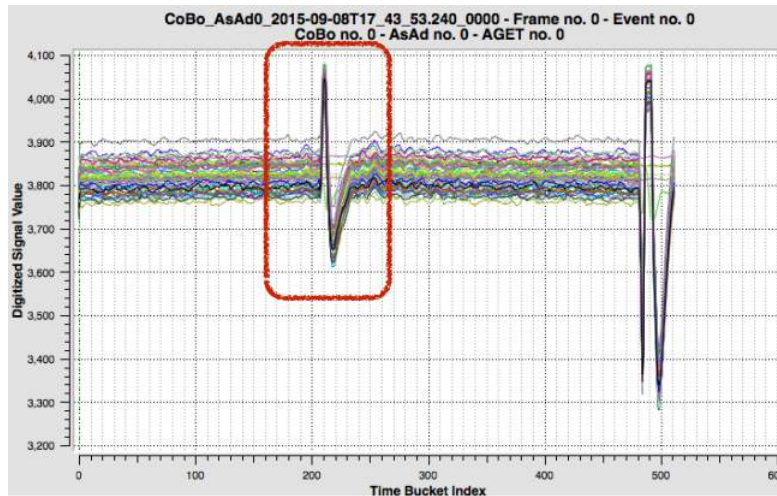


Figure 3.38: Induced signals are readout by AGET Electronics. In this configuration, C_p and C_n are 1000 and 490 pF, respectively.

To test this method, the configuration that C_p and C_n are 1000 and 490 pF was chosen. An external opposite-polarity signal was generated using a timing filter amplifier with an inverted transformer. In Figure 3.39(top), the induced signal from the transition of the gating grid has the negative peak of 182 ADC channels. There are some fluctuations after the gating grid is closed. For reference, each time bucket out of the 512 shown corresponds to 40 ns for this configuration.

As shown in Figure 3.39(bottom), the external signal sending through the ground plane does not perfectly match the induced signal from the gating grid due to the limitation of an electronic module (Tennelec TC-241S). The purpose of this method is to cancel that induced

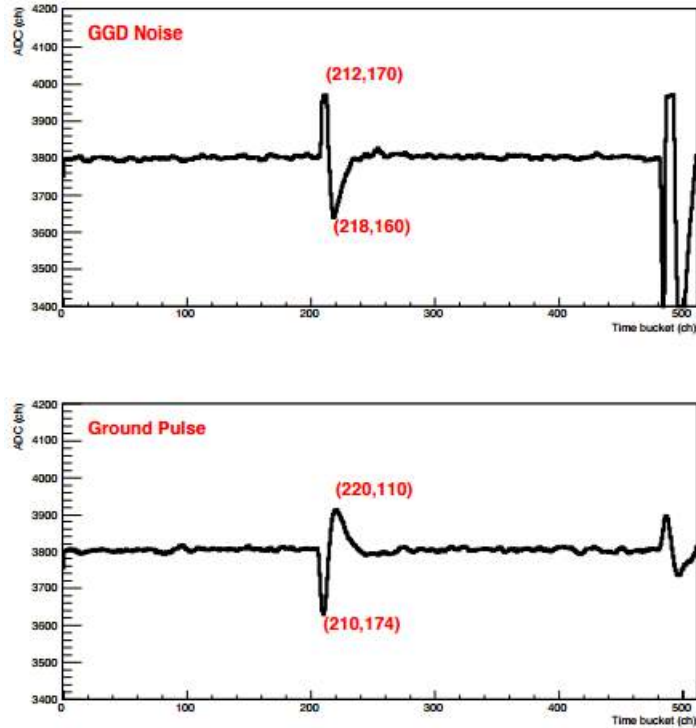


Figure 3.39: Top panel: the induced signal comes from the transition of the gating grid. Bottom panel: the external signal which is used to cancel the noise is sent thru the ground plane.

signal if it is possible or make it to be a small positive signal so that it will not trigger the readout electronics.

In Figure 3.40, the superposition signal between the induced signal of the gating grid (black) and an external signal (red) used to cancel the noise has a small negative peak of 50 ADC channels which is around 1.2 % of the maximum ADC channel (4096 channels).

In the original setup, the ground plane is connected to the body of the TPC via a 50 Ω resistor. We examined at the signal from the ground plane during the transition of the gating grid on the oscilloscope and observed a number of quick oscillations. Clearly, the ground plane is strongly coupled to the gating grid, with an estimated capacitance of 1.5 nF between the positive wires to ground plane and 1.5 nF to ground plane. To reduce the coupling, we shorted the ground plane to ground with a dead short. This brings the negative

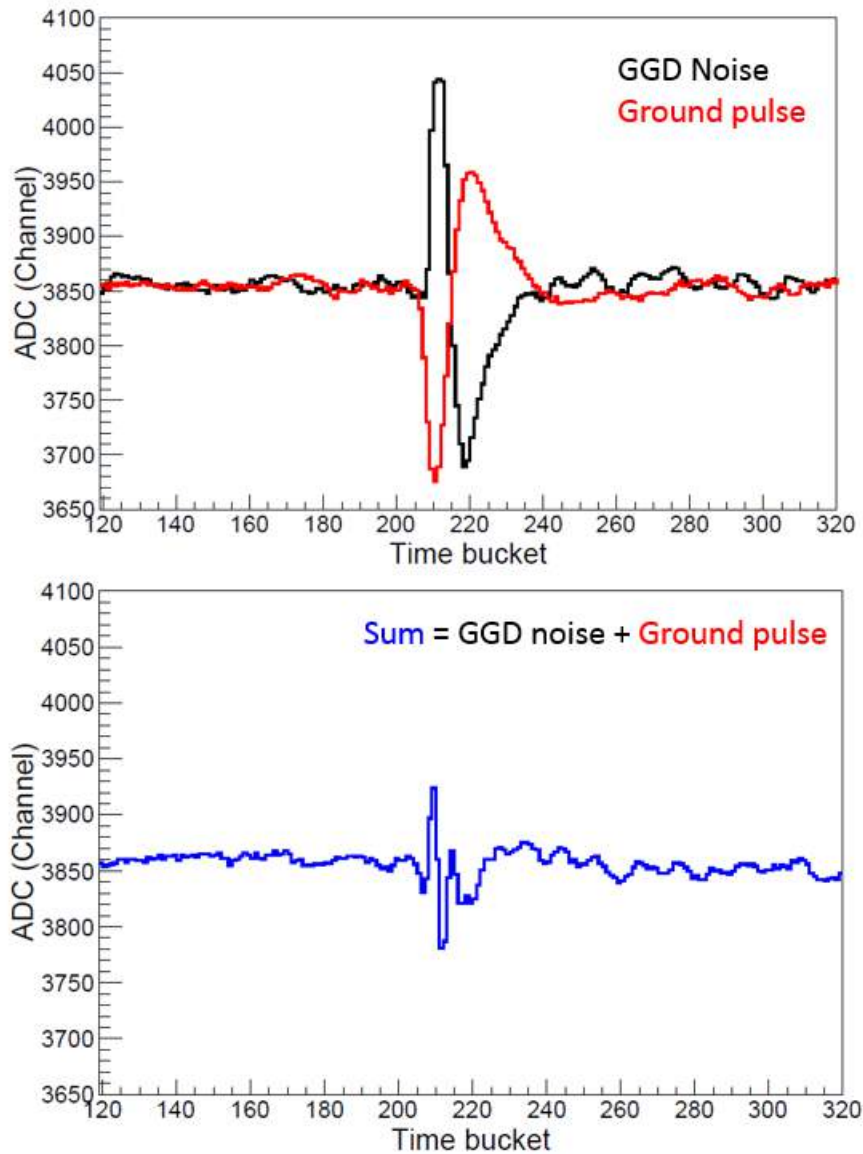


Figure 3.40: Use an external signal (red) which has the opposite polarity if the noise (black) to cancel it. The blue line shows the superposition of those two signal. It has a small negative peak of 50 ADC channels.

peak down to 30 channels. Without opening the TPC, however, we can only do this at the downstream end of the ground plane. A later and more detailed examination showed that the reduction of noise by shorting the ground plane was most effective for pads near the downstream end of the pad plane. It would be interesting to allow the ground plane to be shorted also at the upstream end, but that would require opening the TPC and physically

modifying the the connections to the external ground and for that reason, this has not yet been attempted.

3.3.7 Gating grid driver test

In October 2015, the commissioning experiment of the S π RIT TPC was performed with 200 A MeV ^{79}Se beam outside to SAMURAI magnet. In Figure 3.41, the TPC was complemented by arrays of trigger detectors. To provide centrality selection, we used Multiplicity Trigger Array (MTA) covering the left and right sides of the TPC with 30 modules installed on each sides and the KATANA-Multiplicity arrays, consists of 5 paddles on the downstream left side and 7 paddles on the downstream right side of the TPC. The KATANA-Veto array segment made of three thin scintillators detectors was placed upstream of the KATANA Multiplicity array. The asymmetry of the array is designed for the curved trajectories of the beam and positively charged particles. For the commissioning experiment, the KATANA array was positioned so that the central of KATANA-Veto intercept the beam path. The Active Veto was position at 22 cm upstream of the target so that 4 scintillator detectors surrounding the target generate the veto signal when the beam deviates from the target. All the scintillator detectors were fitted with Multi-Pixel Photon Counters (MPPC). The signals from the S π RIT TPC are read out by the GET electronics (see Section 2.8).

The gating grid test has been done as the following. The beam enters the TPC volume and ionized the gas atoms or molecules. The ionized electrons drift upward to the gating grid. In this test, the anode plane was biased to 680 V so that the number of induced charges do not saturate the read out electronics. The voltage of the cathode was set to -6632 V. To study the transparency of the gating grid as a function of the common average voltage of the gating grid, we bias the gating grid to this value and measure the signal on the pads of the pad

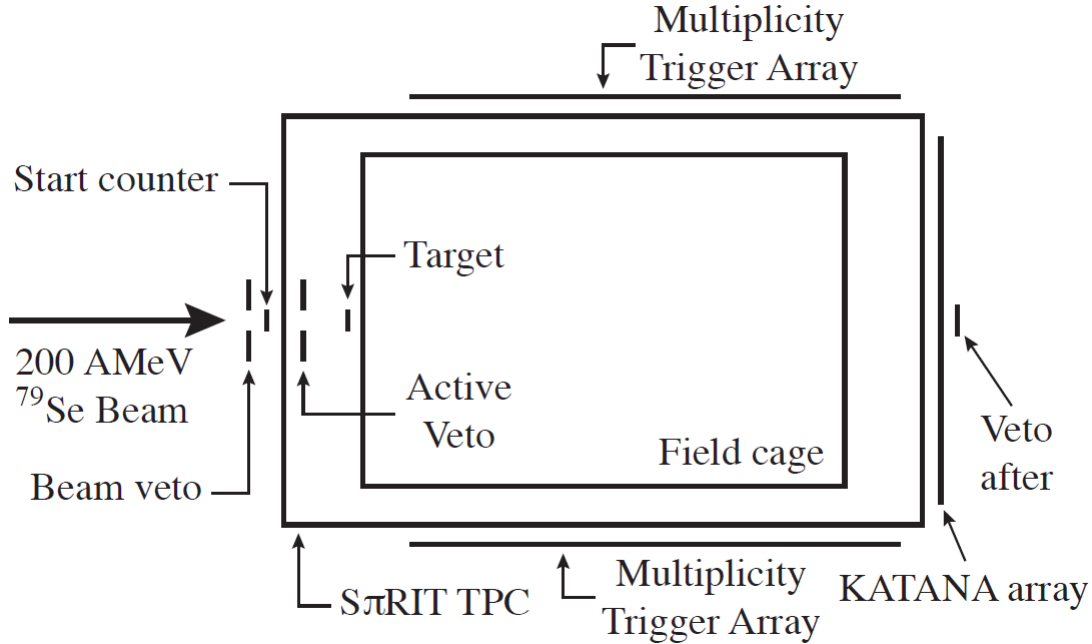


Figure 3.41: A schematic of the commissioning experiment setup of the SπRIT TPC[74].

plane in the SπRIT TPC with the GET electronics readout. These signals are proportional to the number of secondary electrons coming through the gating grid to the anode wires. Then, we measure the gating grid until the induced signals stop increasing and attain a constant corresponding to the condition where the gating grid is transparent to the electrons. If we plot the ratio of signal on the pads divided by the maximum signal attained for a complete transparent gating grid, we obtain the transparency of the gating grid as a function of the gating grid average voltage. We should note that we have also to change the voltages applied to the field cage for each new average gating grid average voltage, as described in Section 2.1.7 in order to obtain the correct drift field for each average gating grid voltage setting. The transparency of the gating grid as a function of the common voltage of the gating grid is shown in Figure 3.42. The performance of the gating grid has been predicted by using Garfield and analytical solution (see Section 3.2). Both Garfield and the analytical solution can predict the transparency of the gating grid accurately. we reiterate that if the voltage

of the cathode is set to a different value as might be expected for a different counter gas, we would also need to adjust the voltage of the gating grid to achieve a full transparency when the gating grid is opened. In this case, we can use the result from the calculation to provide the voltage needed to apply to the gating grid.

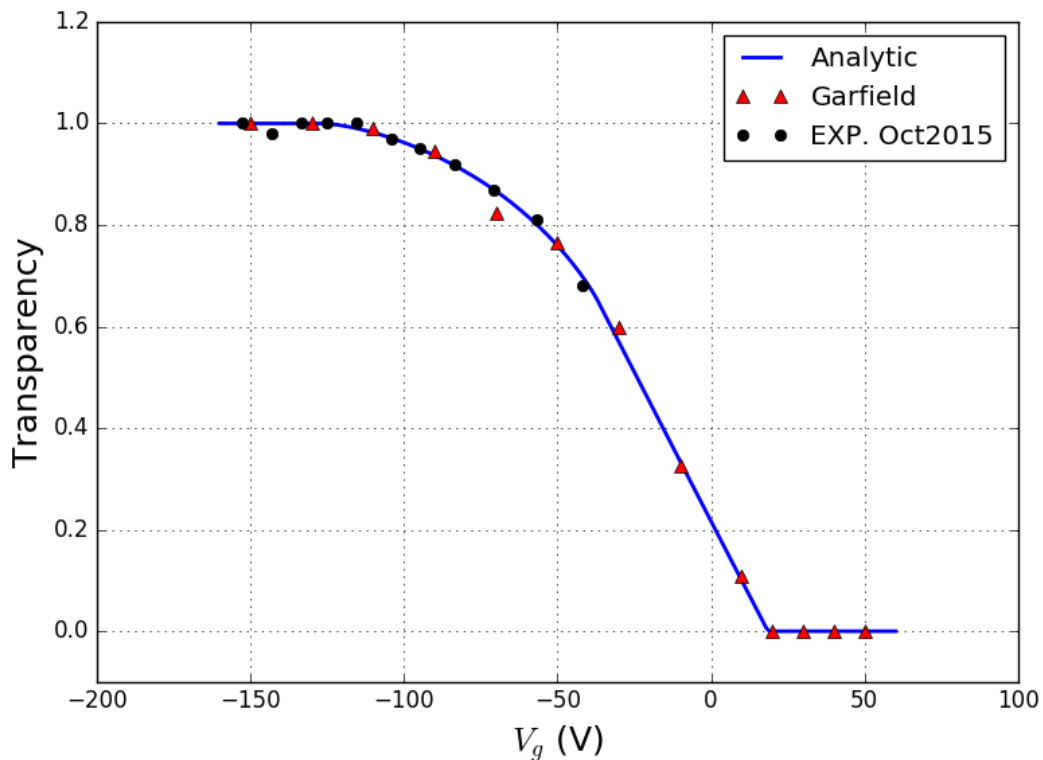


Figure 3.42: Transparency of the gating grid of the $S\pi$ RIT TPC as a function of the common voltage of the gating grid for $V_{cathode} = -6632$ V.

Once the voltage of gating grid that can give a full transparency is known, we have tested the performance of the gating grid in bipolar mode (see Section 3.2.4) which is used to operate the $S\pi$ RIT TPC. The test has been performed as the followings. First of all, the voltages of the cathode and gating grid were set to -6632 and -114.8 V which provide a full transparency for electrons. Then, we applied the offset voltage (ΔV_g) to the alternating wires on the gating grid and measured the signals on the pad plane. The performance of the bipolar gating grid is shown in Figure 3.43. Note that all the gating grid tests have been

performed in the absence of a magnetic field. With $\Delta V_g = 10$ V, we can 50% close the gating grid and the gating grid tends to be completely closed at $\Delta V_g \geq 20$ V. This result relatively agrees with the calculation by Garfield in Figure 3.11 (Section 3.2.4).

We note that the calculated voltage required to close the gating grid is larger for the simulation than for the analytic solution. This occurs because the electrons do not precisely follow the average trajectory given by the electric field lines. This is particularly relevant at higher magnetic field values because the electric field lines near the gating grid wires are not parallel to the magnetic field and this tends to bend the electron trajectories in directions parallel to the gating grid wires. Then random fluctuations about the mean trajectories can allow the electrons to avoid the gating grid and travel to the anode wires. This effect can be modeled by doing Monte Carlo simulations of the electron drift. Such simulations are shown in Figure 3.8.

In the $S\pi$ RIT TPC experiment, the detector will be operated in the magnetic field of 0.5 T. The offset voltage (ΔV_g) required to close the gating grid is ≥ 50 V for 0.5 T. Typically, one would choose a value for ΔV_g that is somewhat larger to compensate for imperfections in the gating grid fabrication. We note that the STAR TPC use a larger value of ΔV_g of ± 75 V to minimize leaks in the gating grid. Thus we have tested the performance of the gating grid and its driver at ± 75 V and it performed satisfactorily. However, the value of ΔV_g is proportional to the induced noise signal when the transition from closed to open state of the gating grid occurs. So there is an incentive to keep ΔV_g as small as possible.

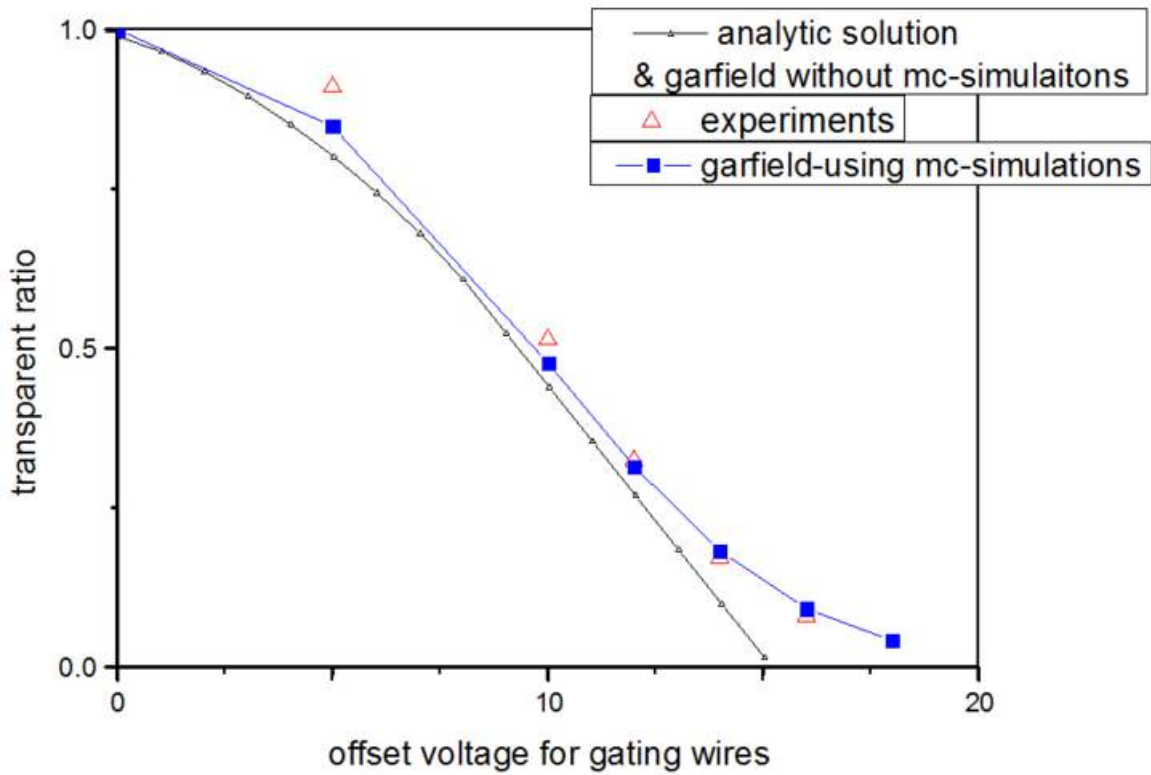


Figure 3.43: Transparency of the gating grid of the S π RIT TPC as a function of the offset voltage (ΔV_g) of the gating grid for $V_{cathode} = -6632$ V.

Chapter 4

Conclusions

4.1 Conclusions

The SAMURAI Pion-Reconstruction and Ion-Tracker Time Projection Chamber ($S\pi$ RIT TPC) has been successfully constructed at Michigan State University as part of an international collaborations to constraint the symmetry energy at supra-saturation density region.

The field properties of the $S\pi$ RIT TPC has been simulated by GARFIELD and ANSYS[®] Maxwell. The result from the simulation shows that the electric field in the drift volume becomes uniform after 2.3 cm from the wall of the field cage. In high density track environment, the distortion of the electric field close to the wall does not significantly affect the track reconstruction of a particle.

The properties of the gating grid of the $S\pi$ RIT TPC has been studied by using GARFIELD and electrostatic analytical solutions. Both GARFIELD and analytical solutions are in a reasonable agreement to describe the transparency of the gating grid as a function of the common average voltage for mono-polar mode and as a function of the offset voltage (ΔV_g) for bipolar mode.

A new gating grid driver for a time projection chamber has been designed to operate the gating grid wires in bipolar mode. The performance of the gating grid driver has been calculated by PSPICE circuit analysis program. According to the simulation, it open and close the gating grid of the $S\pi$ RIT TPC in 0.3 and 2 μ s, respectively. The circuit consists of

2 pairs of N- and P- MOSFET switches and can be adopted to any TPC with the gating grid operated in bipolar mode. We have shown how the PSPICE can be used to understand the properties of the circuit. The gating grid driver has been used successfully in the first beam test of the S π RIT TPC in October, 2015. It will be used on the commissioning experiment of the TPC inside the SAMURAI dipole magnet as well as the first series of the experiments to study heavy ion collisions using the S π RIT TPC at the RIBF in RIKEN, Japan.

BIBLIOGRAPHY

BIBLIOGRAPHY

- [1] E. Pollacco, S. Anvar, H. Baba, P. Baron, D. Bazin, C. Belkhiria, B. Blank, J. Chavas, P. Chomaz, E. Delagnes, F. Druillole, P. Hellmuth, C. Huss, E. Galyaev, B. Lynch, W. Mittig, T. Murakami, L. Nalpas, J.-L. Pedroza, R. Raabe, J. Pibernat, B. Raine, A. Rebi, A. Taketani, F. Saillant, D. Suzuki, N. Usher, and G. Wittwer, *GET: A Generic Electronic System for TPCs for Nuclear Physics Experiments*, Physics Procedia **37** (2012) 1799 – 1804.
- [2] J. Va'vra, *Review of Wire Chamber Aging*, Nucl. Instrum. Meth. **A252** (1986) 547–563.
- [3] C. D. Anderson, *The Positive Electron*, Phys. Rev. **43** (1933) 491–494.
- [4] G. T. Jones, *Positron annihilation in flight*, Physics Education **34** (1999) no. 5, 276.
- [5] H. Hunteler, *Development and Evaluation of a Multiwire Proportional Chamber for a High Resolution Small Animal PET Scanner*. PhD thesis, Westfalische Wilhelms-Universitat Munster Institut fur Kernphysik, 2007.
- [6] G. Charpak, D. Rahm, and H. Steiner, *Some developments in the operation of multiwire proportional chambers*, Nuclear Instruments and Methods **80** (1970) no. 1, 13 – 34.
- [7] A. Breskin, G. Charpak, C. Demierre, S. Majewski, A. Policarpo, F. Sauli, and J. Santiard, *High-accuracy, bidimensional read-out of proportional chambers with short resolution times*, Nuclear Instruments and Methods **143** (1977) no. 1, 29 – 39.
- [8] S. Klein, *The Time Projection Chamber turns 25*, Cern Courier **44** (2004) .
- [9] R. Shane, A. McIntosh, T. Isobe, W. Lynch, H. Baba, et al., *S π RIT: A time-projection chamber for symmetry-energy studies*, arXiv:1409.6343 [physics.ins-det].
- [10] G. F. Knoll, *Radiation Detection and Measurement*. John Wiley & Sons, Inc., 1999.
- [11] W. Blum, W. Riegler, and L. Rolandi, *Particle Detection with Drift Chambers*. Springer, 2008.

- [12] A. Andronic, S. Biagi, P. Braun-Munzinger, C. Garabatos, and G. Tsileidakis, *Drift velocity and gain in argon- and xenon-based mixtures*, Nuclear Instruments and Methods in Physics Research Section A: Accelerators, Spectrometers, Detectors and Associated Equipment **523** (2004) no. 3, 302 – 308.
- [13] R. Bossingham, *Gas Properties*, tech. rep., STAR collaborations, Brookhaven National Laboratory, 1999.
- [14] E. Mathieson, *Induced Charge Distributions in proportional detectors*, tech. rep., Brookhaven National Laboratory, 1991.
- [15] V. Blinov, I. Popkov, and A. Yushkov, *Aging measurements in wire chambers*, Nuclear Instruments and Methods in Physics Research Section A: Accelerators, Spectrometers, Detectors and Associated Equipment **515** (2003) 95 – 107.
- [16] N. N. D. Gupta and S. K. Ghosh, *A Report on the Wilson Cloud Chamber and Its Applications in Physics*, Rev. Mod. Phys. **18** (Apr, 1946) 225–290.
- [17] D. A. Glaser, *Some Effects of Ionizing Radiation on the Formation of Bubbles in Liquids*, Phys. Rev. **87** (Aug, 1952) 665–665.
- [18] D. A. Glaser, *The bubble chamber*, Sci. Am. **192** (1955) no. 2, 46.
- [19] V. E. Barnes, P. L. Connolly, D. J. Crennell, B. B. Culwick, W. C. Delaney, W. B. Fowler, P. E. Hagerty, E. L. Hart, N. Horwitz, P. V. C. Hough, J. E. Jensen, J. K. Kopp, K. W. Lai, J. Leitner, J. L. Lloyd, G. W. London, T. W. Morris, Y. Oren, R. B. Palmer, A. G. Prodell, D. Radojčić, D. C. Rahm, C. R. Richardson, N. P. Samios, J. R. Sanford, R. P. Shutt, J. R. Smith, D. L. Stonehill, R. C. Strand, A. M. Thorndike, M. S. Webster, W. J. Willis, and S. S. Yamamoto, *Observation of a Hyperon with Strangeness Minus Three*, Phys. Rev. Lett. **12** (Feb, 1964) 204–206.
- [20] J. J. Aubert, U. Becker, P. J. Biggs, J. Burger, M. Chen, G. Everhart, P. Goldhagen, J. Leong, T. McCorriston, T. G. Rhoades, M. Rohde, S. C. C. Ting, S. L. Wu, and Y. Y. Lee, *Experimental Observation of a Heavy Particle J*, Phys. Rev. Lett. **33** (Dec, 1974) 1404–1406.
- [21] J. E. Augustin, A. M. Boyarski, M. Breidenbach, F. Bulos, J. T. Dakin, G. J. Feldman, G. E. Fischer, D. Fryberger, G. Hanson, B. Jean-Marie, R. R. Larsen, V. Lüth, H. L. Lynch, D. Lyon, C. C. Morehouse, J. M. Paterson, M. L. Perl, B. Richter, P. Rapidis, R. F. Schwitters, W. M. Tanenbaum, F. Vannucci, G. S. Abrams, D. Briggs, W. Chinowsky, C. E. Friedberg, G. Goldhaber, R. J. Hollebeek, J. A. Kadyk, B. Lulu,

- F. Pierre, G. H. Trilling, J. S. Whitaker, J. Wiss, and J. E. Zipse, *Discovery of a Narrow Resonance in e^+e^- Annihilation*, Phys. Rev. Lett. **33** (Dec, 1974) 1406–1408.
- [22] G. Charpak, R. Bouclier, T. Bressani, J. Favier, and C. Zupancic, *The use of multiwire proportional counters to select and localize charged particles*, Nuclear Instruments and Methods **62** (1968) no. 3, 262 – 268.
- [23] G. Charpak and F. Sauli, *Multiwire proportional chambers and drift chambers*, Nuclear Instruments and Methods **162** (1979) no. 1, 405 – 428.
- [24] J. Marx and D. Nygren, *The Time Projection Chamber*, Phys. Today **31N10** (1978) 46.
- [25] R. M. Barnett, C. D. Carone, D. E. Groom, T. G. Trippe, C. G. Wohl, B. Armstrong, P. S. Gee, G. S. Wagman, F. James, M. Mangano, K. Mönig, L. Montanet, J. L. Feng, H. Murayama, J. J. Hernández, A. Manohar, M. Aguilar-Benitez, C. Caso, R. L. Crawford, M. Roos, N. A. Törnqvist, K. G. Hayes, K. Hagiwara, K. Nakamura, M. Tanabashi, K. Olive, K. Honscheid, P. R. Burchat, R. E. Shrock, S. Eidelman, R. H. Schindler, A. Gurtu, K. Hikasa, G. Conforto, R. L. Workman, C. Grab, and C. Amsler, *Review of Particle Physics*, Phys. Rev. D **54** (Jul, 1996) 1–708.
- [26] L. Landau, *On the energy loss of fast particles by ionization*, J. Phys.(USSR) **8** (1944) 201–205.
- [27] F. Sauli, *Principles of operation of multiwire proportional and drift chambers*, Lectures given in the Academic Training Programme of CERN (1977) .
- [28] S. N. Ahmed, *3 - Gas-filled detectors*, in *Physics and Engineering of Radiation Detection (Second Edition)*, S. N. Ahmed, ed., pp. 157 – 231. Elsevier, second edition ed., 2015.
- [29] R. S. Wolff, *Measurement of the gas constants for various proportional-counter gas mixtures*, Nuclear Instruments and Methods **115** (1974) no. 2, 461 – 463.
- [30] R. Hendricks, *The gas amplification factor in xenon filled proportional counters*, Nuclear Instruments and Methods **102** (1972) no. 2, 309 – 312.
- [31] R. Allemand and G. Thomas, *Nouveau dtecteur de localisation*, Nuclear Instruments and Methods **137** (1976) no. 1, 141 – 149.

- [32] B. Duval, J. Barth, R. Deslattes, A. Henins, and G. Luther, *Position-sensitive X-ray detector*, Nuclear Instruments and Methods in Physics Research **222** (1984) no. 1, 274 – 278.
- [33] G. Luther, P. Cowan, A. Henins, and S. Brennan, *New two dimensional position sensitive proportional detectors using charge division*, Nuclear Instruments and Methods in Physics Research Section A: Accelerators, Spectrometers, Detectors and Associated Equipment **246** (1986) no. 1, 537 – 540.
- [34] H. J. Hilke, *Time projection chambers*, Reports on Progress in Physics **73** (2010) no. 11, 116–201.
- [35] H. Sato, T. Kubo, Y. Yano, K. Kusaka, J. Ohnishi, K. Yoneda, Y. Shimizu, T. Motobayashi, H. Otsu, T. Isobe, T. Kobayashi, K. Sekiguchi, T. Nakamura, Y. Kondo, Y. Togano, T. Murakami, T. Tsuchihashi, T. Orikasa, and K. Maeta, *Superconducting Dipole Magnet for SAMURAI Spectrometer*, Applied Superconductivity, IEEE Transactions on **23** (June, 2013) .
- [36] T. Kobayashi, N. Chiga, T. Isobe, Y. Kondo, T. Kubo, K. Kusaka, T. Motobayashi, T. Nakamura, J. Ohnishi, H. Okuno, H. Otsu, T. Sako, H. Sato, Y. Shimizu, K. Sekiguchi, K. Takahashi, R. Tanaka, and K. Yoneda, *SAMURAI spectrometer for RIbeam experiments*, Nuclear Instruments and Methods in Physics Research Section B: Beam Interactions with Materials and Atoms **317, Part B** (2013) 294 – 304.
- [37] T. Kubo, *In-flight RI beam separator BigRIPS at RIKEN and elsewhere in Japan*, Nuclear Instruments and Methods in Physics Research Section B: Beam Interactions with Materials and Atoms **204** (2003) 97 – 113. 14th International Conference on Electromagnetic Isotope Separators and Techniques Related to their Applications.
- [38] O. Kamigaito, M. Kase, N. Sakamoto, Y. Miyazawa, E. Ikezawa, N. Fukunishi, S. Kohara, M. Fujimaki, M. Hemmi, T. Chiba, Y. Chiba, H. Ryuto, A. Goto, and Y. Yano, *Construction of a booster linac for the RIKEN heavy-ion linac*, Review of Scientific Instruments **76** (2005) no. 1, .
- [39] Y. Yano, *The RIKEN RI Beam Factory Project: A status report*, Nuclear Instruments and Methods in Physics Research Section B: Beam Interactions with Materials and Atoms **261** (2007) no. 1-2, 1009 – 1013.
- [40] G. Rai et al., *A TPC detector for the study of high multiplicity heavy ion collisions*, Nuclear Science, IEEE Transactions on **37** (1990) 56–64.

- [41] F. Sauli, *GEM: A new concept for electron amplification in gas detectors*, Nuclear Instruments and Methods in Physics Research Section A: Accelerators, Spectrometers, Detectors and Associated Equipment **386** (1997) no. 2, 531 – 534.
- [42] Y. Giomataris, P. Rebourgeard, J. Robert, and G. Charpak, *MICROMEAS: a high-granularity position-sensitive gaseous detector for high particle-flux environments*, Nuclear Instruments and Methods in Physics Research Section A: Accelerators, Spectrometers, Detectors and Associated Equipment **376** (1996) no. 1, 29 – 35.
- [43] O. Kiselev, O. Prokofiev, and A. Vorobyov, *Proceedings of the 7th International Wire Chamber Conference Measurement of electron drift velocities and Lorentz angles in fast gas mixtures*, Nuclear Instruments and Methods in Physics Research Section A: Accelerators, Spectrometers, Detectors and Associated Equipment **367** (1995) no. 1, 306 – 310.
- [44] Schultz, G., Charpak, G., and Sauli, F., *Mobilities of positive ions in some gas mixtures used in proportional and drift chambers*, Rev. Phys. Appl. (Paris) **12** (1977) no. 1, 67–70.
- [45] T. Yamashita, H. Kobayashi, A. Konaka, H. Kurashige, K. Miyake, M. Morii, T. Nakamura, T. Nomura, N. Sasao, Y. Fukushima, M. Nomachi, O. Sasaki, F. Suekane, and T. Taniguchi, *Measurements of the electron drift velocity and positive-ion mobility for gases containing CF₄*, Nuclear Instruments and Methods in Physics Research Section A: Accelerators, Spectrometers, Detectors and Associated Equipment **283** (1989) no. 3, 709 – 715.
- [46] K. T. A. L. Burm, *Calculation of the Townsend Discharge Coefficients and the Paschen Curve Coefficients*, Contributions to Plasma Physics **47** (2007) no. 3, 177–182.
- [47] R. Veenhof, *Choosing a gas mixture for the ALICE TPC*, tech. rep., CERN, 2003. ALICE-INT-2003-29.
- [48] J. Gawłowski, J. Maurin, and J. Niedzielski, *Argon ionization detector sensitive to hydrogen*, Journal of Chromatography A **168** (1979) no. 1, 1 – 7.
- [49] E.-G. Kim and J.-L. Bredas, *The nature of the aluminum-aluminum oxide interface: A nanoscale picture of the interfacial structure and energy-level alignment*, Organic Electronics **14** (2013) no. 2, 569 – 574.

- [50] F. Sauli, *Gaseous Radiation Detectors: Fundamentals and Applications*. Cambridge Monographs on Particle Physics, Nuclear Physics and Cosmology. Cambridge University Press, 2014.
- [51] R. Veenhof, *Garfield: recent developments*, Nuclear Instruments and Methods in Physics Research Section A: Accelerators, Spectrometers, Detectors and Associated Equipment **419** (1998) no. 2-3, 726 – 730.
- [52] I. Lehraus, R. Matthewson, and W. Tejessy, *MATERIALS TEST FACILITY FOR THE ALEPH TPC*, tech. rep., CERN, 1989. ALEPH-89-089.
- [53] U. J. Becker, Y. H. Chang, J. F. Donahue, M. E. Sarakinos, G. E. Sasser, and B. R. Smith, *Calibration setup for drift chamber gases*, Nuclear Instruments and Methods in Physics Research Section A: Accelerators, Spectrometers, Detectors and Associated Equipment **306** (1991) no. 1, 194 – 199.
- [54] T. Kunst, B. Gtz, and B. Schmidt, *Precision measurements of magnetic deflection angles and drift velocities in crossed electric and magnetic fields*, Nuclear Instruments and Methods in Physics Research Section A: Accelerators, Spectrometers, Detectors and Associated Equipment **324** (1993) no. 1, 127 – 140.
- [55] U. J. Becker, Y.-H. Chang, J. P. Rodin, and B. R. Smith, *Drift velocity and deflection in non-perpendicular electric and magnetic fields*, Nuclear Instruments and Methods in Physics Research Section A: Accelerators, Spectrometers, Detectors and Associated Equipment **360** (1995) no. 3, 476 – 480.
- [56] W. Betts et al., *Studies of Several Wire nad Pad Configurations for the STAR TPC*, Tech. Rep. 263, STAR Collaboration, 1996.
- [57] E. Gatti, A. Longoni, P. Semenza, and H. Okuno, *Optimum geometry for strip cathodes or grids in MWPC for avalanche localization along the anode wires*, Nucl.Instrum.Meth. **163** (1979) 83–92.
- [58] E. Mathieson and J. Gordon, *Cathode Charge Distributions in Multiwire Chambers. 2: Approximate and Empirical formulae*, Nucl.Instrum.Meth. **A227** (1984) 277–282.
- [59] W. Baldini et al., *A Laser Based Instrument for MWPC Wire Tension Measurement*, tech. rep., CERN, 2007. CERN-LHCb-2007-120.
- [60] T. Liu, C. Horn, A. Junique, C. Lippmann, M. Mager, L. Musa, and T. Richert, *Proceedings of the 2nd International Conference on Technology and Instrumentation in*

Particle Physics (TIPP 2011) Trigger-Induced Mechanical Resonances of Gating Grid Wires in the Multi-Wire Proportional Chambers of the ALICE TPC, Physics Procedia **37** (2012) 472 – 477.

- [61] M. Anderson, J. Berkovitz, W. Betts, R. Bossingham, F. Bieser, R. Brown, M. Burks, et al., *The STAR time projection chamber: a unique tool for studying high multiplicity events at RHIC*, Nuclear Instruments and Methods in Physics Research Section A: Accelerators, Spectrometers, Detectors and Associated Equipment **499** (2003) no. 2-3, 659 – 678.
- [62] H. Sako, H. Sugimura, J. Ahn, Y. Han, S. Hasegawa, S. Hwang, Y. Ichikawa, K. Imai, R. Kiuchi, K. Ozawa, S. Sato, and K. Shirotori, *Development of a prototype GEM TPC with a gating grid for an H-dibaryon search experiment at J-PARC*, Nuclear Instruments and Methods in Physics Research Section A: Accelerators, Spectrometers, Detectors and Associated Equipment **763** (2014) 65 – 81.
- [63] D. Bryman, M. Leitch, I. Navon, T. Numao, P. Schlatter, M. Dixit, C. Hargrove, H. Mes, J. MacDonald, R. Skegg, J. Spuller, R. Burnham, M. Hasinoff, J.-M. Poutissou, G. Azuelos, P. Depommier, J.-P. Martin, R. Poutissou, M. Blecher, K. Gotow, and A. Carter, *Gated grid system used with a time projection chamber*, Nuclear Instruments and Methods in Physics Research Section A: Accelerators, Spectrometers, Detectors and Associated Equipment **234** (1985) no. 1, 42 – 46.
- [64] F. Bohmer, M. Ball, S. Dorheim, C. Hoppner, B. Ketzer, I. Konorov, S. Neubert, S. Paul, J. Rauch, and M. Vandenbroucke, *Simulation of space-charge effects in an ungated GEM-based {TPC}*, Nuclear Instruments and Methods in Physics Research Section A: Accelerators, Spectrometers, Detectors and Associated Equipment **719** (2013) 101 – 108.
- [65] J. Adam, C. Baird, et al., *A study of ageing Effects in wire chamber*, Nucl. Instrum. Meth. **217** (1983) 291–297.
- [66] H. Sipila and M. Jarvinen, *Extended lifetime of a wire chamber*, Nucl. Instrum. Meth. **217** (1983) 298–300.
- [67] P. Nemethy, P. J. Oddone, N. Toge, and A. Ishibashi, *Gated Time Projection Chamber*, Nucl. Instrum. Meth. **212** (1983) 273.
- [68] S. Biagi, *Monte Carlo simulation of electron drift and diffusion in counting gases under the influence of electric and magnetic fields*, Nucl. Instrum. Meth. A **421** (1999) 234–240.

- [69] S. Amendolia, W. Blum, R. Benetta, M. Cherney, F. Fidecaro, J. Froberger, B. Hubbard, R. Jared, I. Lehraus, F. Liello, P. Marocchesi, R. Matthewson, J. May, T. Meyer, E. Milotti, F. Nanni, A. Peisert, M. Price, F. Ragusa, J. Richstein, R. Richter, L. Rolandi, W. Schlatter, J. Sedgbeer, R. Settles, U. Stierlin, M. Takashima, W. Tejessy, G. Tromba, W. Witzeling, S. L. Wu, and W. Wu, *Influence of the magnetic field on the gating of a time projection chamber*, Nuclear Instruments and Methods in Physics Research Section A: Accelerators, Spectrometers, Detectors and Associated Equipment **234** (1985) no. 1, 47 – 53.
- [70] L. W. Nagel and D. O. Pederson, *Simulation Program with Integrated Circuit Emphasis (SPICE)*, tech. rep., Electronics Research Laboratory, College of Engineering, University of California, Berkeley, CA, 1973.
- [71] Cadence Design Systems, *PSPICE*, <http://orcad.com>, June, 2014.
- [72] Vishay Intertechnology, *IRF640 MOSFET Switch*, <http://www.vishay.com/mosfets/list/product-91036/>, 2015.
- [73] Vishay Intertechnology, *IRF9640 MOSFET Switch*, <http://www.vishay.com/mosfets/list/product-91086/>, 2015.
- [74] G. Jhang et al., *Comissioning experiment*, Paper, October, 2015.